Final Report to NASA Johnson Space Center
under NASA Grant No. NAG 9-320
for period 11/1/88 - 1/31/90

ARCHITECTURAL STUDY OF THE DESIGN AND OPERATION OF ADVANCED FORCE FEEDBACK MANUAL CONTROLLERS

by

Dr. Delbert Tesar
Carol Cockrell Curran Chair in Engineering

Whee-kuk Kim
Research Assistant

Department of Mechanical Engineering
University of Texas at Austin
Austin, Texas 78712
(512) 471-3039

January 1990

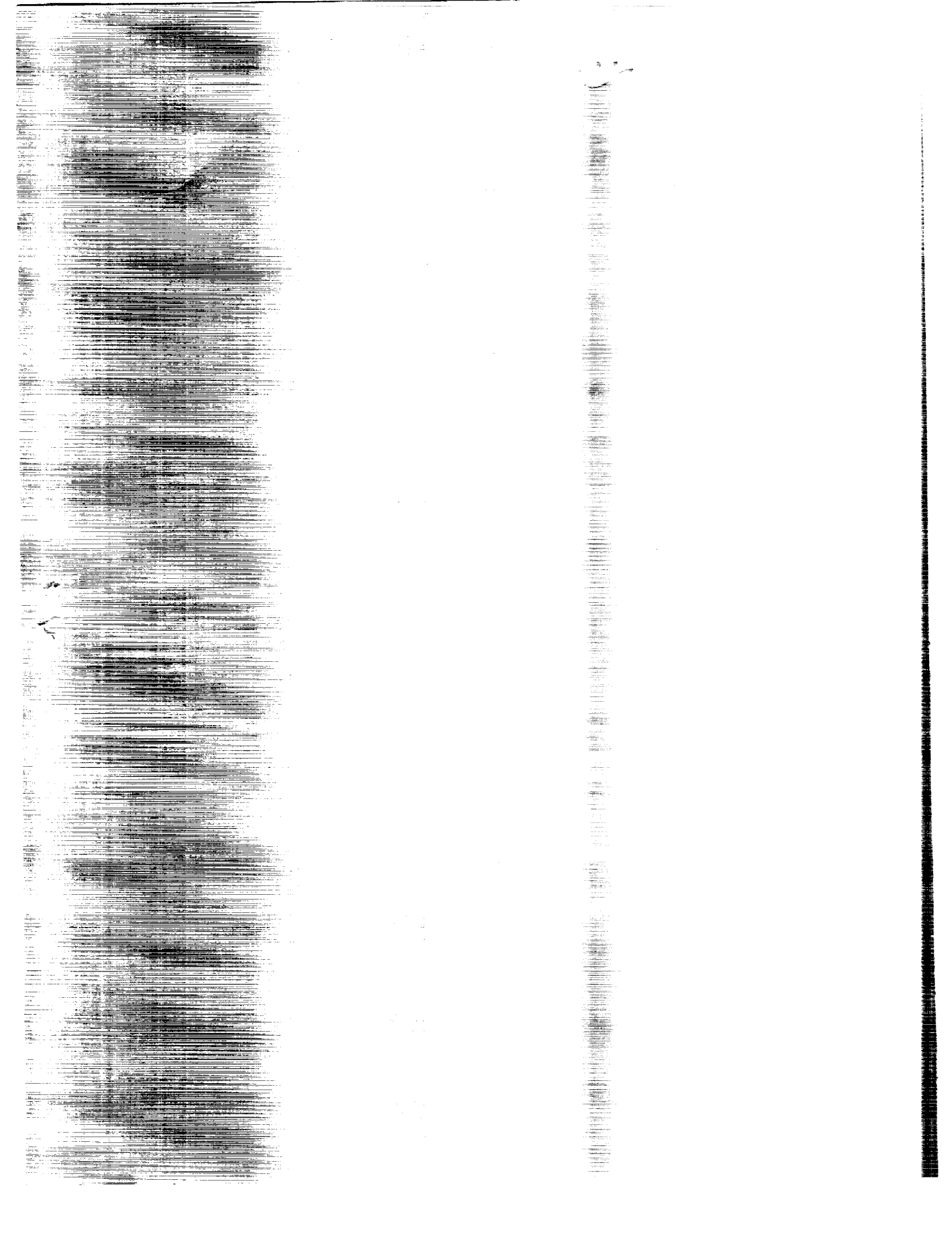

Final Report to NASA Johnson Space Center
under NASA Grant No. NAG 9-320
for period 11/1/88 - 1/31/90

ARCHITECTURAL STUDY OF THE DESIGN AND OPERATION OF ADVANCED FORCE FEEDBACK MANUAL CONTROLLERS

by

Dr. Delbert Tesar
Carol Cockrell Curran Chair in Engineering

Whee-kuk Kim
Research Assistant

Department of Mechanical Engineering
University of Texas at Austin
Austin, Texas 78712
(512) 471-3039

January 1990

ACKNOWLEDGEMENTS

This work was partially supported by the NASA Johnson Space Center (Grant No. NAG 9-320), and the U.S. Department of Energy (Grant No. DOE-FG02-86NE37966). The authors gratefully acknowledge their support.

ABSTRACT

A teleoperator system consists of a manual controller, control hardware/software, and a remote manipulator. It has been employed in either hazardous or unstructured, and/or remote environments (space applications, undersea operations, mining, nuclear reactor maintenance, etc.). In teleoperation, the "man-in-the-loop" is the central concept that brings human intelligence to the teleoperator system. When teleoperation involves contact with an uncertain environment, providing the feeling of "telepresence" to the human operator is one of desired characteristics of the teleoperator system. Unfortunately, most available manual controllers in bilateral or force-reflecting teleoperator systems can be characterized by their bulky size, high costs, or lack of smoothness and transparency, and elementary architectures.

To investigate other alternatives, a force-reflecting, 3 degree of freedom (dof) spherical manual controller is designed, analyzed, and implemented as a test bed demonstration in this research effort. To achieve an improved level of design to meet criteria such as compactness, portability (light weight), and a somewhat enhanced force-reflecting capability, the demonstration manual controller employs high gear-ratio reducers. To reduce the effects of the inertia and friction on the system, various force control strategies are applied and their performance investigated. The spherical manual controller uses a parallel geometry to minimize inertial and gravitational effects on its primary task of transparent information transfer.

As an alternative to the spherical 3-dof manual controller, a new conceptual hybrid (or parallel) spherical 3-dof module is introduced with a full kinematic analysis. Also, the resulting kinematic properties are compared to

those of other typical spherical 3-dof systems. The conceptual design of a parallel 6-dof manual controller and its kinematic analysis is presented. This 6-dof manual controller is similar to the Stewart Platform with the actuators located on the base to minimize the dynamic effects. Finally, a combination of the new 3-dof and 6-dof concepts is presented as a feasible test-bed for enhanced performance in a 9-dof system.

TABLE OF CONTENTS

CHAPTER 1

Introduction

A human's continuous desire to extend his/her vulnerable physical capabilities has been shown in the development of various mechanisms such as the automobile, the space shuttle, robots, etc. As machines become more complex and increasingly self-contained in decision-making capability, the temptation is to assume that they are autonomous.

In fact, what we can surely suggest is that human intervention will be less frequent but, when it is required, it will occur at a higher level and therefore require a better interface (visual, kinesthetic, voice-activated, etc.). Currently, only simple, repetitive tasks can be performed autonomously, without human intervention; almost all unstructured, unpredictable and complex tasks require some human guidance and intelligence. Hence, as system technology develops, there will be a greater need for man-machine interfaces–not less. The man-machine interface has been developed as a natural step in the evolution towards autonomous systems.

The "man-in-the-loop" is the central concept of teleoperation. The essential role of the teleoperation is to increase the level of "telepresence" to the point where the human operator perceives the artificial interface environment as if it were the real environment; a "transparent" interface must exist to maximize

humans' limited sensing and communicative capabilities.

1–1 Teleoperator systems

A teleoperator system consists of a manual controller, control hardware/software, and a remote manipulator. In teleoperation, interactions among a human operator, a teleoperator system, and the task environment are involved. The main function of the teleoperator system is to assist the human operator in performing complex, uncertain tasks in hostile/remote environments (undersea, space, nuclear reactors, mining, etc.). The schematic information flow of teleoperator systems can be described as in Figure 1–1.

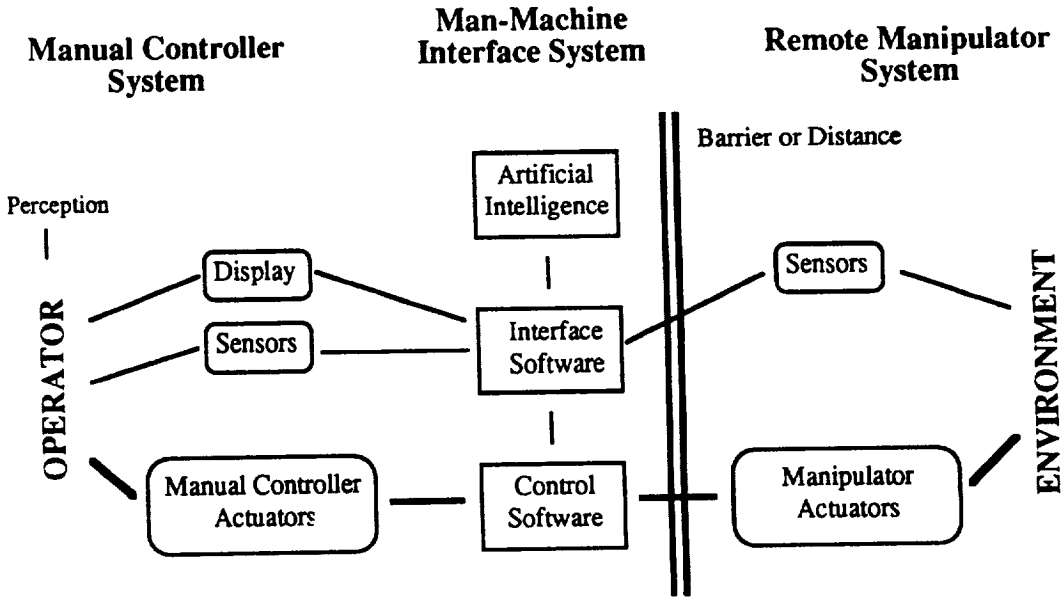

Figure 1–1 INFORMATION FLOW FOR TELEOPERATOR SYSTEMS

In teleoperation, while a human can provide intelligence for the system, the relatively limited capabilities of his/her input-output channels represent the

"bottleneck" of the whole process in Figure 1–2 (adapted from [88]). Human input can be aural, visual, tactile, kinesthetic, olfactory, or gustatory (sense of taste) and human output can be either muscular or vocal. Muscular output can be categorized as locomotional, as in applying force to a manual controller; electrical, as measured by a myoelectric electrode; or positional, as in the motion tracking of an eyeball. Among those human input-output channels; visual, tactile and kinesthetic channels (for input), and muscular channels (for output) are extensively utilized in typical teleoperation (physical manipulation).

To fully utilize these limited input-output channels of a human operator or to enhance the performance of teleoperator systems, these systems must be designed, integrated and controlled properly to provide a realistic feeling of "telepresence" to a human operator.

More specifically, in the design and control of the teleoperator system, the manual controller, the remote manipulator and their control strategies must have characteristics which are suitable to their allocated tasks: human factors and task parameters. Only the most useful sensory information such as reflecting forces, visual information, etc., needs to be provided as long as it does not confuse and distract the operator. Note, however, that when teleoperation involves contact with an unknown environment, a more realistic feel can be provided back to the human operator by directly reflecting the contact force information on the manual controller through its actuators than that limited awareness that can be provided by visual feedback information displayed on a screen. Also machine intelligence must be included to aid the operator in performing tasks effectively if it can be done reliably. Machine intelligence can be included in various forms as described by Sheridan and Verplank[82];

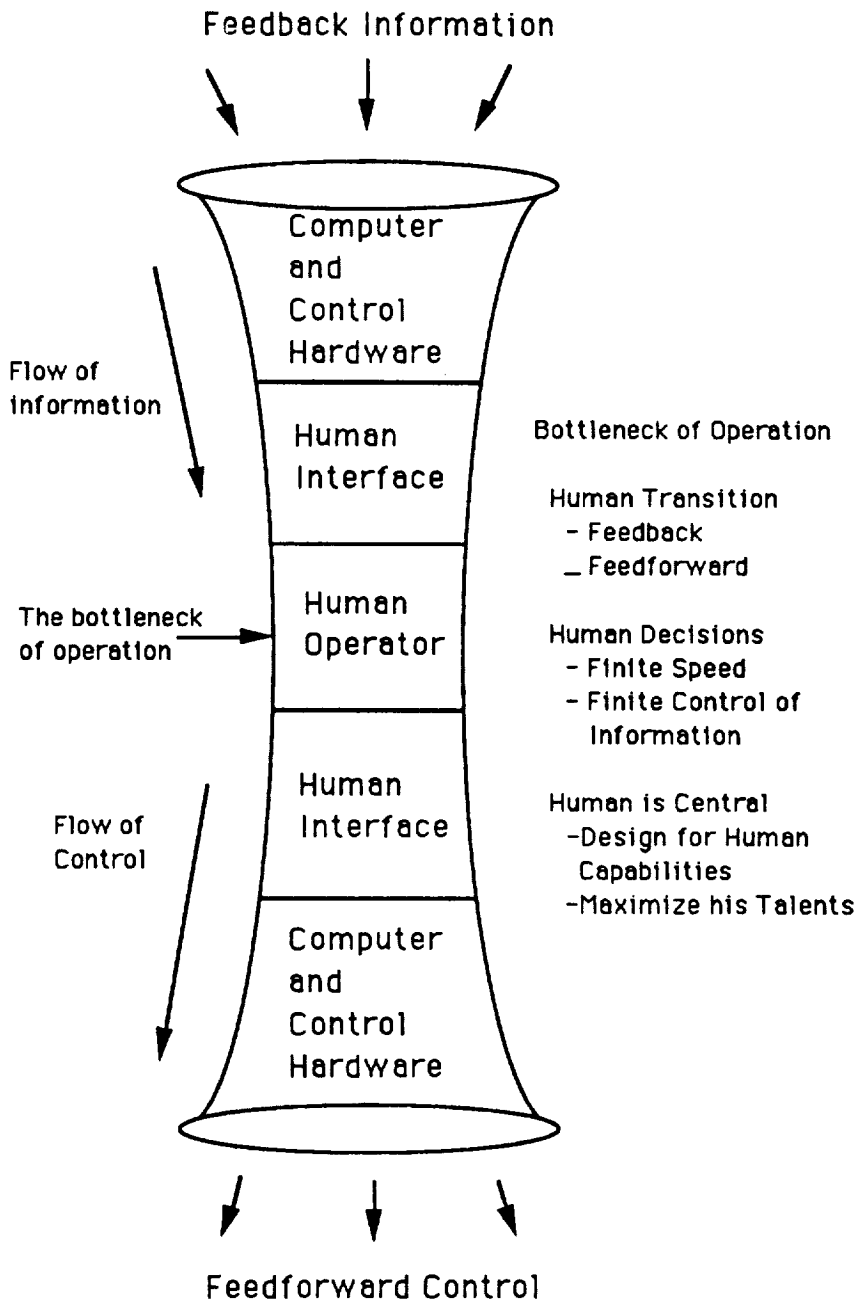

Figure 1–2 THE BOTTLENECK OF OPERATION (ADAPTED FROM LIPKIN AND TESAR [87]).

- *Extend*: the system's capabilities are extended by using the computational base in concert with the operator (such as *filtering* to remove the undesired jitters and jerks, *accomodation* to reduce the undesired excessive contact forces, etc).

- *Relieve*: the machine intelligence can be used to autonomously perform functions which would otherwise distract the attention of the operator.

- *Back up*: operator misconceptions can be corrected by the machine intelligence.

- *Replace*: repetitive tasks can be autonomously performed in order to alleviate the operator's mental and physical fatigue.

As mentioned previously, achieving the feel of "telepresence" is regarded as one of the desired characteristics of the teleoperator system to enhance its performance. Ideally, it could be achieved if either the bilateral or the force-reflecting teleoperator system has no time lag or dynamics between equivalent position and force parameters in the manual controller and the remote manipulator. In other words, the system should behave like two massless systems connected by an infinitely stiff (rigid) mechanical linkage [38]. In practical implementation, however, achieving that ideal behavior is very difficult due to the following limitions: inaccurate system models, nonlinearities (i.e., backlash, friction), communication lag, sensor noise and finite resolution, non-rigid structures, finite actuator power output, etc.

In this work, the design and control of the teleoperator system consisting of only the kinesthetic information transfer will be studied. No other effects of sensory feedback information such as visual and vocal will be discussed.

1–2 Objectives of the current research

One of desired objectives in teleoperator systems is to establish a transparent, universal interface between and man and machine. However, most available manual controllers in bilateral or force-reflecting teleoperator systems can be characterized by their bulky size, high costs, or lack of smoothness and transparency, and elementary architecture. The objective of this work is to investigate on the alternative design and control of compact, light-weight manual controllers with a somewhat improved force-reflecting capability.

In this work, the design and control of a low-cost, universal bilateral portable manual controller and the value of parallel geometry in a manual controller is investigated via actual implementation and demonstration.

To meet or support desired design criteria (i.e., compactness, light-weight, and portability), various force control strategies are investigated for a force- controlled force-reflecting manual controller application through a proof-of-principle one-dof force-reflecting manual controller system which employs a high gear-ratio reducer. Then a force-controlled parallel spherical force-reflecting 3-dof system (called shoulder) is implemented as a demonstration test-bed.

As another alternative for the design of the manual controller, a conceptual 3- dof spherical gimbal module is introduced and analyzed. For comparative purposes, the geometric properties of three different spherical system (i.e., serial structure, hybrid structure, and parallel structure) are investigated. Also for the design of general 6-dof force-reflecting manual controllers, various parallel Stewart Platforms are conceptualized. Kinematic analysis for one of conceptual 6-dof manual controllers, a three-legged Stewart Platform which uses the conceptual gimbal modules as its 2-dof actuator modules, is presented and the

framework for investigating its geometric properties is presented with the preliminary results.

The contents of each chapter are summarized as follows;

In chapter 1, the concept of teleoperator systems is described first. Then the scope of this work is outlined.

In chapter 2, recent developments on bilateral or force-reflecting control strategies are reviewed in detail, including various force control strategies and their stability issues. The design and control aspects in teleoperator systems are presented.

In chapter 3, the general background on teleoperator systems is provided. The historical review on implementations of the teleoperator systems is presented first. The currently available control strategies and software functions for teleoperator system are briefly reviewed. Also classifications of the manual controller and the major teleoperator system evaluation techniques are also briefly described. Finally, various manual controllers are compared for their performance properties.

In chaper 4, the kinematic analysis for the parallel spherical 3-dof system(called shoulder) is presented. It includes reverse position analysis and forward position analysis. The first-order kinematic influence coefficient(KIC) are found using the methods of transfer of generalized coordinates[31][32]. Then the design methods using the first-order kinematic influence coefficient formulation are presented.

In chapter 5, force control strategies for a manual controller application are investigated via a one-dof system implementation. A linear model of a one-dof system is derived and analyzed to examine the effects of the system parameters in force control on the stability of the system. In acutal implemen-

tation, two different non-collocated force sensing methods (digital F/T sensor mounted on the wrist and analog strain gauge attached on the shaft of the gear reducers) are applied and their results are discussed. Then the actual hardware implementations for a parallel spherical 3-dof manual controller is presented. To reduce the inertia and friction of the system, this module employs the simple force control strategy using wrist F/T sensor. Summaries on the system hardware, control software, the F/T sensor interfacing, and design of the encoder's counter circuits, etc., are given.

In chapter 6, a new conceptual spherical 3-dof gimbal module is introduced and its kinematic analysis is presented. Then, kinematic characteristics are investigated via the first-order KIC's and compared to equivalent spherical systems with either the serial structure or the parallel structure.

In chapter 7, various 6-dof manual controllers with parallel structure are investigated. A parallel force-reflecting 9-string 6-dof manual controller is described briefly first. This system has been implemented by the University of Texas Robotics Research Group and interfaced with the Cincinnati Milacron T^3 726 industrial robot. Then various conceptual manual controllers with parallel structure, which basically utilize the Stewart platform structure and modified parallel 2-dof conceptual gimbals, are introduced. In particular, a parallel 6-dof Stewart Platform with 3 legs seems to satisfy most desired design criteria such as compactness, light-weight, etc. Its kinematic analysis is presented.

In chapter 8, conclusions, recommendations and future work on the design and control of the manual controller are discussed.

CHAPTER 2

Issues in Current Control and Design of Teleoperator Systems

2–1 Current issues on control strategies of teleoperator systems

The development of control strategies for teleoperator systems has been relatively slow, limiting the number of strategies currently available. Actually, there have been no major advancements since 1948, when Goertz mechanically implemented a bilateral control strategy. Bejczy et al. generalized the direct joint-to-joint force-reflecting control by utilizing control variables with respect to the universal hand frame via appropriate kinematic transformations[10]. Bilateral control or force-reflecting control, in which the master controller is electronically coupled to the slave manipulator, is still the state-of-the-art in teleoperator system control. Most of the bilateral control and the force-reflecting control in use utilize the servo feedback control which neglects the effects of system dynamics completely. These neglected dynamics due to inertia, varying load, nonlinear friction, backlash, etc., decrease the performance of teleoperation systems.

Miyazaki et. al. recently proposed the bilateral servo controller and the hybrid controller for a master-slave teleoperator system based on the Liapunov stability theory[71]. Their hybrid control scheme uses sensory information to guide and/or modify the human operator's command, noting that most of the

current motion-based bilateral control schemes completely depend on the operator's performance. Furuta et. al. proposed the Variable Internal Model Following control scheme which forces teleoperator systems to follow a reference model which accepts both the operator's input force and the contact force as a command force to the teleoperator system[34]. In their control scheme, a reference model describes a relation between the motion of a master and that of a slave. Fong et al. used local microprocessors in teleoperation either to expedite real time operation by avoiding unnecessary time-lags or to utilize semi-autonomous control, which uses sensory information to modify its motion autonomously when it is necessary (concept of "smart" end effectors, etc.)[30].

Those above mentioned control strategies do not take into account dynamic interactions among the teleoperator, human operator and task environment. However, for the human dynamic models, a tremendous effort was made to understand the adaptive, versatile capabilities of humans[57][106]. Most of the early research focused on a pilot's behavior in aircraft control systems. It resulted in two representative approaches toward human modeling-the algorithmic model and the structural model[70]. Algorithmic models attempt only to mimic the total input-output behavior by estimating the characteristics of the human operator. Structural models attempt to find a series of transfer functions which describe the human system, thus accounting for many human subsystem aspects. However, the human adaptive, versatile behavior seems extremely difficult to characterize and requires further research.

For the bilateral or force-reflecting teleoperator system, Raju et al. presented the methodology for designing a bilateral controller using a two-port impedance network linear model of a one-dof teleoperator system[77]. Their primary objective is to identify the optimal port impedance relations between

the human port and the environment port for better performance in teleoperation, recognizing that the human changes his/her arm impedance consistently to match different task requirements. Their stability analysis is based on the required specifications of desired port impedances. Hannaford experimented with the hard contact behavior of teleoperator systems using a one-dof system[39]. Later he presented the hybrid two-port representation to model the bilateral teleoperator system and also proposed the bilateral-impedance control which requires the estimator to identify the impedances of the human operator and of the task environment on-line[40]. However, estimating the task impedances is not easy and requires further investigation. The bilateral impedance-control has an architecture in which a local servo loop enforces a commanded force and impedance. However, it should be noted that these port-based linear models are based on the linearity of the system, so it only can characterize the teleoperator system around the operating point. For actual multi-dof teleoperator system, these approaches need more study before actual application.

Different from other robotic system applications, teleoperator systems contain various sources of time delay in their operations. The main source of time delay can be described by:

- physical distance between the manual controller and the remote manipulator,
- the cognitive reaction time of the human operator,
- the neuromuscular time delays and lags of the human operator,
- actuator and sensor dynamics of teleoperator systems,
- intensive computation time requirements.

These time delays drastically deteriorate the performance of the teleoperator system. How to minimize/reduce the effects of time delay is regarded as one of the major problem in teleoperator system control. In bilateral or force-reflecting control, when communication time delay is significant such as in deep-sea operations or in space operations, the operator's excessive motion command to the remote manipulator without synchronized reflecting force information could cause excessive contact forces on the remote manipulator and may result in the instability of the system.

In the 1960's, Sheridan and Ferrel showed that the most reliable solution for the time delay is to move the manual controller and wait for feedback before taking the next step[27][81]. Vertut et al.[94] experimented with force-reflecting systems with time delay, and found that only with the severely reduced bandwidth of the system could a stable response be obtained, allowing velocities of only 10 cm/sec. Recently, Anderson et al. proposed a control scheme to cope with the time delay. Their control law maintains passivities between the master and the slave system to keep the closed loop system stable[6][8]. Chapel viewed the force-reflecting control of the teleoperator system to be analogous to the impedance control of the manipulator and investigated the effects of the time delay and the gain scaling on the stability of the system of force-reflecting control using a single-axis model[16]. He showed that by the use of local force feedback, significant improvements to the stability of the system, could be made compared with the conventional bilateral servo feedback controlled manipulator, even without a precise model of the system and parameteric knowledge of the contact environment.

Currently, most industrial manipulators use push buttons/switch boxes to teach the manipulator paths. When the manipulator involves uncertain con-

tact forces (deburring, etc.), a rate control[1] utilizing those push buttons/switch boxes is not sufficient to meet the requirements for those tasks. Hirzinger[43] suggested methods using a force-torque sensor to generate either the desired motion command or the desired force command of the manipulator. The force-torque sensor can be mounted either on the end effector of the manipulator or located at the remote site. The first method is similar to force control in the sense that the human operator senses the external force and provides the command force to the manipulator directly. The second may be seen as rate control in teleoperation using an isotonic (not movable) joystick. However, it also uses the output force of the force sensor (i.e., applied human force) to the manipulator as a command force. These strategies could be very effective when uncertain contacts with the environment are involved or expected. However, the second method may lack the kinesthetic feeling for providing better telepresence to the human operator.

In summary, the current state-of-art controls of teleoperator systems are the bilateral control or the force-reflecting control. To increase the feeling of "telepresence" or to enhance the performance of teleoperator systems further, more attention have been given to the effects of the dynamic interactions of the teleoperator system with task environments and a human operator.[77][39][40] However, those studies are based on the simple linear and/or one-dof model of a teleoperator system. It requires further study for actual application. The time delay, which is one of the most difficult problem in teleoperation, is treated by many researchers.[6][8][16] However, their study investigate the stability problems not the performance of the teleoperator system and it also requires further study to achieve desirable results in teleoperation.

[1]see section 3.2

2–2 Force control and its stability

Since teleoperator systems involve interactions with the human operator and the task environment, the force control strategies may need more attention and need to be better understood to enhance the performance of teleoperator systems. The following will describe the typical force control strategies and their stability issues in robotics applications. There have been many proposed force control strategies for manipulators in the literature. A good review on force control strategies can be found in [101]. Only a few typical force control strategies will be discussed.

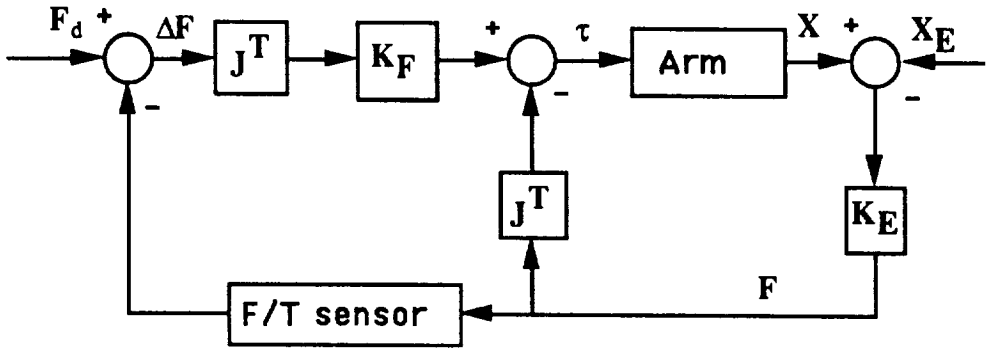

Figure 2–1 EXPLICIT FORCE CONTROL (ADAPTED FROM [101])

Explicit force control in Figure 2–1 has a desired force input and directly utilize the sensed forces to generate the control action[101]. In this control, a desired force is commanded, rather than position or velocity, and the control structure is similar to the proportional motion controller.

In most industrial manipulators, however, they are commanded along some nominal motion trajectory and are based on the servo-control. Therefore, most force control strategies utilize the force feedback information to modify

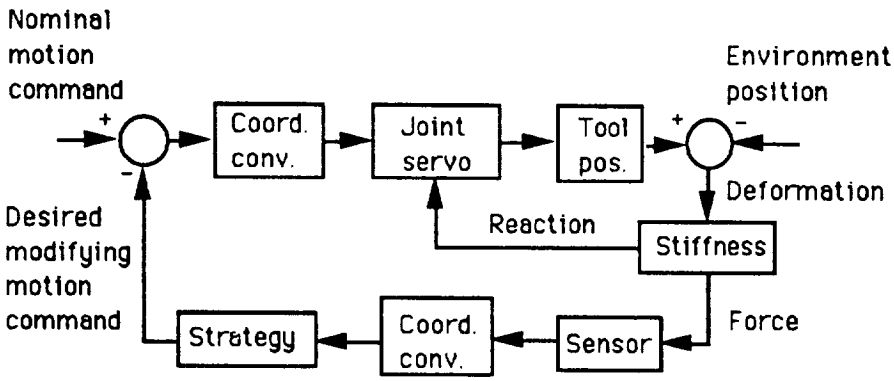

Figure 2–2 GENERAL ARCHITECTURE OF FORCE CONTROL (ADAPTED FROM [101])

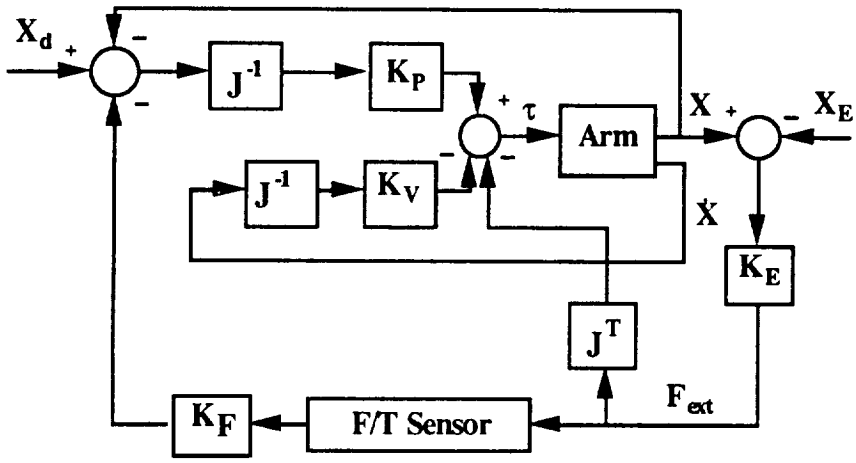

Figure 2–3 STIFFNESS CONTROL (ADAPTED FROM [101])

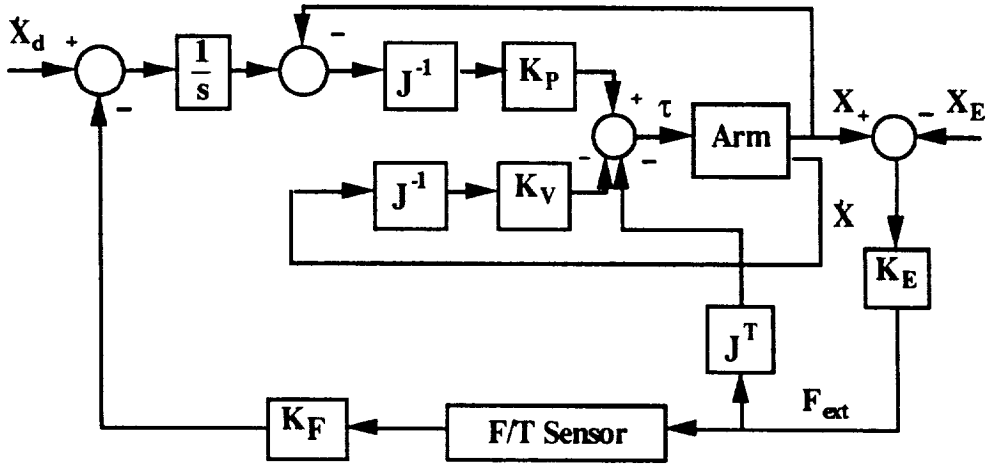

Figure 2–4 DAMPING CONTROL (ADAPTED FROM [101])

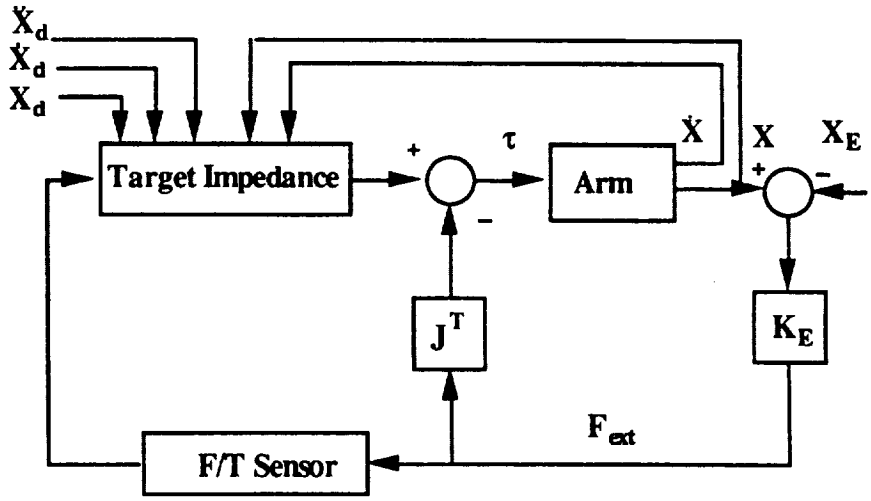

Figure 2–5 IMPEDANCE CONTROL

the nominal motion trajectory as shown in Figure 2–2. Stiffness control, Damping control, and Impedance control, use sensed forces to modify the nominal trajectory by regulating the behavior of the end effector of the manipulator in specified ways; stiffness, damping, or impedance, respectively[45][46][47][80][99]. These classifications are primarily based on how to interpret the force feedback data in the feedback loops as can be seen in Figure 2–2.

For controlling the stiffness of the end effector of the system, two intrinsically different approaches have been suggested. A Remote Center Compliance (RCC) device[102] is attached at the end effector of the manipulator and passively provides the required compliance (i.e, through elastic deformation of the device). The active stiffness control in Figure 2–3 utilizes the force feedback information to modify the motion command to actively generate the desired stiffness effects at the end effector of the manipulator by specifying and multiplying the compliance matrix, K_F, to the sensed forces, F, accordingly. Note that in Figures, K_p and K_v, represents the position gain and velocity gain matrices, respectively and that J represents the Jacobian matrix.

Similar to the stiffness control, the damping control shown in Figure 2–4 uses the sensed force feedback data to modify the nominal velocity command to generate the equivalent damping effect to the system.

The impedance control in Figure 2–5 can be regarded as a generalization of various force control strategies (i.e., the stiffness control, damping control, and force control). It actively regulates the end effector dynamic behavior of the manipulator to external forces. The differential equation representing a linear second order system (i.e., mass-damper-spring system) is generally used as a target impedance of the end effector of the controlled manipulator[98][99][100]. In the literature, most proposed impedance controllers assume the decoupling

and linearization of the end effector dynamics via non-linear feedback control strategies such as computed torque control or its equvalents in operational space, noting that the impedance of the manipulator is configuration-dependent and highly nonlinear[6][95]. The controlled system is known to be locally stable when the target impedance is selected properly[54][55]. Anderson and Spong used the Duality concept between Thevenin and Norton equivalents in network theory to contend that the robot must be controlled consistently with respect to the environment[7]. They identified the impedance control law, which insures that the system could be controlled without steady-state errors, based on the Duality condition .

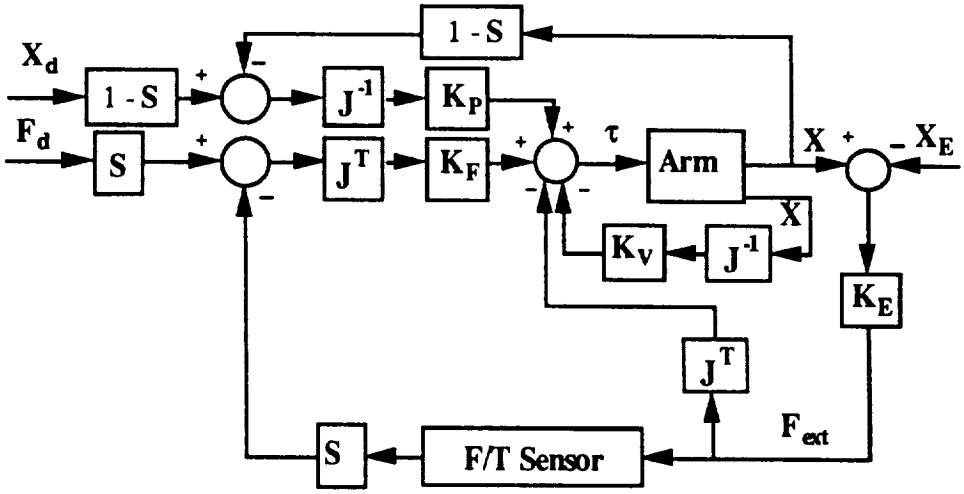

Figure 2–6 HYBRID CONTROL (ADAPTED FROM [101])

Hybrid control demonstrated by Raibert and Craig[76], as shown in Figure 2–6, applies both force control and motion control into two separate subspaces, divided by the selection matrix, $[S]$. The selection matrix is diagonal, with ones or zeros corresponding to whether the subspace is to be position controlled or force controlled, respectively. The determination of the selection

matrix might not be easy for general task environments and it restricts the applications of the otherwise promising hybrid control strategies within only well structured task environments.

The force control problem of a manipulator involving contact with a stiff environment has been extensively considered in the recent literature[4][5][24][25][26]. In motion control strategies based on only motion feedback data, when the manipulator involves contact with a stiff environment, a very high gain position feedback is required to follow the desired commanded motion trajectory. However, due to the noise in the motion feedback data, the control action is dominated by the noise and may result in an unstable response. For the system with force feedback, since the force feedback represents a very high gain position feedback, instability of the system is possible when its gain is increased carelessly. These instabilities were observed by previous researchers[97] and can be characterized by the end effector bouncing back and forth against a contacting surface. The possible sources for those instabilities (or contact instabilities), could be related to the following; environment dynamics, sensor dynamics, nonrigid manipulator links, limited bandwidth of the actuator subsystem, impact energy, nonlinear friction and backlash, etc. Eppinger and Seering used a lumped linear system model to identify possible sources for those instabilities when a simple proportional force control law is applied[24][25]. They showed that in their lumped linear model, the dynamics existing between the actuator and the force sensor is a source for instability in a simple proportional force controlled system. An and Hollerback[5] investigated the stability issue caused by the interaction of the dynamics of the robot with the dynamics of the environment(dynamic stability) using a direct drive arm, and suggested a control law utilizing both wrist sensing and open-loop joint torque control to cope with

these instabilities.

There are other types of instabilities caused by kinematic transformations in certain Cartesian-based force control implementation: kinematic instability introduced by An and Hollerback[4] and kinestetic instability described by Lipkin and Duffy[65] in hybrid control. The kinematic instability is primarily caused by the interaction of the inertia matrix of the robot with the inverse of the Jacobian matrix. The kinestetic instability, referring to the instability associated with the decomposition of force and motion feedback signals to ensure a compatible control command, requires at least three joints to occur and is related to a problem for higher level constraint formulations. To prevent kinesthetic instability, Lipkin and Duffy[66] proposed one formulation of kinestetic filtering which ensures that the decomposition of force and motion is invariant with respect to a change of origin, basis, or scale.

2–3 Design aspects of teleoperator systems

In order to realize the optimum operation of the teleoperator system, human dynamics, teleoperator system dynamics, the task environment and their interactions must be well understood and taken into account. In this section, the design aspects of teleoperator systems are considered. There are clearly many other design aspects of teleoperator systems to consider in addition to those listed in Table 2–1. More detailed descriptions on those design aspects can be found in [90].

The most important manual controller characteristics for the teleoperator system could be listed as follows: *universal*, *bilateral* or *force-reflecting*, *magnitudes of maximum/minimum reflecting forces*, *dextrous working volume*

Table 2–1 DESGIN ASPECTS OF TELEOPERATOR SYSTEM

Geometric Aspects	workspace shape/size and dexterity
	isometric/isotonic
	mobility (degrees of freedom)
	universal/non-universal
	geometrical simplicity
	serial/parallel/hybrid structure
	modularity
	redundancy (in kinematics or actuators)
Control Aspects	digital/analog
	unilateral/bilateral/force-reflecting control
	direct joint/resolved position control
	position/rate control
	position/force/hybrid control (control variables)
	adaptive/non-adaptive control
	bilateral bandwidth and time delay
	compensation capability
	software backup functions (scaling, filtering, etc.)
	computational load
	task environments
	stability
Component Aspects	sensors
	type of transmission/actuator
	backlash/deadband
	friction/stiction
	durability/reliability of hardware
	hand grip/end-effector
Dynamic Aspects	end effector impedance
	effective inertia distribution(isotropic)
	gravity compensation
	compliance/rigidity
Human Factors	human operator dynamics
	resolution of position/reflecting force
	maximum/minimum reflecting force
	compactness/portability of manual controller
	operator fatigue/safety
	ease of operation/training
Others	ease of maintenance
	economics

and *position resolution*, *compact-size*, *light-weight*, *low friction* and *low effective inertia* at hand grip, *adjustable effective impedance* at the hand, and *optimal bilateral bandwidth of the system for time delay*. For the sake of simplicity, only these aspects will be discussed briefly.

Most bilateral teleoperator systems in use are designed to have a geometric similarity between the master and the slave system. The control effort for those systems could be simplified by direct joint-to-joint control between the master and the slave system. The drawbacks of this type of teleoperator system are the bulk of the master system, a fairly large working volume requirement, its weight, and its difficulty in portability. They could actually limit or preclude the practical use of the system, such as in underwater submarine or space applications. For versatile applications of the master to various remote manipulators, it needs to be compact, light and portable while having a large dextrous workspace that does not interrupt the continuous motion of the human arm.

Decoupled designs of the manual controller from the remote manipulator provide more flexiblity for the design of manual controllers to satisfy more of the design criteria mentioned above. It can be achieved at the expense of a little more sophisticated control effort (kinematical transformations are performed with respect to the universal end effector local frames for both the manual controller and the remote system). The detailed analysis on the kinematic mappings among various coordinate frames is provided in Appendix B.

To provide task information to the human operator effectively (i.e., to increase the level of telepresence), bilateral control or force reflecting control are in common use. In bilateral control, reflecting force information is transferred in the form of the sum of the position and velocity errors between the man-

ual controller and the remote manipulator. In force-reflecting control, contact force experienced by the remote manipulator is directly reflected to the manual controller.

The use of the force information in manipulator control has been shown to be very effective to improve the performance of the remote manipulator especially when manipulator contact is involved with the environment. Studies of human performance in teleoperation with and without force information shows improvement of the task completion time by 40 to 50 percent when force information is used[38]. Noting that the human hand is able to sense forces from 0.016 to 4.5 lb_f, the desired minimum/maximum reflecting forces of the manual controller need to be selected accordingly to fully utilize the human capabilities. However, it should be noted that the minimum/maximum reflecting-forces are also related to magnitudes of friction and actuator limitations (for the design of the universal force-reflecting spherical 3-dof manual controller, the continuous maximum reflecting-forces of 5 lb_f and the peak reflecting-forces of 8 to 10 lb_f at the handgrip are used as design goals).

To reduce the confusion or distraction of the human operator, the magnitude of friction and any undesired dynamics of the manual controller should be minimized as much as possible and compensated if they are too large.

Humans are known to have outstanding adaptability for various task environments. Humans operators can change arm impedance depending on the desired task characteristics. It should be noted, however, that as shown by Hogan experimentally in his recent research, the human arm impedance can not be adapted immediately for a changed task requirement, rather it takes 1.2 to 1.5 sec to identify the task environment and to adjust his arm impedance[48]. For more enhanced teleoperator system operations or to handle more sophisti-

cated tasks effectively, the characteristics of the teleoperator system could be adjusted on-line as in bilateral-impedance control suggested by Hannaford[40] or off-line in advance[77] to augment the operator's limited adaptation capability. These adjustable impedance variations of the manual controller and the remote manipulator could expand their current functional capabilities.

Due to the instability arising from the time delay, the bilateral bandwidth of the system must be selected to optimize the system performance. A number of studies have been performed on manipulation with a user variable system time delay, where the time delay associated with the human is assumed negligible and not considered. According to their results, in order to achieve the stable response of the system and a favorable task completion time, time delays of less than 0.1 seconds should not be exceeded in the teleoperator system. In that case, the required bandwidth of the teleoperator system is found to be around 4.5 Hz[14]. The time delay problem is not a subject of this research. Additional detailed studies on time delay can be found in [6][8][27][81].

Finally, the design and control characteristics of three different systems, the industrial robots, the remote system and the manual controller system, are compared in Table 2–2 to show their different functional/design perspectives. It should be transparent from the table that the design and control of manual controllers, industrial robots, and teleoperator systems require the knowledge on their individual task requirements and specifications to optimize their functions. A properly balanced design of a teleoperator system, along with advanced computer/actuator technology and control strategies, will provide a promising future for a teleoperation technology.

Table 2–2 FUNCTIONAL CHARACTERISTICS OF TYPICAL INDUSTRIAL MANIPULATORS, UNIVERSAL BILATERAL MANUAL CONTROLLERS AND REMOTE MANIPULATORS.

Characteristic	Industrial Manipulator	Universal Manual Controller	Remote Manipulator
Functional Nature	Autonomous Repetitive	Manual Teleoperation	Manual Teleoperation
Environment	Simple Structured	Human operator Interface	Complex Uncertain
Size	Large	Compact	Small/Large
Weight	Heavy	Light	Light/Heavy
Actuator Location	Distributed	Centralized Base Mounted	Distributed
Compliance in Drive Transmission	Stiff Rigid Non-Backdrivable	Flexible Backdrivable	Flexible Backdrivable
Friction	Large	Small	Small/Large
Inertia	Large	Small	Small/Large
Load capacity(lb_f)	25-200	2-20	5-200
End-Effector	Specialized	Joy-Stick	Inter-changeable
Control Variables	Joint Actuator Position	End-Effector Position/Force	End-Effector Position/Force
Application	Structured Task	Light Duty	Unstructured Task

CHAPTER 3

General Background on Teleoperator Systems

In this chapter, the general background on the teleoperator system is described. Previous design efforts, currently available control strategies and computer support functions are presented. Also manual controller classifications, their comparison based on performance and properties, and performance evaluation methods are briefly presented.

3–1 Previous work on teleoperator system design

In this section, the typical design efforts for teleoperator systems are briefly reviewed in various application areas.

In the late 1940's, Ray Goertz and his group at the Argonne National Laboratory developed the first mechanical bilateral master-slave system. The master-slave system was developed for the remote manipulation of objects in a highly radioactive environment (a "hot cell")[36]. However, this mechanical master-slave could not be controlled when the two manipulators were more than a few feet apart, because they were physically linked. In 1954, Goertz built the first bilateral force-reflecting servo-manipulator. This manipulator used bilateral servo loops with low friction, high efficiency torque transmission. By 1965,

Argonne National Laboratory had introduced the control concept in which the operator used head-activated controls to move remote site TV cameras.

In 1948, General Mills introduced a simple on/off switch box controller, which used electric motors to control the manipulator in an unilateral sense. In 1958, General Electric began developing the Handyman electrohydraulic manipulator, which included force-reflection, articulated fingers, and an exoskeletal master controller. However, their bulky dimensions made the Handyman impractical[72].

The hazardous environments encountered in space exploration forced NASA to develop advanced teleoperator systems. During the 1970's NASA used such systems to control the soil samplers sent to the Moon and Mars, and began developing the Remote Manipulator System (RMS) for the space shuttle. The RMS teleoperator system used two 3-dof hand controllers, the left hand controller for controlling translational motion of the end effector of the RMS and the right hand for controlling rotational motion[78]. The system primarily uses resolved unilateral rate control, but an emergency backup mode is included to allow for direct manual control of the individual joints. In the future, NASA plans to use teleoperator systems in the assembly and routine maintenance of the space station[2].

Also during the 1970's, the nuclear community began serious efforts to develop teleoperator systems for use in the maintenance of nuclear power plants. In 1977, Teleoperator System Corporation produced the SM-229, a bilateral force-reflecting master/slave manipulator designed for use in nuclear plants[29].

Draper Laboratory at MIT has developed an isometric hand controller which implements resolved motion rate control (introduced by Whitney at MIT)

[98]. While this controller exhibits a very compact design, its limited motion range makes force-reflection and kinesthetic feedback very difficult. In 1985, Landsberger and Sheridan developed a parallel-link arm using cables in tension and a single passive compressive spine. The system can use both resolved motion control and rate control[60].

Artificial Intelligence (AI) concepts were introduced with the development of microcomputer technology. As a result, "supervisory" and "universal" control concepts have been introduced to teleoperator systems. In 1980, Brooks at MIT first demonstrated supervisory control concepts in hardware[11]. Supervisory control can be seen in modern aircraft, chemical plants, steel mills, discrete part manufacturing, and many other applications.

In the early 1980's, Oak Ridge National Laboratory (ORNL) began developing a series of master-slave teleoperator systems for nuclear plant maintenance operations; the Model M-2 Maintenance System and the Advanced Servomanipulator (ASM) system[42][59][69]. The Model M-2 Maintenance System uses two force-reflecting master controllers for two servomanipulator arms, television viewing, lighting, etc. The ASM uses a pair of modular-based bilateral force-reflecting master-slave controllers to increase the reliability of the system. However, the large size and anthropomorphic (elbow-down) geometry of the system restricts its applications.

Since the late 1970's and early 1980's, universal concepts for teleoperator systems have been developed and refined mainly by Hill and Salisbury at Stanford Research Institute (SRI), Bejczy at Jet Propulsion Laboratory (JPL)[43], and Tesar at the Center for Intelligent Machines and Robotics (CIMAR) at the University of Florida and after 1985, at the University of Texas at Austin.

In 1980, JPL and SRI developed a universal, bilateral force-reflecting 6-dof manual controller [10]. The geometry of the controller was chosen to simplify the computational burden. A counter-balancing mechanism was included to minimize gravitational effects. The design effort was directed towards reducing friction, backlash and effective inertia at the handgrip. It is designed to generate 35 oz of force and 70 oz-in of torque at the handgrip with a 12 inch cube workspace. It used the cable/pulley-based counter-balancing and power transmitting mechanism.

In the late 1970's, Tesar at CIMAR developed a unilateral/universal 6-dof nine-string manual controller [64] and a bilateral force-reflecting 4-dof planar controller[13][95]. The nine-string controller has almost negligible effective inertia, while maintaining a reasonable workspace size. It was also an attempt to apply parallel geometry on a manual controller design. The 4-dof controller was developed to evaluate the applicability of both force reflection and redundancy to the manual controller design.

Since 1985, Tesar at the University of Texas developed two force-reflecting manual controllers; a 3-dof 3-string manual controller and a 6-dof 9-string manual controller[3][63][90]. Both manual controllers utilize parallel geometry and showed negligible effective inertia due to its actuator locations on the fixed base. Both controllers were interfaced with the Cincinnati Milacron $T^3 - 726$ Industrial Robot and showed successful performance.

Currently, teleoperator systems are in use in several areas (nuclear, space, military, mining, etc.). In the nuclear industry, teleoperators are used in equipment maintenance and material handling operations in radioactive environments. Various branches of the U.S military are involved in teleoperator system design. The Navy has developed and applied Remotely Operated Vehi-

cles (ROV) for underwater operations. The Army is developing a teleoperator system for material handling applications. And for decades, the Air Force has been applying manual controller (joystick) concepts for aircraft control.

A handful of industrial companies (Kraft Telerobotics Inc., etc.) are marketing complete force-reflecting systems, which are used in hazardous environments (i.e., under-sea opeations). In 1983, Odetics developed a tetherless electromechanical walking machine with a lift-to-weight ratio greater than one [91]. Several foreign countries have also been developing teleoperator systems (the MF3 manipulator vechicle in West Germany, the ME-23 servomanipulator in France, MASCOT in Italy, BILARM-83A in Japan, the RMS arm in Canada, etc.) [15][59]. The success of these operations ensures the continued development and application of industrial teleoperator systems.

3–2 Classification of previous control strategies for teleoperator systems

In this section, the various classical control strategies for teleoperator systems are briefly explained. The fundamental control strategies for teleoperator systems may be divided into three categories:

- The controlled parameters of the manipulator (position, rate, force).
- Type of output space of the manipulator: direct (control of joint angles) or resolved (control in operational space).
- The direction of information flow (unilateral or bilateral)[1]

[1]Bilateral controllers both provide output and receive feedback(position or velocity) from the manipulator; unilateral controllers only provide output to the manipulator.

The typical control strategies which were in popular use are briefly described in the following[12].

Direct Rate Control (DRC): The velocity of each manipulator joint is directly controlled by an individual manual controller output. The operator can adjust the proportional gains or the manipulator-joint-velocity/controller-output ratio. The simple button box controller uses this control mode.

Resolved Rate Control (RRC): The velocity of each degree of freedom in task coordinates[2] is controlled by an individual manual controller output.

Direct Unilateral Position Control (DUPC): The position of each manipulator joint is directly controlled by an individual manual controller output. There is no manipulator information feedback (joint position, velocity) to the manual controller (human operator). It is implicitly assumed that the manipulator dynamics are fast enough to follow the controller input; otherwise, the performance of the system may be deteriorated.

Resolved Unilateral Position Control (RUPC): The position of each manipulator degree of freedom in task coordinates is controlled by an individual manual controller output.

Direct Bilateral Position Control (DBPC): Same as DUPC above, except that position feedback from the manipulator joints can be used to synchronize the motion of the manipulator and the manual controller. This position feedback from the manipulator joints indirectly transfer the contact force information to the manual controller. To improve synchronization, the manual controller joint velocities can be fed forward to the manipulator joint servos, while the manip-

[2]Task coordinates(or world coordinates) are attached to the control point of the manipulator (usually the tool point or the center of the end effector) and/or the manual controller (usually the center of the hand grip). Task coordinates usually coincide with Cartesian coordinates, which feels natural to human operators.

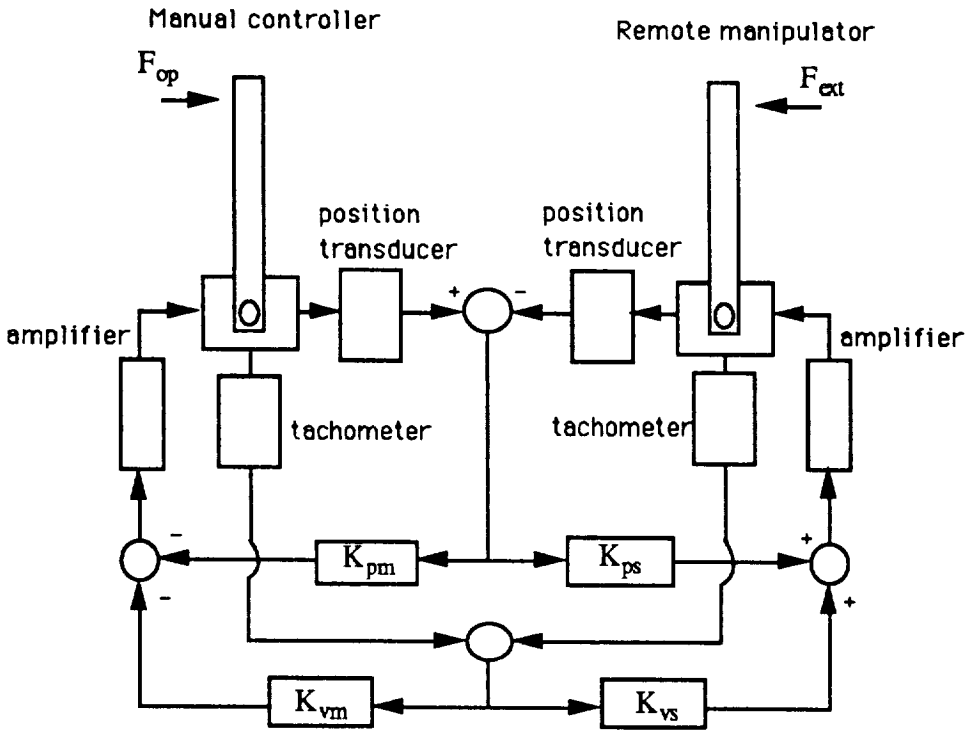

Figure 3–1 DIRECT BILATERAL POSITION CONTROL

ulator joint velocities are fed forward to the manual controller servos as shown in Figure 3–1. This bi-directional error signal results in force-reflection to the manual controller and the manipulator. The DBPC control mode is most commonly used in master-slave teleoperator systems.

Resolved Bilateral Position Control (RBPC): The same as RUPC above, except that position feedback from the manipulator joints can be used to synchronize the motion of the manipulator and the manual controller. This position feedback from the manipulator joints indirectly transfer the contact force information to the manual controller. When a universal manual controller is used in this control mode, the joint displacements and velocities of the controller are combined and resolved to create task coordinate displacements and velocities. The controller coordinates and variables (position and velocity) are thus resolved into manipulator task coordinates and variables. As in DBPC, the manual controller and manipulator joint velocities can be fedforward to each other to initiate force reflection. This type of control comes at a cost, due to the computational burden of converting between coordinate systems. However, most additional control functions (direct scaling of position, velocity, and force in task coordinates, rereferencing, etc.) are available in this mode.

Direct Force-Reflecting Control(DFRC): This control can be applied to only the master-slave teleoperator system. As shown in Figure 3–2, the position of the manipulator is controlled by the output position of the manual controller. Any external forces felt on the manipulator will be reflected on the manual controller. This control can transfer the most sensitive environmental information to the manual controller and has been shown to be very effective in teleoperation involving contacts with an unstructured environment. The main difference of this control from the DBPC is how to transmit the environmental information

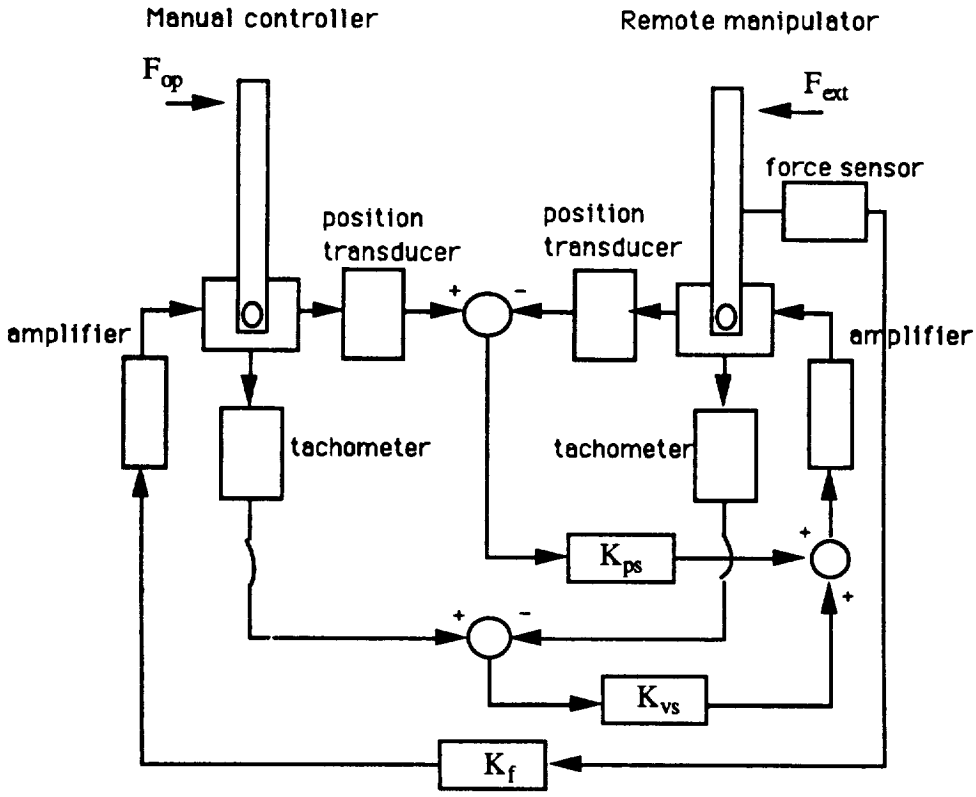

Figure 3–2 DIRECT FORCE-REFLECTING CONTROL

to the manual controller, that is, the DFRC uses direct force feedback and the DBPC uses indirect position/velocity feedback.

Resolved Force-Reflecting Control(RFRC): The same as the above DFRC except that both the manual controller and the remote manipulator are controlled in task coordinates. It allows the independent design of the manual controller from the remote manipulator. Also as in RBPC, most available computer augmenting control functions can be applied in this mode.

Besides the above control strategies, there are other control functions aided by the control software[88].

Motion Filtering: "A process in which extraneous motion that is superimposed upon the control signal by the operator is detected and subsequently deleted."[88] For example, in a miniature replica master-slave system, small command signals from the miniature replica controller are amplified. Filtering smooths out the undesired jitters produced by the human operator (due to fatigue, etc.).

Scaling: The ability to dynamically vary the geometric gain between the manual controller and the manipulator. Scaling allows a single controller to be used for both gross and fine motions (for precision operations) by varying the corresponding gains. Scaling can also be used to create motion constraints on the manual controller to help/guide the operator (motion projection, where zero gain represents zero motion along the corresponding direction). Scaling is only effective when the geometries of the manual controller and the manipulator are decoupled (the universal controller concept).

Re-referencing: Allows the operator to reposition the manual controller to a more comfortable or desirable position, without moving the manipulator. This control function is useful when the motion range of the manipulator is limited

by the workspace of the manual controller, or when the manual controller is in an uncomfortable or undesirable position. Re-referencing allows the operator to increase both the dexterity and the virtual operating range of the controller. As with scaling, re-referencing is effective only when used with universal controllers.

Re-orientation: Allows the operator to compensate for an altered perspective between the manual controller and the manipulator. When the manipulator task coordinates or the visual perspective of a scene are altered, the operator can restore the desired controller/manipulator spatial relationship by transforming the controller output to match the altered perspective. Re-orientation is effective only when used with universal controllers.

Force Reflection: Forces and torques perceived at the end-effector are reproduced at the hand grip of the manual controller, allowing the operator to feel any external forces/torques as if he/she were moving the end-effector itself. Force reflection is extremely helpful during operations in uncertain environments.

Force Indexing: Allows constant manipulator loads (external loads, manipulator wrist weight, etc.) to be subtracted from the forces reflected back to the hand grip of a manual controller, thus reducing undesirable effects (such as operator fatigue). Obviously, force indexing can only be used when force reflection is available (bilateral systems).

Compensation: Reduces or eliminates undesirable dynamic effects, friction, gravitational effects, nonlinear effects, etc. from a teleoperator system. Compensation reduces operator fatigue and improves control, but the software often requires a large amount of high level computation. Compensation techniques should be balanced to enhance individual tasks or teleoperator systems.

Motion Constraints: Artificial constraints are placed on the manipulator to either improve control or protect the system. Motion constraints can be based

on the task environment model, sensory data, etc. Examples include potential force fields (used for trajectory guidance, obstacle avoidance, etc.) and force accommodation (adaptive compensation of unexpected forces/torques applied to the end-effector, useful in insertion tasks, etc.).

Variable Control Point: Allows the operator to simplify the task by electronically selecting the most desirable manipulator control point (tool, wrist, end effector, etc.). Variable control points can only be achieved on decoupled systems (universal controller concept).

Teach and Repeat: Allows the operator to "teach" the manipulator a movement or activity which can be autonomously repeated at a later time. This function is useful for repetitive tasks requiring no human supervision.

3–3 Manual controller classification

Manual controllers may be classified by various aspects:

- Geometry (joystick, replica, master-slave, anthropomorphic, universal, etc.)
- Working volume (button box, joystick, manual controller, etc.)
- Number of degrees of freedom (non-redundant, redundant, etc.)
- Control variables (position isotonic or rate; force isometric, force-induced displacement, hybrid, etc.)
- The direction of information flow (unilateral or bilateral)

Some typical manual controllers are described [12][88]:

Button Box Rate Controller: The simplest type of manual controller is the switch or button box controller. These controllers have individual buttons,

switches and/or knobs to control the velocity of each manipulator joint either directly or in task coordinates. The simplicity of the button box accounts for its widespread use with industrial manipulators; however, button boxes represent the slowest teleoperator control available, with typical performance times 20 to 100 times slower than master-slave controllers.

Small Motion Joystick Controller: This is the classical "joystick", where the motion range is only a few inches at most. The biggest advantage of the joystick is that it has a very small working volume; the biggest disadvantage is that the operator error is amplified along with the control signal. The small motion joystick is usually used as a proportional rate controller , but it can also be used as a position controller. Two 3-DOF joysticks of this type are used to control NASA's RMS Arm.

Isometric Joystick Controller: The isometric (immovable) proportional rate controller exhibits a very compact design, requiring a minimum of working volume. Transducers (strain gauges) within the manual controller measure the forces applied by the operator, which are used to control the manipulator velocity either directly or in task coordinates. Due to its small motion range, the isometric manual controller is not capable of reflecting forces applied to the manipulator.

Isotonic Manual Controller: An isotonic (constant force) manual controller uses resolved position control for two or more degrees of freedom in limited work volumes. A "trackball" is an example of this type of controller. Isotonic controllers are not suitable for force reflection.

Hybrid Manual Controller: The hybrid controller combines aspects of the isotonic and isometric controllers, but they are mutually exclusive for a given degree of freedom. There are two basic implementation philosophies: concurrent and

sequential. In a concurrent controller, each degree of freedom is separately controlled by an input force, position, or displacement. In a sequential controller, each degree of freedom can be controlled by a combination of input force, position, or displacement by alternating between isotonic and isometric modes.

Replica Manual Controller: The replica controller is a scaled-down duplicate of the manipulator, which allows the operator to control huge, high payload manipulators. Due to geometric scaling, all operator input is amplified, including undesirable jitters and any nonlinear properties of the controller (backlash, etc.); this makes the performance of high-precision tasks difficult. In addition, most control function software (for re-referencing, scaling, etc.) cannot be adapted to the replica master controller, because of the geometric coupling between the manipulator and the controller.

Master-Slave Teleoperator System: Two geometrically similar manipulators are interfaced such that the operator controls one manipulator (the master) while the other (the slave) duplicates the motion of the master. Control of the master-slave teleoperator system is quite simple, as long as the master and slave manipulators remain close geometrical replicas (maintaining their geometric and dynamic similarities). However, as in the case of the replica manual controller, the geometric similarity (direct joint-to-joint coupling) between master and slave prevents the use of control function software for performance enhancement.

Anthropomorphic Manual Controller: Anthropomorphic controllers are used to maximize the human operator's own control capability by using the human arm as the geometrical base. The manipulator is usually geometrically similar to the anthropomorphic controller. These controllers show good performance within humans' dexterous range, but are restricted in certain tasks (i.e., operations requiring high precision, complex geometries, etc.) which may be more effectively

accomplished with a non-anthropomorphic geometry.

Universal Manual Controller: As a result of rapid advancements in computer technology, it is now possible (with proper transformation software) to interface a manipulator with a geometrically dissimilar manual controller, called a "universal controller". The ability to adapt to manipulators with different geometries provides the universal controller with many promising advantages. With the universal controller, the position and velocity of both the manipulator and the manual controller can be controlled in task coordinates, which feels more natural to the operator.

While all of the manual controllers have their own particular merits and demerits, the master-slave, anthropomorphic, and universal manual controllers appear to have clear advantages over the others. The ability to apply a variety of interface and control functions ("natural" control with force and proprioceptive feedback, reduced operator workload, reduced training time and expense, reduced probability of errors, etc.) enhances the performance of these controllers.

A comparison of the master-slave, anthropomorphic, and universal controllers clarifies the differences between them. Master-slave controllers have direct configuration feedback (due to the duplicate geometry of the controller and manipulator), but they may lack in anthropomorphism and compactness. Anthropomorphic controllers often lack compactness and versatility, and their functional capabilities may be limited by the human operator. Universal controllers are versatile and compact, but they lack direct anthropomorphism and configuration feedback.

It should be noted that the main difference between a master-slave controller and a universal controller lies in the geometrical coupling/decoupling

to the manipulator. Due to its geometrical dependence on a particular slave manipulator, the performance of a master-slave teleoperator system would be dramatically reduced if used as a universal controller (e.g., if it was linked to a slave of different geometry), because the controller design may not be compact or ergonomic. While a universal controller cannot be made to mimic the master-slave's direct configuration feedback, its versatility and ergonomic design make it the most promising controller, because the controller and the manipulator can be specially designed for their particular requirements. Tables 3–1 (adapted from [88]) and 3–2, and Figure 3–3 (adapted from [88]) compare the functional properties and performance of various manual controllers.

3–4 Performance evaluation of teleoperator systems

While many evaluation techniques have been proposed for quantifying the performance of teleoperator systems and their various control modes, there is no industry standard. Performance is usually evaluated either by measuring the mean task-completion time or by counting the number of errors occurring during a specified task. While the time ratio performance measurement techniques are currently the most popular, the error/success ratio techniques are also important in teleoperator system evaluation. It should be noted that time ratio measurements are valid only when comparing tasks of the same complexity (same degree of constraint)[28][56][67][88][96].

- *Information-Based Performance (Fitt's Law)*: Base the teleoperator system performance upon an index of difficulty:

$$I_d = log_2(\frac{2A}{B}) \tag{3–4.1}$$

where

I_d = index of difficulty (Fitt's index).

A = distance between targets in a repetitive motion.

B = the width of the target (tolerance).

Fitt's Law is defined as:

$$T = aI_d + b \tag{3-4.2}$$

where

T = task completion time.

a and b are determined experimentally.

- *Unit-Task Completion Time* - Measurement of the completion time for a specified unit task, such as "insert", "grasp", etc.

- *Task/Time Ratio*: Comparison of task completion time between the teleoperator system and a human operator.

- *Error/Task Success Ratio*: Compares the number of errors expected using various teleoperator systems during a specified task.

Bilateral master-slave systems have demonstrated the best performance of all teleoperator systems (based on time ratio evaluation techniques), yet they are still 2 to 15 times slower than a human. All other systems are currently 3 to 10 times slower than the bilateral system, which suggests that increasing the level of telepresence improves performance. However, other control modes should not be completely overlooked, as they often perform better than bilateral master-slave systems in certain applications.

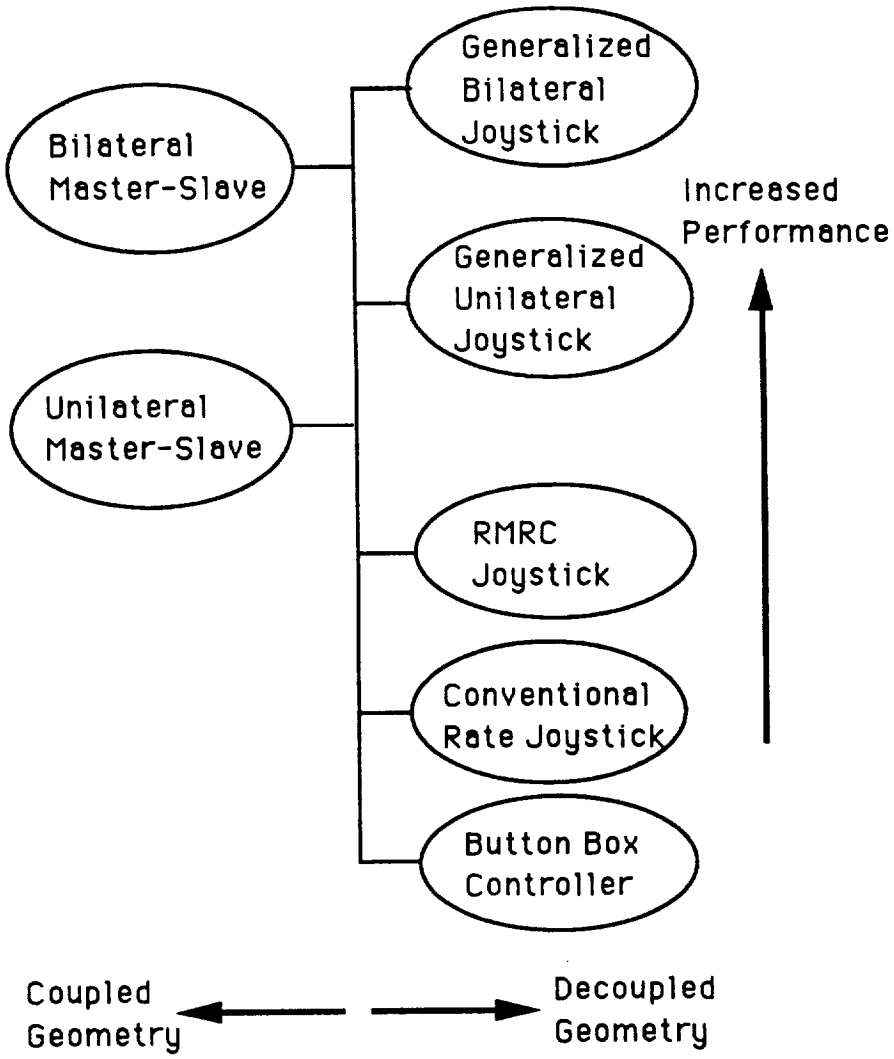

Figure 3–3 RANKING OF VARIOUS MAN-MACHINE TECHNOLOGIES BY LEVEL OF PERFORMANCE (ADAPTED FROM [88]).

Table 3–1 FUNCTIONAL PROPERTIES OF MANUAL CONTROLLERS (ADAPTED FROM [88]).

Functional Property	rate button box	isometric rate control	master slave	anthropo-morphic	universal bilateral	redundant universal bilateral
motion filtering		•	•	•	•	•
motion constraints			•	•	•	•
resolved motion control			•	•	•	•
compensation			•	•	•	•
force reflection			•	•	•	•
variable control point					•	•
scaling					•	•
re-referencing					•	•
re-orientation					•	•
intelligence						•

Table 3–2 PERFORMANCE CHARACTERISTICS OF MANUAL CONTROLLERS (ADAPTED FROM [88]).

Evaluation Criteria	rate button box	isometric rate control	master/ slave	anthropo-morphic	universal bilateral	redundant universal bilateral
task performance time	poor	fair	best	good	good	good
decoupled interface	yes	yes	no	no	yes	yes
natural motion	poor	fair	very good	excellent	very good	very good
control device implemen-tation	simple	simple	direct	direct	difficult	difficult
attainable accuracy	poorest	fair	good	good	good	good
cost	lowest	low	moderate	high	moderate	highest
reliability	very good	good	good	poor	good	fair
control mode applicability	poorest	poor	fair	fair	very good	excellent
computa-tational burden	lowest	moderate	low	low	high	very high
compactness & size	best	excellent good	poor	poor	very good	good
dexterity	worst	fair	good	good	very good	excellent

CHAPTER 4

Kinematic Analysis of the Parallel Spherical 3-dof System

The kinematic design of the robotic manipulator requires various considerations to accomplish the desired system performance. Due to its kinematic and dynamic simplicity and its dextrous large working volume, most current robotic systems in use are primarily based on a serial structure. However, its low structural stiffness and low load capacity represent disadvantageous characteristics for its versatile applications.

The parallel structure could, in general, have larger load capacity and higher structural stiffness than the serial structure. Heavy actuators could be located toward and/or on the base and parallelism increases the structural rigidity. However, as the number of degrees of freedom of parallel systems increases, both the complexity of the kinematic/dynamic analysis and the computational burden increase. Only a restricted design of the parallel system could be useful.

Most of available bilateral or force-reflecting manual controllers use elementary architectures (serial structure). However, as discussed, the parallel structure represents promising aspects for bilateral or force-reflecting manual controller applications such as locations of actuators on the grounded base, structural stiffness, etc.

A 3-dof parallel spherical shoulder system has been studied for its possible applications to robotic systems by several researchers[18][20][68]. In this chapter, the kinematic and dynamic analysis for the parallel 3-DOF spherical shoulder system are reviewed, and the forward position analysis is presented for a universal manual controller application.

4–1 Mobility analysis

The degrees of freedom of the spherical shoulder could be confirmed by the general mobility criterion, called Grübler's or Kutzback's criterion[50],

$$M = m(n-1) - \sum_{i=1}^{g}(u_i) \qquad (4\text{–}1.1)$$

where M: mobility

m: the dimension of maximum output space of n bodies

n: the number of completely unconstrained bodies

g: the number of joints

u_i: the number of constraints on joint i.

In this formula, the dimension of the maximum output space of n bodies, m, requires more considerations. In general, spatial motion represents 6 dimensional space motion. However, due to the lack of geometrical generality in certain situations, the full 6 dimensional motion space could not be covered by the mechanism; because of singularity points, the motion space of a mechanism could be reduced by more than one-dof.

As in the planar motion mechanism, the spherical shoulder has its nine joint axes co-intersecting at a common point, thus constraining the motion to be purely spherical. For convenience, the simplified schematic of the shoulder

is given in Figure 4–1. In actuality, the number of degrees of freedom of the mechanism is restricted to three dimensional spherical space; the motion path of any point on the link is restricted to the surface of the sphere which has an origin at the common intersecting point.

With the substitution of $m = 3$ into the above mobility criterian (assuming spherical motion of the mechanism), the mobility, M, would be obtained as below;

$$M = 3(8 - 1) - 2 \times 9 = 3.$$

However, when we insert $d = 6$ into the criterion without the above consideration (assuming general spatial motion of the mechanim), the mobility, M, could result in;

$$M = 6(8 - 1) - 5 \times 9 = -3.$$

By examining the mobility results from these two cases, it can be seen that the

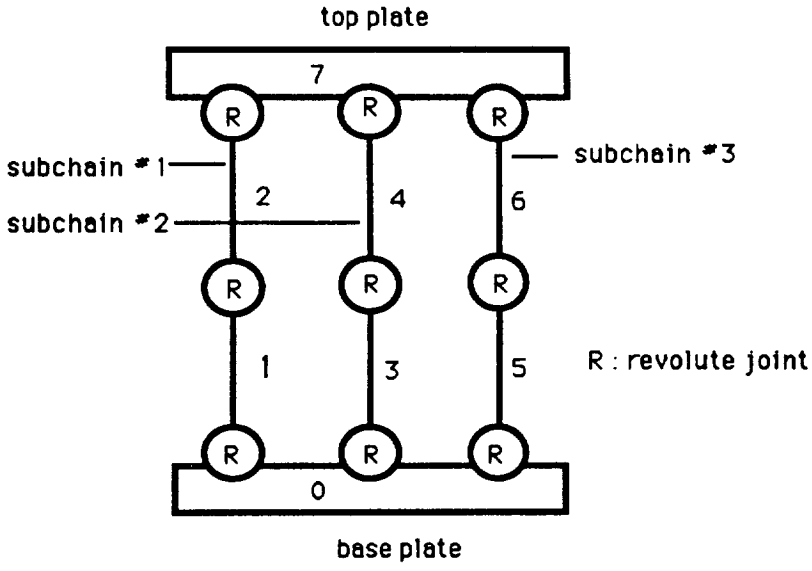

Figure 4–1 SIMPLIFIED SCHEMATICS OF THE SHOULDER

number of overconstraints imposed on the system are six (they are different by six). When some of these six overconstraints are removed, the shoulder would not increase its mobility (3-dof) at all, but it could decrease the structual rigidity of the mechanism. Note also that due to its overconstraints, the shoulder system becomes structurally indeterminate and requires compatibility conditions for its force and torque analysis[20].

4–2 Kinematic description

The shoulder system, shown in Figure 4–2, is a multi-loop, spherical mechanism. It consists of a lower (or base) ternary, three serial subchains, and a upper (or top) ternary. Each serial subchain consists of three revolute joints (since they are serially connected, it can be represented as a RRR dyad). To satisfy the geometric constraints for a parallel spherical 3-dof motion, nine joint axes intersect at a common point. In this section, kinematic parameters of the shoulder are briefly described or reviewed. Note, however, that to directly be applicable as a modular component in a multi-dof manipulator, the local frames for the mechanism will be defined slighly differently from the previous works[18].

The rotation axis direction for each revolute joint is denoted as a unit vector, $\boldsymbol{s}_n^m$, as shown in Figure 4–3. The superscript, m, shall denote the subchain and the subscript, n, shall denote the joint. The two reference unit vectors perpendicular to the lower ternary plate and to the upper ternary plate are denoted as $\boldsymbol{s}_b$ and $\boldsymbol{s}_t$, respectively. The base frame fixed on the lower ternary ($\boldsymbol{x}_b\ \boldsymbol{y}_b\ \boldsymbol{z}_b$) and the top frame fixed on the upper ternary ($\boldsymbol{x}_t\ \boldsymbol{y}_t\ \boldsymbol{z}_t$), are defined. Three serial subchains are defined as open linkages connecting those two bases and top frames. The orientation of any link in a serial subchain, m, can be

described by a minimum of two vectors attached to the link, namely, $\boldsymbol{s}_i^m$ and $\boldsymbol{a}_{ij}^m$. The unit vector, $\boldsymbol{a}_{ij}^m$, is defined by

$$\boldsymbol{a}_{ij}^m = \boldsymbol{s}_i^m \times \boldsymbol{s}_j^m. \tag{4-2.2}$$

The transformation matrix, $[{}^m R_r^j]$, representing the jth local frame direction cosine with respect to the reference frame r, can be expressed as shown below,

$$[{}^m R_r^j] = [\boldsymbol{a}_{ij}^m \ \boldsymbol{s}_i^m \times \boldsymbol{a}_{ij}^m \ \boldsymbol{s}_i^m]. \tag{4-2.3}$$

The twist angles, which are defined as rotation angles about the axis, $\boldsymbol{a}_{ij}^m$, between two subsequent revolute axes, $\boldsymbol{s}_i^m$ and $\boldsymbol{s}_j^m$, are fixed geometric properties of each binary link and denoted by α_{ij}^m. Mathmatically it can be represented by

$$\cos\alpha_{ij}^m = \boldsymbol{s}_i^m \cdot \boldsymbol{s}_j^m. \tag{4-2.4}$$

To describe the offset angles between the subchain frames and reference frames(base and top frames), apex angles and edge displacement angles are defined. Apex angles, representing twist angles between the lower ternary reference unit vector, $\boldsymbol{s}_b$, and the lower joint axis, $\boldsymbol{s}_1^m$, and the upper joint axis, $\boldsymbol{s}_3^m$, and the upper ternary reference unit vector, $\boldsymbol{s}_t$ are denoted as α_{01}^m (or α_{b1}^m) and α_{34}^m (or α_{3t}^m), respectively as shown in Figure 4–3. In mathmatical form, apex angles can be written as follows;

$$\cos\alpha_{01}^m = \boldsymbol{s}_b \cdot \boldsymbol{s}_1^m, \ \textit{where } m = 1,2,3, \ \textit{for lower ternary}, \tag{4-2.5}$$

$$\cos\alpha_{34}^m = \boldsymbol{s}_3^m \cdot \boldsymbol{s}_t, \ \textit{where } m = 1,2,3, \ \textit{for upper ternary}. \tag{4-2.6}$$

Edge displacement angles which represent offset rotation angles about lower (upper) ternary reference unit vectors, $\boldsymbol{s}_b(\boldsymbol{s}_t)$, between the lower (upper) ternary

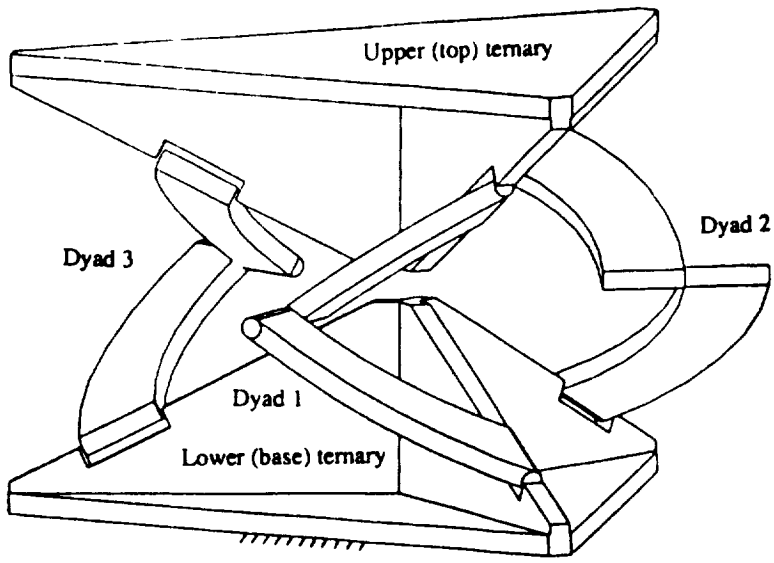

Figure 4–2 A SHOULDER MODULE

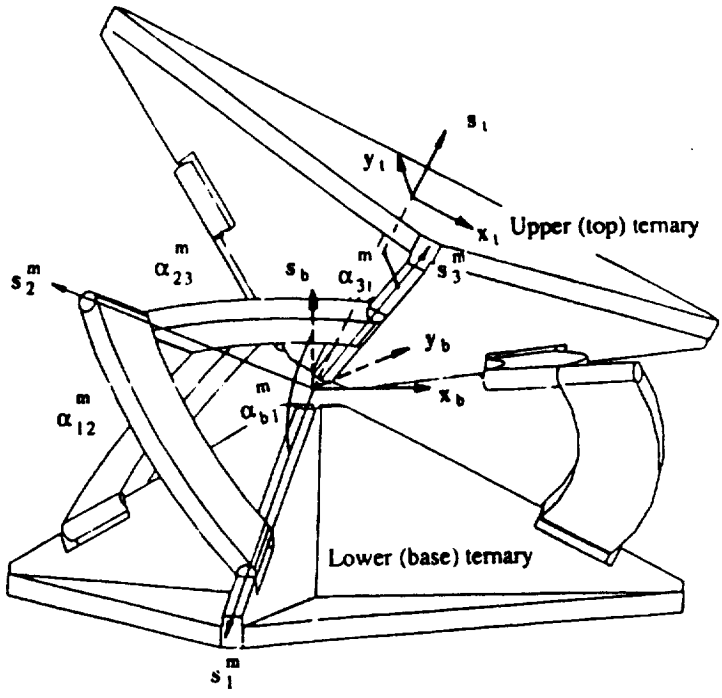

Figure 4–3 KINEMATIC REPRESENTATION OF THE SHOULDER

reference frame and the local frames, are denoted as $\gamma_{01}^m(\gamma_{34}^m)$. The unit vector describing the orientation of the ternary links are defined as

$$\boldsymbol{a}_{01}^m = \boldsymbol{s}_b \times \boldsymbol{s}_1^m, \ \textit{where } m = 1,2,3. \ \textit{for lower ternary}, \tag{4–2.7}$$

$$\boldsymbol{a}_{34}^m = \boldsymbol{s}_3^m \times \boldsymbol{s}_t, \ \textit{where } m = 1,2,3. \ \textit{for upper ternary}. \tag{4–2.8}$$

Based upon the above parameter notations, the complete kinematic description of each serial subchain can be represented as in Table 4–1. In the table, S_{ii}^m represents the offset distance along the local rotational joint axis, $\boldsymbol{s}_i^m$, and ϕ_i^m represents the active joint angular displacement about the local rotational joint axis, $\boldsymbol{s}_i^m$. In Figure 4–3, the schematic representation for kinematic parameters for a serial subchain of the shoulder system is shown.

4–3 Coordinate system and transformation

To represent the relative input and output position and orientation of the shoulder, two reference coordinate systems are required. Since the geometry of the shoulder allows only the rotational motion about the common intersection point, the origins of all local coordinates are located at that point. One body fixed coordinate system, fixed to the lower ternary, provides the references for input positions and is denoted as a base frame ($\boldsymbol{x}_b$, $\boldsymbol{y}_b$, $\boldsymbol{z}_b$). The other body fixed coordinate system, fixed to the upper ternary, provides the references for output positions and is denoted as a top frame ($\boldsymbol{x}_t$, $\boldsymbol{y}_t$, $\boldsymbol{z}_t$). For convenience, these two coordinate systems are defined so that they coincide at the reference position.

The output position of the shoulder system is represented by Euler angles denoted by μ_1, μ_2, and μ_3. These Euler angles can be represented by the

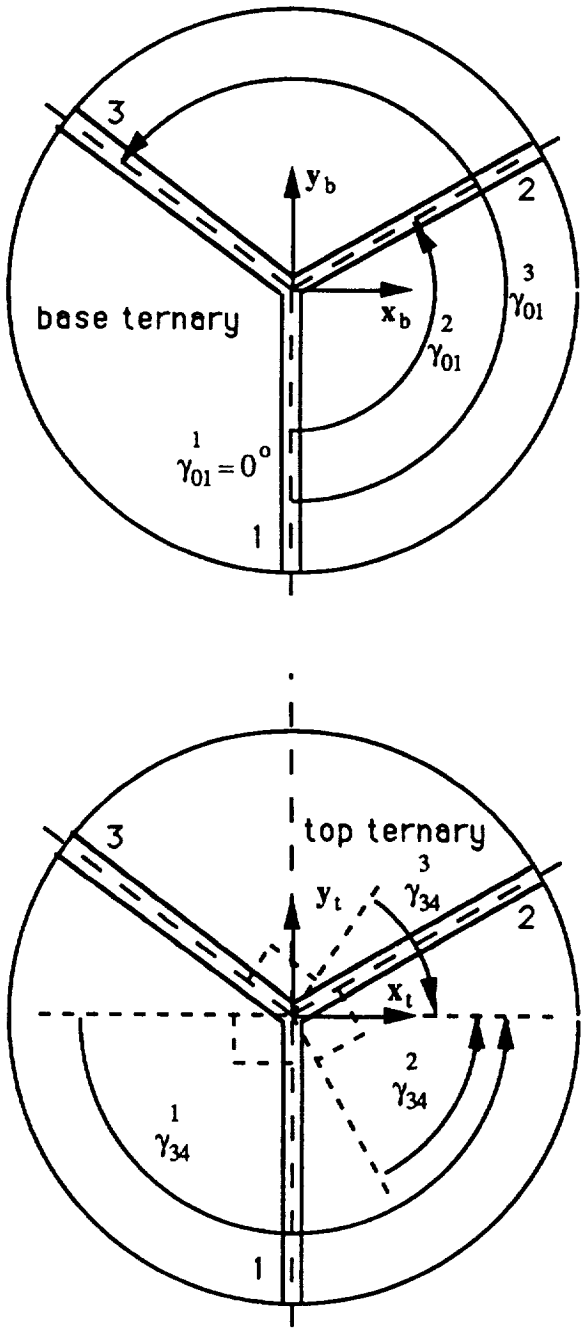

Figure 4–4 EDGE DISPLACEMENT ANGLES

Table 4–1 KINEMATIC PARAMETERS OF THE SHOULDER

Serial subchain # 1					
subchain	joint	S_{ii}^m	ϕ_i	a_{ii+1}	α_{ii+1}^m
base ternary	0(b)	0	γ_{01}^1	0	$\alpha_{01}^1(\alpha_{b1}^1)$
1	1	0	ϕ_1^1	0	α_{12}^1
1	2	0	ϕ_2^1	0	α_{23}^1
1	3	0	ϕ_3^1	0	$\alpha_{34}^1(\alpha_{3t}^1)$
top ternary	4(t)	0	γ_{34}^1	0	0
Serial subchain # 2					
subchain	joint	S_{ii}^m	ϕ_i	a_{ii+1}	α_{ii+1}^m
base ternary	0(b)	0	γ_{01}^2	0	$\alpha_{01}^2(\alpha_{b1}^2)$
2	1	0	ϕ_1^2	0	α_{12}^2
2	2	0	ϕ_2^2	0	α_{23}^2
2	3	0	ϕ_3^2	0	$\alpha_{34}^2(\alpha_{3t}^2)$
top ternary	4(t)	0	γ_{34}^2	0	0
Serial subchain # 3					
subchain	joint	S_{ii}^m	ϕ_i	a_{ii+1}	α_{ii+1}^m
base ternary	0(b)	0	γ_{01}^3	0	$\alpha_{01}^3(\alpha_{b1}^3)$
3	1	0	ϕ_1^3	0	α_{12}^3
3	2	0	ϕ_2^3	0	α_{23}^3
3	3	0	ϕ_3^3	0	$\alpha_{34}^3(\alpha_{3t}^3)$
top ternary	4(t)	0	γ_{34}^3	0	0

equivalent transformation matrix, or direction cosines of the top ternary body fixed coordinate frame with respect to the base ternary body fixed coordinate frame. That is,

$$
\begin{aligned}
[R_b^t] &= Rot(x,\mu_1)Rot(y,\mu_2)Rot(z,\mu_3) \\
&= \begin{bmatrix} 1 & 0 & 0 \\ 0 & c\mu_1 & -s\mu_1 \\ 0 & s\mu_1 & c\mu_1 \end{bmatrix} \begin{bmatrix} c\mu_2 & 0 & s\mu_2 \\ 0 & 1 & 0 \\ -s\mu_2 & 0 & -c\mu_2 \end{bmatrix} \begin{bmatrix} c\mu_3 & -s\mu_3 & 0 \\ s\mu_3 & c\mu_3 & 0 \\ 0 & 0 & 1 \end{bmatrix} \\
&= \begin{bmatrix} s\mu_2 c\mu_3 & -s\mu_2 s\mu_3 & s\mu_2 \\ s\mu_1 s\mu_2 c\mu_3 + c\mu_1 s\mu_3 & -s\mu_1 s\mu_2 s\mu_3 + c\mu_1 c\mu_3 & -s\mu_1 c\mu_2 \\ -c\mu_1 s\mu_2 s\mu_3 + s\mu_1 c\mu_3 & c\mu_1 s\mu_2 s\mu_3 + s\mu_1 c\mu_3 & c\mu_1 c\mu_2 \end{bmatrix} \qquad (4\text{–}3.9)
\end{aligned}
$$

or

$$[R_b^t] = [\boldsymbol{a}_t \;\; \boldsymbol{s}_t \times \boldsymbol{a}_t \;\; \boldsymbol{s}_t] \qquad (4\text{–}3.10)$$

where the superscript, t, and the subscript, b, denote the top ternary body fixed reference coordinate frame and the base ternary body fixed reference coordinate frame, respectively.

Now, for the serial subchain of the shoulder, any intermediate local coordinate systems may be defined and their direction cosines be provided for future references.

$$[R_r^b] = [\boldsymbol{a}_b \;\; \boldsymbol{s}_b \times \boldsymbol{a}_b \;\; \boldsymbol{s}_b] \qquad (4\text{–}3.11)$$

$$[R_r^b][Rot(z,\gamma_{01}^m)] = [\boldsymbol{a}_{01} \;\; \boldsymbol{s}_b \times \boldsymbol{a}_{01} \;\; \boldsymbol{s}_b] \qquad (4\text{–}3.12)$$

$$[R_r^b][Rot(z,\gamma_{01}^m)][Rot(x,\alpha_{01}^m)] = [\boldsymbol{a}_{01} \;\; \boldsymbol{s}_1 \times \boldsymbol{a}_{01} \;\; \boldsymbol{s}_1] \qquad (4\text{–}3.13)$$

$$[R_r^b][Rot(z,\gamma_{01}^m)][Rot(x,\alpha_{01}^m)][Rot(z,\phi_1^m)] = [\boldsymbol{a}_{12} \;\; \boldsymbol{s}_1 \times \boldsymbol{a}_{01} \;\; \boldsymbol{s}_1] \qquad (4\text{–}3.14)$$

$$[R_r^b][R_b^1][Rot(x,\alpha_{12}^m)] = [\boldsymbol{a}_{12} \;\; \boldsymbol{s}_2 \times \boldsymbol{a}_{12} \;\; \boldsymbol{s}_2] \qquad (4\text{–}3.15)$$

$$[R_r^b][R_b^1][Rot(x,\alpha_{12}^m)][Rot(z,\phi_2^m)] = [\boldsymbol{a}_{23} \;\; \boldsymbol{s}_2 \times \boldsymbol{a}_{23} \;\; \boldsymbol{s}_2] \qquad (4\text{–}3.16)$$

$$[R_r^b][R_b^1][R_1^2][Rot(x,\alpha_{23}^m)] = [\boldsymbol{a}_{23}\ \boldsymbol{s}_3 \times \boldsymbol{a}_{23}\ \boldsymbol{s}_3] \tag{4-3.17}$$

$$[R_r^b][R_b^1][R_1^2][Rot(x,\alpha_{23}^m)][Rot(z,\phi_3^m)] = [\boldsymbol{a}_{34}\ \boldsymbol{s}_3 \times \boldsymbol{a}_{34}\ \boldsymbol{s}_3] \tag{4-3.18}$$

$$[R_r^b][R_b^1][R_1^2][R_2^3][Rot(x,\alpha_{34}^m)] = [\boldsymbol{a}_{34}\ \boldsymbol{s}_t \times \boldsymbol{a}_{34}\ \boldsymbol{s}_t] \tag{4-3.19}$$

$$[R_r^b][R_b^1][R_1^2][R_2^3][Rot(x,\alpha_{34}^m)][Rot(z,\gamma_{34}^m)] = [\boldsymbol{a}_t\ \boldsymbol{s}_t \times \boldsymbol{a}_t\ \boldsymbol{s}_t] \tag{4-3.20}$$

where

$$[R_b^1] \equiv [Rot(z,\gamma_{01}^m)][Rot(x,\alpha_{01}^m)][Rot(z,\phi_1^m)] \tag{4-3.21}$$

$$[R_1^2] \equiv [Rot(x,\alpha_{12}^m)][Rot(z,\phi_2^m)] \tag{4-3.22}$$

$$[R_2^3] \equiv [Rot(x,\alpha_{23}^m)][Rot(z,\phi_3^m)] \tag{4-3.23}$$

$$[R_3^t] \equiv [Rot(x,\alpha_{34}^m)][Rot(z,\gamma_{34}^m)]. \tag{4-3.24}$$

Note that $[R_i^k] = [R_i^j][R_j^k]$, represents the direction cosines of the kth local frame with respect to the ith local frame, and that any local vector, $\boldsymbol{r}^{(k)}$, in kth local coordinate frame can be expressed in ith coordinate frame by

$$\boldsymbol{r}^{(i)} = [R_i^k]\boldsymbol{r}^{(k)}. \tag{4-3.25}$$

4–4 Reverse position analysis

Finding the angular displacements of the dyad joints when the output position of the system (upper ternary link) is specified, is referred to as the reverse position analysis. In the shoulder system, three base joints from each serial subchain are actuated. To locate the shoulder system at a specified position/orientation, these three actuated joint angular positions need to be determined. In this section, the reverse position analysis for the shoulder is presented.

Given an output position or orientation of the system in terms of Euler angles, three independent sets of equations can be written for each serial subchain.

$$[R_b^t] = [{}^m R_b^t] \; for \; m = 1, 2, 3, \tag{4–4.26}$$

where m denotes the serial subchain. The left hand side is a desired output transformation matrix of the system given in equation (4–3.9) and the right hand side is written in terms of the serial subchain variables as below,

$$[{}^m R_b^t] = [{}^m R_b^1][{}^m R_1^2][{}^m R_2^3][{}^m R_3^t] \; for \; m = 1, 2, 3 \tag{4–4.27}$$

where

$$[{}^m R_b^1] = [Rot(z, \gamma_{01}^m)][Rot(x, \alpha_{01}^m)][Rot(z, \phi_1^m)] \tag{4–4.28}$$

$$[{}^m R_1^2] = [Rot(x, \alpha_{12}^m)][Rot(z, \phi_2^m)] \tag{4–4.29}$$

$$[{}^m R_2^3] = [Rot(x, \alpha_{23}^m)][Rot(z, \phi_3^m)] \tag{4–4.30}$$

$$[{}^m R_3^t] = [Rot(x, \alpha_{34}^m)][Rot(z, \gamma_{34}^m)]. \tag{4–4.31}$$

Transformation matrices in the above equations, $[{}^m_m R_b^1]$, $[{}^m R_1^2]$, $[{}^m R_2^3]$, and $[{}^m R_3^t]$, represent the relative rotation between neighboring local link coordinate systems. Thus the orientation of the third link in the first coordinates are given by the matrix product

$$[{}^m R_1^3] = [{}^m R_1^2][{}^m R_2^3]. \tag{4–4.32}$$

For brevity, throughout the subsequent analysis, the following notations are used; $c\phi_n^m \equiv \cos(\phi_n^m)$, $s\phi_n^m \equiv \sin(\phi_n^m)$, etc. Then each transformation matrix can be written in detail as follows;

$$[{}^m R_b^1] = \begin{bmatrix} c\gamma_{01}^m c\phi_1^m - s\gamma_{01}^m c\alpha_1^m s\phi_1^m & -c\gamma_{01}^m s\phi_1^m - s\gamma_{01}^m c\alpha_1^m c\phi_1^m & s\gamma_{01}^m s\alpha_1^m \\ s\gamma_{01}^m c\phi_1^m - c\gamma_{01}^m c\alpha_1^m s\phi_1^m & -s\gamma_{01}^m s\phi_1^m - c\gamma_{01}^m c\alpha_1^m c\phi_1^m & -c\gamma_{01}^m s\alpha_1^m \\ s\alpha_1^m s\phi_1^m & s\alpha_1^m c\phi_1^m & c\alpha_1^m \end{bmatrix} \tag{4–4.33}$$

$$[{}^m R^n_{n-1}] = \begin{bmatrix} c\phi^m_n & -s\phi^m_n & 0 \\ c\alpha^m_{(n-1)n} s\phi^m_n & c\alpha^m_{(n-1)n} c\phi^m_j & -s\alpha^m_{(n-1)n} \\ s\alpha^m_{(n-1)n} s\phi^m_n & s\alpha^m_{(n-1)n} c\phi^m_n & c\alpha^m_{(n-1)n} \end{bmatrix} \quad (4\text{–}4.34)$$

$$[{}^m R^t_3] = \begin{bmatrix} c\gamma^m_{34} & -s\gamma^m_{34} & 0 \\ c\alpha^m_{34} s\gamma^m_{34} & c\alpha^m_{34} c\gamma^m_{34} & -s\alpha^m_{34} \\ s\alpha^m_{34} s\gamma^m_{34} & s\alpha^m_{34} c\gamma^m_{34} & c\alpha^m_{34} \end{bmatrix}. \quad (4\text{–}4.35)$$

Noting from the geometry of the shoulder that vectors, $\boldsymbol{s}^m_3$ for $m = 1, 2, 3$, are fixed to the upper ternary plate, the equation (4–4.27) can be rearranged in following form;

$$[{}^m R^t_b] = [{}^m R^1_b][{}^m R^2_1][Rot(x, \alpha^m_{23})][Rot(z, \phi^m_3)][{}^m R^t_3]. \quad (4\text{–}4.36)$$

Now, premultipling $[{}^m R^1_b]^T$ and postmultiplying $[{}^m R^t_3]^T[Rot(z, \phi^m_3)]^T$ on both sides yields

$$[{}^m R^b_1][{}^m R^t_b][{}^m R^3_t][Rot(z, \phi^m_3)]^T = [{}^m R^2_1][Rot(x, \alpha^m_{23})]. \quad (4\text{–}4.37)$$

The orthogonal property of the rotation matrices has been used in the above manipulations; that is, the inverse of the orthogonal matrix is equal to the transpose of the matrix. In this equation, the last columns of the transformation matrices represent the direction cosines of vectors, $\boldsymbol{s}^{m(1)}_3$ for $m = 1, 2, 3$, with respect to the local frame 1. Noting that

$$\begin{aligned} \boldsymbol{s}^m_3 &= [R^t_b][{}^m R^3_t][Rot(z, \phi^m_3)]^T \begin{Bmatrix} 0 \\ 0 \\ 1 \end{Bmatrix} \\ &= [R^t_b][{}^m R^3_t] \begin{Bmatrix} 0 \\ 0 \\ 1 \end{Bmatrix} \\ &= [\boldsymbol{a}_t \ \boldsymbol{s}_t \times \boldsymbol{a}_t \ \boldsymbol{s}_t] \begin{bmatrix} c\gamma^m_{34} & s\gamma^m_{34} c\alpha^m_{34} & s\gamma^m_{34} s\alpha^m_{34} \\ -s\gamma^m_{34} & c\gamma^m_{34} c\alpha^m_{34} & c\gamma^m_{34} s\alpha^m_{34} \\ 0 & -s\alpha^m_{34} & c\alpha^m_{34} \end{bmatrix} \begin{Bmatrix} 0 \\ 0 \\ 1 \end{Bmatrix}, \end{aligned} \quad (4\text{–}4.38)$$

vectors, $\boldsymbol{s}_3^m$, can be obtained by

$$\boldsymbol{s}_3^m = s\gamma_{34}^m s\alpha_{34}^m \boldsymbol{a}_t^m + c\gamma_{34}^m s\alpha_{34}^m \boldsymbol{s}_t^m \times \boldsymbol{a}_t^m + c\alpha_{34}^m \boldsymbol{s}_t^m. \tag{4–4.39}$$

Now, let's define a local coordinate, called dth local frame, as follows

$$[{}^m R_b^d] \equiv [Rot(z, \gamma_{01}^m)][Rot(x, \alpha_{01}^m)] \tag{4–4.40}$$

where

$$[{}^m R_b^d] = \begin{bmatrix} c\gamma_{01}^m & -s\gamma_{01}^m c\alpha_{01}^m & s\gamma_{01}^m s\alpha_{01}^m \\ s\gamma_{01}^m & c\gamma_{01}^m c\alpha_{01}^m & -c\gamma_{01}^m s\alpha_{01}^m \\ 0 & s\alpha_{01}^m & c\alpha_{01}^m \end{bmatrix}. \tag{4–4.41}$$

Note that

$$\boldsymbol{s}_3^{m(d)} = [{}^m R_b^d]^T \boldsymbol{s}_3^m \tag{4–4.42}$$

and

$$[{}^m R_b^1]^T = [Rot(z, \phi_1^m)]^T [{}^m R_b^d]^T. \tag{4–4.43}$$

Substituting equations (4–4.42) and (4–4.43) into (4–4.37), and using equation (4–4.38), the third column of RHS of the equation (4–4.37), representing local unit vectors, $\boldsymbol{s}_3^{m(d)}$, can be written as follows

$$[Rot(z, \phi_1^m)]^T \boldsymbol{s}_3^{m(d)} = [{}^m R_1^2][Rot(x, \alpha_{23}^m)] \begin{Bmatrix} 0 \\ 0 \\ 1 \end{Bmatrix}. \tag{4–4.44}$$

Now, for brevity, local vectors, $\boldsymbol{s}_3^{m(d)}$ for $m = 1, 2, 3$, are denoted as

$$\boldsymbol{s}_3^{m(d)} \equiv \begin{Bmatrix} x_3^{m(d)} \\ y_3^{m(d)} \\ z_3^{m(d)} \end{Bmatrix}. \tag{4–4.45}$$

These components can be found in terms of the known parameters in the reverse position analysis and are considered as constants in the following analysis. With substitution of the equation (4–4.45) into the equation (4–4.44), we have

$$x_3^{m(d)} c\phi_1^m + y_3^{m(d)} s\phi_1^m = s\phi_2^m s\alpha_{23}^m \tag{4–4.46}$$

$$-x_3^{m(d)} s\phi_1^m + y_3^{m(d)} c\phi_1^m = -c\alpha_{12}^m c\phi_2^m s\alpha_{23}^m - s\alpha_{12}^m c\alpha_{23}^m \tag{4–4.47}$$

$$z_3^{m(d)} = -s\alpha_{12}^m c\phi_2^m s\alpha_{23}^m + c\alpha_{12}^m c\alpha_{23}^m. \tag{4–4.48}$$

Multiply the equation (4–4.47) by -$s\alpha_{12}^m$ and the equation (4–4.48) by $c\alpha_{12}^m$, and add these two results. Then we get

$$s\alpha_{12}^m (x_3^m s\phi_1^m + y_3^m c\phi_1^m) + c\alpha_{12}^m z_3^m = c\alpha_{23}^m, \ for \ m = 1, 2, 3. \tag{4–4.49}$$

Substituting the tan-half angle representations into this equations,

$$s\phi_1^m = \frac{2t_1^m}{1 + (t_1^m)^2}, \ and \ c\phi_1^m = \frac{1 - (t_1^m)^2}{1 + (t_1^m)^2}, \ where \ t_1^m = \tan(\frac{\phi_1^m}{2}), \tag{4–4.50}$$

yields

$$A(t_1^m)^2 + Bt_1^m + C = 0 \tag{4–4.51}$$

where

$$A = y_3^{m(1)} s\alpha_{12}^m + x_3^{m(1)} c\alpha_{12}^m - c\alpha_{23}^m \tag{4–4.52}$$

$$B = 2x_3^{m(1)} s\alpha_{12}^m \tag{4–4.53}$$

$$C = -y_3^{m(1)} s\alpha_{12}^m + z_3^{m(1)} c\alpha_{12}^m - c\alpha_{23}^m. \tag{4–4.54}$$

From this quadratic equation (4–4.51), two solutions can be obtained and they represent the two different closures of each serial RRR dyad shown in Figure 4–5.

$$t_1^m = \frac{-B \pm \sqrt{B^2 - 4AC}}{2A}. \tag{4–4.55}$$

The desired angles, ϕ_1^m, can be obtained by substituting the results into equation (4–4.50)

$$\phi_1^m = 2 \arctan(t_1^m) \tag{4–4.56}$$

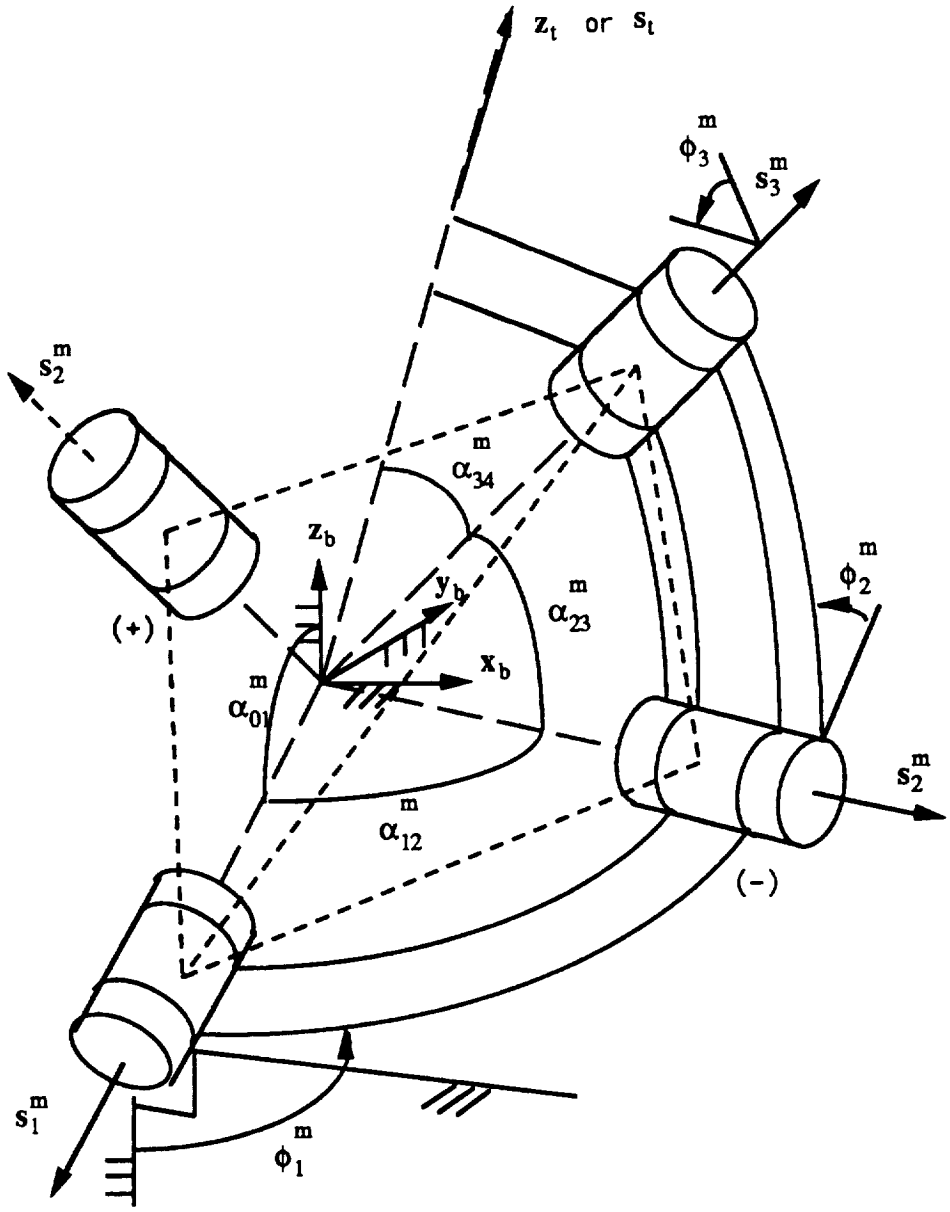

Figure 4–5 TWO CLOSURES OF THE RRR DYAD

Another joint angular displacements, ϕ_2^m for $m = 1, 2, 3$, can be obtained by back substituting obtained values for ϕ_1^m's into the equation (4–4.46) and (4–4.48)

$$\phi_2^m = \arctan(\frac{s\phi_2^m}{c\phi_2^m}) \tag{4–4.57}$$

where

$$s\phi_2^m = \frac{x_3^m c\phi_1^m + y_3^m s\phi_1^m}{s\alpha_{23}^m} \tag{4–4.58}$$

$$c\phi_2^m = \frac{c\alpha_{12}^m c\alpha_{23}^m - z_3^{m(d)}}{s\alpha_{12}^m s\alpha_{23}^m}. \tag{4–4.59}$$

Note that in derivation of the kinematic equations for the shoulder, ϕ_3^m's of all three dyads of the shoulder are not required when the output transformation or its equivalent Euler angles are known as in reverse position analysis. In particular, for kinesthetic coupling in teleoperator system applications, only the first order Kinematic Influence Coefficients(KIC's) are required. The vectors, $\boldsymbol{s}_1^m$, $\boldsymbol{s}_2^m$, and $\boldsymbol{s}_3^m$, which are required to compute the first order KIC's of the shoulder, can be obtained as follows

$$\boldsymbol{s}_1^m = [{}^m R_b^1] \begin{Bmatrix} 0 \\ 0 \\ 1 \end{Bmatrix}, \tag{4–4.60}$$

$$\boldsymbol{s}_2^m = [{}^m R_b^2] \begin{Bmatrix} 0 \\ 0 \\ 1 \end{Bmatrix} \text{ or } \boldsymbol{s}_2^m = [{}^m R_b^1] \begin{Bmatrix} 0 \\ -s\alpha_{12}^m \\ c\alpha_{12}^m \end{Bmatrix} \tag{4–4.61}$$

and

$$\boldsymbol{s}_3^m = [{}^m R_b^3] \begin{Bmatrix} 0 \\ 0 \\ 1 \end{Bmatrix} \text{ or } \boldsymbol{s}_3^m = [{}^m R_b^2] \begin{Bmatrix} 0 \\ -s\alpha_{23}^m \\ c\alpha_{23}^m \end{Bmatrix}. \tag{4–4.62}$$

4–5 Forward position analysis

Finding the end-effector position/orientation of the manipulator with the joint displacement angles measured is referred to as the forward position

analysis. In universal teleoperator system applications, whether unilateral or bilateral, the handgrip position/orientation of the manual controller must be computed and is given as a command to the remote manipulator. In serial manipulators, forward position analysis is a relatively simple process. However, in parallel manipulators, forward position analysis is an involved process, especially when measured joint displacement angles are related to geometrical constraints for the desired output position/orientation. For a parallel system with measured joint displacement angles along one serial subchain, the forward position analysis becomes that for a serial manipulator. In certain cases, the locations for position transducers for parallel mechanisms are restricted, due to mechanical interferences or requirements for higher resolution. In the following section, the forward position analysis of the 3-dof shoulder for three measured joint displacement angles, ϕ_1^1, ϕ_1^2, and ϕ_1^3, is presented. With these choices for measured joint angles, the above mentioned problems can be avoided.

From the equation (4–4.27), the following two loop constraints equations can be written as,

$$[{}^1R_b^1][{}^1R_1^2][{}^1R_2^3][{}^1R_3^t] = [{}^mR_b^1][{}^mR_1^2][{}^mR_2^3][{}^mR_3^t] \ for\ m = 2,3. \qquad (4\text{–}5.63)$$

Premultiplying $[{}^mR_b^1]^T$ and postmultiplying $[{}^mR_3^t]^T$ to equation (4–5.63) yields

$$[{}^mR_b^1]^T[{}^1R_b^t][{}^mR_3^t]^T = [{}^mR_1^2][{}^mR_2^3] = [{}^mR_1^3] \ for\ m = 2,3 \qquad (4\text{–}5.64)$$

where

$$[{}^1R_b^t] = [{}^1R_b^1][{}^1R_1^2][{}^1R_2^3][{}^1R_3^t]. \qquad (4\text{–}5.65)$$

Noting that the local vector, $s_3^{m(1)}$ are only a function of the second joint angular displacement, ϕ_2^m, the last columns of the above equation (4–5.64) can be used.

That is,

$$[{}^m R_b^1]^T [{}^1 R_b^t][{}^m R_3^t]^T \begin{Bmatrix} 0 \\ 0 \\ 1 \end{Bmatrix} = [{}^m R_1^2][{}^m R_2^3] \begin{Bmatrix} 0 \\ 0 \\ 1 \end{Bmatrix} = [{}^m R_1^3] \begin{Bmatrix} 0 \\ 0 \\ 1 \end{Bmatrix} \quad for\ m = 2, 3. \tag{4-5.66}$$

The LHS of equation (4–5.66) can be expressed in the following functional form in terms of three joint displacement angles (ϕ_1^1, ϕ_1^2, and ϕ_1^3),

$$\boldsymbol{s}_3^{m(1)} = \begin{Bmatrix} [{}^m R_1^3]_{13}(\phi_1^1, \phi_2^1, \phi_3^1) \\ [{}^m R_1^3]_{23}(\phi_1^1, \phi_2^1, \phi_3^1) \\ [{}^m R_1^3]_{33}(\phi_1^1, \phi_2^1, \phi_3^1) \end{Bmatrix} \equiv \begin{Bmatrix} x^{m(1)} \\ y^{m(1)} \\ z^{m(1)} \end{Bmatrix} \quad for\ m = 2, 3. \tag{4-5.67}$$

And the RHS can be written as

$$\boldsymbol{s}_3^{m(1)} = \begin{Bmatrix} s\phi_2^m s\alpha_{23}^m \\ -c\alpha_{12}^m s\alpha_{23}^m c\phi_2^m - s\alpha_{12}^m c\alpha_{23}^m \\ -s\alpha_{12}^m s\alpha_{23}^m c\phi_2^m + c\alpha_{12}^m c\alpha_{23}^m \end{Bmatrix} \quad for\ m = 2, 3. \tag{4-5.68}$$

Multiply $-s\alpha_{12}^m$ to the y component and $c\alpha_{12}^m$ to the z component of the equations (4–5.66) and add those results to obtain the desired constraint equations for the shoulder as below

$$c\alpha_{23}^m = -s\alpha_{12}^m y^{m(1)} + c\alpha_{12}^m z^{m(1)} \quad for\ m = 2, 3. \tag{4-5.69}$$

The equations (4–5.69) may be expressed in more specific form as below,

$$D_1^*(\phi_1^1, \phi_3^1, \phi_1^2)c\phi_2^1 + E_1^*(\phi_1^1, \phi_3^1, \phi_1^2)s\phi_2^1 = F_1^*(\phi_1^1, \phi_1^2) \tag{4-5.70}$$

$$D_2^*(\phi_1^1, \phi_3^1, \phi_1^3)c\phi_2^1 + E_2^*(\phi_1^1, \phi_3^1, \phi_1^3)s\phi_2^1 = F_2^*(\phi_1^1, \phi_1^3) \tag{4-5.71}$$

Note that these constraint equations are functions of two unknown joint angular displacements, ϕ_2^1 and ϕ_3^1 since three joint displacement angles, ϕ_1^1, ϕ_1^2 and ϕ_1^3 are provided.

From the equations (4–5.70) and (4–5.71), it seems that with either ϕ_2^1 or ϕ_3^1 known, the other variables can be obtained uniquely. However, in real

implementation, the measurement errors from the redundant joint such as either ϕ_2^1 or ϕ_3^1, is introduced so that both constraint equations may not be satisfied. The obtained solutions showed a very high sensitivity to the measurement errors and direct substitution of the measured angle, either ϕ_3^1 or ϕ_2^1 into (4–5.70) and (4–5.71), resulted in unacceptable results.

Once joint angles along one of the serial subchains are determined, the output transformation matrix of the shoulder system can be computed using the equation (4–4.27). Euler angles, μ_1, μ_2 and μ_3, representing the output rotational transformation matrix of the shoulder, can be also found directly from the equations (4–3.9) and (4–4.27) as follows:

$$s\mu_2 = ({}^m R_b^t)_{13} \tag{4–5.72}$$

$$\tan\mu_1 = \frac{-({}^m R_b^t)_{23}/c\mu_2}{({}^m R_b^t)_{33}/c\mu_2} \tag{4–5.73}$$

$$\tan\mu_3 = \frac{-({}^m R_b^t)_{12}/c\mu_2}{({}^m R_b^t)_{11}/c\mu_2}. \tag{4–5.74}$$

In actual shoulder system implementation, only one set of solutions, ϕ_2^m, where $m = 1, 2, 3$, are selected and maintained during its operation. The shoulder is not allowed to pass through singularity points to change its configuration ($\phi_2^m = 0°$, or $180°$), at any time.

4–5.1 Forward position analysis in explicit form

In this section, forward position analysis for the same three measured joint displacement angles, ϕ_1^1, ϕ_1^2, and ϕ_1^3 is derived in explicit form. With the direct substitution for the three measured joint displacement angles into equations (4–5.70) and (4–5.71), the following form of the equations can be

found.

$$D_1(\phi_3^1)c\phi_2^1 + E_1(\phi_3^1)s\phi_2^1 = F_1(\phi_3^1) \tag{4–5.75}$$

$$D_2(\phi_3^1)c\phi_2^1 + E_2(\phi_3^1)s\phi_2^1 = F_2(\phi_3^1) \tag{4–5.76}$$

Now, applying Cramer's rule into the above equations, we have

$$c\phi_2^1 = \frac{F_1E_2 - E_1F_2}{D_1E_2 - E_1D_2} \tag{4–5.77}$$

and

$$s\phi_2^1 = \frac{D_1F_2 - F_1D_2}{D_1E_2 - E_1D_2}. \tag{4–5.78}$$

Substituting the above results into the trigonometric functions, $(c\phi_2^1)^2 + (s\phi_2^1)^2 = 1$, yields:

$$f(\phi_3^1) = (F_1E_2 - E_1F_2)^2 + (D_1F_2 - F_1D_2)^2 - (D_1E_2 - E_1D_2)^2 = 0. \tag{4–5.79}$$

Note that this equation is a function of only $c\phi_3^1$ and $s\phi_3^1$. When tangent-half angle representations are applied

$$s\phi_3^1 = \frac{2t}{1+t^2}, \quad c\phi_3^1 = \frac{1-t^2}{1+t^2}, \quad where\ t \equiv \tan(\frac{\phi_3^1}{2}) \tag{4–5.80}$$

they can be written in polynomial forms,

$$g(t) = 0. \tag{4–5.81}$$

Actually, this equation (4–5.81) is an eighth-order ploynomial, and finding its solution would require a major computational effort. Also, the correct solution should be selected out of eight possible configurations. Because of those problems, this approach for forward position analysis may not be a good approach in real time applications. Note that only real solutions of the eighth-order polynomial equation represent the real possible configurations of the shoulder.

4–5.2 Forward position analysis via numerical method

The explicit form of forward position anlaysis for three measurable joint angles, ϕ_1^1, ϕ_1^2, and ϕ_1^3, is computationally intensive and may be difficult to achieve in real time as discussed in the previous section. A numerical approach for the forward position analysis is considered as an alternative for practical implementations. Equations (4–5.70) and (4–5.71) are rewritten in the following form for direct numerical application:

$$C_1(\phi_2^1, \phi_3^1) = 0 \tag{4–5.82}$$

$$C_2(\phi_2^1, \phi_3^1) = 0. \tag{4–5.83}$$

To solve the above two nonlinear equations simultaneously, various kinds of numerical techniques could be applied. With a simple iterative Newton-Raphson's method, solutions within an acceptable error bound can be obtained within two to three iterations. However, both the simulation and actual operation results revealed that when the initial guesses for the joint angles are not sufficiently close to the actual joint angles, the solutions neither converged toward the answers quickly nor gave the correct answers. This is expected and confirms the existence of the other possible forward position solutions of the shoulder for those measured joint displacements as discussed before.

After obtaining the numerical solutions for ϕ_2^1 and ϕ_3^1, the remaining joint angles, ϕ_2^2, ϕ_3^2, ϕ_2^3, and ϕ_3^3 may be computed. To do so, first, the forward position analysis along the one serial sub-chain, of which all joint displacement angles are identified in the above numerical method, is performed to find the output ternary transformation matrix or its equivalent Euler angles. Then, by performing the reverse position analysis along the other two serial sub-chains,

the remaining joint displacement angles can be computed.

4–5.3 Consideration on the location of position transducers

In the previous sections, it has been shown that the shoulder could have multiple possible configurations in the reverse position analysis. Two configurations exist along each serial sub-chain making eight system configurations possible. Likewise, in the forward position analysis of the parallel shoulder system, the number of possible configurations depends on which three measured joint angles are chosen. The proper locations of the three position transducers are considered shortly. Obviously, the measurement of three joint angles along any one serial subchain of the shoulder provides the simplest equations for forward position analysis. From the other two serial subchains four possible configurations can be obtained (two configurations for each serial subchain). It should be noted, however, that the possible mechanical interferences of the position transducers in the middle joint with the other links may leave no room for transducers at these joints. In the actual hardware design of the shoulder as a manual controller, discussed in Chapter 5, the large workspace as well as the compactness of the shoulder has been emphasized and not enough room for the position transducers is left in the middle joints. Thus the measurements of the middle joint displacement angles, ϕ_2^1, ϕ_2^2, and ϕ_2^3, are not considered.

The other selections are the three joint angles for actual implementation, ϕ_1^1, ϕ_1^2, and ϕ_1^3. These selections are most preferable since all of the position transducers are placed with the actuators on the base. With high-ratio gear reducers at the actuators, high resolutions for angular position could be obtained. For these three measured joint angles, the detailed analysis is already discussed in the section 4-5 and is not repeated.

More than three joints angles could be measured among ϕ_1^1, ϕ_1^2, ϕ_1^3, ϕ_3^1, ϕ_3^2, and ϕ_3^3, as alternatives. Particularly, with any four known joint angles including three base joint angles, the forward position solution can be obtained without too much computational effort. However, in actual implementation, measuring additional joint angles could produce a certain amount of conflicting measurement errors, violating the constraints, and thus resulting in an uncertain forward position solution. However, the extra joint displacement angle can be used as an initial guess to expedite and/or test the numerical calculation.

4–6 KIC of the parallel spherical 3-dof shoulder

To analyze multi-loop parallel systems, it is often difficult to obtain the kinematic and dynamic model directly with respect to the desired generalized variables. To avoid this kind of difficulty, Freeman and Tesar[32] suggest a method using intermediate variables (generalized universal variables). In their approach, the kinematic and dynamic model with respect to those intermediate variables are found first. Then the desired kinematic and dynamic model with respect to the specified variables are computed, using the geometric relations between the intermediate variables and the desired variables (called the generalized transfer of coordinates). This approach is based on the differential equations (holononic equations) and typically the task rate variables such as end-effector positional/rotational velocities are selected as intermediate rate variables to reduce the computational burden. Note, however, that due to the intermediate transformation from the generalized variables to the intermediate variables, any mathematical singularities between them would invalidate these formulations.

To represent the output ternary angular position of the shoulder, the Euler angles given in equation (4-3.9) are used. However, the direct time derivatives of Euler angles do not represent the output ternary differential motion in universal Cartesian space. In fact, they rather represent the differential motion in joint space that is equivalent to the corresponding Euler angles. If it is recalled that Euler angles are defined as succesive rotations with respect to local axes, it can be seen that it can be represented the serial wrist with appropriate kinematic parameters. That is,

$$\begin{aligned} Rot(x,\mu_1)Rot(y,\mu_2)Rot(z,\mu_3) &= Rot(z,90°)Rot(x,90°) \\ & \quad Rot(x,\mu_1+90°)Rot(x,90°)Rot(z,\mu_2+90°) \\ & \quad Rot(x,90°)Rot(z,\mu_3). \end{aligned} \tag{4–6.84}$$

In the spherical shoulder system analysis, absolute angular velocities of the output ternary are chosen as output (intermediate) rate variables. It is also assumed that each serial subchain of the shoulder is not in any singularity configurations, whether geometrical or mathematical.

To find the KIC's of the shoulder that relates input joint angular velocities either to the output ternary absolute angular velocities or to the local angular velocities with respect to the local frame fixed on the output ternary, use the following relations between the absolute angular velocity and the local angular velocity in the local frame fixed on the output ternary.

$$\boldsymbol{\omega} = [R_b^t]\dot{\boldsymbol{\mu}} \tag{4–6.85}$$

or

$$\dot{\boldsymbol{\mu}} = [R_b^t]^T\boldsymbol{\omega} \tag{4–6.86}$$

where $\boldsymbol{\omega} = [\omega_1\ \omega_2\ \omega_3]^T$, represents the absolute angular velocity of the upper ternary plate and $\dot{\boldsymbol{\mu}} = [\dot{\mu}_1\ \dot{\mu}_2\ \dot{\mu}_3]^T$, denote the local angular velocity in the local frame fixed on the upper ternary plate.

For each serial subchain, the differential relations between the absolute angular velocities, $\boldsymbol{\omega}$, and the joint angular velocities, $\dot{\boldsymbol{\phi}}^m$, can be written

$$\boldsymbol{\omega} = [{}^mG^u_{\boldsymbol{\phi}}]\dot{\boldsymbol{\phi}}^m \ for\ m = 1,2,3. \tag{4-6.87}$$

where

$$\dot{\boldsymbol{\phi}}^m = [\dot{\phi}^m_1\ \dot{\phi}^m_2\ \dot{\phi}^m_3]^T \ for\ m = 1,2,3. \tag{4-6.88}$$

Note that the superscript, m, denotes the serial subchain; for example, $[{}^mG^u_{\boldsymbol{\phi}}]$ represents the first-order KIC between the output rate variables and the joint angular velocities of the serial subchain, m. When $[{}^mG^u_{\boldsymbol{\phi}}]$, for $m = 1,2,3$, are not singular, the equation (4–6.87) can be written as

$$\dot{\boldsymbol{\phi}}^m = [{}^mG^u_{\boldsymbol{\phi}}]^{-1}\boldsymbol{\omega} \ for\ m = 1,2,3. \tag{4-6.89}$$

It can be noted that in the above inverse process, the geometric constraints are embedded implicitly. Let actuated joint variables be denoted as $\boldsymbol{\phi}_a$=$[\phi^1_1\ \phi^2_1\ \phi^3_1]$. Then from equation (4–6.89) we have

$$\dot{\boldsymbol{\phi}}^1_1 = [{}^1G^u_{\boldsymbol{\phi}}]^{-1}_{1;}\boldsymbol{\omega} \tag{4-6.90}$$

$$\dot{\boldsymbol{\phi}}^2_1 = [{}^2G^u_{\boldsymbol{\phi}}]^{-1}_{1;}\boldsymbol{\omega} \tag{4-6.91}$$

$$\dot{\boldsymbol{\phi}}^3_1 = [{}^3G^u_{\boldsymbol{\phi}}]^{-1}_{1;}\boldsymbol{\omega}, \tag{4-6.92}$$

where $[{}^1G^u_{\boldsymbol{\phi}}]^{-1}_{n;}$ represents the nth row of $[{}^1G^u_{\boldsymbol{\phi}}]^{-1}$. In matrix form, it can be rewritten as

$$\dot{\boldsymbol{\phi}}_a = [G^u_{\boldsymbol{\phi}_a}]^{-1}\boldsymbol{\omega} \tag{4-6.93}$$

where

$$[G^u_{\phi_a}]^{-1} = \begin{bmatrix} [{}^1G^u_\phi]^{-1}_{1;} \\ [{}^2G^u_\phi]^{-1}_{1;} \\ [{}^3G^u_\phi]^{-1}_{1;} \end{bmatrix} \qquad (4\ 6.94)$$

Then the KIC is obtained from the equation (4–6.93)

$$\boldsymbol{\omega} = [G^u_{\phi_a}]\dot{\boldsymbol{\phi}}_a. \qquad (4\text{–}6.95)$$

The local KIC between the absolute angular velocities in the local moving frame and the actuated joint velocities can be found by substituting equation (4–6.95) into (4–6.86),

$$\dot{\boldsymbol{\mu}} = [R^t_b]^T[G^u_{\phi_a}]\dot{\boldsymbol{\phi}}_a = [G^\mu_{\phi_a}]\dot{\boldsymbol{\phi}}_a \qquad (4\text{–}6.96)$$

where

$$[G^\mu_{\phi_a}] = [R^t_b]^T[G^u_{\phi_a}]. \qquad (4\text{–}6.97)$$

4–7 Static torque analysis

The KIC matrix, $[G^u_\phi]$, also represents the relation between the input torque and the output torque of the system. To find the desired force relations, the virtual work principle can be used. The virtual displacement is defined as a hypothetical infinitesimal displacement consistent with the applied forces and forces of constraints at a given instant. The work done in a virtual displacement is called virtual work. The virtual work principle describes the static equilibrium state of the system, for which the sum of the virtual work of the forces of constraints is zero. It states that the sum of the virtual work done by the applied forces to the system is zero,

$$\delta W = T^T_\phi \cdot \delta\boldsymbol{\phi} + T^T_u \cdot \delta\boldsymbol{u} = 0, \qquad (4\text{–}7.98)$$

where T_ϕ and T_u represent the generalized forces applied to the system at equibilium. Since the differential displacements from the geometry are related by

$$\delta \boldsymbol{u} = [G_\phi^u]\delta\boldsymbol{\phi}, \tag{4-7.99}$$

subsitute equation (4-7.99) into (4-7.98) to find

$$(T_\phi^T + T_u^T[G_\phi^u])\delta\boldsymbol{\phi} = 0, \tag{4-7.100}$$

or

$$T_\phi = -[G_\phi^u]^T T_u. \tag{4-7.101}$$

4-8 Geometric analysis

In the previous sections, we obtained the KIC matrices which contain the geometric information of the system. In this section, the methods for geometric analysis and their results for the shoulder are briefly reviewed. These analyses are primarily based on the KIC matrices. Let $\dot{\boldsymbol{u}}$ represent the generalized output rate variables and $\dot{\boldsymbol{\phi}}$ the input rate variables. Then the first-order differential relation can be written as

$$\dot{\boldsymbol{u}} = [G_\phi^u]\dot{\boldsymbol{\phi}}. \tag{4-8.102}$$

Noting that a KIC matrix $[G_\phi^u]$ is dependent of the displacement variables, geometric characteristics of the system can be investigated via the matrix. To analyze the KIC matrices, the various properties of the matrices could be utilized. These include maximum/minimum eigenvalues, determinant, condition number, maximum/minimun singular values, etc[9][16][105].

By utilizing the norm of the KIC matrix, the input/output bounds could be found as follows. Note that

$$\dot{\boldsymbol{u}}^T \cdot \dot{\boldsymbol{u}} = \dot{\boldsymbol{\phi}}^T([G_\phi^u]^T[G_\phi^u])\dot{\boldsymbol{\phi}}. \tag{4-8.103}$$

Dividing the equation (4–8.103) by $\dot{\phi}^T \cdot \dot{\phi}$ yields

$$\frac{\dot{u}^T \cdot \dot{u}}{\dot{\phi}^T \cdot \dot{\phi}} = \frac{\dot{\phi}^T([G_\phi^u]^T[G_\phi^u])\dot{\phi}}{\dot{\phi}^T \cdot \dot{\phi}}. \tag{4–8.104}$$

Let $\lambda_{min}^2, \lambda_1^2, \ldots, \lambda_{max}^2$ represent the eigenvalues of the matrix, $[G_\phi^u]^T[G_\phi^u]$. It can be noted that since the matrix, $[G_\phi^u]^T[G_\phi^u]$, is a real symmetric matrix, its eigenvalues are always real. The bound of the equation (4–8.104) can be written based on Rayleigh's principle[86] as

$$\lambda_{min}^2 \leq \frac{\dot{\phi}^T([G_u^\phi]^T[G_u^\phi])\dot{\phi}}{\dot{\phi}^T \cdot \dot{\phi}} \leq \lambda_{max}^2. \tag{4–8.105}$$

Using equations (4–8.103) and (4–8.105), we have

$$\lambda_{min}^2 \|\dot{\phi}\|^2 \leq \|\dot{u}\|^2 \leq \lambda_{max}^2 \|\dot{\phi}\|^2 \tag{4–8.106}$$

where $\| \cdot \|^2 = \dot{x}^T \cdot \dot{x}$ is used. This equation implies that the eigenvalues of the matrix, $[G_\phi^u]^T[G_\phi^u]$, are directly related to the transmission characteristics between the input and output velocities. Note that since the singular values of the matrix $[G_\phi^u]$, $\sigma_{min}, \ldots, \sigma_{max}$, are the square roots of the eigenvalues of $[G_\phi^u]^T[G_\phi^u]$,

$$\sigma_i = \lambda_i, \tag{4–8.107}$$

singular values of $[G_\phi^u]$ can be used directly instead of computing the eigenvalues of $[G_\phi^u]^T[G_\phi^u]$. The computation of singular values are not sensitive to the matrix condition and can provide very stable matrix properties. Finding singular values are preferable to computing the eigenvalues directly[58]. Note also that the $r = rank([G_\phi^u])$ nonzero singular values of $[G_\phi^u]$ and $[G_\phi^u]^T$ are the same. That is, the singular values of $[G_\phi^u]^T[G_\phi^u]$ are the same as $[G_\phi^u][G_\phi^u]^T$.

Also for the given bound of the input velocities, another interpretation can be made. Let

$$\|\dot{\boldsymbol{\phi}}\|^2 = \dot{\boldsymbol{\phi}}^T \cdot \dot{\boldsymbol{\phi}} \leq 1. \tag{4-8.108}$$

The bound of the output velocities could be found using equation (4-8.102)

$$\dot{\boldsymbol{\phi}}^T \cdot \dot{\boldsymbol{\phi}} = \dot{\boldsymbol{u}}^T([G_{\boldsymbol{\phi}}^{\boldsymbol{u}}][G_{\boldsymbol{\phi}}^{\boldsymbol{u}}]^T)^{-1}\dot{\boldsymbol{u}} \leq 1. \tag{4-8.109}$$

This equation represents the ellipsoid (called manipulability ellipsoid[105] or velocity ellipsoid[17]), and the geometrical shapes of this ellipsoid provide the velocity bound between input and output;that is, the inverse of the square roots of the eigenvalues of $([G_{\boldsymbol{\phi}}^{\boldsymbol{u}}][G_{\boldsymbol{\phi}}^{\boldsymbol{u}}]^T)^{-1}$ represents the principal axes of the ellipsoid. This ellipsoid can indicate the transmission characteristics of a manipulator at a specific configuration. By examining the inverse of the square root of the maximum/minimum eigenvalues of the matrix(i.e., minimum/maximum radius of the ellipsoid), $([G_{\boldsymbol{\phi}}^{\boldsymbol{u}}][G_{\boldsymbol{\phi}}^{\boldsymbol{u}}]^T)^{-1}$, the information on the maximum/minimum transmission ratios between the input and the output velocities could be obtained.

Also the determinant of the matrix can be used to examine transmission characteristics. The square root of the determinant of the matrix $[G_{\boldsymbol{\phi}}^{\boldsymbol{u}}]^T[G_{\boldsymbol{\phi}}^{\boldsymbol{u}}]$, which is a product of all singular values of $[G_{\boldsymbol{\phi}}^{\boldsymbol{u}}]$, is proportional to the area of the ellipsoid. The condition number, which is defined as a ratio of the maximum eigenvalue to the minimum eigenvalue of a matrix can also be used. The square root of the condition number of the matrix $[G_{\boldsymbol{\phi}}^{\boldsymbol{u}}]^T[G_{\boldsymbol{\phi}}^{\boldsymbol{u}}]$ (or a ratio of the maximum singular value to the minimum singular value of the matrix $[G_{\boldsymbol{\phi}}^{\boldsymbol{u}}]$), represents the uniformity of the transmission characteristics at the configuration of interest.

Now, let's consider the torque transmission characteristics. Let $\boldsymbol{\tau}$ and $\boldsymbol{f}$ represent the input and output torque applied to the system. The procedure

from the above can be used. Using

$$\boldsymbol{\tau} = [G_{\phi}^{u}]^{T}\boldsymbol{f}, \tag{4-8.110}$$

we have

$$\boldsymbol{\tau}^{T}\cdot\boldsymbol{\tau} = \boldsymbol{f}^{T}[G_{\phi}^{u}][G_{\phi}^{u}]^{T}\boldsymbol{f}. \tag{4-8.111}$$

Dividing the equation by $\boldsymbol{f}^{T}\cdot\boldsymbol{f}$ yields

$$\frac{\boldsymbol{\tau}^{T}\cdot\boldsymbol{\tau}}{\boldsymbol{f}^{T}\cdot\boldsymbol{f}} = \frac{\boldsymbol{f}^{T}[G_{\phi}^{u}][G_{\phi}^{u}]^{T}\boldsymbol{f}}{\boldsymbol{f}^{T}\cdot\boldsymbol{f}}. \tag{4-8.112}$$

Then the bound of the above expression can be obtained based on Rayleigh's principle as below

$$\lambda_{min}^{2} \leq \frac{\boldsymbol{\tau}^{T}\cdot\boldsymbol{\tau}}{\boldsymbol{f}^{T}\cdot\boldsymbol{f}} \leq \lambda_{max}^{2}. \tag{4-8.113}$$

By taking inverse of the equation and multiplying $\boldsymbol{\tau}^{T}\cdot\boldsymbol{\tau}$, we get

$$\frac{\|\boldsymbol{\tau}\|^{2}}{\lambda_{max}^{2}} \leq \|\boldsymbol{f}\|^{2} \leq \frac{\|\boldsymbol{\tau}\|^{2}}{\lambda_{min}^{2}} \tag{4-8.114}$$

where $\|\cdot\|^{2} = \dot{\boldsymbol{x}}^{T}\cdot\dot{\boldsymbol{x}}$ are used.

Again, for visual interpretation, we follow a similar procedure as follows. For the given bound of input torques,

$$\|\boldsymbol{\tau}\|^{2} = \boldsymbol{\tau}^{T}\cdot\boldsymbol{\tau} \leq 1, \tag{4-8.115}$$

the bound of the output torques could be expressed using equation (4-8.115).

$$\boldsymbol{\tau}^{T}\cdot\boldsymbol{\tau} = \boldsymbol{f}^{T}[G_{\phi}^{u}][G_{\phi}^{u}]^{T}\boldsymbol{f} \leq 1 \tag{4-8.116}$$

The above equation represents the ellipsoid (called force ellipsoid[17]). For the input/output torque transmission bounds, the same analysis for the matrix, $[G_{\phi}^{u}][G_{\phi}^{u}]^{T}$, could be applied. By comparing equation (4-8.109) and (4-8.116),

dual relations between the velocity and torque transmission characterisitcs can be seen; that is, the maximum/minimum velocity transmission direction represents the minimum/maximum torque transmission direction.

In the previous research on the kinematic design of the shoulder, the square roots of both maximum and minimum eigenvalues of the matrix $[G_{\phi}^{u}]^{T}[G_{\phi}^{u}]$ for velocity transmission characteristics between input and output (or maximum and minimum singular value of $[G_{\phi}^{u}]$) are thoroughly examined throughout the workspace of the shoulder system to find the optimal kinematic design parameters such as twist angles, and apex angles[68]. Figure 4–6 and 4–7 show the results from the previous work with the optimal kinematic parameters (i.e., $\alpha_{01} = 130°$, $\alpha_{12} = 90°$, $\alpha_{23} = 90°$ and $\alpha_{34} = 50°$).

The plots containing geometric information of three variables, μ_1, μ_2 and μ_3, were obtained as follows; 1) for each incremented value of μ_3, draw the contour plot of the square root of maximum/minimum eigenvalues for varying μ_1 and μ_2, 2) then contour plots for each μ_3 are overlayed onto one plot. From these plots, the geometric characteristics of the specific shoulder with optimal kinematic parameters can be understood before implementing the actual shoulder system.

However, it should be noted that the above results from the geometric analyis is conservative since the Euclidean norm used in the above analysis, $\|\cdot\|$, does not exactly represent the bound of the actual joint torque and velocity input even after with appropriate normalization. Rather, the bound of the actual joint torque and velocity can be represented by the infinite norm, $\|\cdot\|_{\infty}$,

$$\|\boldsymbol{x}\|_{\infty} \equiv \max_{i} |x_i|. \tag{4–8.117}$$

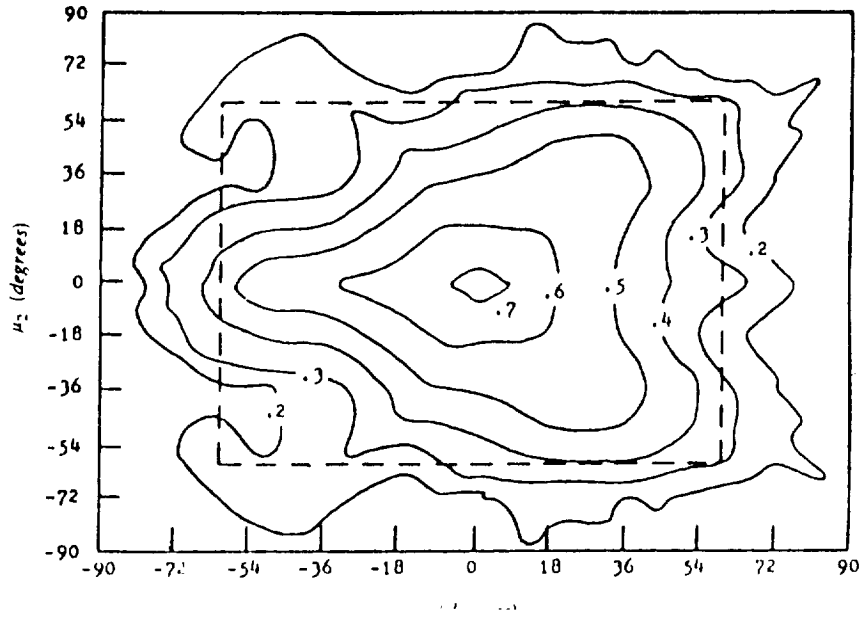

Figure 4–6 CONTOUR PLOT OF THE SHOULDER (σ_{min}) (ADAPTED FROM [68])

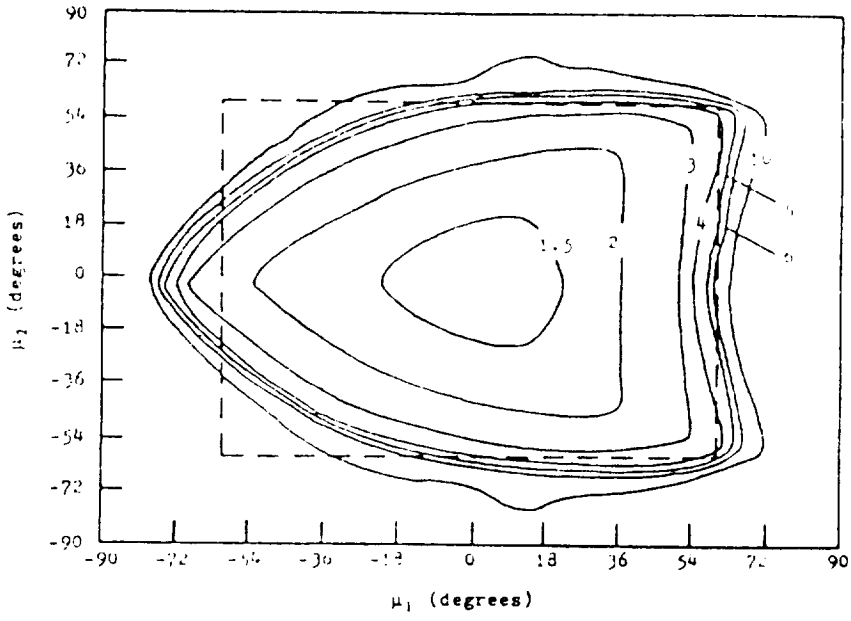

Figure 4–7 CONTOUR PLOT OF THE SHOULDER (σ_{max}) (ADAPTED FROM [68])

4–9 Second order kinematic influence coefficient

With the direct differentiation of the equation (4–6.95) with respect to time, we obtain

$$\ddot{\boldsymbol{u}} = [G^{u}_{\phi_a}]\ddot{\boldsymbol{\phi}}_a + \dot{\boldsymbol{\phi}}_a^T[H^{u}_{\phi_a\phi_a}]\dot{\boldsymbol{\phi}}_a \tag{4–9.118}$$

where

$$\frac{d}{dt}[G^{u}_{\phi_a}] \equiv \dot{\boldsymbol{\phi}}_a^T[H^{u}_{\phi_a\phi_a}] \tag{4–9.119}$$

and

$$[H^{u}_{\phi_a\phi_a}]_{i,j} \equiv \frac{\partial^2 \boldsymbol{u}}{\partial\phi_{a_i}\partial\phi_{a_j}}. \tag{4–9.120}$$

The explicit form or its direct computation of the desired second-order kinematic influence coefficient, $[H^{u}_{\phi_a\phi_a}]$, via the above definition, is very difficult and complicated. However, one explicit form of both the first-order and second-order KIC's of the shoulder system can be found without difficulty. That is, $[G^{\phi_a}_{u}]$ in explicit form is first obtained, then by direct differentiation of the $[G^{u}_{\phi_a}]$ with respect to time, $[H^{\phi_a}_{uu}]$ could be obtained. That is,

$$\ddot{\boldsymbol{\phi}}_a = [G^{\phi_a}_{u}]\ddot{\boldsymbol{u}} + \dot{\boldsymbol{u}}^T[H^{\phi_a}_{uu}]\dot{\boldsymbol{u}} \tag{4–9.121}$$

where

$$\frac{d}{dt}[G^{\phi_a}_{u}] \equiv \dot{\boldsymbol{u}}^T[H^{\phi_a}_{uu}]. \tag{4–9.122}$$

Once they are obtained, by direct application of the transfer of coordinates methods which are presented in detail in Appendix A, the desired KIC's with respect to specified input variables could be obtained. Also the procedures of finding the dynamic model of the parallel system are provided in Appendix A. A more detailed derivation can be found in [32]. The detailed derivations for the dynamic model of the shoulder system are not included for purposes of brevity.

CHAPTER 5

Control Technology for a Force-reflecting Spherical 3-dof Manual Controller

To design a portable, universal force-reflecting manual controller, light and compact components are necessary requirements. However, currently available motor torque-to-weight ratios are not sufficient for that purpose and in any case, the cost of these specialized motors is very high. Hydraulic or pneumatic systems can provide very high transmission ratios but their maintenance problems (i.e. working fluid leakages) are major disadvantages. A cable driven system is light and has good transmission ratios. However, its low mechanical stiffness, low bandwidth, the requirement of more actuators than the desired dofs of the system, difficulty in maintenance and calibration, etc., are undesirable. Direct drive motors have an improved torque-to-weight ratio but still their direct use in a light-weight portable manual controller is not adequate in terms of the required torque-to-weight ratios.

In this chapter, implementation of an actual universal force-reflecting manual controller employing high gear-ratio reducers and its corresponding control strategies are discussed. The 3-dof manual controller has parallel geometry. The parallel structure allows all three actuators to be located on the base plate of the shoulder. Thus the effect of the inertial and gravitational forces of the sys-

tem is minimized. With high gear-ratio reducers, the effective motor armature inertia and friction on the system are increased and they are directly related to the gear ratio used. The increased inertia and friction is reduced or compensated by utilizing force feedback. That is, the manual controller is electronically backdriven.

It has been shown in the literature that force control can exhibit unstable characteristics (i.e, dynamic instability) when the system interacts with the environment[4][5][24][25]. For the force-controlled manual controller, the human arm (as the environment) interacts with the manual controller. The closed loop system is required to be stable for those varying human arm characteristics.[1] Since the human hand's grip of the manual controller can be characterized as a "soft contact", relatively higher force feedback gain can be applied without causing an unstable response by the system. This high force feedback gain in a force-controlled manual controller in combination with proper gear-ratio reducer-motor combination leads us to the design of a compact and portable manual controller.

A simple single-dof actuator system consisting of the harmonic drive reducer and servo-disk motor is described and its simplified linear model is derived first. Through the analysis of the linear system model, the effects of system components such as the stiffness of the gear train, the sensor stiffness, the human arm impedance, and the allowable range of force feedback gain are discussed. Force control using either wrist sensing (digital) or joint sensing (analog) is applied to an actual one-dof system. The one-dof system uses one

[1]For an average adult male, the inertia of the forearm about the elbow is estimated around J_h=$0.06N-m-sec^2$=$8.4\ oz-in-sec^2$, the range of stiffness is $1. \leq K_h \leq 200\ N-m/rad$, or $140 \leq K_h \leq 28000 oz-in/rad$ and the range of the damping ratio is $0.15 \leq \zeta_h \leq 1.5$, where the damping contant can be obtained by $B_h = J_h(2\zeta_h\sqrt{K_h/J_h})$[1].

of the three joint actuator sub-system in the 3-dof shoulder system. Then, the implementation of the parallel universal/bilateral, spherical 3-dof manual controller system and its hardware/software interfaces are presented. In actual implementation, the optimal kinematic parameters of the shoulder as given in Table 5–3 are used. The minimum required kinematic equations of the system for the force-reflecting manual controller application are also presented in this Chapter.

5–1 Analysis of the one-dof system force control

In most kinematic and dynamic analyses, systems are assumed to have ideal characteristics. That is, backlash, friction, nonlinear/unmodeled dynamic effects, cogging, etc. in the system are neglected. However, in practice, those effects become significant unless caution is taken in the design and control of the system.

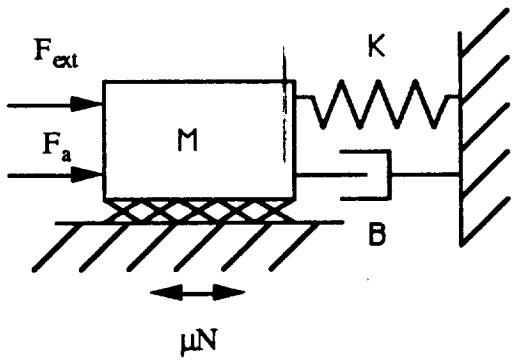

Figure 5–1 LINEAR SECOND ORDER SYSTEM WITH COULOMB FRICTION

Now, consider a linear second-order system with Coulomb friction as shown in Figure (5–1). The dynamic equation representing the system can be

written as

$$M\ddot{x} + B\dot{x} + Kx \pm \mu N = F_{ext} + F_a \tag{5-1.1}$$

where M, B, K represents the mass, damping constant, and stiffness of the system, respectively, and F_{ext} and F_a represents the external force applied to the system and the controlled input force, respectively. When the control law,

$$F_a = K_f F_{ext} - K_v\dot{x} - K_p x, \tag{5-1.2}$$

is applied to the above system, the closed loop system can be represented as

$$\frac{M}{K_f + 1}\ddot{x} + \frac{B + K_v}{K_f + 1}\dot{x} + \frac{K + K_p}{K_f + 1}x \pm \frac{\mu N}{K_f + 1} = F_{ext}. \tag{5-1.3}$$

From this equation, it can be seen that the velocity and position feedback modify the damping and stiffness of the system only. However, the force feedback modifies not only all the effective system parameters (scaling of the mass, damping constant, and stiffness of the system) but also the disturbances(i.e., coulomb friction). That is, the force feedback rejects disturbances both from the unmodeled dynamics and from uncertainties associated with the task. This force feedback control is applied to the manual controller to reduce the inertia and friction on the system from the high gear-ratio transmission system.

In this section, through a one-dof system analysis and its implementation, the problems associated with the force control strategies in the manual controller applications are examined. In particular, the following aspects are considered:

- The effect of human hand grip of the system, noting that the characteristics (impedance) of the human arm can vary.

- The effect of the force feedback gain, which is essentially high gain position feedback, and its allowable range without causing instability to the system.

- The compensation for non-linear friction.
- The effect of elasticity in the drive train.

5–1.1 Description of the one-dof system

The one-dof system shown in Figure 5–2 consists of a 12" link and an integrated actuator, which includes a servo-disk motor, an optical incremental encoder, an analog tachometer, and a harmonic drive reducer with 60:1 gear ratio. For force sensing, a 6-dof wrist force/torque sensor is mounted at the handgrip, and a torque strain gauge is attached on the output shaft of the harmonic drive reducer. The one-dof system is driven by a PWM amplifier in the current mode and controlled by μVAX II computer.

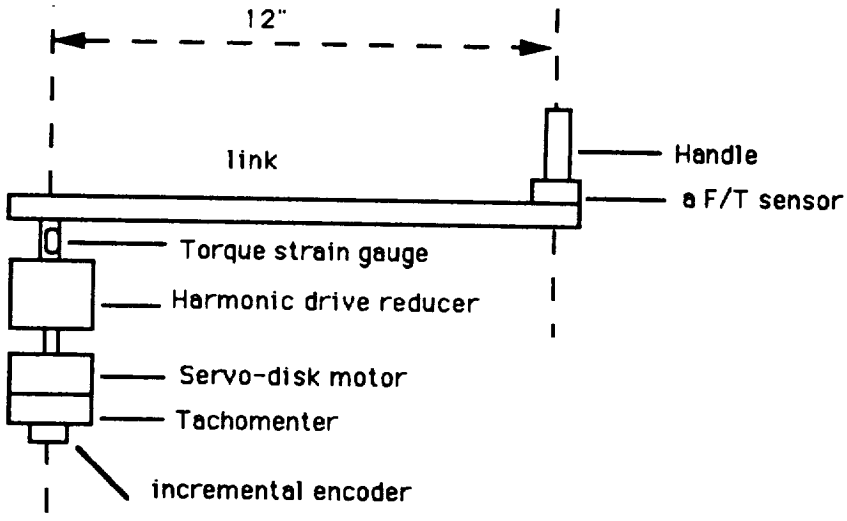

Figure 5–2 SCHEMATIC OF A ONE-DOF SYSTEM

Harmonic drive gear reducers have very attractive features over the other transmission systems such as low backlash, compactness, and high torque-to-weight transmission ratio. However, the low stiffness of the system is regarded

as its main disadvantage. In the actual harmonic drive system, in addition to the expected static friction, the large magnitudes of cogging forces are felt in the backdrive mode (i.e., the use of the harmonic drive system as a speed increaser) and measured as shown in Figure 5–3. They are believed to arise from non-ideal gear contacts and misalignments of the wave generator. This nonlinear friction

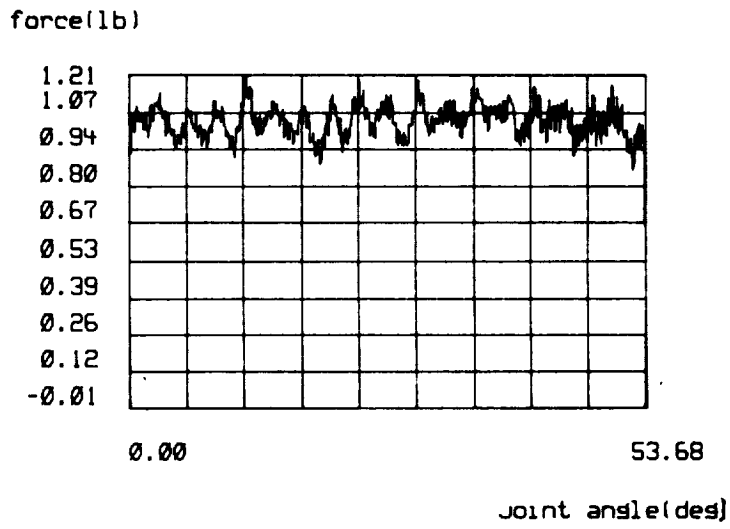

Figure 5–3 STATIC AND VARYING FRICTION OF THE HARMONIC DRIVE SYSTEM IN BACK DRIVE MODE

is very difficult to compensate for. For the one-dof system implementation, the unit with the least magnitude of nonlinear varying friction out of three actuator systems is used to study the effect of the nonlinear varying friction.

In the next section, the amplifier-in-current-mode is briefly discussed. A design of a low-pass filter is then described. And finally, a simplified linear model and its analysis of the one-dof system are presented.

5–1.2 Amplifier-in-current-mode system model

The schematics of a torque controlled system can be represented as in Figure 5–4. Its equivalent block diagram is shown in Figure 5–5. A transfer function between input command voltage and the current applied to the armature of the motor can be obtained as

$$\frac{I_a}{V_d} = \frac{A}{L_a s + R_a + AR_o}, \tag{5–1.4}$$

and a transfer function between back-emf voltage (regarded as a disturbance in current mode) and the current applied to the armature of the motor can be written as

$$\frac{I_a}{V_{emf}} = \frac{1}{L_a s + R_a + AR_o} \tag{5–1.5}$$

where

s:Laplace variable,

I_a : current applied to the armature of the motor,

V_d : command input voltage signal,

V_{emf} : back emf. voltage,

A : voltage amplifier gain,

L_a : armature inductance,

R_a : armature resistance.

R_o: sensing registance

In the above equations, it is assumed that the mechanical time constant is sufficiently larger than the electrical time constant so that the effect of the mechanical system dynamics to the electrical system is negligible. Since the gain of the voltage amplifier (operational amplifier gain A) is very large, the effect of back-emf voltage to the armature current becomes negligible as can be seen

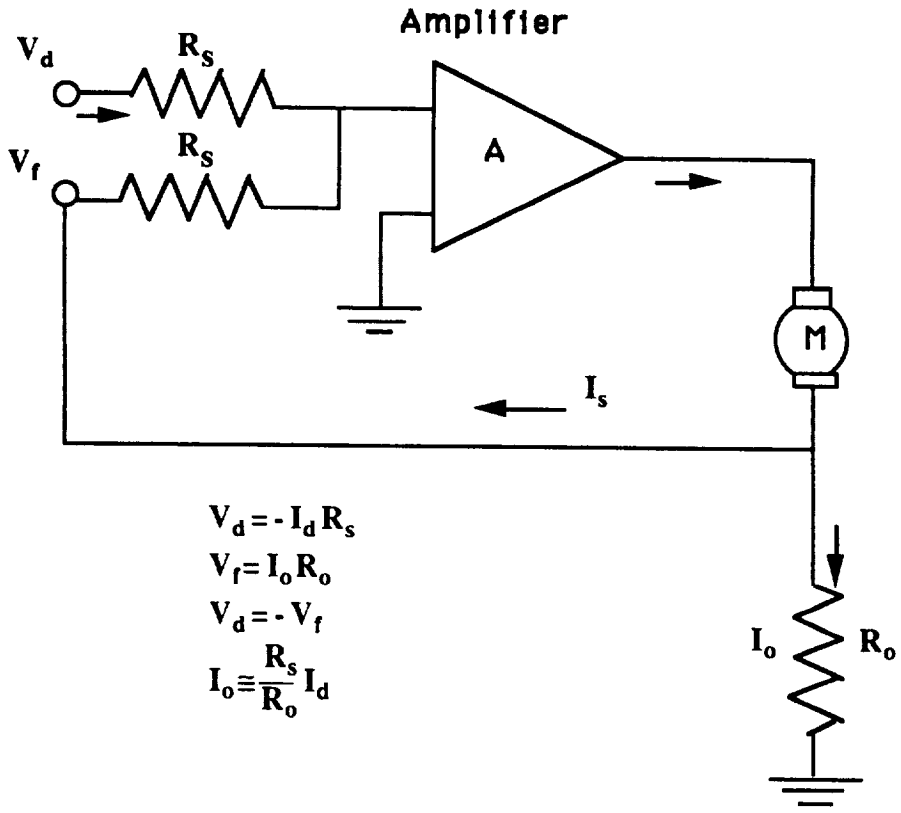

Figure 5–4 TORQUE CONTROL SYSTEM

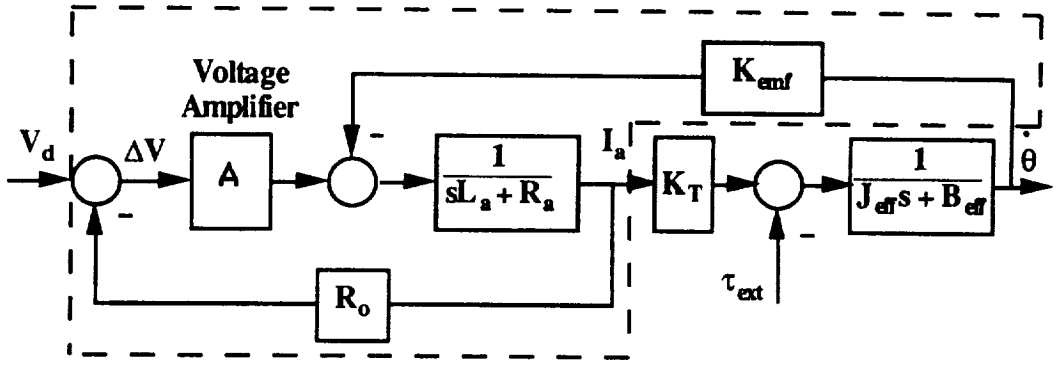

Figure 5–5 EQUIVALENT CURRENT AMPLIFIER

from equation (5–1.5). The amplier-in-current-mode can be approximated as a pure voltage-to-current converter with gain, $K_i = 1/R_o$. That is,

$$\frac{I_a}{V_d} \approx K_i. \tag{5–1.6}$$

Note that as the current feedback gain, R_o, becomes zero, the above system becomes a voltage amplifier.

5–1.3 Digital filter design

The general digital filter in the z transform domain can be expressed as

$$H(z) = \frac{Y(z)}{X(z)} = \sum_{k=0}^{m} \frac{a_k z^{-k}}{1 + \sum_{k=1}^{l} b_k z^{-k}} \tag{5–1.7}$$

or

$$y_n = \sum_{k=0}^{m} a_k x_{n-k} - \sum_{k=1}^{L} b_k y_{n-k} \tag{5–1.8}$$

where y_n and x_n represent current state and output of the system, respectively, and the subscript $n-k$ represents the kth previous state or output.

In the design of the filter for both the shoulder system and one-dof system, the first order Butterworth analog model is used

$$H(s) = \frac{1}{1 + \frac{s}{\omega_c}} \tag{5–1.9}$$

where ω_c is a desired cutoff frequency in the analog model. For the low pass filter, using the following bilinear transformation

$$s = \frac{z-1}{z+1} \tag{5–1.10}$$

the cutoff frequency, ω_a, in actual digital filter design can be found as follows. Substituting $s = j\omega_a$ and $z = e^{j\omega_c T}$ into the above bilinear transform equation

yields

$$j\omega_a = \frac{e^{j\omega_c T} - 1}{e^{j\omega_c T} + 1} = \frac{j\sin(\omega_c T/2)}{\cos(\omega_c T/2)} = j\tan(\frac{\omega_c T}{2}) \qquad (5\text{–}1.11)$$

or

$$\omega_a = \tan(\pi f_n T). \qquad (5\text{–}1.12)$$

Where T represents the sampling period and f_n represents the desired cutoff frequency, $\frac{\omega_c}{2\pi}$. By applying the above bilinear transform into the first order Butterworth model equation, we get

$$H(z) = \frac{\omega_a}{\omega_a + \frac{z-1}{z+1}} = \frac{\frac{\omega_a}{1+\omega_a} + \frac{\omega_a}{1+\omega_a}z^{-1}}{1 + \frac{\omega_a - 1}{1+\omega_a}z^{-1}} \qquad (5\text{–}1.13)$$

or

$$y_n = \frac{\omega_a}{1+\omega_a}x_n + \frac{\omega_a}{1+\omega_a}x_{n-1} - \frac{\omega_a - 1}{1+\omega_a}y_{n-1}. \qquad (5\text{–}1.14)$$

5–1.4 A one-dof system model and its analysis

The schematics of a one-dof system is given in Figure 5–2 and its simplified linear model is shown in Figure 5–6. Note that a similar model is used in [24][25] to examine the stability issue on force control. In Figure 5–6, it is assumed that a human hand continuously holds the manual controller during its operation. In this model, the harmonic drive system is represented as a linear spring and damper, the inertia of the motor and wave generator of the harmonic drive system is lumped together, and human arm's characteristics are represented as a linear second order system[77]. The inertia of both the armature and the wave generator, and the viscous damping constant for the actuator system are represented by J_a, and B_a, respectively. The damping and the stiffness of the gear train are represented by B_g^* and K_g. The relative damping between the actuator and the link is denoted as B_g. Note that both the stiffness

of the shaft and the structual flexibility of the link are included in K_g. The combined inertia of the link, of the force sensor, and of the handgrip are denoted by J_L. The damping and spring constants of the sensor are represented by B_s and K_s. The inertia, damping constant, and spring constant representing the human arm's characteristics are denoted by J_h, B_h, and K_h, respectively. And τ_a, θ_a, and x_h denote the applied actuator torque, the joint angular displacement, and the hand displacement, respectively.

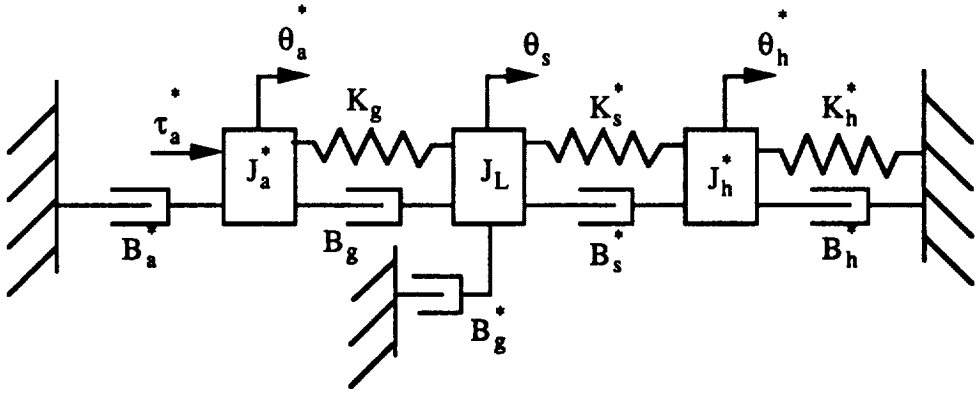

Figure 5–6 SIMPLIFIED LINEAR MODEL OF A ONE-DOF SYSTEM

Each parameter is converted in its equivalent form with respect to its joint angular displacements as shown in Figure 5–6. That is,

$$\tau_a^* = N\tau_a,\ \theta_a^* = \frac{\theta_a}{N}, \theta_h^* = \frac{x_h}{l}, \tag{5–1.15}$$

and

$$J_a^* = N^2 J_a,\ B_a^* = N^2 B_a,\ K_s^* = N^2 K_s,\ B_s^* = l^2 B_s,\ J_h^* = J_h,\ B_h^* = B_h,\ K_h^* = K_h, \tag{5–1.16}$$

where N and l represent the physical gear ratio and link length. The dynamic equation of the simplified system can be obtained as below

$$\tau_a^* = J_a^*\ddot{\theta}_a^* + B_a^*\dot{\theta}_a^* + K_g(\theta_a^* - \theta_s) + B_g(\dot{\theta}_a^* - \dot{\theta}_s) \tag{5–1.17}$$

$$0 = J_L\ddot{\theta}_s - K_g(\theta_a^* - \theta_s) - B_g(\dot{\theta}_a^* - \dot{\theta}_s) + K_s^*(\theta_s - \theta_h^*) + B_s^*(\dot{\theta}_s - \dot{\theta}_h^*) + B_g^*\dot{\theta}_s \quad (5\text{–}1.18)$$

$$0 = J_h^*\ddot{\theta}_h^* + B_h^*\dot{\theta}_h^* + K_h^*\theta_h^* - K_s^*(\theta_s - \theta_h^*) - B_s^*(\dot{\theta}_s - \dot{\theta}_h^*). \quad (5\text{–}1.19)$$

From the above equations, the following open loop transfer functions can be obtained.

$$\frac{\theta_a^*(s)}{\tau_a^*(s)} = \frac{N_4(s)}{D(s)}, \quad (5\text{–}1.20)$$

$$\frac{\theta_s(s)}{\tau_a^*(s)} = \frac{N_3(s)}{D(s)}, \quad (5\text{–}1.21)$$

$$\frac{\theta_h^*(s)}{\tau_a^*(s)} = \frac{N_2(s)}{D(s)}, \quad (5\text{–}1.22)$$

where

$$N_4(s) = (J_L s^2 + (B_g + B_g^* + B_s^*)s + K_g + K_s^*)(J_h^* s^2 + (B_s^* + B_h^*)s + K_s^* + K_h^*) - (B_s^* s + K_s^*)^2, \quad (5\text{–}1.23)$$

$$N_3(s) = (J_h^* s^2 + (B_s^* + B_h^*)s + K_s^* + K_h^*)(B_g s + K_g), \quad (5\text{–}1.24)$$

$$N_2(s) = (B_g s + K_g)(B_s^* s + K_s^*), \quad (5\text{–}1.25)$$

$$D(s) = (J_a^* s^2 + (B_g + B_g^* + B_a^*)s + K_g)(J_L^* s^2 + (B_g + B_s^*)s + K_g + K_s^*)(J_h^* s^2 + (B_s^* + B_h^*)s + K_s^* + K_h^*) - (J_h^* s^2 + (B_s^* + B_h^*)s + K_h^* + K_s^*)(B_g s + K_g)^2 - (J_a^* s^2 + (B_a^* + B_g)s + Kg)(B_s^* s + K_s^*)^2. \quad (5\text{–}1.26)$$

When the simple proportional force control law as below is applied to the system,

$$\tau_a^* = K_f(\tau_d^* - \tau_c^*), \quad (5\text{–}1.27)$$

the contact force measured from a force sensor can be written by

$$\tau_c^* = K_s^*(\theta_s - \theta_h^*) = K_s^*\tau_a^*\left(\frac{\theta_s}{\tau_a^*} - \frac{\theta_h^*}{\tau_a^*}\right). \quad (5\text{–}1.28)$$

Note that motion characteristics of the manual controller employing the above proportional force control law can be expressed as below by inserting equation (5–1.27) into (5–1.20)-(5–1.22) as below,

$$\frac{\theta_a^*(s)}{\tau_d^*(s) - \tau_c^*(s)} = K_f \frac{N_4(s)}{D(s)}, \tag{5–1.29}$$

$$\frac{\theta_s(s)}{\tau_d^*(s) - \tau_c^*(s)} = K_f \frac{N_3(s)}{D(s)}, \tag{5–1.30}$$

$$\frac{\theta_h^*(s)}{\tau_d^*(s) - \tau_c^*(s)} = K_f \frac{N_2(s)}{D(s)}. \tag{5–1.31}$$

Now, by letting $\tau_c^* = 0$ in equation (5–1.27) and using (5–1.21), (5–1.22), and (5–1.28), the open loop transfer function of the system between the applied desired torque and the output contact torque, T_o, can be obtained as below,

$$T_o(s) = \frac{\tau_c^*(s)}{\tau_d^*(s)} = K_f K_s^* \left(\frac{\theta_s(s)}{\tau_a^*(s)} - \frac{\theta_h(s)}{\tau_a^*(s)}\right). \tag{5–1.32}$$

The closed loop system characteristics for the different values of force control gain, K_f, can be investigated by examining the root locus plot of the above open loop transfer function. The general characteristic of the root locus plot for the current one-dof system model can be represented as shown in Figure 5–7 (adapted from [24]). From the figure, it can be seen that as force feedback gain increases, the system becomes less stable (i.e., when feedback gain is larger than the critical gain value at the crossing point on the imaginary axis).

The shape of the root locus plot depends on the various system component parameters: that is, actuator, gear train, sensor and task dynamics (i.e., human arm parameters associated with manual controller applications). The range of force feedback gain that does not cause instability in the system, is of interest in this analysis while maintaining desired system bandwidth in manual controller applications (5 Hz). In the following, the parametric effect of the

Table 5–1 SYSTEM PARAMETERS OF THE ONE-DOF SYSTEM

Actuator system	
Total actuator system inertia(J_a)	0.0038 $oz-in-sec^2$
Motor damping constant(B_a^*)	0.34378 $lb-in/(rad/sec)$
Harmonic drive system	
Gear ratio(N)	60:1
Tortional spring rate(K_g)	
(0 - 20 % of rated torque)	23,000 $lb-in/radian$
(20 - 100% of rated torque)	120,000 $lb-in/radian$
Damping constant(B_g^*)	1.85622 $lb-in/(rad/sec)$
F/T 15/50 Sensor Stiffness	
xy linear stiffness(K_s)	9680. lb/in
z linear stiffness	30184. lb/in
xy rotational stiffness	27234. $lb-in/rad$
z rotational stiffness	28790. $lb-in/rad$
Human forearm	
effective inertia about elbow(J_h^*)	0.525 $lb-in-sec^2$
damping constant(B_h^*)	21.6 $\sim$ 100.8 $lb-in-sec/rad$
stiffness(K_h^*)	288. $\sim$ 1440 $lb-in/rad$
Effective link/sensor/handle inertia(J_L)	1.0946 $lb-in-sec^2$

system components in a force-controlled manual controller are discussed, using the current system model with the estimated actual system parameters.

In Table 5–1, system parameters for the actual one-dof system are given.[2] The combined linear viscous damping constant for both the motor and the harmonic drive system, $B_a^* + B_g^*$, is estimated to be 2.2 $lb-in/(rad/sec)$.

[2]For the torsional spring rate of the harmonic drive system, the value K_g= 23000$lb-in/rad$ is used noting that the applied torque does not exceed 20% of the rated torque of the harmonic drive system. For the sensor stiffness, K_s= 9680lb/in is used noting that the applied torque is along the local x direction of F/T sensor frame. The effects of the relative damping of the gear train and the sensor damping is neglected: $B_g = 0.$ and $B_s = 0.$ are used. The length of human forearm, 12in, is used.

The estimation is based on the following equation,

$$\tau_a = \tau_c + (B_a^* + B_g^*)\omega_{ss}. \qquad (5\text{–}1.33)$$

That is, from the τ_a vs. ω_{ss} plot, τ_c represents intersection point with τ_a axis and $(B_a^* + B_g^*)$ represents the slope, $\frac{\tau_a - \tau_c}{\omega_{ss}}$. Where τ_c represents the Coulomb torque, τ_a applied torque to the system, and ω_{ss} angular velocity at the steady state. However, in the actual system, the nonlinear components such as Coulomb friction torque increases the stability bound and a much higher linear viscous damping constant than the estimated value could be used in the model when certain conditions of the input or disturbances are met (i.e., the results of the various kinds of the "describing function" are dependent of the dominant frequency of both input and disturbance and of their magnitudes)[35][93].

Figure 5–8 shows the Bode plot and the phase plot for the open loop transfer function with unit feedback (i.e., K_f=1) of the current system model. In that figure, the tight grip status is assumed.[3] The gear train dynamics of this system model shows the resonance around 31 Hz and it is directly related to the stability of the system. To reduce its effect, the low pass filter is included in the forward closed path. The open loop transfer function of the system with the low pass filter is obtained by multiplying $1/(\tau s + 1)$ to the original open loop transfer function given in equation (5–1.32). That is,

$$T_o^*(s) = \frac{\tau_c^*(s)}{\tau_d^*(s)} = K_f K_s^* \left(\frac{1}{\tau s + 1}\right)\left(\frac{\theta_s(s)}{\tau_a^*(s)} - \frac{\theta_h(s)}{\tau_a^*(s)}\right). \qquad (5\text{–}1.34)$$

The following analysis is based on the low pass filtered system model. The cutoff frequency of the low pass filter, 5 Hz, is used.[4]

[3]For simplicity, human arm impedances are roughly distinguished as soft grip and tight grip. The soft grip represents 30% of the tight grip. The tight grip in this analysis is characterized roughly as $B_h^* = 100.lb - in - sec/rad$ and $K_h^* = 1440lb - in/rad$[1].

[4]see the section 5-1.6.

From the Bode plot and the phase plot of the system in Figure 5–9, it can be seen that effects of the resonance is reduced to increase the stability margin of the system (i.e., positive gain margin and positive phase margin). The bandwidth of the system is inevitably decreased. In manual controller applications, however, the desired bandwidth (5 Hz [14]) is relatively small and the use of the low pass filter is acceptable.

To investigate the effects of the flexibility of the gear train, the sensor, and of human dynamics in force-controlled manual controller applications, parameters are varied about the estimated system parameters in Table 5–1. First, the human arm characterisitcs are varied. From Figures 5–9 and 5–10, it can be seen that a stiffer human arm tends to produce larger positive gain margins of the system than softer human arm. As a result, slightly higher force feedback gain can be applied to the system but their differences are quite small. However, as the stiffness of the human arm is increased further (as with a stiff wall contacts which occurs in robotic applications), the stability margin is reduced as shown in Figure 5–11. This implies that in manual controller applications of force control, a much wider range force feedback gain can be applied to obtain the desired system performance (i.e., "power steering" effect).

For simplicity, only the tight grip condition is considered in the following discussion. As shown in Figure 5–9, the sensor dynamics are relatively fast with current model parameters and its effects are almost negligible. When a soft sensor is used, which has much slower dynamics than the gear train dynamics, the system bandwidth is decreased and results in undesirable dynamics as shown in Figure 5–12; where the gain margin and phase margin are reduced. However, it can be seen in Figure 5–13 that as the gear train stiffness increases, the system becomes more stable and that this increased stiffness of the gear

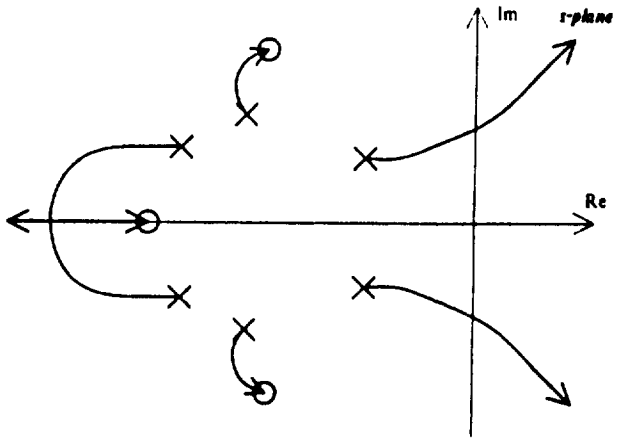

Figure 5–7 THE GENERAL SHAPE OF THE ROOT LOCUS PLOT OF THE CURRENT SYSTEM MODEL (ADAPTED FROM [24]).

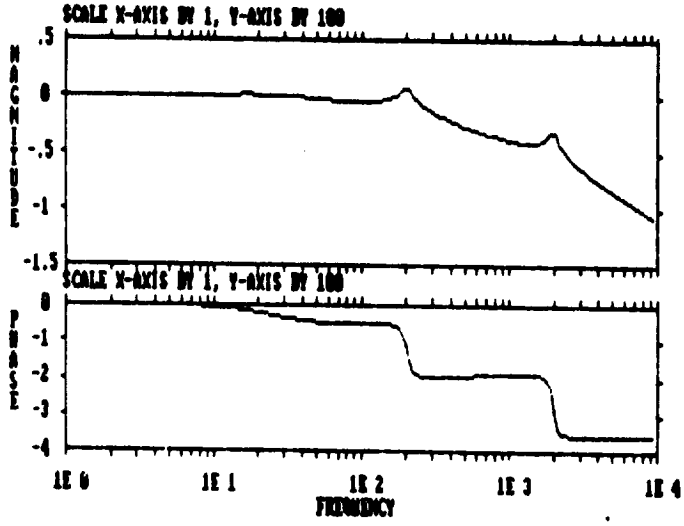

Figure 5–8 THE BODE AND PHASE PLOT OF THE CURRENT SYSTEM MODEL WITH TIGH GRIP CONDITION

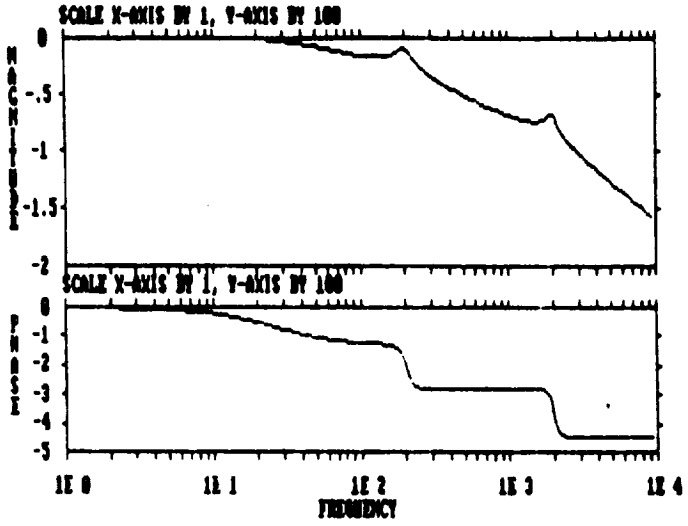

Figure 5–9 THE BODE AND PHASE PLOT OF THE LOW PASS FILTERED (5 Hz) SYSTEM MODEL WITH TIGHT GRIP CONDITION

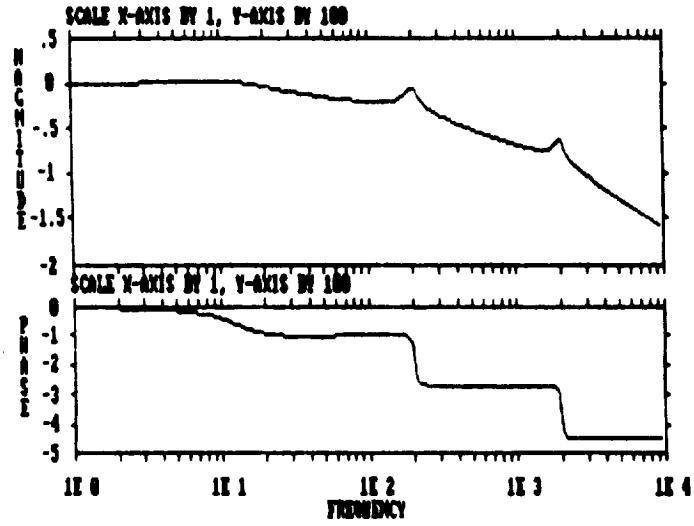

Figure 5–10 THE BODE AND PHASE PLOT OF A LOW PASS FILTERED SYSTEM WITH SOFT GRIP CONDITION

train represents the most important system parameters.

In the above analysis, the form of the characteristic equation of the open loop transfer function is assumed to be fixed. However, it can be noted that by using inner velocity and position feedback at a faster sampling rate than that for the force feedback, the effective system characteristics can be varied. The poles of the open loop transfer function of the system can be moved to the desired locations if desired.

In the following, actual experimental results for the one-dof system are discussed. In the experiment, the following aspects are investigated;

- Friction and inertia compensation.
- Force control performance in manual controller application (electronic backdrivability or "power steering").

5–1.5 Friction compensation

In the design of manual controllers, the magnitude of the friction, especially Coulomb friction, is an important characteristic to consider. The magnitude of Coulomb friction is directly related to the thresholds for the operator's command forces and to the magnitude of the reflecting forces. To reduce the relative magnitude of friction in the system, dither signals of various ranges of frequency are applied, but these cause very uncomfortable chattering for the operator who holds the system. The dither signal is not considered further in this study and regarded as inappropriate for the manual controller application.

Direct force feedback using force sensing via wrist force sensing (digital) has been studied for friction compensation. This scheme is shown to be very effective by reducing the magnitude of Coulomb friction down to an average

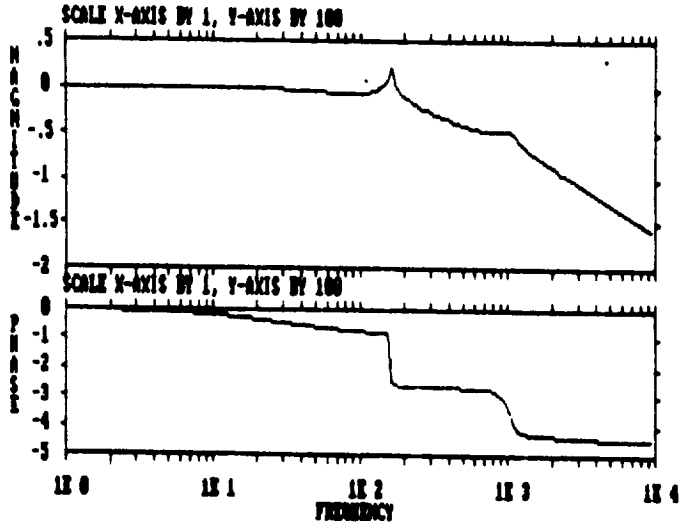

Figure 5–11 THE BODE AND PHASE PLOT OF A LOW PASS FILTERED SYSTEM MODEL WITH HARD CONTACT

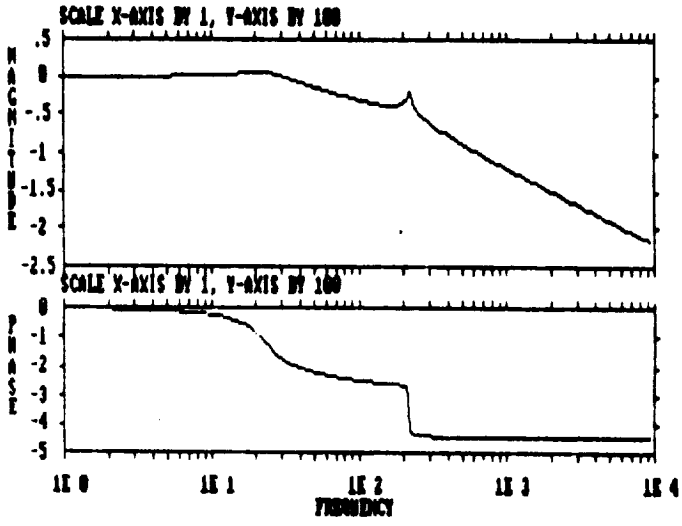

Figure 5–12 THE BODE AND PHASE PLOT OF A LOW PASS FILTERED SYSTEM MODEL WITH SOFT SENSOR

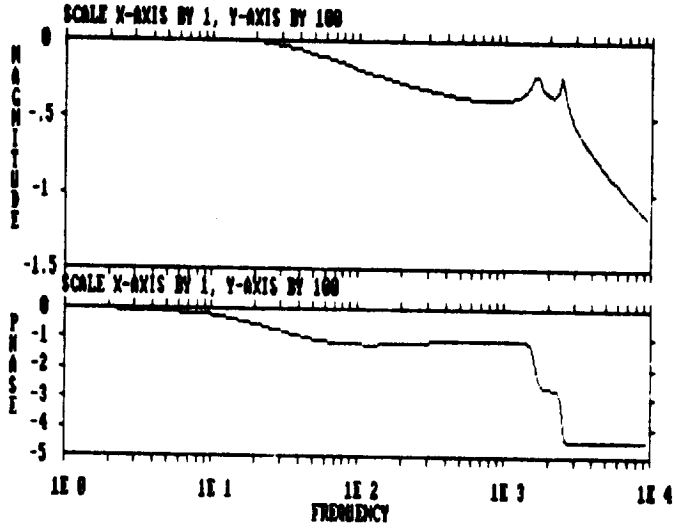

Figure 5–13 THE BODE AND PHASE PLOT OF A LOW PASS FILTERED SYSTEM MODEL WITH STIFF GEAR TRAIN

of $0.25lb_f$ from an average of $1.0lb_f$ at the handgrip of the one-dof system as shown in Figures 5–3 and 5–14. This excellent performance due to friction compensation also justifies force control implementation to the manual controller.

However, the harmonic drive system in back drive mode shows a varying nonlinear friction in addition to the Coulomb friction. The magnitude of the varying nonlinear friction depends on the specific drive unit. This varying nonlinear friction could confuse the operator's feel and reduce the level of telepresense drastically. Observing that the varying nonlinear friction of the harmonic drive system has a position-dependent characteristic, direct friction compensation based on the position-related friction model as given below can

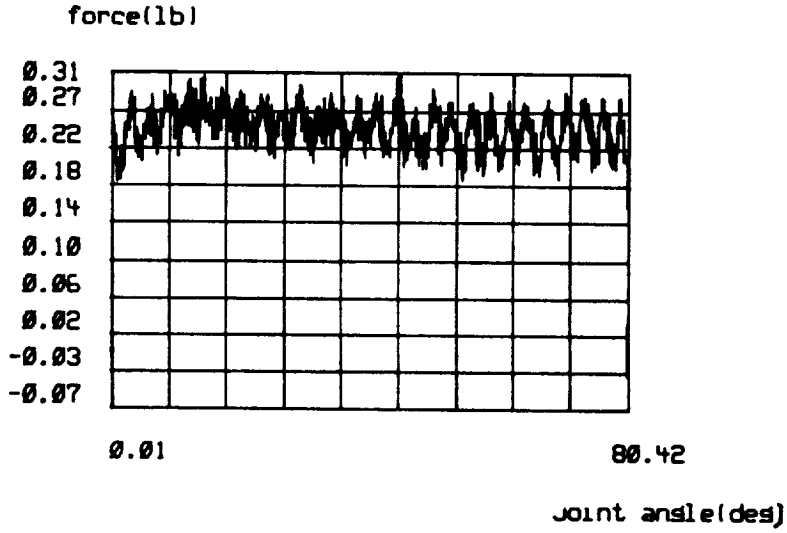

Figure 5–14 STATIC AND VARYING FRICTION OF THE HARMONIC DRIVE SYSTEM IN THE BACK DRIVE MODE AFTER COMPENSATION

be applied,

$$\tau_{comp} = A\sin\left(\frac{2\pi}{\left\{\begin{array}{l} \textit{the number of teeth of the flexspline} \\ \textit{of the harmonic drive system} \end{array}\right\}} + \psi\right) \qquad (5\text{–}1.35)$$

where ψ is adjusted to match the phases of the compensating torque to the actual friction. However, it turns out to be ineffective due mainly to the unmodeled elasticity of the flexspline of the harmonic drive system.

In an effort to achieve a better friction/inertia compensation, another force feedback control method using an analog torque inner loop has been implemented. This feedback control scheme uses an analog signal directly measured from the strain gauge attached on the output shaft of the harmonic drive system. The measured signal is directly fed back to the current amplifier to drive the motor as shown in Figure 5–15. When the structural flexibilities of the link between the wrist sensor and the joint torque sensor (i.e., strain gauge in this

case) is negligible, this local force feedback is basically the same as the wrist sensed force feedback except it is an analog signal which reduces the digital effects (i.e., sampling time delay). As expected, noting that the digital control loop sampling frequency is relatively high at 210 Hz and the link of the one-dof system is very rigid; the two responses of the digital and analog force feedback control schemes showed no significant difference, in terms of the friction/inertia compensation.

The compensation of varying nonlinear friction showed no improvement with the above methods. It would be costly in terms of higher quality components and the development of sophisticated control schemes (i.e., adaptive filter, etc.) to obtain better compensation for the nonlinear friction.

5–1.6 Force control implementation on a one-dof system

The force control is applied to the actual one-dof system. In the actual system, high frequency noises are observed as shown in Figure 5–3 and 5–14. These are believed to come from either the nonideal gear contact or the force/torque sensor. To find the proper cutoff frequency of the first-order low-pass filter of the wrist sensor, various magnitudes of external forces and various cutoff frequency low-pass filters are applied to the system. Through extensive trial and error searches and noting that the desired manual controller bandwidth is more than 5 Hz, the 5 Hz cutoff frequency is selected to be most appropriate for the system.

For finger contact with the manual controller, no serious noise from the F/T sensor is observed. However, the dynamic noise measured by the F/T sensor becomes significant when actuator command forces and/or operator's command forces are applied. With the use of the 5 Hz low-pass filter the F/T

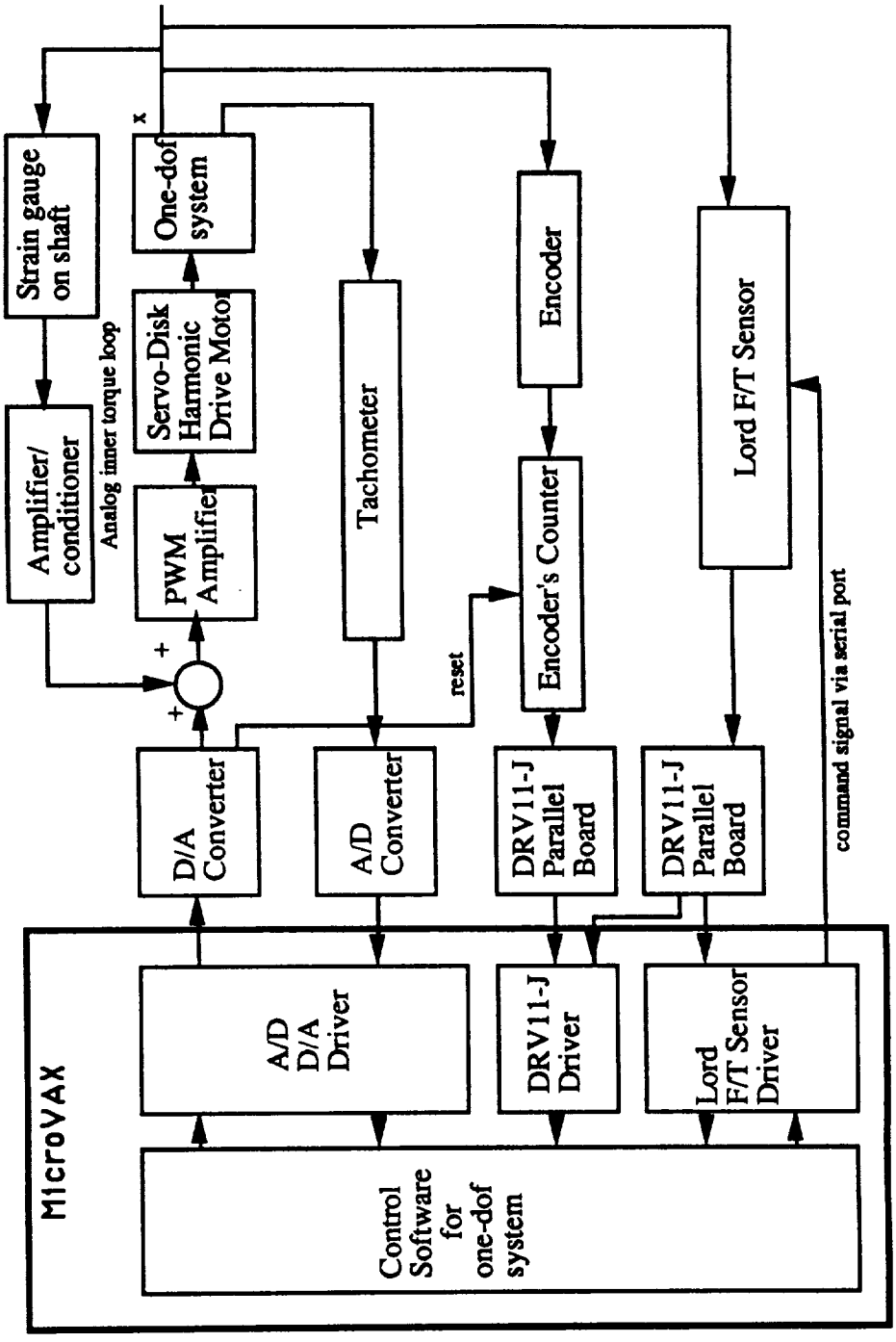

Figure 5–15 ANALOG INNER TORQUE LOOP DIAGRAM

sensor noise was reduced significantly.

Note, however, that the magnitude of human arm jittering becomes more significant as the human hand grips the handle of the manual controller more tightly as shown in Figure 5–16. These undesired jittering force inputs to the force-controlled manual controller need to be filtered out.

As can be seen in the previous analysis of the simplified one-dof model, the system tends to be stabilized with a low-pass filter of lower cutoff frequency (below 3 Hz). The higher force feedback gain can be applied without causing the instability of the system but its response is too sluggish for the operator due to the reduced bandwidth of the system. Also the performance of friction compensation becomes ineffective. As the cutoff frequency of the filter is increased, the stable margin of the system is decreased, which results in a feasible force feedback gain that is relatively low.

The experimental observations are summarized as below.

1. Without the use of the low pass filter in the closed loop system, the system shows instability for very low force feedback gain. This is mainly due to the dynamics (i.e., flexibility) of the harmonic drive system.

2. The cutoff frequency of the first-order low pass filter(5 Hz) is selected based on the system component limitations such as human arm jittering, sensor noise, resonance of the system, required system bandwidth, etc.

3. When a low pass filter with relatively higher cutoff frequency is placed in the closed control system, the system becomes unstable with relatively lower force feedback gain.

4. Tighter grip of the human hand introduces undesired human jittering into

the system as shown in Figure 5–16.

5. Fairly large force feedback gain ($K_f = 3$) can be applied to the system with the low-pass filter with $5Hz$ cutoff frequency. The apparent inertia/friction of the system can be reduced by $1/(K_f+1)$ times of the actual system inertia/friction by using the following control law;

$$T_a = T_{ref} + K_f l(F_{ref} - F_{op}) \qquad (5\text{–}1.36)$$

where

T_a : actuating control torque,

T_{ref} : desired reflecting torque, lF_{ref},

F_{ref} : desired reflecting force at handgrip,

F_{op} : human command force at handgrip,

K_f : force feedback gain,

l : link length.

5–1.7 Discussion of the one-dof system experiment

From the anlaysis and implementation of the one-dof manual controller, the performance of force control applied to the manual controller will now be discussed. The manual controller which uses the high gear-ratio reducer results in a design that is compact and portable. In this particular one-dof system, the stable response of the force-controlled system can be obtained with the force feedback gain up to $K_f = 3$. This implies the reduction of the inertia and friction of the system by $1/(K_f + 1)$ times. Also, the effects of the system components are discussed using the results of the simplified one-dof system where actual estimated values of system parameters are applied.

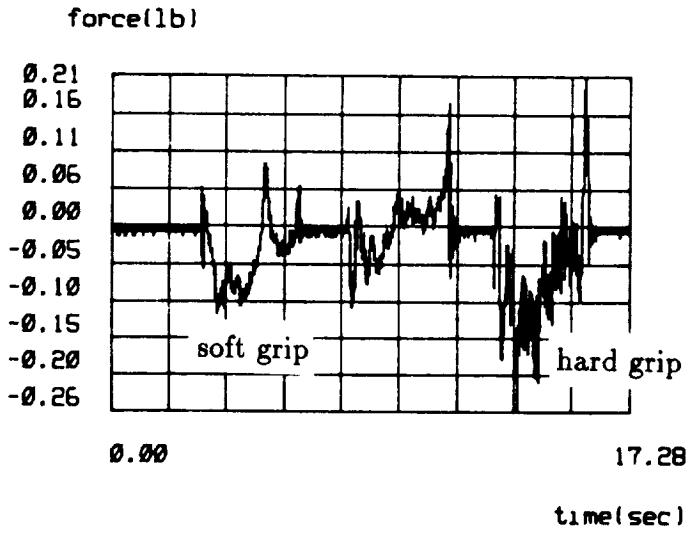

Figure 5–16 EXAMPLE OF A HUMAN OPERATOR JITTERING WITH SOFT AND HARD GRIP

In addition to the simple proportional force control law and the first-order low pass filter, various control schemes can be applied: PI control, PD control, PID control, lead/lag compensation, etc. However, due to the use of the high gear-ratio reducer the magnitude of the stiction is fairly large. Thus, any integral control law may not be suitable since it may introduce limit cycles[[93]]. Also, the integral control tends to destabilize the system by adding a pole at the origin and is not considered.

When the gear train dynamics are negligible, the PD control and lead compensator could be used to increase the system bandwidth further. Also, as mentioned earlier, by applying proper position and velocity feedbacks, the poles of the open loop transfer function can be moved to the desired locations. And much higher force feedback gain could be applied to the system to reduce the magnitude of both friction and inertia of the system, while maintaining the desired bandwidth of the system. These suggestions require further study.

5–2 Integration of the shoulder system

The main design goal for this system development is an implementation of a compact and portable universal force-reflecting 3-dof manual controller system with large dextrous working volume and with a somewhat improved reflecting-force capability. The implemented parallel 3-dof shoulder system consists of the shoulder hardware, actuators, a shoulder mounting frame, a 6-dof F/T sensor, and a handgrip as shown in Figure 5–17. The manual controller is capable of reflecting 50 $lb_f - in$ torques about the common intersection point. [5]

To provide the capability of adjusting the impedance of the system, each actuated joint contains a servo-disk motor integrated with incremental optical encoder and analog tachometer for measuring angular position and velocity. A 6-dof wrist force/torque sensor (Lord F/T 15/50) is mounted at the handgrip (upper ternary) of the system to measure applied human arm command forces. Note that with appropriate sensory feedback, the effective system characteristics could be adjusted to achieve the desired optimal characteristics of the manual controller for varying task characteristics.

To achieve the desired design criteria in this implementation (such as higher torque-to-weight ratio and torque-to-size ratio), each actuator is integrated with a harmonic drive system with a 60 : 1 gear-ratio. Each actuator unit is interfaced with the pulse-width-modulated (PWM) amplifier which is set in the current mode so that the current output proportional to the given voltage signal could be produced. The command voltage signal comes either from the computer via a D/A converter (digital-to-analog converter) or from

[5] Or, with respect to the handgrip of the manual controller, 10 $lb_f - in$ forces along tangential direction of the sphere of 5" radius, and 50 $lb_f - in$ torque about the normal axis to the sphere, when the handgrip is located 5" from the common intersection point.

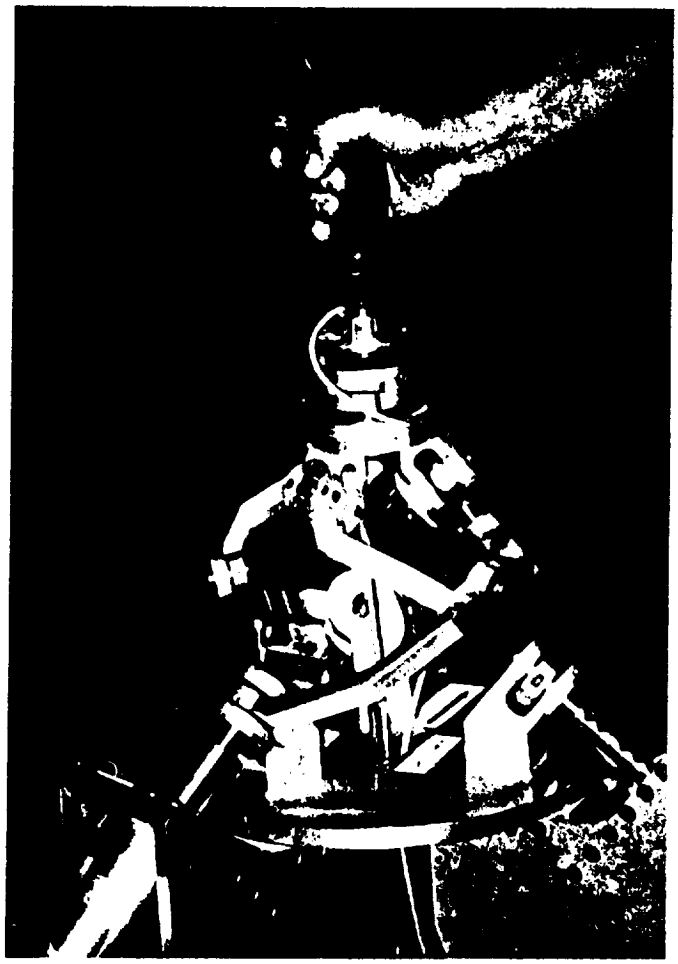

Figure 5–17 THE IMPLEMENTED SHOULDER SYSTEM

strain gauges directly (analog inner torque loop). The sampling period for the force controlled 3-dof manual controller system using a F/T sensor in μVAX II computer was about 45 Hz.

The hardware interface diagram of the shoulder system is represented in Figure 5–18. In the following, hardware design, transducers and their interfaces in the force-reflecting manual controller are explained.

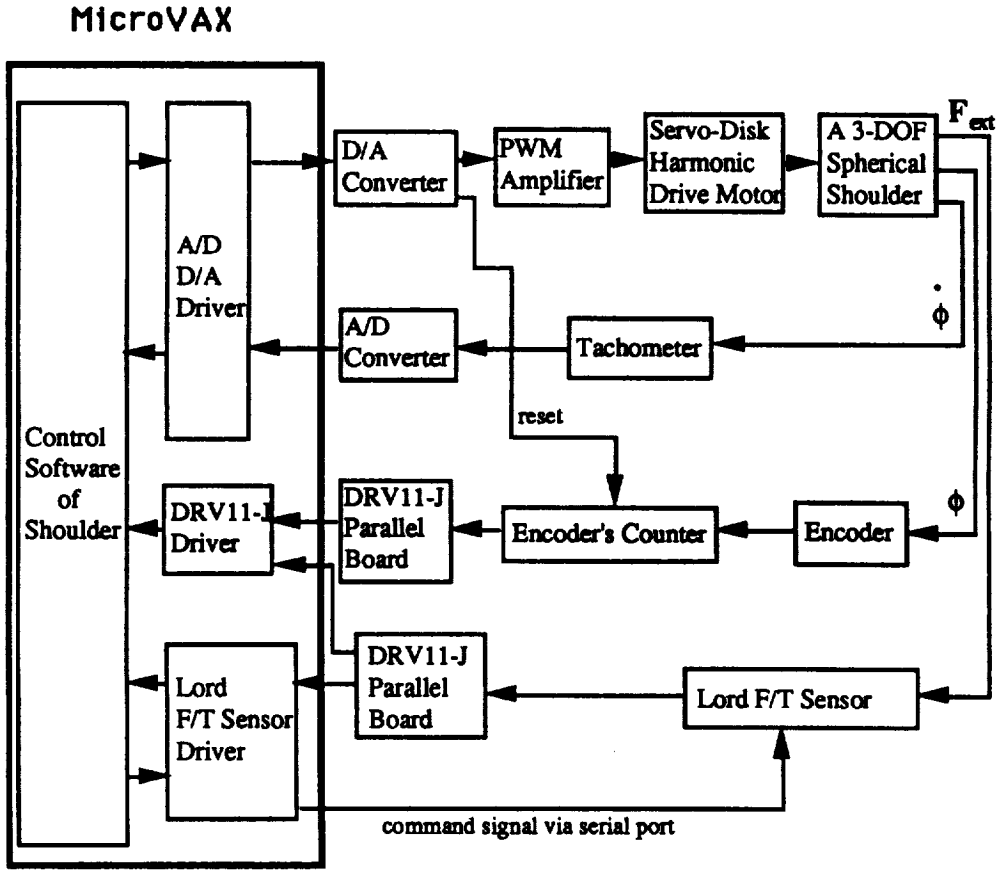

Figure 5–18 HARDWARE INTERFACE DIAGRAM OF THE SHOULDER SYSTEM

5–2.1 Digital computer interfaces

A μVAX II computer is used as the main processor for the control of the shoulder system. An A/D board (ADV11-C), three D/A boards (AAV11-C), and two parallel interface boards (DRV11-J) are interfaced with the μVAX II. An A/D board could be configured to receive 16 single-ended 12-bit channels or 8 differential 12-bit channels. It is configured with 16 single-ended channels in the bipolar mode to receive an input signal from -10V to +10V. Out of three D/A boards, each of which has four channels, only one D/A board is used for this purpose; three channels are used to send torque command voltage signals to the PWM amplifiers and one is used to reset the encoder counter IC's. One parallel interface board (DRV11-J) is interfaced with the encoder counter circuits and the other with the F/T sensor processor. Each board could receive up to 4 sets of parallel 16-bit digital inputs.

5–2.2 Actuator system interfaces

Each actuator unit of the shouder system consists of a servo-disk motor, a harmonic drive reducer, an encoder, and an analog tachometer. Each actuator is driven by the PMI VXA 48-8-16 PWM amplifier[73].

The servo-disk motor has low electric inductance, low armature inertia, and has a rotor shaped like a disk with a printed circuit on it. Its main chracteristics is summarized as: 1) it has low cogging; 2) it has low electrical and mechanical time constants; and 3) it has low friction. The harmonic drive reducer is also a very compact transmission system and has a very high torque-to-weight ratio and low backlash[21].

The PWM amplifier provides two control options; velocity mode and

current mode[[73]]. In velocity mode, the amplifier behaves as a voltage-to-voltage amplifier, and the actuator velocity can be servo controlled since the amplifier uses either the tachometer feedback or back emf voltage feedback. In current mode, the amplifier behaves as a voltage-to-current amplifier, and the actuator torque can be controlled directly. In the control of the shoulder system, the current mode for the PWM amplifier is selected to reflect directly the desired forces back to the human operator. The bandwidth of the amplifier in the current mode is over 500 Hz so that its dynamics can be neglected in this manual controller application.

5–2.3 Encoder and tachometer interfaces

The incremental encoder generates the two quadrature voltage signals which are separated by a 90° phase shift. To decode the encoder output signal, a counting circuit utilizing HP HCTL-2016 IC's and a clocking circuit was designed. It was interfaced with the μVAX II computer via a 16-bit parallel interface board (DRV11-J). Since the HP HCTL-2016 IC produces 16 bit data through an 8-bit data bus requiring two independent accesses for high and low bytes, direct interface with μVAX II through the parallel interface board is difficult[[42]]. However, since the HP HCTL-2016 IC allows us to select the high or low byte data, two IC's are used to read a 16-bit data simultaneously through DRV11-J; one IC for the high byte and the other for the low byte. Since the incremental optical encoder could not provide an absolute joint angle, the counter circuit is initialized (reset) via one D/A channel (ADV11-C) when necessary.

Tachometers generating voltage signal proportional to the angular velocity are connected to the A/D board (AAV11-C). The diagrams for encoder's circuit, clock, and interfaces to the μVAX II computer, as well as specifica-

tions on encoder, tachometer, and DRV11-J parallel interface board are given in Appendix C.

5–2.4 F/T sensor interfaces

A 6-dof force/torque sensor system shown in Figure 5–19, consists of a F/T sensor hardware and its microprocessor. It provides several options for its output. Resolved force/torque output with respect to its local frame could be either in ASCII format or in binary format. In binary format, a F/T sensor force/torque output can be interfaced via the serial port (RS-232C) and its maximum sampling time could reach up to 100 Hz at 19200 baud rate. The raw data from the eight strain gauges could be read via the 16-bit parallel port and its maximum sampling rate is 440 Hz.

To reduce the sampling time during the actual operation of the shoulder, the strain gauge raw data is read directly via the parallel interface board (DRV11-J) and is resolved into the force/torque data with respect to its local frame. This resolution is accomplished by postmultiplying the calibration matrix to the strain gauge raw data in the μVAX II computer;

$$\begin{Bmatrix} resolved \\ force\ data \end{Bmatrix} = \begin{bmatrix} 6\ by\ 8\ calibration \\ matrix \end{bmatrix} \begin{Bmatrix} strain\ gauge \\ raw\ data \end{Bmatrix} - \begin{Bmatrix} strain\ gauge \\ offset \end{Bmatrix} \tag{5–2.37}$$

where the calibration matrix (6 by 8) for the F/T 15/50 Lord sensor is provided by the Lord company and given in Table 5–2. The sampling time for receiving the strain gauge raw data and for resolving those into the 6-dof force/torque in local cartesian frame is estimated at around 210 Hz (4.7 msec).

The detailed interface timing diagrams between F/T sensor and DRV11-J parallel interface board, and more specifications for the F/T sensor are given

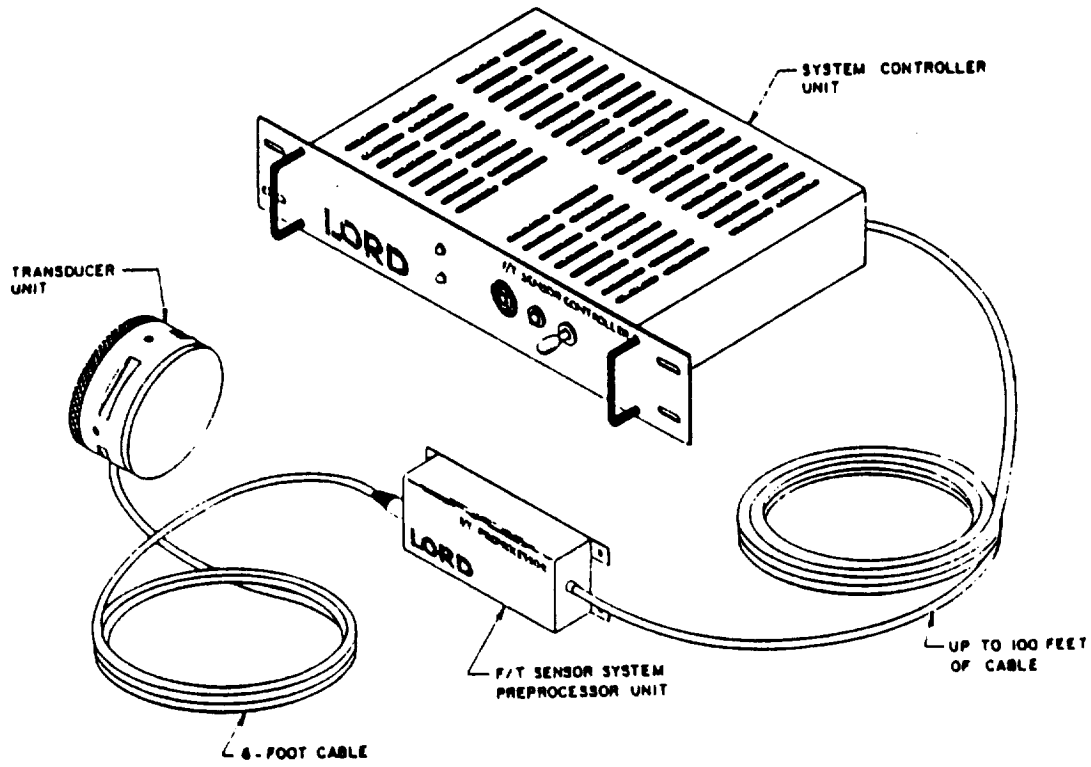

Figure 5–19 THE LORD F/T SENSOR TRANSDUCER UNIT

Table 5–2 CALIBRATION MATRIX FOR A LORD F/T 15/50 SENSOR(COURTESY OF LORD COMPANY.

-.008566	-.481377	-.021868	-.011668	.030515	-.484092
-.007523	.018417	.732219	-.009798	-.986898	.015415
-.016445	-.002691	.733218	.987109	-.002936	.025436
.477910	.006338	-.036908	-.029870	-.001069	-.478979
-.002648	-.019316	.729692	.003892	1.007737	.013018
.005620	.483959	-.029810	-.002368	-.038984	-.485869
.016343	.005190	.736930	-.987992	.000095	.011809
-.478067	-.009919	-.016050	.030900	.007561	-.490032

in Appendix C. Note that command characters to the F/T sensor have been sent through the serial port (RS232C) and remained active when the strain gauge raw data through the parallel interface board are being received. More information can be found in [53].

5–2.5 Shoulder hardware design

The shoulder system hardware consists of an upper ternary, three RRR dyads, a lower ternary, and a mounting frame. In the actual design of the three dyads, however, mechanical interference is one of main factors limiting the working volume of the system. Therefore, the shape of binary links are slightly modified to maximize the working volume as shown in Figure 5–20. The working volume of the shoulder system is defined, based on the geometric properties (i.e., maximum/minimum singular values of the first order KIC) to secure the desirable input/output velocity/torque transmission characteristics(i.e., $\sigma_{min} = 0.2$ and $\sigma_{max} = 5.$) and can be represented via the following Euler angles[68];

$$\mu_1 = 50^\circ,\ \mu_2 = 50^\circ,\ \mu_3 = 40^\circ. \qquad (5\text{–}2.38)$$

The actual motion range of the shoulder system is far larger than the above

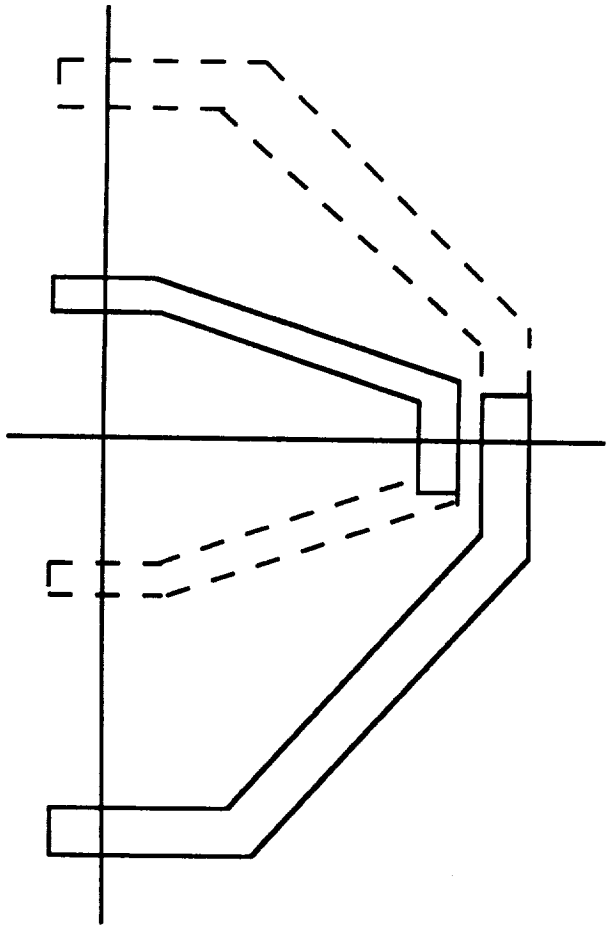

Figure 5–20 NESTED DESIGN OF A DYAD

given values. However, the geometric characteristics of the shoulder are such that some regions could not provide the desired transmission characteristics of either the velocities or the torques between input joints and output ternary. The more detailed schematic design figures for the whole shoulder system components can also be found in [20].

5–2.6 Kinematic equations for the shoulder

From previous research, the optimal geometric parameter values of the shoulder system were found based on the input/output transmission characteristics of both the velocity and the force/torque as shown in Table 5–3. In the actual analysis and implementation of the shoulder system, these parameter values are used. Definitions of the parameters can be found in Chapter 4.

Table 5–3 OPTIMAL GEOMETRIC PARAMETERS OF THE SHOULDER

	serial subchain # 1	serial subchain # 2	serial subchain # 3
the upper ternary edge displacement angles	$\gamma_{01}^{1} = 0$	$\gamma_{01}^{2} = 120°$	$\gamma_{01}^{3} = 240°$
the lower ternary edge edge displacement angle	$\gamma_{34}^{1} = 180°$	$\gamma_{34}^{2} = 60°$	$\gamma_{34}^{3} = -60°$
twist angle	$\alpha_{01}^{1} = 130°$	$\alpha_{01}^{2} = 130°$	$\alpha_{01}^{3} = 130°$
twist angle	$\alpha_{12}^{1} = 90°$	$\alpha_{12}^{2} = 90°$	$\alpha_{12}^{3} = 90°$
twist angle	$\alpha_{23}^{1} = 90°$	$\alpha_{23}^{2} = 90°$	$\alpha_{23}^{3} = 90°$
twist angle	$\alpha_{34}^{1} = 50°$	$\alpha_{34}^{2} = 50°$	$\alpha_{34}^{3} = 50°$

As can be seen from the Table 5–3, the optimal geometric parameters of the shoulder used in actual implementation happen to have a simple geometry (i.e., twist angles for each serial subchain are right angles and edge displacement angles are defined to make the system symmetric). Therefore, a set of simplied

kimematic equations can be obtained.

In the forward position analysis, the output transform matrix or its equivalent Euler angles(μ_1, μ_2, μ_3) of the shoulder and other joint angular displacements, ϕ_2^m and ϕ_3^1 for $m = 1, 2, 3$, of the implemented system are found as follows, given three measured joint angular displacements, ϕ_1^m for $m = 1, 2, 3$. The same notations defined in Chapter 4 are used in the following analysis. The superscript denotes the subchain and the subscript denote the joint. By substituting the given geometric parameters for the shoulder into the equation (4-5.68), we have

$$\boldsymbol{s}_3^{m(1)} = \begin{Bmatrix} s\phi_2^m \\ 0 \\ -c\phi_2^m \end{Bmatrix} \; for \; m = 2, 3. \tag{5–2.39}$$

Noting that the y components of $\boldsymbol{s}_3^{m(1)}$, is zero, the constraint equations can be found directly from equations (4-5.67) and (4-5.68) as below.

$$y^{m(1)} = 0 \; for \; m = 2, 3. \tag{5–2.40}$$

Solving these two constraint equations via an iterative numerical method (see section 4-5.2), ϕ_2^1 and ϕ_3^1 can be found. Then, the output transformation matrix of the shoulder, $[^1R_b^t]$, is computed by substituting three joint angular displacements along one serial subchain # 1 into equation (4-5.65). To compute ϕ_2^2 and ϕ_2^3, the equation (4-5.67) is written again,

$$\boldsymbol{s}_3^{m(1)} = [^mR_b^1]^T[^1R_b^t][^mR_3^t]^T \begin{Bmatrix} 0 \\ 0 \\ 1 \end{Bmatrix} \equiv \begin{Bmatrix} x^{m(1)} \\ y^{m(1)} \\ z^{m(1)} \end{Bmatrix}. \tag{5–2.41}$$

From equation (5–2.39) and (5–2.41), ϕ_2^m can be found as follows

$$\phi_2^m = \arctan\left(\frac{x^{m(1)}}{-z^{m(1)}}\right) \; for \; m = 2, 3. \tag{5–2.42}$$

The first order KIC's($[G^u_\phi]$) of the shoulder between the absolute angular velocities of the output coordinates and the actuated three base joint angular velocities can be obtained using equations (4-6.90) - (4-6.97). The $[G^u_{\phi_a}]^{-1} = [G^{\phi_a}_u]$ can be obtained in explicit form and are provided as below

$$\dot{\phi}_a = [G^u_{\phi_a}]^{-1}\dot{u} \tag{5-2.43}$$

where

$$[G^u_{\phi_a}]^{-1} = \begin{bmatrix} [^1G^u_\phi]^{-1}_{1;} \\ [^2G^u_\phi]^{-1}_{1;} \\ [^3G^u_\phi]^{-1}_{1;} \end{bmatrix}. \tag{5-2.44}$$

The first row components are obtained from the subchain #1

$$[^1G^u_\phi]^{-1}_{1;1} = \frac{c\phi^1_1 c\phi^1_2}{s\phi^1_2} \tag{5-2.45}$$

$$[^1G^u_\phi]^{-1}_{1;2} = -s\alpha^1_{01} - \frac{s\phi^1_1 c\phi^1_1 c\alpha^1_{01}}{s\phi^1_2} \tag{5-2.46}$$

$$[^1G^u_\phi]^{-1}_{1;3} = -c\alpha^1_{01} + \frac{s\phi^1_1 c\phi^1_2 s\alpha^1_{01}}{s\phi^1_2}. \tag{5-2.47}$$

The second row components are obtained form the subchain #2,

$$[^2G^u_\phi]^{-1}_{1;1} = \frac{c\gamma^2_{01} c\phi^2_1 c\phi^2_2}{s\phi^2_2} + s\gamma^2_{01}(s\alpha^2_{01} + \frac{s\phi^2_1 c\phi^2_2 c\alpha^2_{01}}{s\phi^2_2}) \tag{5-2.48}$$

$$[^2G^u_\phi]^{-1}_{1;2} = \frac{s\gamma^2_{01} c\phi^2_1 c\phi^2_2}{s\phi^2_2} - c\gamma^2_{01}(s\alpha^2_{01} + \frac{s\phi^2_1 c\phi^2_2 c\alpha^2_{01}}{s\phi^2_2}) \tag{5-2.49}$$

$$[^2G]^{-1}_{1;3} = -c\alpha^2_{01} + \frac{s\phi^2_1 c\phi^2_2 s\alpha^2_{01}}{s\phi^2_2}. \tag{5-2.50}$$

The last row components are obtained from the subchain #3,

$$[^3G^u_\phi]^{-1}_{1;1} = \frac{c\gamma^3_{01} c\phi^3_1 c\phi^3_2}{s\phi^3_2} + s\gamma^3_{01}(s\alpha^3_{01} + \frac{s\phi^3_1 c\phi^2_2 c\alpha^3_{01}}{s\phi^3_2}) \tag{5-2.51}$$

$$[^3G^u_\phi]^{-1}_{1;2} = \frac{s\gamma^3_{01} c\phi^3_1 c\phi^3_2}{s\phi^3_2} - c\gamma^3_{01}(s\alpha^3_{01} + \frac{s\phi^3_1 c\phi^3_2 c\alpha^3_{01}}{s\phi^3_2}) \tag{5-2.52}$$

$$[{}^3G^u_\phi]^{-1}_{1;3} = -c\alpha^3_{01} + \frac{s\phi^3_1 c\phi^3_2 s\alpha^3_{01}}{s\phi^3_2}. \tag{5-2.53}$$

Then the local KIC's of the shoulder system can be obtained using equation (4-6.97)

$$[G^\mu_{\phi_a}] = [R^i_b]^T [G^u_{\phi_a}] \tag{5-2.54}$$

noting that

$$[G^u_{\phi_a}] = [G^{\phi_a}_u]^{-1}. \tag{5-2.55}$$

Note that as discussed briefly in the Chapter 4, the second-order KIC, $[H^{\phi_a}_{uu}]$, can be obtained directly by differentiating the above explicit expression of $[G^{\phi_a}_u]$. Then using the transfer of coordinate methods, any desired second-order KIC's can be obtained as shown in Appendix A.

5–2.7 Force feedback transformation

The wrist force/torque sensor is located on the top ternary plate of the shoulder system as shown in Figure 5–21. Since the universal output coordinates are selected as the local coordinates fixed to the top ternary but having the origin at the common intersection point of the nine joint axes of the shoulder system, the 6-dof force/torque sensor output (which is represented in its local coordinate frame), should be transformed into its equivalent forces in the universal output coordinates.

To find the desired transform equation, denote two independent generalized variables for each set of coordinates, $\mu = [x\ y\ z\ \theta_x\ \theta_y\ \theta_z]^T$ for universal coordinates and $\mu = [x^*\ y^*\ z^*\ \theta^*_x\ \theta^*_y\ \theta^*_z]^T$ for force/torque sensor coordinates. Then the geometric relation can be identified as,

$$\delta\mu^* = [G^{\mu^*}_\mu]\delta\mu \tag{5-2.56}$$

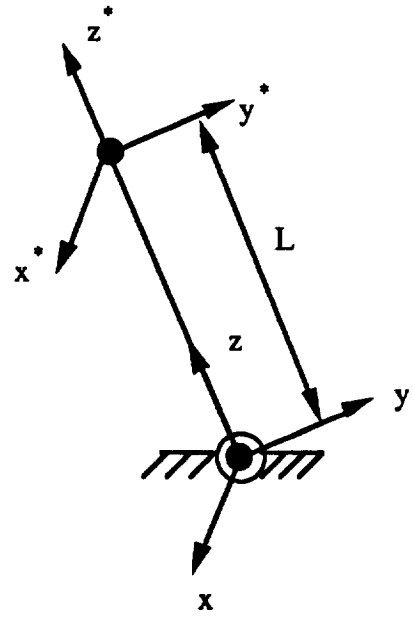

Figure 5–21 LOCAL FRAMES OF A F/T SENSOR AND A UPPER TERNARY PLATE

where

$$\delta\boldsymbol{\mu} = [\delta\mu_x\ \delta\mu_y\ \delta\mu_z\ \delta\theta_x\ \delta\theta_y\ \delta\theta_z]^T, \tag{5–2.57}$$

$$\delta\boldsymbol{\mu}^* = [\delta\mu_x^*\ \delta\mu_y^*\ \delta\mu_z^*\ \delta\theta_x^*\ \delta\theta_y^*\ \delta\theta_z^*]^T \tag{5–2.58}$$

and

$$[G_{\mu}^{\mu^*}] = \begin{bmatrix} 1 & 0 & 0 & 0 & L & 0 \\ 0 & 1 & 0 & -L & 0 & 0 \\ 0 & 0 & 1 & 0 & 0 & 0 \\ 0 & 0 & 0 & 1 & 0 & 0 \\ 0 & 0 & 0 & 0 & 1 & 0 \\ 0 & 0 & 0 & 0 & 0 & 1 \end{bmatrix}. \tag{5–2.59}$$

In the above equation, L represents the distance between a force/torque sensor origin and a common intersection point of the nine axes. The virtual work principle implies,

$$\boldsymbol{\tau}^T\delta\boldsymbol{\mu} = \boldsymbol{\tau}^{*T}\delta\boldsymbol{\mu}^* \tag{5–2.60}$$

where $\tau = [f_x\ f_y\ f_z\ \tau_x\ \tau_y\ \tau_z]^T$ and $\tau^* = [f_x^*\ f_y^*\ f_z^*\ \tau_x^*\ \tau_y^*\ \tau_z^*]^T$. Using the equation (5–2.59) and (5–2.60) yields

$$\tau = [G_\mu^{\mu^*}]^T \tau^* \tag{5–2.61}$$

However, noting that no translation of the shoulder is allowed, the following equations can be directly applied in force/torque transform equations to reduce the computational efforts.

$$\begin{aligned} \tau_x &= -Lf_y^* + \tau_x^* \\ \tau_y &= Lf_x^* + \tau_y^* \\ \tau_z &= \tau_z^* \end{aligned} \tag{5–2.62}$$

The torque in active joints driven by the system actuators can now be obtained by

$$\tau_\phi = [G_\phi^\mu]^T \tau_\mu. \tag{5–2.63}$$

5–2.8 Control strategies for the shoulder

The dynamic equations for the manual controller in joint coordinate variables can be expressed in the following form,

$$T_a = [I_{\phi\phi}^*]\ddot{\phi} + \dot{\phi}^T [P_{\phi\phi\phi}^*]\dot{\phi} + [G_\phi^\mu]^T F_{op} + T_g + T_f \tag{5–2.64}$$

where the left hand side(T_a) represents the actuator torque, the first term ($[I_{\phi\phi}^*]\ddot{\phi}$) in right hand side represents the effective inertia force of the actuators and links, the second term ($\dot{\phi}^T [P_{\phi\phi\phi}^*]\dot{\phi}$) represents the Coriolis forces and centrifugal forces, the third term ($[G_\phi^\mu]^T F_{op}$) is the human operator's command force, the fourth term (T_g) are the gravitational forces, and the last term (T_f) are the friction forces. The definitions of dynamic system parameters and the general derivation of the dynamic equations for the serial and parallel manipulator either in joint variables or in operational space variables are provided in Appendix A.

Since the operating conditions of the manual controller can be typically characterized by low speed operations, the effects of nonlinear dynamics such as Coriolis and centrifugal forces becomes less significant and is neglected. Only the inertial, gravitational, or friction forces are considered. Particularly, since the parallel geometry of the shoulder system allows the heavy actuators to be located toward or on the grounded base, the effects of those inertial and gravitational forces are also minimized. It can be noted that due to the use of the high gear-ratio transmission systems, the off-diagonal terms (i.e., inertia coupling terms) in the inertia matrix, $[I^*_{\phi\phi}]$, become insignificant and only the effects of the inertia and friction of the actuators have significant influences on the performance of the system. This decoupled system dynamics could simplify its dynamic controller design. The decoupled force control law could be applied directly to each joint.

From those consideration, equation (5–2.64) can be simplied as below;

$$T_a = [I^*_{\phi\phi}]\ddot{\phi} + [G^{\mu}_{\phi}]^T F_{op} + T_g + T_f \qquad (5\text{–}2.65)$$

The simple proportional force control law using a wrist force/torque sensing (non-collocated) is applied to the shoulder system. The simplified block diagram representing the implemented control loop is shown in Figure 5–22 and the applied force control law is

$$T_a = T_{ref} + [G^{\mu}_{\phi}]^T [K_f](F_{ref} - F_{op}) \qquad (5\text{–}2.66)$$

where T_a : actuating control torque,

$[G^{\mu}_{\phi}]$: Jacobian matrix of the shoulder or J

$[K_f]$: force control gain matrix, which is diagonal,

T_{ref} : desired reflecting torque at joint, or $[G^{\mu}_{\phi}]^T F_{ref}$,

F_{ref} : desired reflecting force at handgrip,

F_{op} : measured human operator arm command force at handgrip.

Substituting equations (5–2.66) into (5–2.65) yields

$$F_{ref} - F_{op} = [I + K_f]^{-1}[G_\phi^\mu]^{-T}([I_{\phi\phi}^*]\ddot{\phi} + T_g + T_f). \qquad (5\text{–}2.67)$$

This implies that the apparent system characteristics can be modified by the force feedback gain matrix $[I + K_f]$. In actual implementation, the first-order low-pass filter is included in the closed system to reduce effects of the high frequency noise coming from either the gear-train or force/torque sensor as discussed in the previous sections. The complete control flow chart of the controlled

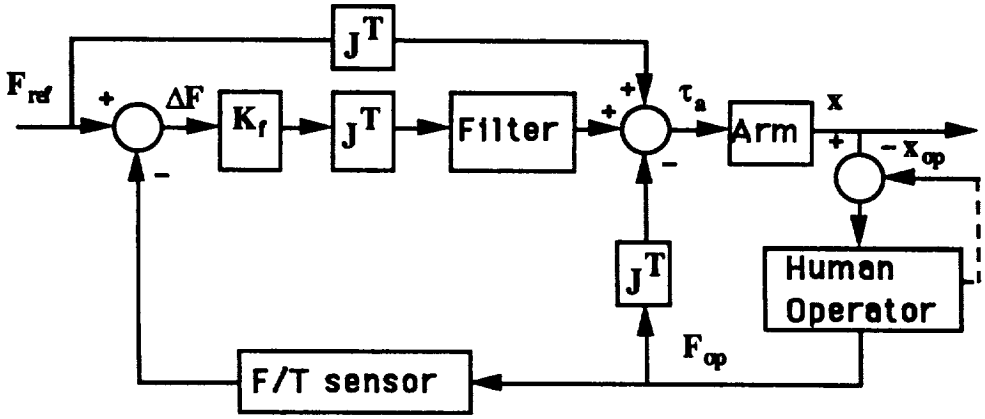

Figure 5–22 BLOCK DIAGRAM OF THE FORCE-CONTROLLED MANUAL CONTROLLER

force-reflecting system is given in Figure 5–23. The output variables of the shoulder system are represented as Euler angles as in equation (4-3.9) and its input variables are reflecting torques in the moving coordinates fixed on the top plate.

5–2.9 Shoulder system experiment and discussion

In general, parallel robotic systems involve a significant amount of computational burden. However, for the implemented shoulder system, due to its

SHOULDER FLOWCHART DIAGRAM AS A MANUAL CONTROLLER

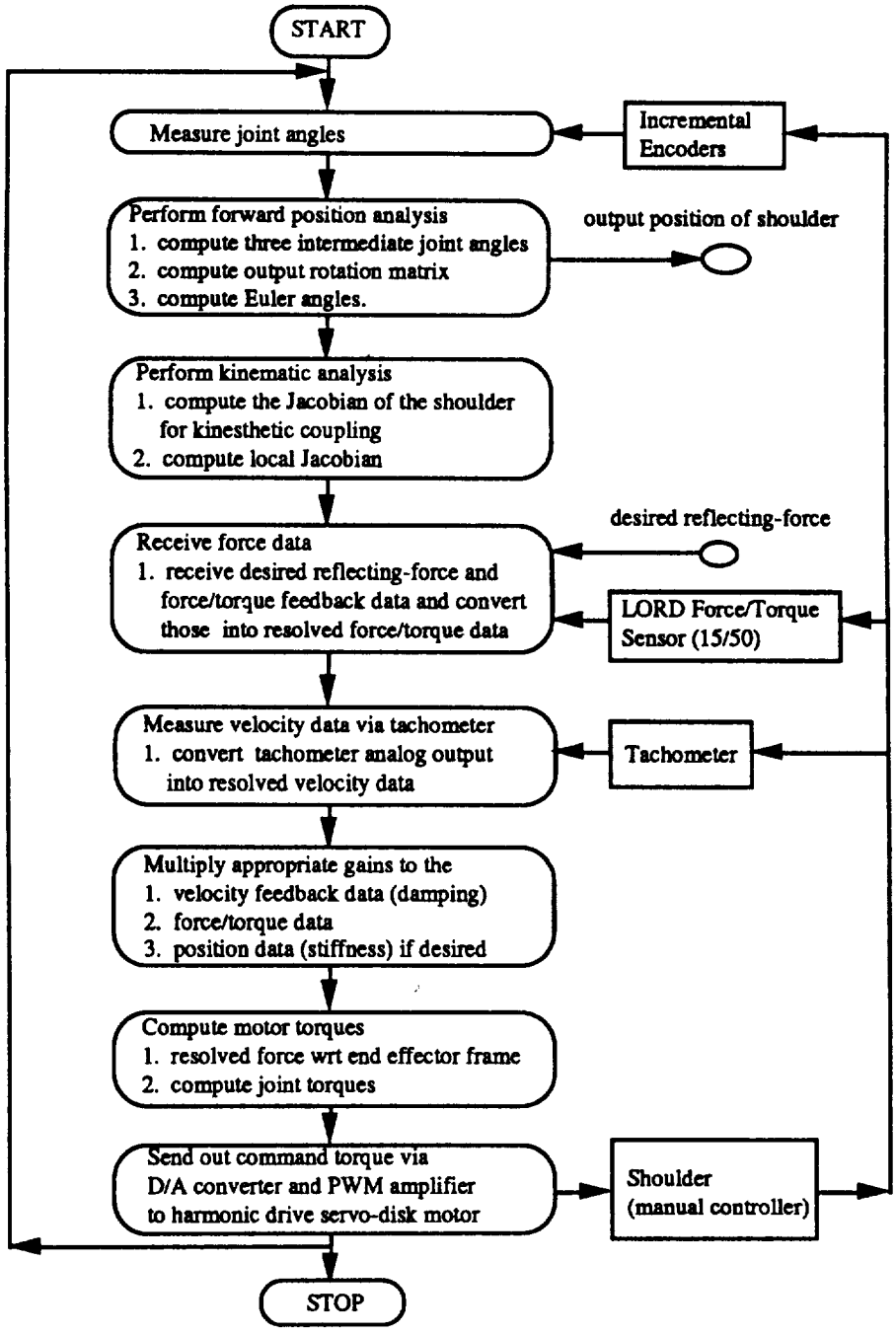

Figure 5–23 FLOWCHART OF THE FORCE-REFLECTING MANUAL CONTROLLER

simple kinematic parameters (i.e., twist angles are 0° or 90°) and the location of the heavy actuators on the grounded base, the computational burden for the system is drastically simplified. The total analytical and computational burden is not significant and a relatively simple gravitational compensation scheme is required.

The implemented shoulder system exhibits significant magnitudes of friction and inertia forces from the high gear-ratio reducers in the actuator modules. The magnitude of static friction in the system is compensated for via direct force feedback to a level where the human operator is not disturbed. However, nonlinear varying friction coming from either the actuators or non-ideal gear contacts of the harmonic drive system is the main disturbance that deteriorates the performance of the manual controller.

As discussed in sections 5.1, various factors such as the gripping status of the operator, the elasticity of the gear train(harmonic drive system), the magnitude of the varying friction(gear cogging), etc., turn out to be related to the potential for instability.

In the actual system, the magnitude of varying friction of one of three acutator systems is significantly larger than the other two actuator systems. The uncompensated nonlinear friction of the unit dominates the system behavior, deteriorating its overall performance. When the decoupled force control using joint sensing torque from the strain gauge is applied to each joint, the uncompensated nonlinear varying friction of the actuator with largest magnitude of varying nonlinear friction represents undesirable chattering responses and dominates the system response. However, with the unit replaced, much better system performance can be expected. To avoid undesirable nonlinear friction, extreme caution should be made to find units which have acceptable

non-linear varying friction when the harmonic drive reducer units are selected for manual controller application.

Through these implementations, the application of the high gear-ratio reducers to the manual controller with force feedback control is tested and a compact, light-weight force-reflecting manual controller system is designed. Also the parallel geometry is effectively utilized for more advanced manual controller designs. Some of attractive features of the implemented manual controller are summarized as below.

- By the use of the optimal kinematic parameters as shown in Table 5–3, the desired working volume is secured. Also, in the actual hardware design, the mechanical interferences are avoided to secure a large dextrous working volume.

- The dynamic effects of the manual controller can be simplified or neglected by locating all heavy actuators on the grounded base.

- The simple proportional control strategy is applied and very effective due to the simplified dynamics of the system. With force feedback control, the magnitudes of the friction and the apparent system inertia are reduced significantly.

- The gravitational force is minimized.

- The simple and symmetric kinematic parameters greatly reduces the computatonal burden.

- A high mechanical stiffness is obtained.

- The redundant position sensors are placed to provide the flexibility for emergency or component failure.

5–2.10 Example of shoulder system teleoperation application

The 3-dof universal/force-reflecting hand controller is applied to the control of the simulated HERMIES III mobile system and of the simulated 7-dof CESARm in an obstacle-strewn environment animated on a Silicon Graphics Work Station at the University of Texas. This is a preliminary step for the actual teleoperation application of the shoulder system to control both the actual HERMIES III and CESARm at the Oak-Ridge National Labaratory.

The position data of the shoulder system (the output Euler angles) is provided to the Silicon Graphics Work Station to animate the motion of the HERMIES III and the CESARm and in return, the potential forces representing the information of the relative distances between the controlled system and obstacles are reflected back to the manual controller. In the force-reflecting controller, the local force control loop is closed to compensate or to reduce the inertia and friction of the system, and the reflecting force is used as a desired nominal force as shown in Figure 5–22. The interface diagram for the shoulder-Silicon graphic work station is given in Figure 5–24. More detailed descriptions on the control of these two systems can be found in [87].

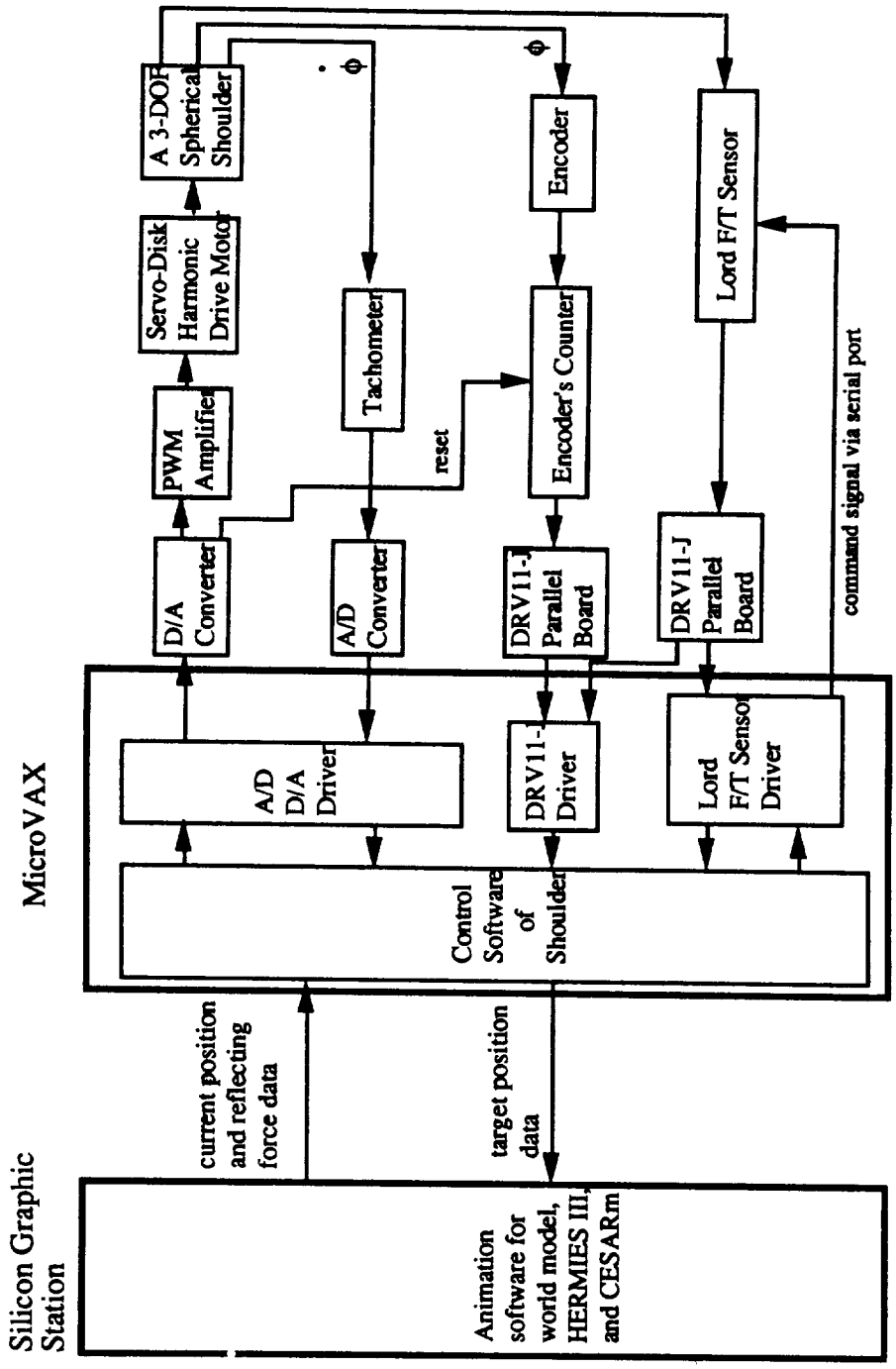

Figure 5–24 INTERFACE DIAGRAM FOR SHOULDER-SILICON GRAPHIC STATION

CHAPTER 6

A New Conceptual Design of a 3-dof Spherical Gimbal Module

Both the serial structure and the parallel structure have advantages and disadvantages when applied to robotic systems. The serial structure is geometrically simple, compact, and has a large, dextrous workspace. However, the cantilever nature of the serial structure exhibits low stiffness and results in serious static and/or dynamic deflection and positional errors at the end effector of the manipulator under the influence of a large payload. The distributed location of actuators throughout manipulator structure may also produce undesirable inertial and gravitational effects which reduce the payload capacity of the serial manipulator.

The parallel structure conceivably provides higher mechanical stiffness than the serial structure resulting in decreased end effector deflection. The parallel structure allows the actuators to be located at the base of the device. However, the kinematic and dynamic complexity, the smaller range of motion, etc., reduces the wide application of parallel structures.

Combining the advantages of both a serial structure and a parallel structure, desirable characteristics can be achieved through a hybrid structure. A hybrid structure is composed of parallel sub-structures which are linked together serially. More detailed comparisons between serial and parallel structures

can be found in [19][83].

This chapter introduces a new conceptual hybrid (or parallel) spherical 3-dof system. The description and kinematic analysis is presented in detail. Also included is the comparative kinematic analysis on various structural spherical 3-dof wrists: a parallel spherical 3-dof system (discussed in chapter 5 and 6), a serial spherical 3-dof system, and a new hybrid (or parallel) spherical 3-dof system. The first order kinematic influence coefficients are used to investigate their respective kinematic properties.

6–1 Kinematic analysis for a conceptual 3-dof gimbal module

A new conceptual hybrid spherical 3-dof mechanism, a parallel six-bar $6R$[1](or it may be represented as $RPRRPR$) linkage, is shown in Figure 6–1. The six joint axes must have a common intersection point to satisfy the geometric requirement for spherical motion. The parallel structure of the linkage allows two actuators to be placed at the grounded base, thus reducing effective inertia and gravitational forces.

Another new parallel spherical 3-dof mechanism can be conceptualized by modifying the 3-dof rotational hybrid device discussed above, or by adding a 3-dof spherical joint as shown in Figure 6–2. Again all joint axes of the system must have a common intersecting point to satisfy the geometric requirement for spherical motion. In this configuration, a parallel 3-dof linkage provides active 2-dof torque inputs and a spherical joint provides an active one-dof torque input. Note that this 3-dof spherical joint can be realized by mounting a one-

[1]It may be noted that due to the special geometry used in this system, each translational motion along the prismatic joint can be represented as a rotational motion about an equivalent rotational axis. The equivalent rotational axis passes through the common intersection point and is perpendicular to the translational motion surface.

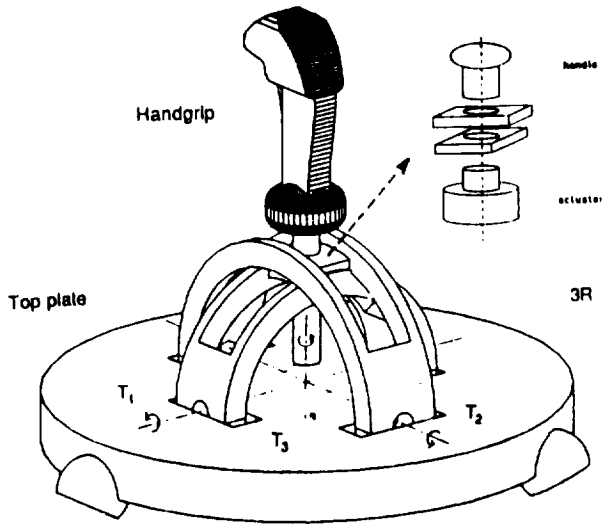

Figure 6–1 A CONCEPTUAL HYBRID SPHERICAL 3-DOF MECHANISM

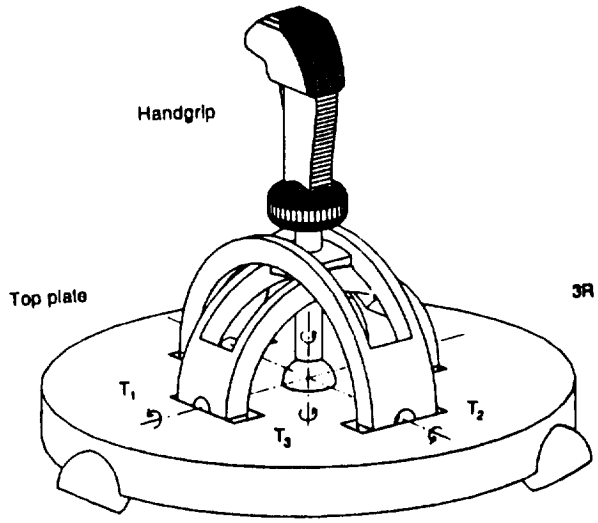

Figure 6–2 A CONCEPTUAL PARALLEL SPHERICAL 3-DOF MECHANISM

dof actuator on a 2-dof gimbal. Again the parallel structure allows the three required actuators to be located on the grounded base. The following sections present mobility analyses and the description of the kinematic analyses of the new spherical 3-dof mechanisms.

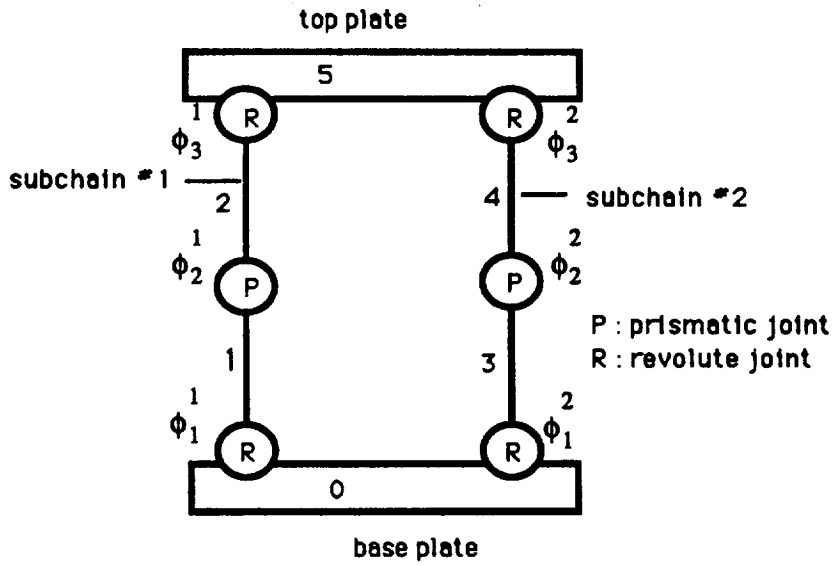

Figure 6–3 SCHEMATICS OF A CONCEPTUAL HYBRID 3-DOF SYSTEM

6–1.1 Mobility analysis

The first step in the conceptual design process is to determine the mobilities of the spherical 3-dof mechanisms. The simplified schematics of the hybrid and the parallel spherical 3-dof mechanisms are shown in Figure 6–3 and 6–4. Utilizing the general mobility criterion given in equation (4-1.1), the mobility for the hybrid 3-dof mechanism can be checked using the following equation:

$$M = m(n-1) - \sum_{i=1}^{g} u_i = 3(6-1) - (2 \times 6) = 3, \qquad (6\text{–}1.1)$$

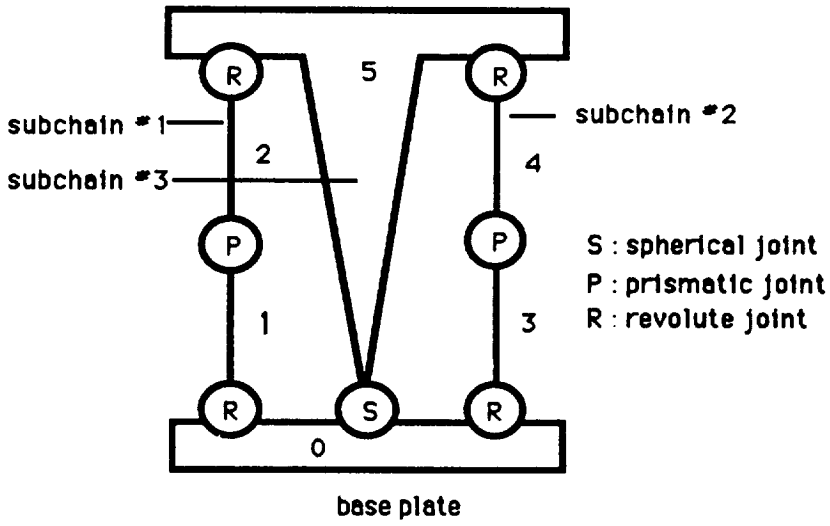

Figure 6–4 SCHEMATICS OF A CONCEPTUAL PARALLEL 3-DOF SYSTEM

The mobility for the 3-dof parallel mechanism is:

$$M = m(n-1) - \sum_{i=1}^{g} u_i = 3(6-1) - (2 \times 6 + 1 \times 0) = 3. \qquad (6\text{–}1.2)$$

Note that due to the special geometry, the dimension of maximum output space in the above mobility analyses, $m = 3$, is used.

6–1.2 Kinematic description

The parallel spherical 3-dof system is a multi-loop mechanism consisting of a base plate, a six-bar linkage ($6R$), and a 3-dof spherical joint (S or $\widehat{RRR}$). The system is connected in parallel to the six-bar linkage in a manner necessary to generate a spherical 3-dof motion. The base coordinate system ($\boldsymbol{x}_b$, $\boldsymbol{y}_b$, $\boldsymbol{z}_b$), representing a reference frame, is located at the base plate. The coordinate system ($\boldsymbol{x}_t$, $\boldsymbol{y}_t$, $\boldsymbol{z}_t$), representing the output of the system, is shown in Figure 6–6. Consider the six-bar linkage, driven from two base joints, providing two-dof torque inputs. Without loss of generality and for simplicity, two actuated

base joint axes are located perpendicular to each other and coincide with x_b and y_b, respectively, as shown in Figures 6–5 and 6–6. An additional actuated revolute joint axis from a spherical joint, which independently provides actuated one-dof input torque, coincides with z_t. To represent output spherical motion of the mechanism, the Euler angles, μ_1, μ_2, and μ_3, are chosen so that the Euler angles coincide with joint variables of the serial subchain 1. That is $\mu_n = \phi_n^1$ for $n = 1, 2, 3$. The Euler angles define the rotational matrices:

$$[R_b^t] = [R(x, \mu_1)][R(y, \mu_2)][R(z, \mu_3)]. \tag{6–1.3}$$

The Euler angle definition with the above coordinate system definition avoid the problem of mathematical singularity within the workspace of the mechanism. The values of the Euler angles

$$-90° < \mu_1 < 90°, -90° < \mu_2 < 90°, and -90° < \mu_3 < 90°, \tag{6–1.4}$$

cause no mechanical singularities of the mechanisms to exist. The joint variables are represented as ϕ_n^m. The superscript, m, denotes the subchain and the subscript, n, denotes the joint of the subchain.

The conceptual hybrid spherical 3-dof system uses the same six-bar linkage ($6R$) used in the parallel system. Similar notation and coordinate systems are applied to the parallel system as shown in Figure 6–5. The actual motion of the 3-dof spherical joint in the parallel system can be arranged to satisfy $\mu_n = \phi_n^3$ for $n = 1, 2, 3$ such that both the hybrid system and the parallel system may be represented by the same kinematics. The following kinematic analysis is based on this premise for consistency. Thus the analysis can be applied to both the conceptual parallel mechanism and the conceptual hybrid mechanism.

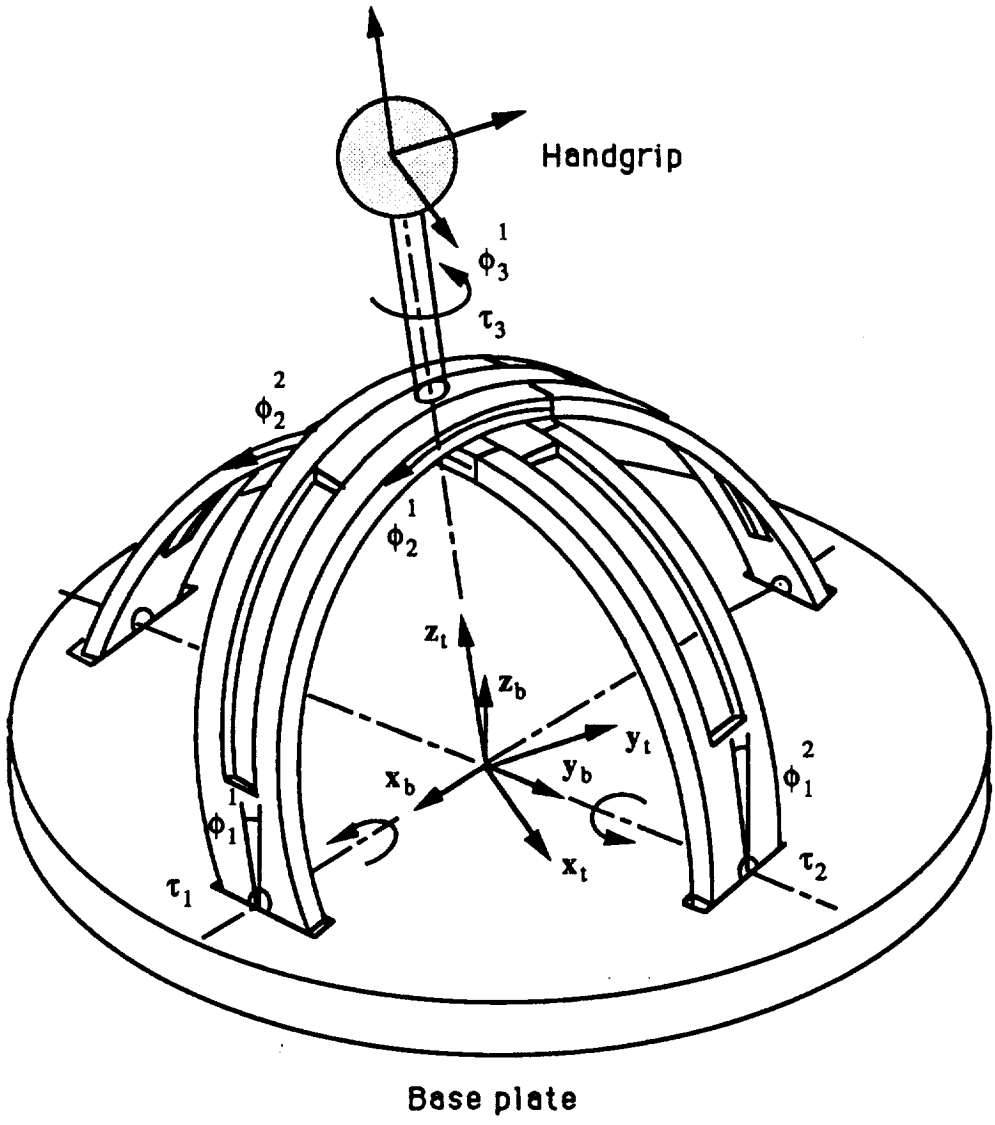

Figure 6–5 KINEMATIC REPRESENTATION OF A HYBRID SYSTEM

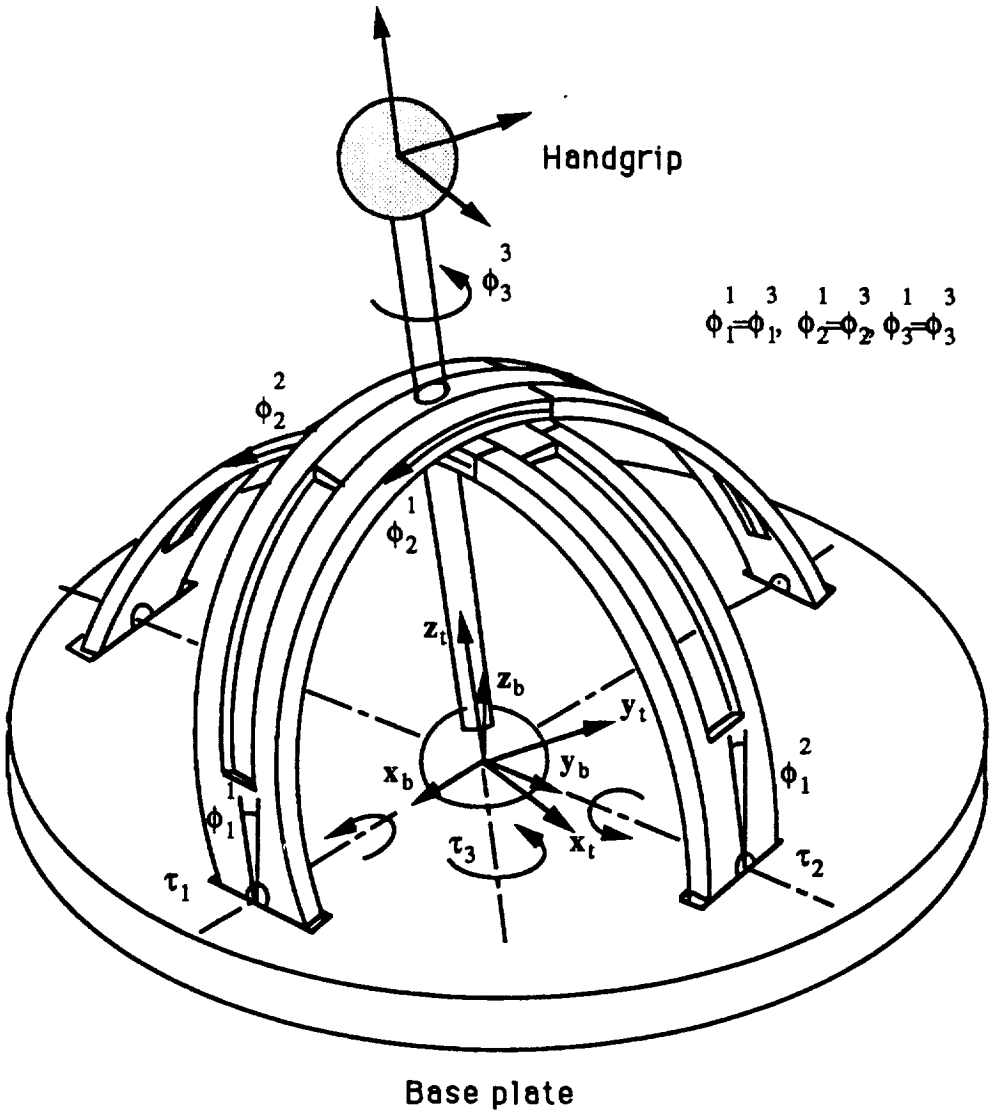

Figure 6–6 KINEMATIC REPRESENTATION OF A PARALLEL SYSTEM

6–1.3 Forward position analysis

The forward position analysis requires the output transformation matrix or the equivalent Euler angles, given the input joint angles. The following analysis assumes that three joint angles, ϕ_1^1, ϕ_1^2, and ϕ_3^1 are measured and known quantities. It can simply be realized by mounting position transducers at the corresponding joints.

From the geometry, the output vector, $\boldsymbol{z}_t$, can be represented in either as

$$\boldsymbol{z}_t = [Rot(x, \phi_1^1)][Rot(y, \phi_2^1)] \begin{Bmatrix} 0 \\ 0 \\ 1 \end{Bmatrix} \tag{6–1.5}$$

or

$$\boldsymbol{z}_t = [Rot(y, \phi_1^2)][Rot(x, \phi_2^2)] \begin{Bmatrix} 0 \\ 0 \\ 1 \end{Bmatrix}. \tag{6–1.6}$$

Where

$$\begin{aligned} [Rot(x, \phi_1^1)][Rot(y, \phi_2^1)] &= \begin{bmatrix} 1 & 0 & 0 \\ 0 & c\phi_1^1 & -s\phi_1^1 \\ 0 & s\phi_1^1 & c\phi_1^1 \end{bmatrix} \begin{bmatrix} c\phi_2^1 & 0 & s\phi_2^1 \\ 0 & 1 & 0 \\ -s\phi_2^1 & 0 & c\phi_2^1 \end{bmatrix} \\ &= \begin{bmatrix} c\phi_2^1 & 0 & s\phi_2^1 \\ s\phi_1^1 s\phi_2^1 & c\phi_1^1 & -s\phi_1^1 c\phi_2^1 \\ -c\phi_1^1 s\phi_2^1 & s\phi_1^1 & c\phi_1^1 c\phi_2^1 \end{bmatrix} \end{aligned} \tag{6–1.7}$$

and

$$\begin{aligned} [Rot(y, \phi_1^2)][Rot(x, \phi_2^2)] &= \begin{bmatrix} c\phi_1^2 & 0 & s\phi_1^2 \\ 0 & 1 & 0 \\ -s\phi_1^2 & 0 & c\phi_1^2 \end{bmatrix} \begin{bmatrix} 1 & 0 & 0 \\ 0 & c\phi_2^2 & -s\phi_2^2 \\ 0 & s\phi_2^2 & c\phi_2^2 \end{bmatrix} \\ &= \begin{bmatrix} c\phi_1^2 & s\phi_1^2 s\phi_2^2 & s\phi_1^2 c\phi_2^2 \\ 0 & c\phi_2^2 & -s\phi_2^2 \\ -s\phi_1^2 & c\phi_1^2 s\phi_2^2 & c\phi_1^2 c\phi_2^2 \end{bmatrix}. \end{aligned} \tag{6–1.8}$$

Equating equations (6–1.5) and (6–1.6) results in the following three constraints equations,

$$sin\phi_2^1 = sin\phi_1^2 cos\phi_2^2, \tag{6–1.9}$$

$$sin\phi_1^1 cos\phi_2^1 = sin\phi_2^2, \tag{6–1.10}$$

$$cos\phi_1^1 cos\phi_2^1 = cos\phi_1^2 cos\phi_2^2. \tag{6–1.11}$$

Noting $\boldsymbol{z}_t \cdot \boldsymbol{z}_t = 1$, the following two independent constraint equations can be derived from the equations (6–1.9), (6–1.10) and (6–1.11)

$$\tan\phi_2^2 = \tan\phi_1^1 \cos\phi_1^2, \tag{6–1.12}$$

$$\tan\phi_2^1 = \tan\phi_1^2 \cos\phi_1^1. \tag{6–1.13}$$

Because three joint angular displacements, ϕ_1^1, ϕ_1^2 and ϕ_3^1 are known, only ϕ_2^1 needs to be computed. From the equation (6–1.13)

$$\phi_2^1 = \arctan(\tan\phi_1^2 \cos\phi_1^1). \tag{6–1.14}$$

Finally, noting that $\mu_n = \phi_n^1$, for $n = 1, 2, 3$, the desired output transformation matrix can be obtained using the equation (6–1.3).

6–1.4 Reverse position analysis

In the reverse position analysis, the output transformation matrix or its equivalent Euler angles, μ_n for $n = 1, 2, 3$, are known and joint angles, ϕ_1^1, ϕ_1^2, and ϕ_3^1, need to be found. Noting $\phi_n^1 = \phi_n^3$ and $\mu_n = \phi_n^1$, for $n = 1, 2, 3$, and using equation (6–1.3), the three joint angles, ϕ_1^1, ϕ_2^1, and ϕ_3^3, can be found. Then by using the equation (6–1.13), ϕ_1^2 can be computed from

$$\phi_1^2 = arctan(tan\phi_2^1 sec\phi_1^1). \tag{6–1.15}$$

6–1.5 The first order kinematic influence coefficient

As discussed in chapter 4 and 5, the output velocity of the spherical motion may be represented with respect to either the local moving body-fixed

frame or the global frame. To obtain the first order kinematic influence coefficient, which represents the geometric relationship between two independent sets of generalized rate variables, the method of the transfer of generalized coordinates is used [32].

Let $\dot{\boldsymbol{u}}$ represent the universal generalized rate variables and $\dot{\boldsymbol{\phi}}$ represent the joint rate variables. The differential relationship between them for the serial system can be written using the equation (A-2.8);

$$\dot{\boldsymbol{u}} = [G^{u}_{\phi}]\dot{\boldsymbol{\phi}} = [\boldsymbol{s}_1\ \boldsymbol{s}_2\ \boldsymbol{s}_3]\dot{\boldsymbol{\phi}}. \tag{6-1.16}$$

For the serial subchain $m = 1$, we have

$$\dot{\boldsymbol{u}} = [\boldsymbol{s}^1_1\ \boldsymbol{s}^1_2\ \boldsymbol{s}^1_3]\dot{\boldsymbol{\phi}}^1 = \begin{bmatrix} 1 & 0 & s\phi^1_2 \\ 0 & c\phi^1_1 & -s\phi^1_1 c\phi^1_2 \\ 0 & s\phi^1_1 & c\phi^1_1 c\phi^1_2 \end{bmatrix} \begin{Bmatrix} \dot{\phi}^1_1 \\ \dot{\phi}^1_2 \\ \dot{\phi}^1_3 \end{Bmatrix}. \tag{6-1.17}$$

Assuming that the above matrix is invertible (i.e., the system is not at singularity point),

$$\dot{\boldsymbol{\phi}}^1 = [\boldsymbol{s}^1_1\ \boldsymbol{s}^1_2\ \boldsymbol{s}^1_3]^{-1}\dot{\boldsymbol{u}} = \begin{bmatrix} 1 & \frac{s\phi^1_1 s\phi^1_2}{c\phi^1_2} & -\frac{c\phi^1_1 s\phi^1_2}{c\phi^1_2} \\ 0 & c\phi^1_1 & s\phi^1_1 \\ 0 & -\frac{s\phi^1_1}{c\phi^1_2} & \frac{c\phi^1_1}{c\phi^1_2} \end{bmatrix} \begin{Bmatrix} \dot{u}_1 \\ \dot{u}_2 \\ \dot{u}_3 \end{Bmatrix}. \tag{6-1.18}$$

Likewise, for the serial subchain $m = 2$, we have

$$\dot{\boldsymbol{u}} = [\boldsymbol{s}^2_1\ \boldsymbol{s}^2_2\ \boldsymbol{s}^2_3]\dot{\boldsymbol{\phi}}^2 = \begin{bmatrix} 0 & c\phi^2_1 & s\phi^2_1 c\phi^2_2 \\ 1 & 0 & -s\phi^2_2 \\ 0 & -s\phi^2_1 & c\phi^2_1 c\phi^2_2 \end{bmatrix} \begin{Bmatrix} \dot{\phi}^2_1 \\ \dot{\phi}^2_2 \\ \dot{\phi}^2_3 \end{Bmatrix} \tag{6-1.19}$$

and

$$\dot{\boldsymbol{\phi}}^2 = [\boldsymbol{s}^2_1\ \boldsymbol{s}^2_2\ \boldsymbol{s}^2_3]^{-1}\dot{\boldsymbol{u}} = \begin{bmatrix} \frac{s\phi^2_1 s\phi^2_2}{c\phi^2_2} & 1 & \frac{c\phi^2_1 s\phi^2_2}{c\phi^2_2} \\ c\phi^2_1 & 0 & -s\phi^2_1 \\ \frac{s\phi^2_1}{c\phi^2_2} & 0 & \frac{c\phi^2_1}{c\phi^2_2} \end{bmatrix} \begin{Bmatrix} \dot{u}_1 \\ \dot{u}_2 \\ \dot{u}_3 \end{Bmatrix}. \tag{6-1.20}$$

For the serial subchain $m = 3$ for the parallel configuration, the differential relationship between the universal variables, $\dot{\boldsymbol{u}}$, and joint rate variables, $\dot{\boldsymbol{\phi}}$ can

be represented by the equations (6–1.17) and (6–1.18), by considering the fact $\phi_n^3 = \phi_n^1 = \mu_n$ for $n = 1, 2, 3$. For both the hybrid and the parallel system, the inverse of the desired first order kinematic influence coefficients between universal rate variables, $\dot{u}$, and actuating joint variables, $\dot{\phi}_a$, can be obtained by use of equations from equations (6–1.18) and (6–1.20) as follows:

$$\dot{\phi}_a = [G_u^{\phi_a}]\dot{u} = \begin{bmatrix} 1 & \frac{s\phi_1^1 s\phi_2^1}{c\phi_2^1} & -\frac{c\phi_1^1 s\phi_2^1}{c\phi_2^1} \\ \frac{s\phi_1^2 s\phi_2^2}{c\phi_2^2} & 1 & \frac{c\phi_1^2 s\phi_2^2}{c\phi_2^2} \\ 0 & -\frac{s\phi_1^1}{c\phi_2^1} & \frac{c\phi_1^1}{c\phi_2^1} \end{bmatrix} \begin{Bmatrix} \dot{u}_1 \\ \dot{u}_2 \\ \dot{u}_3 \end{Bmatrix} \tag{6–1.21}$$

where actuated joint variables, ϕ_a, are denoted by

$$\phi_a = [\phi_1^1 \ \phi_1^2 \ \phi_3^1]^T. \tag{6–1.22}$$

By inverting the above equation, we can find the desired KIC matrix from

$$\dot{u} = [G_{\phi_a}^u]\dot{\phi}_a, \tag{6–1.23}$$

where

$$[G_{\phi_a}^u] = \frac{\begin{bmatrix} \frac{c\phi_1^1}{c\phi_2^1} + \frac{s\phi_1^1 c\phi_1^2 s\phi_2^2}{c\phi_2^1 c\phi_2^2} & 0 & \frac{s\phi_1^1 s\phi_2^1 c\phi_1^2 s\phi_2^2}{c\phi_2^1 c\phi_2^2} + \frac{c\phi_1^1 s\phi_2^1}{c\phi_2^1} \\ -\frac{c\phi_1^1 s\phi_1^2 s\phi_2^2}{c\phi_2^1 c\phi_2^2} & \frac{c\phi_1^1}{c\phi_2^1} & -\frac{c\phi_1^1 s\phi_2^1 s\phi_1^2 s\phi_2^2}{c\phi_2^1 c\phi_2^2} - \frac{c\phi_1^2 s\phi_2^2}{c\phi_2^2} \\ -\frac{s\phi_1^1 s\phi_1^2 s\phi_2^2}{c\phi_2^1 c\phi_2^2} & \frac{s\phi_1^1}{c\phi_2^1} & 1 - \frac{s\phi_1^1 s\phi_2^1 s\phi_1^2 s\phi_2^2}{c\phi_2^1 c\phi_2^2} \end{bmatrix}}{\frac{c\phi_1^1}{c\phi_2^1} + \frac{s\phi_1^1 c\phi_1^2 s\phi_2^2}{c\phi_2^2 c\phi_2^1}}. \tag{6–1.24}$$

The KIC matrix between the local moving body-fixed frame and joint input, $[G_\phi^\mu]$, can also be determined using equation (4-6.97).

6–2 The first order KIC of a serial wrist

A serial wrist shown in Figure 6–7 has the same Euler angle representations used for the two other structural mechanisms: hybrid and parallel

mechanisms. It is investigated in the following comparative analysis. Note that $[R_b^t]$= $[R(x,\phi_1)]$ $[R(y,\phi_2)][R(z,\phi_3)]$. The first-order KIC of the serial 3-dof spherical mechanism can be found using equation (A-2.8) as follows;

$$\dot{u} = [G_\phi^u]\dot{\phi} \tag{6-2.25}$$

where

$$[G_\phi^u] = [s_1\ s_2\ s_3] = \begin{bmatrix} 1 & 0 & s\phi_2 \\ 0 & c\phi_1 & -s\phi_1 c\phi_2 \\ 0 & s\phi_1 & c\phi_1 c\phi_2 \end{bmatrix}. \tag{6-2.26}$$

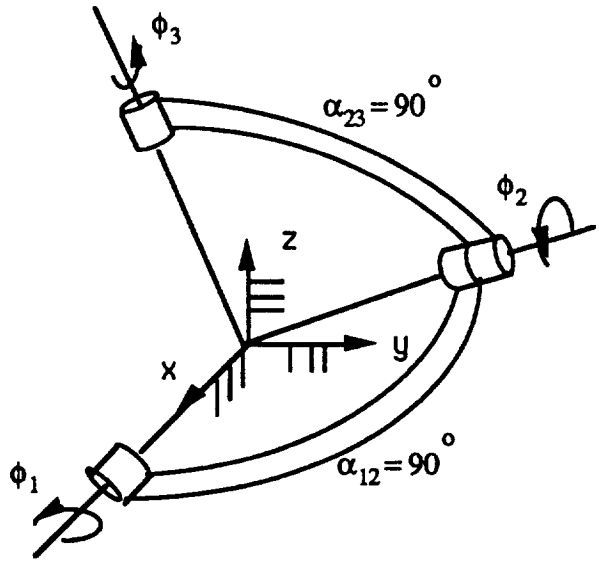

Figure 6–7 A SERIAL 3-DOF WRIST

6–3 Comparative study on geometric characteristics of various spherical wrists

The KIC's of three different spherical systems has been obtained. This section compares the kinematic properties of the three spherical mechanisms.

A square root of a condition number of the matrix, $[G_\phi^u][G_\phi^u]^T$, can be used to examine geometric properties of the three spherical mechanisms. Both minimum and maximum transmission characteristics can be reflected using the value of the square root. However, as discussed previously, the ratio of the maximum singular value to the minimum singular value of $[G_\phi^u]$ represents the square root of a condition number of the matrix $[G_\phi^u][G_\phi^u]^T$. Therefore, singular values are computed directly and the ratios of the maximum singular value to the minimum singular value are used instead.

In general, one of the most desirable characteristics of the system is to achieve uniform input and output velocity/torque transmission characteristics in all directions at any configuration of the system, or equivalently to have the condition number equal to 1. Since the condition number is always greater than or equal to 1 by definition, the large condition number implies nonuniform transmission characteristics and is therefore not desirable.

The plots in Figures 6–8, 6–9 and 6–10 show ratios of the maximum singular values to the minimum singular value within the specified workspace for the three different mechanisms. Both μ_1 and μ_2 are varied from $-85°$ to $-85°$ with μ_3= 0° fixed. From equations (5-1.24) and (5-1.26), both the serial mechanism and the hybrid mechanism have the first-order KIC's independent of the joint variable ϕ_3. Since $\mu_3 = \phi_3^1$, they are also independent of μ_3. Therefore, the overall characteristics of both the serial and the hybrid mechanisms can be represented by the given three-dimensional surface plots. The workspace with desired transmission characteristics may be obtained directly from the three dimensional surface plots by defining the threshold value of the condition number. However for the parallel system (shoulder) as explained in chapter 4, three-dimensional surface plots are required to identify the workspace with desirable

transmission characteristics for equally separated μ_3 values (for example, $-60°$, $-30°$, $0°$, $30°$, and $60°$). For the purposes of this analysis, the accurate size of the workspace of the three spherical systems is not a major concern. Instead the general properties of the three mechanisms are discussed as followings.

As illustrated in Figures 6–8 - 6–10, the largest dextrous workspace with desired kinematic properties is characteristic of the serial mechanism. Only within the relatively small workspace(i.e., $-50° \leq \mu_1,\ \mu_2 \leq 50°$, $-40° \leq \mu_3 = 0 \leq 40°$), the parallel system maintains desirable kinematic properties[68]. Note that the comparison is based on kinematic properties only. For other characteristics such as inertial and gravitational effects and mechanical stiffnesses, the parallel system may indeed be more desireable as contended by many researchers[19][52][85]. However, the new conceptual mechanism represents very promising properties in both kinematic and dynamic aspects. It has a relatively large dextrous workspace as shown in Figure 6–9, and the parallel structure increases mechanical stiffness. The device also allows most of the actuators to be placed toward ground, minimizing inertial and gravitational effects. The simple kinematics of the system represent another desirable feature.

6–4 Discussion and conclusion

A new conceptual hybrid (or parallel) spherical structure is introduced and the kinematic analysis has been presented. To evaluate its geometric characteristics, the first-order KIC's of three different spherical systems (serial wrist, shoulder, and new spherical wrist) have been compared. The results shows that the conceptual system represents better transmission characteristics and/or larger dextrous workspace than the parallel dyad shoulder. Also the paral-

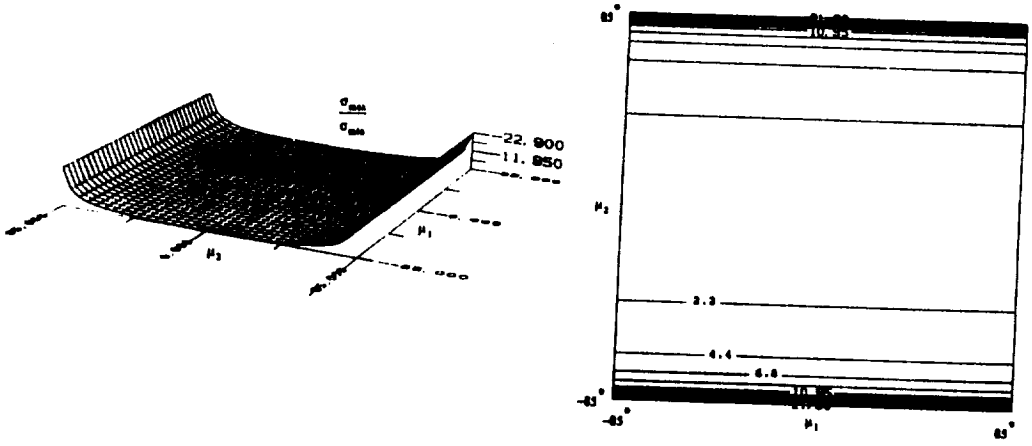

Figure 6–8 COUTOUR AND THREE-DIMENSIONAL PLOTS OF THE SERIAL SPHERICAL 3-DOF MECHANISM

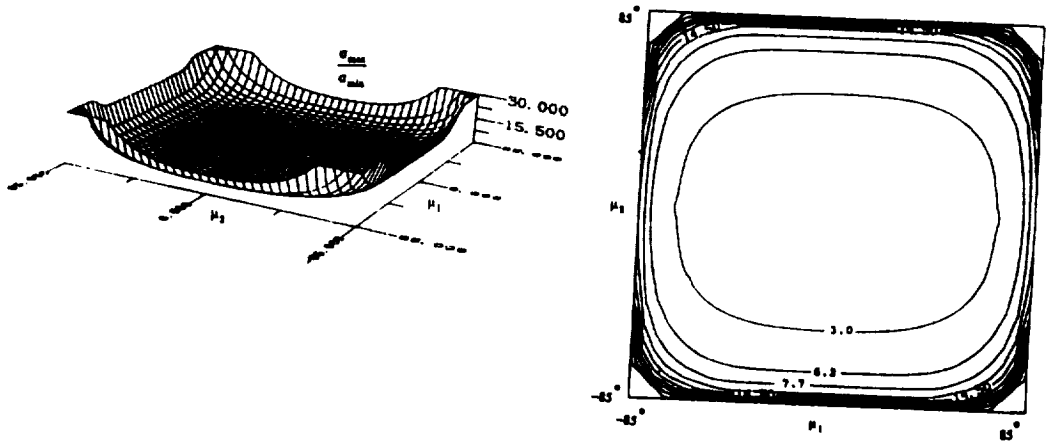

Figure 6–9 COUTOUR AND THREE-DIMENSIONAL PLOTS OF THE HYBRID SPHERICAL 3-DOF MECHANISM

lel structure provides mechanical stiffness and allows actuators to be placed toward ground, minimizing inertial and gravitational effects. The simple kinematics represents another desireable aspect. From these considerations, the new spherical system is very promising in both kinematics and dynamics. As a 3-dof force-reflecting manual controller, the new spherical system seems to have promising features, such as low inertia and simple kinematics.

Finally, it should be noted that when ϕ_3^1 in a hybrid system and ϕ_3^3 in a parallel system are constant, either of these systems becomes a two-dof parallel system. This type of system permits two actuators to be located at the base which is a very desirable feature for a force-reflecting manual controller. In the following chapter, a conceptual 6-dof system using the 2-dof parallel system as a system component is introduced and analyzed.

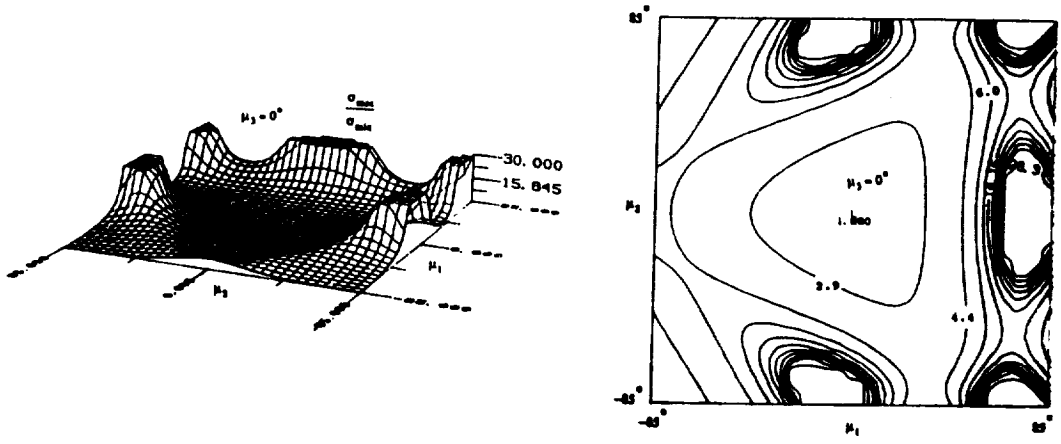

Figure 6–10 COUTOUR AND THREE-DIMENSIONAL PLOTS OF THE PARALLEL SPHERICAL 3-DOF MECHANISM

CHAPTER 7

Conceptual Design of a Parallel 6-dof Manual Controller

In the literature, the advantages of parallel geometry in the design of the manipulators have been discussed and much effort has been devoted to this advanced topic in mechanical design of manipulators [49][52][61][85][104]. A parallel 6-dof manipulator, the Stewart platform, was first described by Stewart and applied to flight simulators[85]. As shown in Figure 7–1, this type of system uses actuated prismatic joints and the workspaces is quite limited. Also the prismatic actuators are not backdrivable so tasks requiring compliance of the manipulator are not feasible. However, due to the higher mechanical stiffness of the parallel structure, manipulators with parallel structures have been applied to tasks requiring high precision under load.

The design of the force-reflecting manual controllers requires consideration of many issues. In the previous chapters, the conceptual design of a spherical 3-dof manual controller has been introduced and investigated. In this chapter, a design of a 6-dof force-reflecting manual controller is discussed. For the design of force-reflecting manual controllers, parallel geometry has been applied to the design of the universal 9-string force-reflecting 6-dof manual controller developed at the University of Texas[3][63]. The structure of this device is basically similar to the Stewart platform 6-dof parallel system.

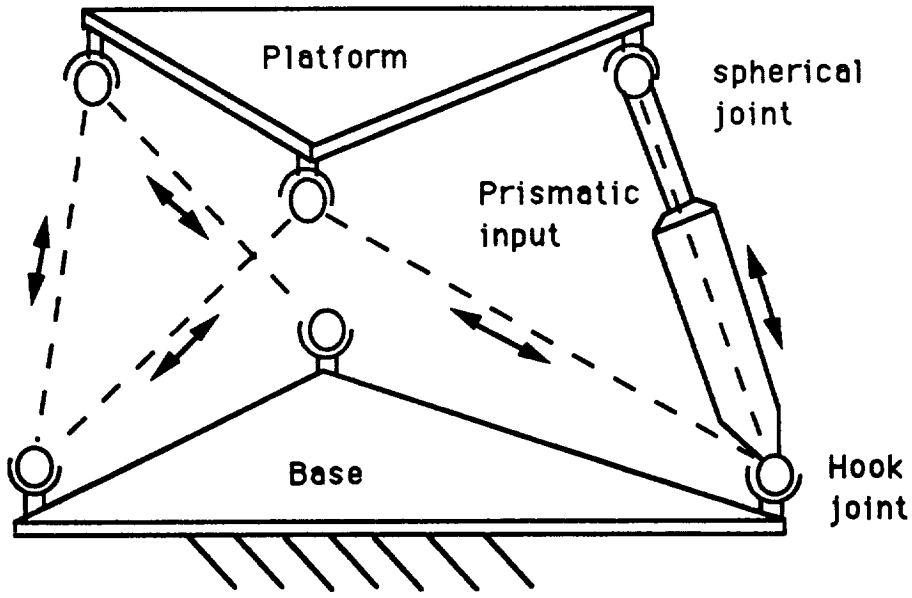

Figure 7–1 GENERAL STEWART PLATFORM

In this chapter, a brief description and performance evaluations of the 9-string force-reflecting manual controller are presented first. Next, one of the conceptual force-reflecting manual controllers, which has a parallel structure, is analyzed in detail. This conceptual manual controller seems to have advantages such as compactness, portability, light-weight, minimum effective inertia, mechanical rigidity, etc. The analysis provides an initial framework to investigate the kinematic properties and feasibility as a force-reflecting manual controller application of the device.

7–1 A 9-string force-reflecting 6-dof manual controller

A 9-string force-reflecting 6-dof manual controller is shown in Figure 7–2. The system utilizes the similar geometry of the unilateral 9-string 6-dof manual controller developed by Tesar et al. at the University of Florida[64].

The design of the 9-string force-reflecting 6-dof manual controller provides the desired force-reflection by employing nine actuators to control nine string tensions. Three constant-pressure air cylinders provide constant compression forces which the strings are unable to supply. The actual 9-string force-reflecting 6-dof manual controller system is interfaced to a the Cincinnati Milacron T^3-726 Industrial Robot via the μVAX II system as shown in Figure 7–3 and 7–4. Various system operation modes[1], including force-reflection, scaling, filtering, resolved rate control, resolved position control, etc. have been successfully demonstrated at the University of Texas at Austin[63].

The dominant features and limitations of the 9-string force-reflecting 6-dof manual controller are summarized below. The advantages are:

- 0-10 lb forces and 0-40 $in-lb$ torques can be reflected within the dextrous workspace which is defined by a 10 inch diameter of sphere. The larger workspace of the manual controller, an 18 inch diameter of sphere, can be defined with lower reflecting force capacity.

- The kinematic analysis requirements(computational burden) is reduced due to the use of redundant position transducers (motion of each string is measured by a potentiomenter).

- Due to the use of redundant actuators, nine actuators and three constant-pressure air cylinders to control 6-dof reflecting forces, both the magnitude of the reflecting-force and the size of the dextrous workspace are increased.

- The workspace does not contain singularities.

[1]see chapter 3 for general background on the teleoperator system

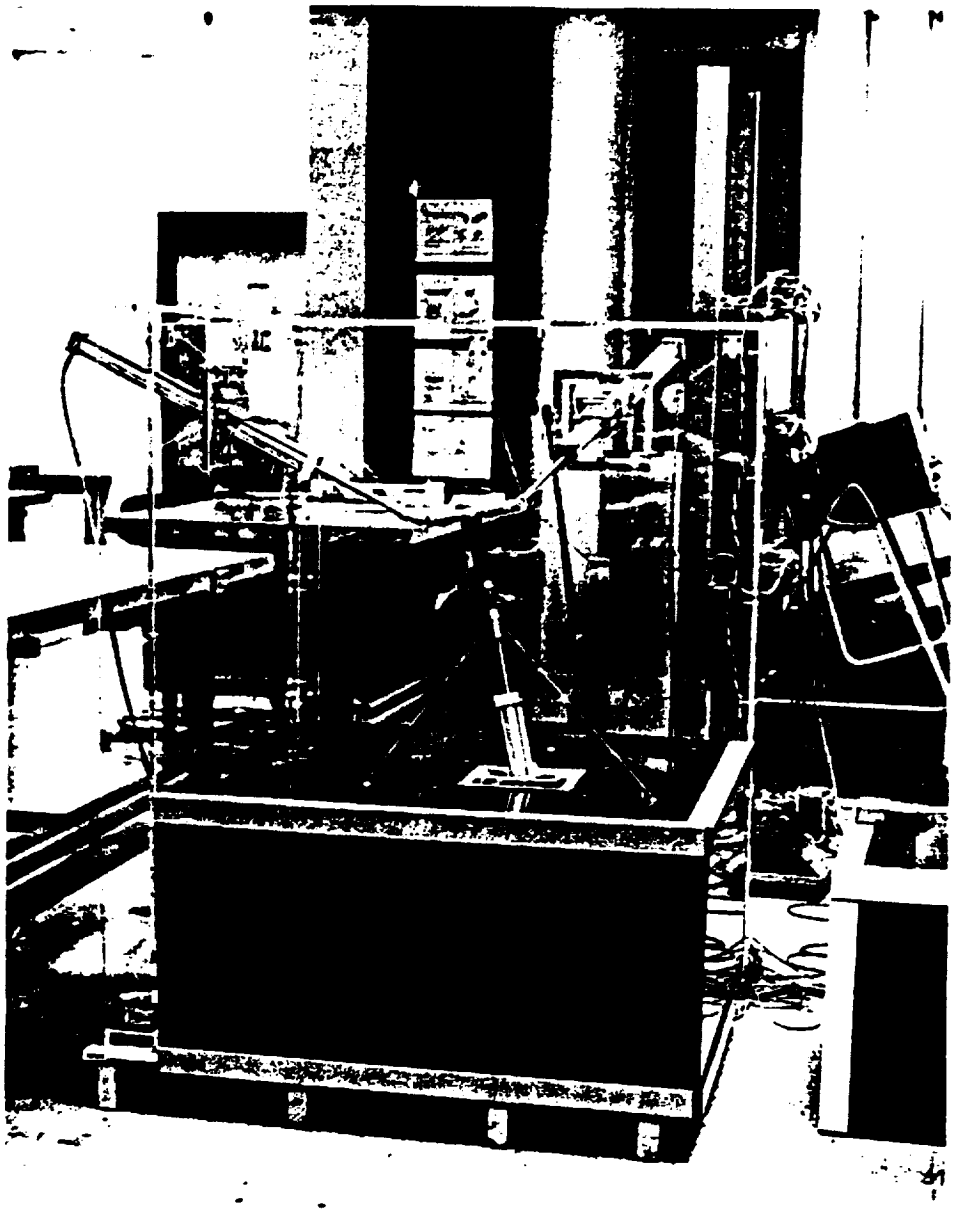

Figure 7–2 A 9-STRING FORCE-REFLECTING MANUAL CONTROLLER

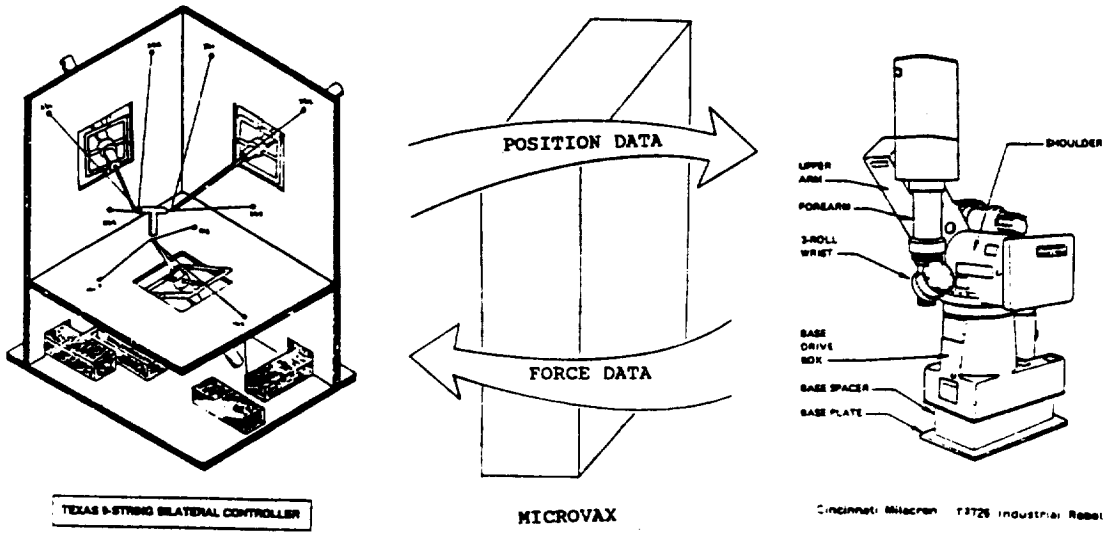

Figure 7–3 SCHEMATIC OF THE INFORMATION FLOW BETWEEN THE 9-STRING FORCE-REFLECTING MENUAL CONTROLLER AND T^3-726 CINCINNATI MILACRON INDUSTRIAL ROBOT

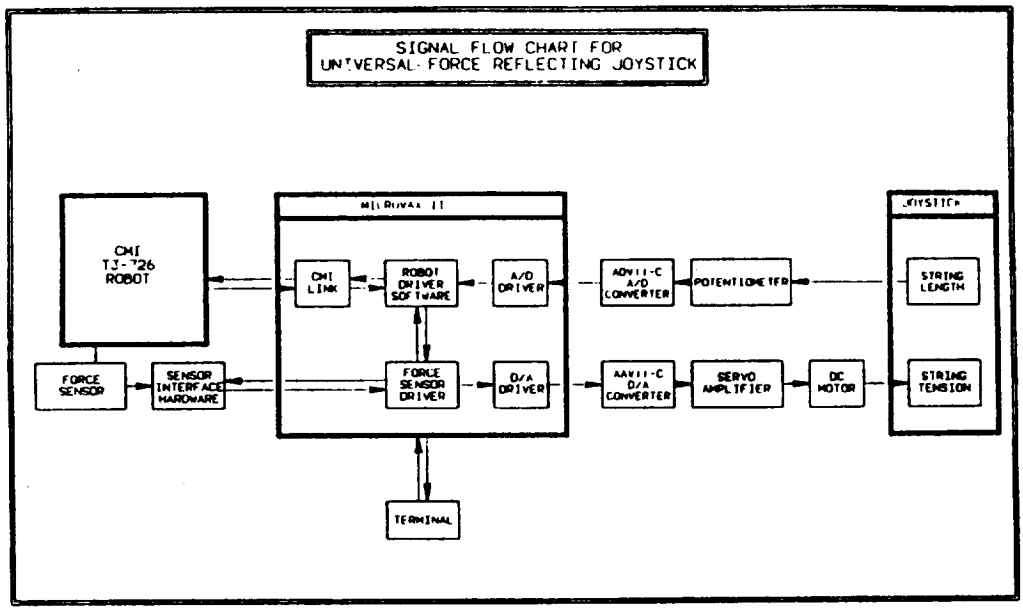

Figure 7–4 SIGNAL FLOW CHART FOR UNIVERSAL FORCE-REFLECTING MANUAL CONTROLLER

- All nine of the actuators are located on the fixed base plate, reducing most of the effective inertia and gravitational effects. Cables are used to transmit the reflecting forces, making the system virtually massless.

The limitations are:

- The volume of the manual controller is rather bulky.
- Due to the use of the cables, the system is not mechanically stiff.
- Due to the use of the pneumatic and prismatic cylinders, the system has lower bandwidth, and friction from the pneumatic cylinders is significant.

7–2 Conceptual design of a 6-dof manual controller

The parallel geometry of the 9-string manual controller exhibits various beneficial features as a force-reflecting manual controller. However, most of advantages of the parallel structure are not effectively used. For example, it is not mechanically stiff and the size is bulky. Conceptual designs of force-reflecting manual controllers, which use parallel geometry and exhibit desirable design features such as compactness, portability, etc., are now introduced.

Based on the Stewart 6-dof system configuration, various parallel force-reflecting 6-dof manual controllers may be conceptualized; for example, SPS, $\widehat{RR}PS$, and $\widehat{RR}RS$, which represent kinematic configurations of each subchain of a parallel system. In this study, configurations using the ball and socket joints on the top plate are considered for the sake of the simplicity. Because it is not easy to find a compact, efficient backdrivable linear actuator with an electric drive, configurations using prismatic joints are not considered.

Two configurations, which have basically the $\widehat{RR}RS$ and $RRRS$ configurations, may be conceptualized. A 6-dof parallel system with 3 legs and with 6 legs are shown in Figures 7–5 and 7–6. A 6-dof parallel system with 6 legs may require considerable computational effort. Mechanical interferences among six legs may also reduce the size of the workspace considerably. However, a 6-dof parallel system with 3 legs can use the conceptual hybrid (or parallel) system introduced in the previous chapter as a 2-dof gimbal module at the base. The resulting system allows all six actuators, which are required to provide 6-dof reflecting forces, to be located at the base. Thus the properties of the system which are best suited for a force-reflecting manual controller application are maintained.

7–2.1 Mobility analysis

The simplified schematic of the 6-dof system is shown in Figure 7–7. In the figure, each 2-dof parallel system module is represented as its equivalent serial representation, that is, RR. Now, using the general mobility criterion given in equation (4-1.1), the mobility of the 6-dof system is

$$M = m(n-1) - \sum_{i=1}^{g} u_i = 6 \times 7 - (3 \times 3 + 5 \times 3 + 4 \times 3) = 6. \qquad (7\text{–}2.1)$$

7–2.2 Description of the 6-dof bilateral parallel manual controller with 3 legs

The 6-dof manual controller in Figure 7–5 has three legs which connect the base and the top plates in parallel. Each leg consists of two parallel actuated joints($\widehat{RR}$) at the base, one passive revolute joint(R) in the middle of the leg,

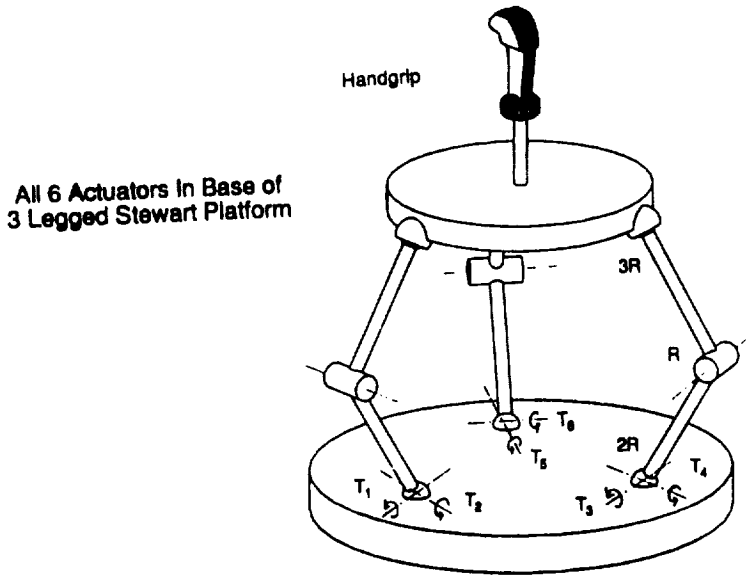

Figure 7–5 A CONCEPTUAL 6-DOF 3-LEGGED STEWART PLATFORM

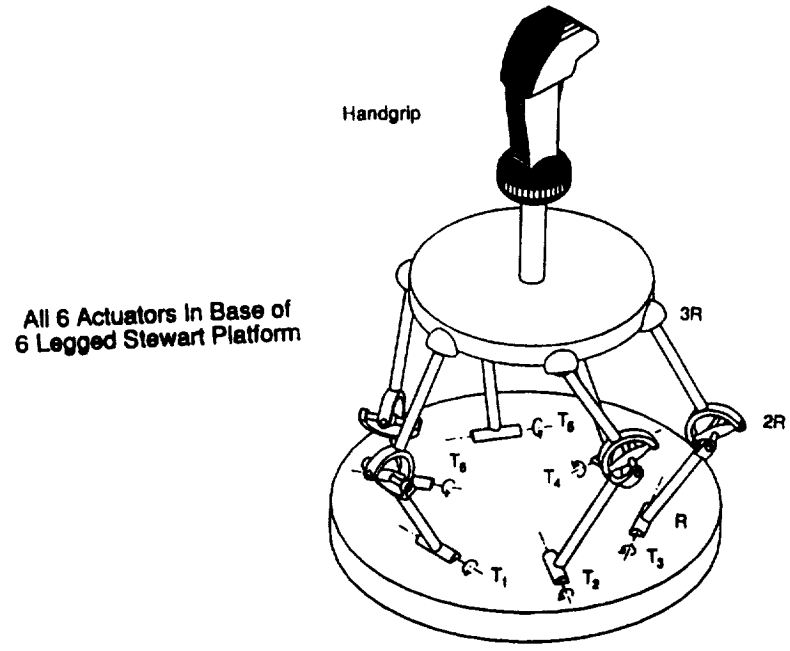

Figure 7–6 A CONCEPTUAL 6-DOF 6-LEGGED STEWART PLATFORM

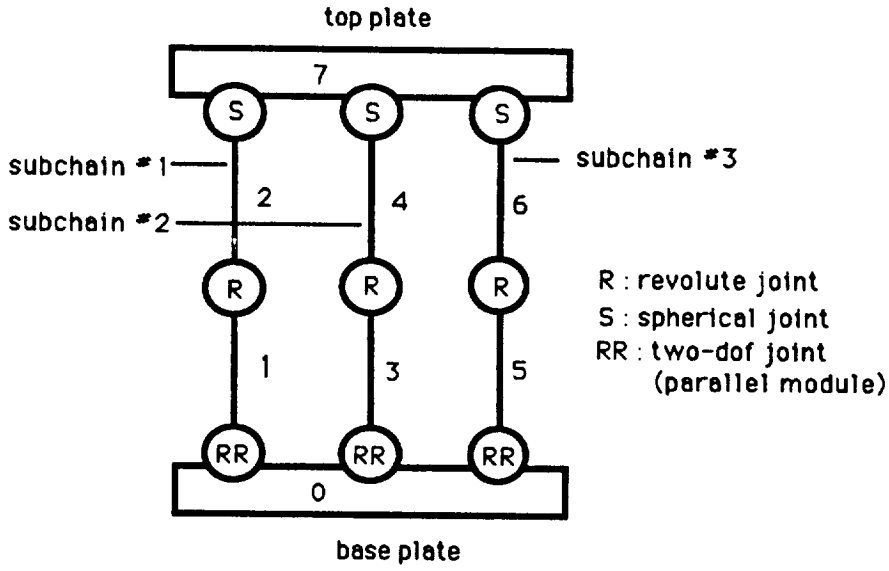

Figure 7–7 SCHEMATICS OF A CONCEPTUAL 6-DOF SYSTEM

and a passive ball and socket joint(S) at the top plate. The three 2-dof actuated joints at the base (6 actuators in total) provide 6-dof forces to the top plate. Note that this geometry is similar to the 6-dof 9-string force-reflecting manual controller. However, by not using bulky pneumatic cylinders and wires to actuate the manual controller, the three-legged controller provides greater compactness and higher overall stiffness with less friction than the 9-string manual controller. Also, because all six actuators are mounted on the base plate, the effects of the effective inertia and gravitational force are minimized.

7–2.3 Coordinate systems and transformation

For simplicity and without loss of generality, let the locations of the ball and socket joints on the top plate be distributed symmetrically as shown in Figure 7–8. The three radii are located in 120° increments on the plate (that is, $\gamma_{t1} = 0°$, $\gamma_{t2} = 120°$, and $\gamma_{t3} = 240°$). The locations of the actuated joints

on the base plate are arranged in a similar fashion, $\gamma_{b1} = 0$, $\gamma_{b2} = 120°$, and $\gamma_{b3} = 240°$.

The origin of the moving coordinate system ($\boldsymbol{x}_t\ \boldsymbol{y}_t\ \boldsymbol{z}_t$) fixed on the top plate is defined at the center of the top plate and the axis perpendicular to the top plate is defined as the local coordinate axis $\boldsymbol{z}_t$. The reference coordinate system ($\boldsymbol{x}_b\ \boldsymbol{y}_b\ \boldsymbol{z}_b$) fixed on the base plate is defined similarly as shown in Figure 7–8.

r and R represent the radii of the base and top plates from the origin of the moving coordinate system to the center of the ball and socket joints, and from the origin of the reference (or global) coorinate system to the common intersection point of the hybrid 2-dof gimbal module, respectively. The symbols l_1^m and l_2^m represent the lengths of the upper link and the lower link, respectively. The joint variables of the parallel 2-dof gimbal module are denoted by ϕ_{1h}^m and ϕ_{2h}^m. The joint displacement of the middle joint between the lower link and the upper link is denoted by ϕ_3^m. With this notation, the superscript denotes the subchain and the subscript denotes the joint.

Also $\boldsymbol{R}_t$ and $[R_b^t]$ denote the global position vector to the origin of the moving coordinate system from the origin of the global frame and transformation matrix of the moving coordinate system with respect to the reference coordinate system, respectively. The symbols θ_x, θ_y, and θ_z represent Euler angles equivalent to $[R_b^t]$. That is, $[R_b^t]$= $[Rot(x,\theta_x)][Rot(y,\theta_y)]$ $[Rot(z,\theta_z)]$. Also, $\boldsymbol{r}_{ctm}^{(t)}$ and $\boldsymbol{r}_{ctm}$ denote the position vectors from the origin of the moving coordinate system to the three contact positions, represented in the moving coordinate frame and in the global frame (in this case, in the base frame), respectively. $\boldsymbol{R}_{bm}$ denotes the global position vector to the common intersection point of the parallel 2-dof system from the origin of the global frame.

For simplicity in the following analysis, it is assumed that the control point coincides with the origin of the moving coordinate system. Also, intermediate variables, ϕ_1^m and ϕ_2^m, are introduced to simplify the kinematic analysis where ϕ_1^m and ϕ_2^m represent joint angles for the serial 2-dof system equivalent to the hybrid 2-dof gimbal module. Select intermediate variables such that $\phi_1^m = \phi_{1h}^m$ as in the previous analysis of Chapter 6.

Initially, the kinematic analysis is performed with respect to the new set of joint variables, $\phi^m = (\phi_1^m \ \phi_2^m \ \phi_3^m)^T$. Then, using constraint equations given in equations (6-1.13) and (6-1.14), the desired kinematic analysis with respect to the actual parallel joint variables, $\phi^m = (\phi_1^m \ \phi_{2h}^m \ \phi_3^m)^T$, is obtained.

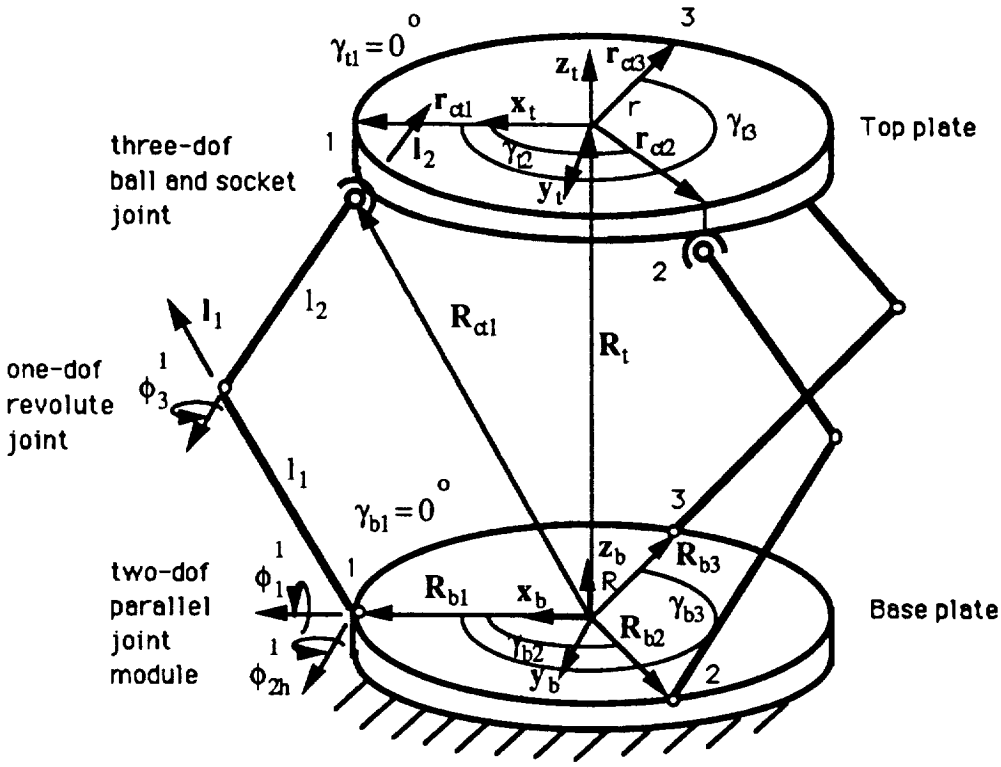

Figure 7–8 KINEMATIC REPRESENTATION OF A CONCEPTUAL 6-DOF SYSTEM

7–2.4 Reverse position analysis

For reverse position analysis, the output position and orientation of the system is known and the joint angles (ϕ_{1h}^m, ϕ_{2h}^m, and ϕ_3^m) are unknown. Noting $\boldsymbol{r}_{ctm}^{(t)}$'s and $\boldsymbol{R}_{bm}$'s are fixed constants and may be written as

$$\boldsymbol{r}_{ct1}^{(t)} = (r,\ 0,\ 0), \tag{7–2.2}$$

$$\boldsymbol{r}_{ct2}^{(t)} = (r\cos\gamma_{t2},\ r\sin\gamma_{t2},\ 0), \tag{7–2.3}$$

$$\boldsymbol{r}_{ct3}^{(t)} = (r\cos\gamma_{t3},\ r\sin\gamma_{t3},\ 0) \tag{7–2.4}$$

and

$$\boldsymbol{R}_{b1} = (R,\ 0,\ 0), \tag{7–2.5}$$

$$\boldsymbol{R}_{b2} = (R\cos\gamma_{b2},\ R\sin\gamma_{b2},\ 0), \tag{7–2.6}$$

$$\boldsymbol{R}_{b3} = (R\cos\gamma_{b3},\ R\sin\gamma_{b3},\ 0). \tag{7–2.7}$$

The global position vectors to the center of the ball and socket joint on the top plate from the origin of the global frame, $\boldsymbol{R}_{ctm}$, can be represented with respect to the moving coordinate system

$$\boldsymbol{R}_{ctm} = \boldsymbol{R}_t + [R_b^t]\boldsymbol{r}_{ctm}^{(t)} = \boldsymbol{R}_t + \boldsymbol{r}_{ctm} \ for\ m = 1,2,3, \tag{7–2.8}$$

where

$$\boldsymbol{r}_{ctm} = [R_b^t]\boldsymbol{r}_{ctm}^{(t)} \ for\ m = 1,2,3. \tag{7–2.9}$$

Also

$$\boldsymbol{R}_{ctm} = \boldsymbol{R}_{bm} + l_1\boldsymbol{l}_1^m + l_2\boldsymbol{l}_2^m,\ for\ m = 1,2,3. \tag{7–2.10}$$

Equating equations (7–2.8) and (7–2.10) results in

$$\boldsymbol{R}_{ctm} = \boldsymbol{R}_t + \boldsymbol{r}_{ctm} = \boldsymbol{R}_{bm} + l_1\boldsymbol{l}_1^m + l_2\boldsymbol{l}_2^m \ for\ m = 1,2,3. \tag{7–2.11}$$

The local unit vectors, $\boldsymbol{l}_1^m$ and $\boldsymbol{l}_2^m$ for $m = 1, 2, 3$ as shown in Figure 7–8 may be found as follows;

$$\begin{aligned} \boldsymbol{l}_1^m &= [Rot(z, \gamma_{bm})][Rot(x, \phi_1^m)][Rot(y, \phi_2^m)] \begin{Bmatrix} 0 \\ 0 \\ 1 \end{Bmatrix} \\ &= \begin{Bmatrix} c\gamma_{bm} s\phi_2^m + s\gamma_{bm} s\phi_1^m c\phi_2^m \\ s\gamma_{bm} s\phi_2^m - c\gamma_{bm} s\phi_1^m c\phi_2^m \\ c\phi_1^m c\phi_2^m \end{Bmatrix}, \end{aligned} \tag{7–2.12}$$

and

$$\boldsymbol{l}_2^m = [Rot(z, \gamma_{bm})][Rot(x, \phi_1^m)][Rot(y, \phi_2^m)][Rot(y, \phi_3^m)] \begin{Bmatrix} 1 \\ 0 \\ 0 \end{Bmatrix} \tag{7–2.13}$$

where ϕ_3^m represents the angular displacements about the local $\boldsymbol{y}$ axis from the lower link to the upper link in clockwise sense plus 90°. For convenience, define

$$\phi_{23}^m \equiv \phi_2^m + \phi_3^m \tag{7–2.14}$$

Apply this to equation (7–2.13) to find

$$\boldsymbol{l}_2^m = \begin{Bmatrix} c\gamma_{bm} c\phi_{23}^m - s\gamma_{bm} s\phi_1^m s\phi_{23}^m \\ s\gamma_{bm} c\phi_{23}^m + c\gamma_{bm} s\phi_1^m s\phi_{23}^m \\ -c\phi_1^m s\phi_{23}^m \end{Bmatrix}. \tag{7–2.15}$$

For convenience, the index representing subchain identification will be omitted unless further clarification is necessary. Substituting equations (7–2.8-7–2.10) and (7–2.12-7–2.14) into the equation (7–2.11) yields

$$R_{ctx} - R_{bx} = l_1(c\gamma_b s\phi_2 + s\gamma_b s\phi_1 c\phi_2) + l_2(c\gamma_b c\phi_{23} - s\gamma_b s\phi_1 s\phi_{23}) \tag{7–2.16}$$

$$R_{cty} - R_{by} = l_1(s\gamma_b s\phi_2 - c\gamma_b s\phi_1 c\phi_2) + l_2(s\gamma_b c\phi_{23} + c\gamma_b s\phi_1 s\phi_{23}) \tag{7–2.17}$$

$$R_{ctz} - R_{bz} = l_1 c\phi_1 c\phi_2 - l_2 c\phi_1 s\phi_{23}. \tag{7–2.18}$$

Multiplying $s\gamma_b$ to equation (7–2.16) and $-c\gamma_b$ to equation (7–2.17) and adding the results gives

$$s\phi_1(l_1c\phi_2 - l_2s\phi_{23}) = (R_{ctx} - R_{bx})s\gamma_b - (R_{cty} - R_{by})c\gamma_b. \tag{7–2.19}$$

Dividing equation (7–2.18) by (7–2.19) yields

$$\tan\phi_1 = \frac{(R_{ctx} - R_{bx})s\gamma_b - (R_{cty} - R_{by})c\gamma_b}{R_{ctz} - R_{bz}} \tag{7–2.20}$$

or

$$\phi_1 = \arctan\frac{(R_{ctx} - R_{bx})s\gamma_b - (R_{cty} - R_{by})c\gamma_b}{R_{ctz} - R_{bz}}. \tag{7–2.21}$$

After multipling $c\gamma_b$ to equation (7–2.16) and $s\gamma_b$ to equation (7–2.17), adding the results, and manipulating gives

$$l_2c\phi_{23} = -l_1s\phi_2 + (R_{ctx} - R_{bx})c\gamma_b + (R_{cty} - R_{by})s\gamma_b. \tag{7–2.22}$$

Rearrange the equation (7–2.18)

$$l_2s\phi_{23} = l_1c\phi_2 - \frac{(R_{ctz} - R_{bz})}{\cos\phi_1}. \tag{7–2.23}$$

Squaring equations (7–2.22) and (7–2.23) and adding the results yields

$$As\phi_2 + Bc\phi_2 = C \tag{7–2.24}$$

where

$$A = (R_{ctx} - R_{bx})c\gamma_b + (R_{cty} - R_{by})s\gamma_b, \tag{7–2.25}$$

$$B = \frac{(R_{ctz} - R_{bz})}{\cos\phi_1}, \tag{7–2.26}$$

and

$$C = \frac{A^2 + B^2 + (l_1)^2 - (l_2)^2}{2l_1}. \tag{7–2.27}$$

By substituting the tan-half angle representations, that is,

$$t = \tan\frac{\phi_2}{2},\ s\phi_2 = \frac{2t}{1+t^2},\ c\phi_2 = \frac{1-t^2}{1+t^2}, \tag{7-2.28}$$

into the equation (7-2.24), the tan-half angle is obtained

$$t = \frac{A \pm \sqrt{A^2 + B^2 - C^2}}{C + B} \tag{7-2.29}$$

or

$$\phi_2 = 2\arctan(t). \tag{7-2.30}$$

Two solutions in equation 7-2.29 represent two different closures of the subchain shown in Figure 7-9. The joint angle ϕ_3 can be obtained by substituting values of ϕ_2 into equation (7-2.18) as follows

$$s\phi_{23} = \frac{R_{ctz} - R_{bz} - l_1 c\phi_1 c\phi_2}{-l_2 c\phi_1}. \tag{7-2.31}$$

Using equation (7-2.14) and (7-2.31),

$$\phi_3 = \arcsin\frac{R_{ctz} - R_{bz} - l_1 c\phi_1 c\phi_2}{-l_2 c\phi_1} - \phi_2. \tag{7-2.32}$$

Once the desired joint angles, ϕ_j^m for $m, j = 1, 2, 3$, are obtained, the hybrid actuated joint angle, ϕ_{2h},can be found from equation (6-1.15).

7-2.5 Forward position analysis

From the geometry, the following two loop equations (6 independent equations) with six unknowns can be obtained

$$\boldsymbol{R}_{ct2} - \boldsymbol{R}_{ct1} = [R_b^t](\boldsymbol{r}_{ct2}^{(t)} - \boldsymbol{r}_{ct1}^{(t)}) \tag{7-2.33}$$

and

$$\boldsymbol{R}^{ct3} - \boldsymbol{R}^{ct1} = [R_b^t](\boldsymbol{r}_{ct3}^{(t)} - \boldsymbol{r}_{ct1}^{(t)}). \tag{7-2.34}$$

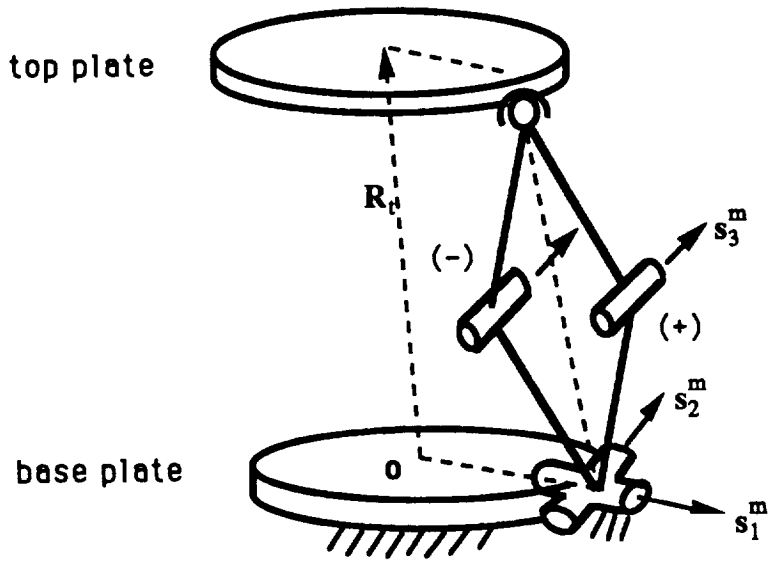

Figure 7–9 TWO DIFFERENT CLOSURE OF A SERIAL SUBCHAIN OF A CONCEPTUAL 6-DOF SYSTEM

The LHS of the above equations is represented by ϕ_3^m for $m = 1, 2, 3$, when ϕ_1^m and ϕ_{2h}^m for $m = 1, 2, 3$ are known. And the RHS is represented by the desired Euler angles θ_m for $m = 1, 2, 3$. To solve these equations simultaneously to find the desired Euler angles, iterative numerical solutions may be required which is not desirable due to the increased computation burden. Therefore, it is assumed that the joint angles, ϕ_1^m, ϕ_{2h}^m, and ϕ_3^m for $m = 1, 2, 3$, are measured to simplify the forward position analysis.

Using equation (6-1.14), the equivalent serial joint angles, ϕ_2^m, can be obtained directly. Then using equation (7–2.10), (7–2.12), and (7–2.15), the position vectors of contact points on the top plate, $\boldsymbol{R}_{ctm}$, for $m = 1, 2, 3$, can be obtained. Since the control point is located at the center of the equilateral triangle formed by three ball and socket joints, the control point position vector,

$\boldsymbol{R}_t$, can be found by

$$\boldsymbol{R}_t = \frac{1}{3}(\boldsymbol{R}_{ct1} + \boldsymbol{R}_{ct2} + \boldsymbol{R}_{ct3}) \tag{7-2.35}$$

and the direction cosine of the output transformation, $[R_b^t] = [\boldsymbol{x}\ \boldsymbol{y}\ \boldsymbol{z}]$, can be obtained as follows;

$$\boldsymbol{x} = \frac{\boldsymbol{R}_{ct1} - \boldsymbol{R}_t}{|\boldsymbol{R}_{ct1} - \boldsymbol{R}_t|} \tag{7-2.36}$$

$$\boldsymbol{y} = \frac{\boldsymbol{R}_{ct2} - \boldsymbol{R}_{ct3}}{|\boldsymbol{R}_{ct2} - \boldsymbol{R}_{ct3}|} \tag{7-2.37}$$

$$\boldsymbol{z} = \boldsymbol{x} \times \boldsymbol{y} \tag{7-2.38}$$

7–2.6 First order KIC derivation

Let $\boldsymbol{u}$ denote the universal output displacement vector,

$$\boldsymbol{u} = (x_t\ y_t\ z_t\ \theta_x\ \theta_y\ \theta_z)^T. \tag{7-2.39}$$

To simplify the analysis, the intermediate variables, $\boldsymbol{c}$, representing three ball and socket joint variables are defined as below;

$$\boldsymbol{c} \equiv (\boldsymbol{c}_1\ \boldsymbol{c}_2\ \boldsymbol{c}_3)^T \equiv (x_{ct1}\ y_{ct1}\ z_{ct1}\ x_{ct2}\ y_{ct2}\ z_{ct2}\ x_{ct3}\ y_{ct3}\ z_{ct3})^T. \tag{7-2.40}$$

By differentiating equation (7-2.8) with respect to time, the following relations can be obtained;

$$\dot{\boldsymbol{c}}_m = \dot{\boldsymbol{R}}_t + \frac{d}{dt}([R_b^t]\boldsymbol{r}_{ctm}^{(t)}) = \dot{\boldsymbol{R}}_t + \frac{d}{dt}(\boldsymbol{r}_{ctm})\ for\ m = 1,2,3 \tag{7-2.41}$$

where

$$\dot{\boldsymbol{c}}_m = (\dot{x}_{ctm}\ \dot{y}_{ctm}\ \dot{z}_{ctm})^T. \tag{7-2.42}$$

And it can be rewritten as

$$\dot{\boldsymbol{c}}_m = \dot{\boldsymbol{R}}_t + \omega \times \boldsymbol{r}_{ctm}\ for\ m = 1,2,3, \tag{7-2.43}$$

where $\boldsymbol{\omega}$ represents the absolute angular velocity of the top plate (or moving frame)

$$\boldsymbol{\omega} = (\omega_x \ \omega_y \ \omega_z)^T \tag{7-2.44}$$

and

$$\boldsymbol{R}_t = (\dot{x}_t \ \dot{y}_t \ \dot{z}_t)^T. \tag{7-2.45}$$

Again, the equation (7-2.43) can be written as follows

$$\dot{\boldsymbol{c}} = [G_u^c]\dot{\boldsymbol{u}} \tag{7-2.46}$$

where

$$[G_u^c] = \begin{bmatrix} \{{}^1G_u^c\} \\ \{{}^2G_u^c\} \\ \{{}^3G_u^c\} \end{bmatrix} \tag{7-2.47}$$

and

$$[{}^mG_u^c] = \begin{bmatrix} 1 & 0 & 0 & 0 & r_{ctmz} & -r_{ctmy} \\ 0 & 1 & 0 & -r_{ctmz} & 0 & r_{ctmx} \\ 0 & 0 & 1 & r_{ctmy} & -r_{ctmx} & 0 \end{bmatrix} \ for\ m = 1,2,3. \tag{7-2.48}$$

In the above equation, $\dot{\boldsymbol{u}}$ represents

$$\dot{\boldsymbol{u}} \equiv (\dot{x}_t \ \dot{y}_t \ \dot{z}_t \ \omega_x \ \omega_y \ \omega_z)^T \tag{7-2.49}$$

and the components of $\boldsymbol{r}_{ctm}$ as below is substituted into the equation,

$$\boldsymbol{r}_{ctm} = (r_{ctmx} \ r_{ctmy} \ r_{ctmz})^T. \tag{7-2.50}$$

Now, to find the differential relations between joint rate variables and intermediate variables, we differentiate equation (7-2.10) with respect time for each subchain to find

$$\dot{\boldsymbol{c}_m} = [{}^mG_\phi^c]\dot{\boldsymbol{\phi}}^m \ for\ m = 1,2,3. \tag{7-2.51}$$

where

$$\dot{\phi}^m = (\dot{\phi}_1^m \ \dot{\phi}_2^m \ \dot{\phi}_3^m)^T, \tag{7-2.52}$$

and

$$[G_\phi^c]_{1;1} = l_1 s\gamma_b c\phi_1 c\phi_2 - l_2 s\gamma_b c\phi_1 s\phi_{23} \tag{7-2.53}$$

$$[G_\phi^c]_{1;2} = l_1(c\gamma_b c\phi_2 - s\gamma_b s\phi_1 s\phi_2) - l_2(c\gamma_b s\phi_{23} + s\gamma_b s\phi_1 c\phi_{23}) \tag{7-2.54}$$

$$[G_\phi^c]_{1;3} = -l_2(c\gamma_b s\phi_{23} + s\gamma_1 s\phi_1 c\phi_{23}) \tag{7-2.55}$$

$$[G_\phi^c]_{2;1} = -l_1 c\gamma_b c\phi_1 c\phi_2 + l_2 c\gamma_b c\phi_1 s\phi_{23} \tag{7-2.56}$$

$$[G_\phi^c]_{2;2} = l_1(s\gamma_b c\phi_2 + c\gamma_b s\phi_1 s\phi_2) - l_2(s\gamma_b s\phi_{23} - c\gamma_b s\phi_1 c\phi_{23}) \tag{7-2.57}$$

$$[G_\phi^c]_{2;3} = -l_2(s\gamma_b s\phi_{23} - c\gamma_1 s\phi_1 c\phi_{23}) \tag{7-2.58}$$

$$[G_\phi^c]_{3;1} = -l_1 s\phi_1 c\phi_2 + l_2 s\phi_1 s\phi_{23} \tag{7-2.59}$$

$$[G_\phi^c]_{3;2} = -l_1 c\phi_1 s\phi_2 - l_2 c\phi_1 c\phi_{23} \tag{7-2.60}$$

$$[G_\phi^c]_{3;3} = -l_2 c\phi_1 c\phi_{23} \tag{7-2.61}$$

Note that in the above equation, the superscript, m, is omitted for convenience.

To find the first-order KIC between hybrid input variables, ϕ_h^m=(ϕ_1^m ϕ_{2h}^m ϕ_3^m)^T, and intermediate variables, c_m, for each subchain, as in

$$\dot{c}_m = [{}^mG_{\phi_h}^c]\dot{\phi}_h^m, \tag{7-2.62}$$

differentiate the equation (6-1.13) with respect to time to find

$$\dot{\phi}_2 = -\cos^2\phi_2 \ \tan\phi_{2h} \ \sin\phi_1 \ \dot{\phi}_1 + \frac{\cos\phi_1 \ \cos^2\phi_2}{\cos^2\phi_{2h}}\dot{\phi}_{2h}. \tag{7-2.63}$$

Substituting this result into equation (7–2.51) yields the desired $[{}^mG_{\phi_h}^c]$. Assuming that $[{}^mG_{\phi_h}^c]$ is not singular, take the inverse of $[{}^mG_{\phi_h}^c]$ in (7–2.62) to obtain

$$\dot{\phi}_h^m = [{}^mG_c^{\phi_h}]\dot{c}_m \ for \ m = 1,2,3. \tag{7-2.64}$$

Combining the three equations obtained from each subchain and noting equation (7-2.40) we have

$$\dot{\phi}_h = (\dot{\phi}_h^1 \ \dot{\phi}_h^2 \ \dot{\phi}_h^3)^T = [G_c^{\phi_h}]\dot{c} \tag{7–2.65}$$

$$[G_c^{\phi_h}] = \begin{bmatrix} [^1G_c^{\phi_h}] & 0 & 0 \\ 0 & [^2G_c^{\phi_h}] & 0 \\ 0 & 0 & [^3G_c^{\phi_h}] \end{bmatrix} \tag{7–2.66}$$

From this equation, by selecting corresponding rows to actuated joints (i.e., ϕ_a=(ϕ_1^1 ϕ_{2h}^1 ϕ_1^2 ϕ_{2h}^2 ϕ_1^3 ϕ_{2h}^3)^T), the following equations can be obtained,

$$\dot{\phi}_a = [G_c^{\phi_a}]\dot{c}. \tag{7–2.67}$$

Substituting equation (7–2.46) into this equation yields

$$\dot{\phi}_a = [G_c^{\phi_a}]\dot{c} = [G_c^{\phi_a}][G_u^c]\dot{u} = [G_u^{\phi_a}]\dot{u}. \tag{7–2.68}$$

Finally, for nonsingular $[G_u^{\phi_a}]$, the desired first order KIC can be found as in

$$\dot{u} = [G_{\phi_a}^u]\dot{\phi}_a \tag{7–2.69}$$

where

$$[G_{\phi_a}^u] = [G_u^{\phi_a}]^{-1}. \tag{7–2.70}$$

7–2.7 Kinematic properties and workspace determination

This section investgates the first-order KIC of a conceptual 6-dof mechanism. The geometrical properties of the system are studied. To examine the geometric properties, the ratio of maximum-to-minimum singular values of the first-order KIC, $\frac{\sigma_{max}}{\sigma_{min}}([G_{\phi_a}^u])$, can be used as in Chapter 6. However, unlike the pure rotational system or the pure translational system, the general special motion involves both the translational and the rotational motions. The differential

equations in (7–2.69) can be rewritten as

$$\left\{ \begin{array}{c} \boldsymbol{v} \\ \boldsymbol{\omega} \end{array} \right\} = \left[\begin{array}{c} G_p \\ G_{jk} \end{array} \right] \dot{\boldsymbol{\phi}}_a. \tag{7–2.71}$$

When the translational motion and the rotational motion are investigated separately as below, the result does not represent general 6-dof motion characteristics. That is, singular values of the decoupled translational and rotational motion satisfy the following conditions,

$$\sigma_i(\left[\begin{array}{c} G_p^u \\ 0 \end{array} \right]),\ \sigma_i(\left[\begin{array}{c} 0 \\ G_{jk}^u \end{array} \right]) \leq \max \sigma([G_{\phi_a}^u])\ for\ i = 1, 2, \ldots 6 \tag{7–2.72}$$

since

$$\|[G_{\phi_a}^u]\| = max \frac{\sqrt{\boldsymbol{v}^T \boldsymbol{v} + \boldsymbol{\omega}^T \boldsymbol{\omega}}}{\|\dot{\phi}_a\|} \tag{7–2.73}$$

$$\|[G_p^u\| = max \frac{\sqrt{\boldsymbol{v}^T \boldsymbol{v}}}{\|\dot{\phi}_a\|} \tag{7–2.74}$$

$$\|[G_{jk}^u]\| = max \frac{\sqrt{\boldsymbol{\omega}^T \boldsymbol{\omega}}}{\|\dot{\phi}_a\|} \tag{7–2.75}$$

where

$$\left\{ \begin{array}{c} \boldsymbol{v} \\ \boldsymbol{\omega} \end{array} \right\} = \left[\begin{array}{c} G_p \\ 0 \end{array} \right] \dot{\boldsymbol{\phi}}_a \tag{7–2.76}$$

and

$$\left\{ \begin{array}{c} \boldsymbol{v} \\ \boldsymbol{\omega} \end{array} \right\} = \left[\begin{array}{c} 0 \\ G_{jk} \end{array} \right] \dot{\boldsymbol{\phi}}_a. \tag{7–2.77}$$

In order to treat the translation and the rotation simultaneously, the ratio of the nominal value of the translational velocity to the nominal value of the rotational velocity (v_o/ω_o) are introduced into the equation (7–2.71) to obtain

$$\left\{ \begin{array}{c} \boldsymbol{v} \\ \boldsymbol{\omega}^* \end{array} \right\} = \left[\begin{array}{c} G_p \\ \frac{v_o}{\omega_o} G_{jk} \end{array} \right] \dot{\boldsymbol{\phi}}_a \tag{7–2.78}$$

where

$$\omega^* = \frac{v_o}{\omega_o}\omega. \tag{7-2.79}$$

This equation implies that when the condition number of the normalized matrix becomes 1, the ratio of the output translational velocity to the output angular velocity becomes v_o/ω_o, with any given input joint velocity bound.

Now, consider the KIC in terms of the torque transmission characteristics. The relations representing the input and the output torque can be written as

$$\tau = [G^u_{\phi_a}]^T f \tag{7-2.80}$$

or

$$\tau = [G_p^T \; G_{jk}^T] \begin{Bmatrix} f_u \\ \tau_u \end{Bmatrix}. \tag{7-2.81}$$

Normalize the above KIC with respect to the desired output ratios of the force and the torque (f_{uo}/τ_{uo}). Then, the KIC can be rewritten as

$$\tau = [G_p^T \; \frac{\tau_{uo}}{f_{uo}} G_{jk}^T] \begin{Bmatrix} f_u \\ \tau_u^* \end{Bmatrix} \tag{7-2.82}$$

where

$$\tau_u^* = \frac{f_{uo}}{\tau_{uo}}\tau_u. \tag{7-2.83}$$

Again, when the normalized KIC has the condition number close to 1, the desired ratio of the output force and the output torque can be achieved. It can be noted from equations (7–2.78) and (7–2.82) that the dual relation between velocity and torque exists. Depending on the application requirements, the desired velocity ratios (v_o/ω_o) or the desired torque ratio ratio (f_{uo}/τ_{uo}) can be selected accordingly.

For the design of the force-reflecting manual controller, once the ratio of nominal values for the translational and rotational velocities can be selected

based on the desired output of the translation and rotation, the optimal system parameters can be searched which make the condition number of the normalized KIC close to 1.[2] When the ratio of the torque (f_{uo}/τ_{uo}) is based on the desired force-reflecting capability, the required actuator torques could be minimized.[3]

By investigating ratios of maximum-to-minimum singular values of the above normalized first-order KIC, the workspace of the system, which has desirable velocity or torque transmission characteristics, can be searched and determined. This process is a very involved due to the large number of the system parameters: that is, geometric parameters (such as the link lengths, radii R and r) and the components of the six dimensional motion variables (i.e., $\boldsymbol{u}$). For the system with normalized system parameters (i.e., $l_n^m = 1$, $R = 1$, $r = 1$, for $m = 1,2,3$, $n = 1,2$) and with the fixed output orientation of the top plate, the contour plots and surface plots (3-dimensional) are shown in Figures 7–10 and 7–11, and Figures 7–12 and 7–13. The Figures 7–10 and 7–11 represent the $y - z$ plane at $x = 0$, and the Figures 7–12 and 7–13 represent the $x - y$ plane at $z = 1.5$. Note that in the above plots, the desired output ratio, 1, whether for velocity ratio or for torque ratio, is used: that is, the singular values of the original first order KIC $[G_\phi^u]$ is directly investigated.

[2]For example, based on rough dextrous human motion of the human arm, $v_o = 40$ *in/sec* and $\omega_o = 6$ *rad/sec* can be used.

[3]For example, the average values of force range of the human right arm in an aircraft control stick, 15.5" in front of seated subject, are:

- 96.3, 83.3 *lb* for pushing, pulling,
- 38., 29. *lb* for force to left, right,
- 1.09 *lb* – *ft* for maximum torque on a 2" diameter knob.[74]

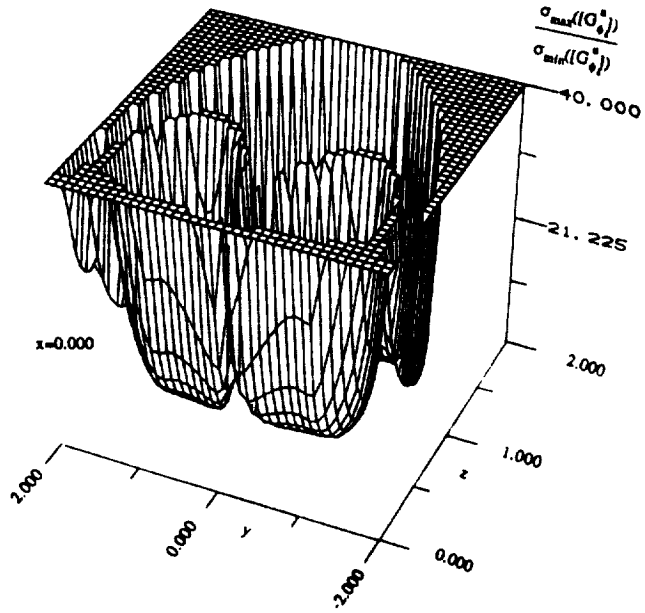

Figure 7–10 SURFACE PLOTS IN Y-Z PLANE OF THE 6-DOF STEWART PLATFORM

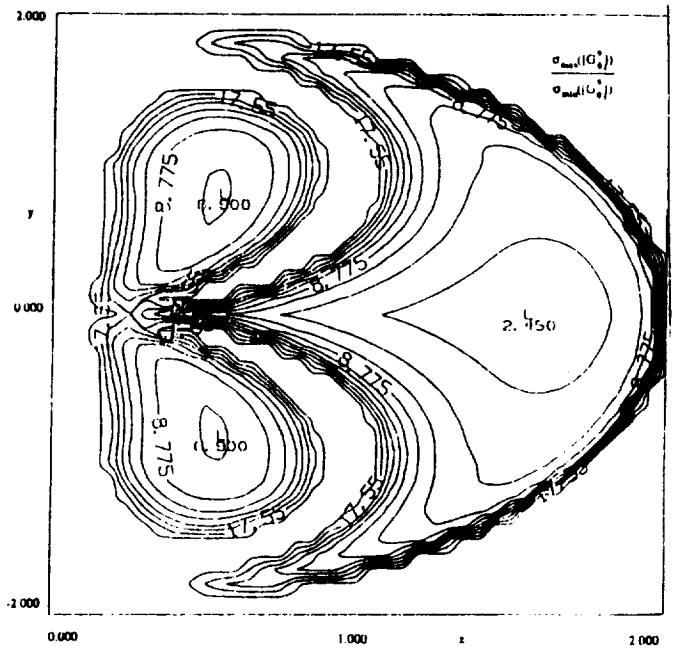

Figure 7–11 CONTOUR PLOTS IN X-Y PLANE OF THE 6-DOF STEWART PLATFORM

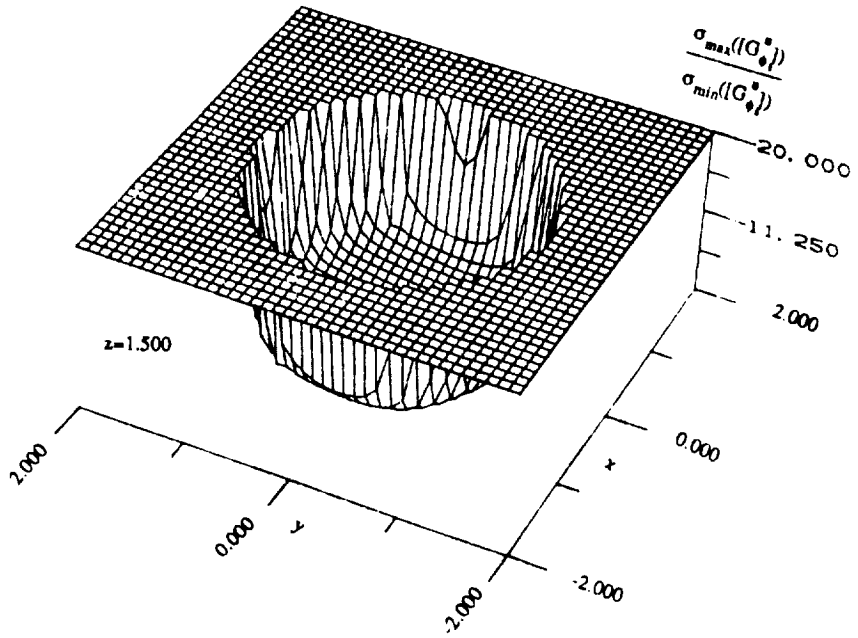

Figure 7–12 SURFACE PLOTS IN Y-Z PLANE OF THE 6-DOF STEWART PLATFORM

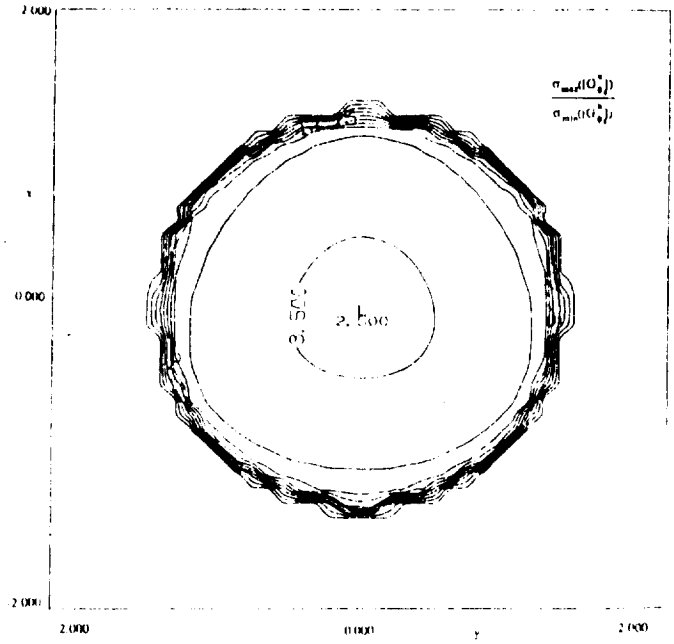

Figure 7–13 CONTOUR PLOTS IN X-Y PLANE OF THE 6-DOF STEWART PLATFORM

7–3 Discussion and conclusion

The new conceptual hybrid system introduced in chapter 6 is integrated into a conceptual design of a parallel 6-dof manual controller and the kinematic analysis has been presented. In this study, only initial work has been done to investigate geometric characteristics of the system and one design method for a general 6-dof system is suggested. For a normalized set of system parameters, representative contour plots are provided and they show promises. However, the conceptual 6-dof system needs to be investigated further; that is, the optimal kinematic parameters need to be more fully understood in terms of the geometric characteristics for a force-reflecting manual controller application.

The spherical 3-dof parallel system may be combined with the 6-dof manual controller shown in Figure 7–14 to represent a multi-functional test-bed of a 9-dof system. The redundant degrees of freedom permits secondary objectives (singularity avoidance, power minimization, optimal transmission characteristics, etc.) and requires further research for the manual controller application. Also the use of the redundant actuators, as shown in a 9-string manual controller, increases workspace with desired torque transmission characteristics and also requires further study.

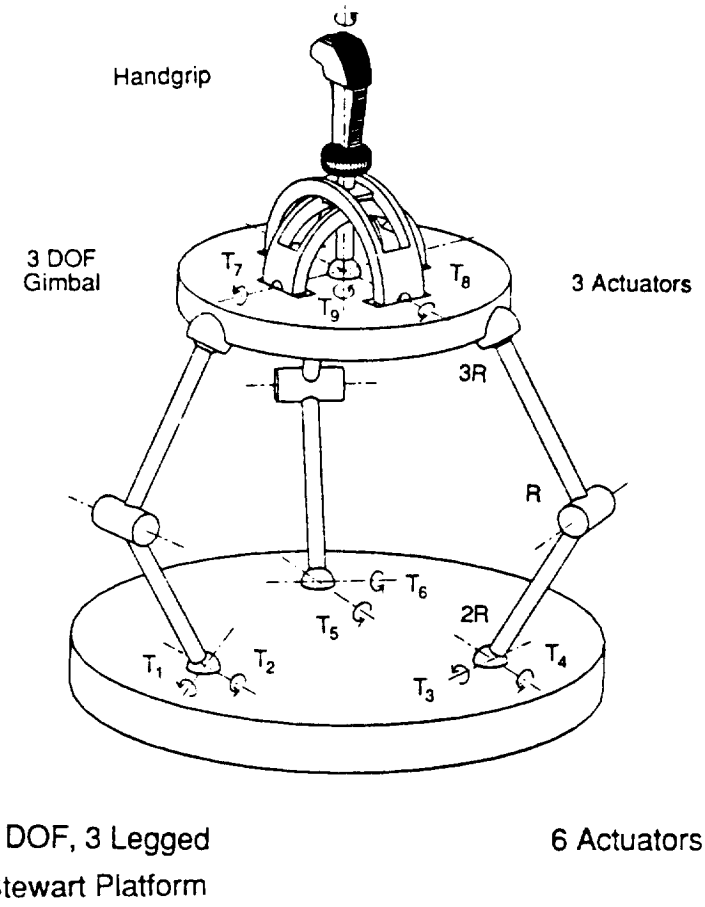

Figure 7–14 A CONCEPTUAL 9-DOF REDUNDANT MANUAL CONTROLLER

CHAPTER 8

Conclusions and Recommendations

Most of the available manual controllers in bilateral or force-reflecting teleoperator systems can be characterized by their bulky size, heavy weight, high costs, or lack of smoothness and transparency, and elementary architecture.

In this effort, the design issues for manual controllers for advanced teleoperator systems are discussed in Chapter 2. The previous design work and the general background on teleoperator system are reviewed in Chapter 3. Also, existing control strategies and computer supporting functions are reviewed. By means of this review, design criteria such as compactness, light-weight, portability, force-reflection, etc., in universal manual controllers are listed as most important issues. In this research, the design and control of the manual controller which meets those characteristics are studied and evaluated in an actual demonstration manual controller.

Force control strategies are studied through a one-dof system implementation to investigate its performance to the force-reflecting manual controller in Chapter 5. The desired characteristics of the system components in force-controlled manual controller applications are briefly evaluated in terms of a simple linear one-dof system model. In particular, from the model (i.e., from the Bode plot and phase plot) it can be seen that the flexibility of the gear train

system is not desirable for force-controlled manual controller applications and that a low pass filter reduces undesirable effect of the gear train flexibility.

A demonstration force-reflecting, 3-dof spherical manual controller is analyzed, designed and implemented as described in Chapter 4 and 5. The system has a parallel geometry to place all of actuators on the base plate, reducing dynamic effect of the actuators. To achieve an improved level of design to meet criteria such as compactness, portability (light weight) and a somewhat enhanced force-reflecting capability, the demonstration manual controller employs high gear-ratio reducers and is force-controlled using wrist sensed forces. The implemented manual controller is capable of reflecting 50 $in - lb_f$ torque about the common intersection point of all joint axes of the shoulder. The force-reflecting controller runs at 45 Hz in a μVAX computer and has been successfully applied to the control of an animated HERMIES model and an CESARm model (of ORNL) on a Silicon Graphics workstation.

As an alternative design for the spherical 3-dof manual controller, a new conceptual hybrid (or parallel) spherical 3-dof gimbal module system is introduced with a full kinematic analysis in Chapter 6. Also the resulting kinematic properties are compared to those of other typical spherical 3-dof systems. The new system is very promising both in its kinematics and in its dynamics. Kinematically, it is simple to reduce the computational complexity and has a relatively large dextrous workspace compared to the purely parallel spherical system. Dynamically, due to the use of the parallel geometry, all of the actuators can be placed near the base plate, reducing the inertial and gravitational effects. Also much higher mechanical stiffness can be expected.

As a framework for an enhanced universal force-reflecting 6-dof manual controller development, a 9-string force-reflecting 6-dof manual controller de-

scribed in Chapter 7 has been implemented and interfaced with the Cincinnati Milacron T^3-726 Industrial Manipulator. The manual controller used a parallel mechanical structure and employed redundant actuators (i.e., 9 actuators and three constant air pressure cylinders). The force-reflecting manual controller can be either position-controlled or velocity-controlled. Also, computer supporting functions such as filtering, scaling, etc., have been implemented. However, the overall bulky size of this manual controller is regarded as one of its disadvantages.

The various 6 to 9-dof test-bed manual controllers are conceptualized in Chapter 7. These manual controllers are the Stewart Platform which uses only revolute joints. In particular, when the new spherical gimbal module, as introduced in Chapter 6, is added to a conceptual design of a parallel 6-dof 3-legged manual controller, the system becomes a versatile test-bed for force-reflecting manual controller evaluation for enhanced human performance. In this work, only a design framework such as position analysis and first-order kinematic analysis has been presented to investigate geometric characteristics of the system. The geometric properties of the system with normalized geometric parameters are also presented.

The modeling approach for serial or parallel linkages is briefly reviewed in Appendix A. Those modeling formulations are used throughout this study. The various kinematic transformations required in the universal teleoperator system operations are reviewed and one method for scaling for the rotation is suggested in Appendix B.

The remarks and conclusions of this effort can be summarized below.

- A review of current literature and our own laboratory development has been presented in Chapters 2 and 3. This review has lead to the identi-

fication of the most important design and control issues. Design criteria such as compactness, light-weight, portability, force-reflection, and others have been considered in these chapters. (See Section 2.3.)

- The application of force control to a manual controller system for enhanced performance has been studied in Section 5.1. In particular, a simplified linear model (i.e., from the Bode plot and phase plot) shows the flexibility of the gear train system is detrimental to force-controlled manual controller applications. A low pass filter reduces the undesirable effect of the gear train flexibility giving the overall system greater stability. (See Section 5.1.4.)

- A force-reflecting, 3-dof, spherical, demonstration, manual controller has been implemented in Section 5.2. The manual controller is a test-bed to investigate the effectiveness of a parallel structure in a manual controller application. It also allows a performance evaluation of a force-controlled manual controller. This manual controller has been sucessfully applied to the control of an animated HERMIES model and CESARm model (of ORNL) on a Silicon Graphics workstation.

- Various 3-dof structural design architectures for manual controllers have been investigated: serial, hybrid, an parallel wrists. The new hybrid (or parallel) mechanism, as introduced in Section 6.1, showed excellent kinematic and dynamic charateristics compared to the other mechanisms. (See Section 6.3 for the comparisons.)

- As a frame work for the development of an enhanced, general, force-reflecting, 6-dof manual controller, a 9-string universal force-reflecting

manual controller, with a parallel structure, has been implemented and interfaced with the Cincinnati Milacron T^3-726 industrial manipulator as discussed in Section 7.1. The operational software that provides such features as position control, velocity control, filtering, scaling, etc., has been developed and implemented to the teleoperator system.

- Various 6-dof to 9-dof test-bed manual controllers have been conceptualized in Section 7.2. The most promising design conceptualized is a 3-legged, 6-dof manual controller. This design provides an excellent combination of force reflection, compactness, portability, etc. A preliminary analysis of the first order geometric properties of the mechanism has been completed using normalized geometric parameters. Further investigation will be required to identify the optimal parameters for enhanced design for a force-reflecting manual controller.

In this study, the design and control of the force-reflecting manual controller has been the major objectives of the research. In most available bilateral control or force-reflecting control strategies in teleoperation, the manual controller regulates the motion of the remote manipulator by providing the motion command. It reflects the contact forces experienced by the remote manipulator back to the human operator. However, when the remote manipulator makes contact with the environment, direct force command may be more useful than direct motion command. In other words, the command contact forces are provided to the remote manipulator from the manual controller and in return, the manual controller reflects the current motion of the remote manipulator to provide kinesthetic feeling. This control strategy has an inverted information flow from the acceptedforce-reflecting teleoperator system. This inverse communication-

command scenario needs to be investigated further for its application and its performance in teleoperation.

Also the application of both redundancy in degrees of freedom as in a 9-dof test-bed manual controller and redundancy in actuators within the manual controller design as in the 9-string manual controller should be investigated further. The extra degrees of freedom can be used to achieve secondary objectives such as dexterity, joint torque minimization, etc. of the manual controller. The extra actuators can increase the dextrous working volume that has better torque transmission characteristics. The application for these two features and their effect on the manual controller system requires further study for more enchanced manual controller system performance.

APPENDIX A

Kinematic and Dynamic Modeling of Serial Manipulators

In this section, a brief review of the kinematic representation and modeling and dynamic modeling of the serial and parallel manipulators is given. These modeling approaches for serial manipulators are developed by Thomas and Tesar, and later extended for parallel manipulators by Freeman and Tesar. They are used in the analysis of the various systems in the previous chapters. More details can be found in [32][92].

A–1 Kinematic representation, coordinate systems of the serial manipulator

Serial manipulators are represented kinematically as a sequence of rigid links joined by one-dof lower pair connectors(revolute joints(R) and primatic joints(P)) as shown in Figure A–1, without any loss of generality since the other lower pair connectors can be represented as combinations of the revolute and prismatic joints. Now, S_j(or S_{jj}) denotes the offset distance along the joint axis, $\boldsymbol{s}_j$, between the two links that the joint connects; and θ_j(or θ_{jj}) denotes the relative rotation about $\boldsymbol{s}_j$ between these two links. For each joint j, one of these dimensions has a fixed value(denoted by double subscripts) and the other

is the input reference parameter for the joint. The link jk connecting successive joints j and k is defined by the fixed geometric parameters a_{jk}, which is the perpendicular distance between the joint axes (measured along the common perpendicular $\boldsymbol{a}_{jk}$), and α_{jk}, the twist angle between the axes measured in a right-hand sense about $\boldsymbol{a}_{jk}$. As shown in Figure A–1, a fixed cartesian reference system ($\boldsymbol{x}$, $\boldsymbol{y}$, $\boldsymbol{z}$) is located with the $\boldsymbol{z}$ axis directed along the first joint axis, $\boldsymbol{s}_1$. The geometric parameters for the first joint are measured with respect to the $\boldsymbol{x}$ axis, which is chosen arbitrarily (except that it intersects $\boldsymbol{s}_1$ at right angles).

The position of the body in space is uniquely defined by the orientation of the body and the position coordinates of some point fixed in the body. The orientation of each link can be defined by the two vectors, $\boldsymbol{s}_j$ and $\boldsymbol{a}_{jk}$. These two vectors, representing the joint and link axes, form the basis for a body fixed cartesian reference system($\boldsymbol{x}^{(j)}$, $\boldsymbol{y}^{(j)}$, $\boldsymbol{z}^{(j)}$) with the $\boldsymbol{x}^{(j)}$ axis lying along $\boldsymbol{a}_{jk}$ and $\boldsymbol{z}^{(j)}$ along $\boldsymbol{s}_j$. The superscript in parentheses indicates a vector in body-fixed coordinates. Then the rotational matrix, which relates the jth body-fixed frame to a coordinate system with the same origin but with axes parallel to the fixed reference axes, can be represented

$$[R_b^j] = [\boldsymbol{a}_{jk}\ \boldsymbol{s}_j \times \boldsymbol{a}_{jk}\ \boldsymbol{s}_j]. \tag{A–1.1}$$

Note that $\boldsymbol{p} = [R_b^j]\boldsymbol{p}^{(j)}$, where $\boldsymbol{p}$ and $\boldsymbol{p}^{(j)}$ are the position vectors of a point P from the origin of the jth body-fixed frame represented in absolute and body-fixed (j) references. The absolute position of a point P in reference frame can be obtained

$$\boldsymbol{P} = \boldsymbol{R}_j + [R_b^j]\boldsymbol{P}^{(j)} \tag{A–1.2}$$

where $\boldsymbol{P}$ and $\boldsymbol{P}^{(j)}$ are the positions of a point represented in absolute and body-fixed(j) references, and $\boldsymbol{R}_j$ represents the position vector of the origin of the jth

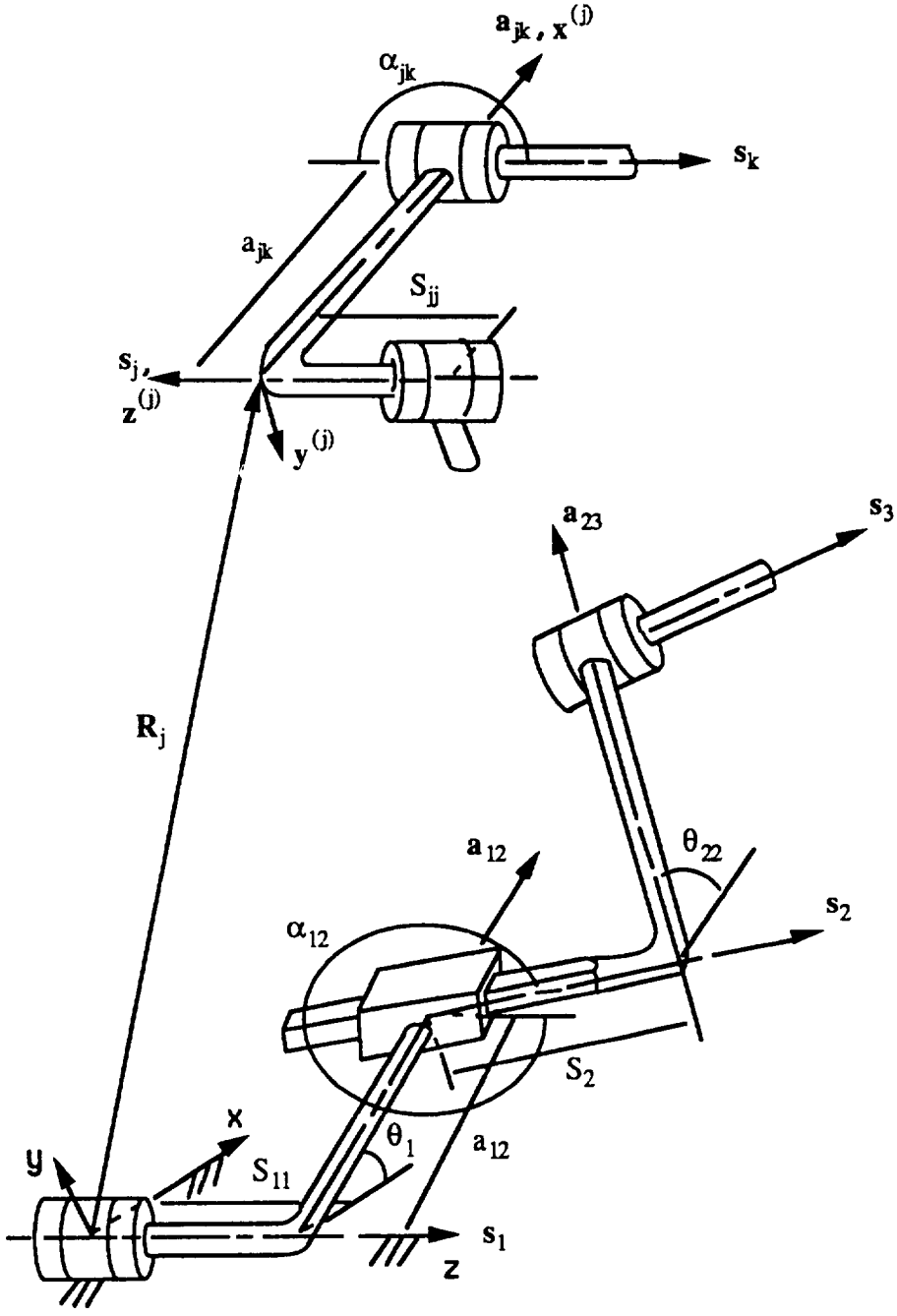

Figure A–1 KINEMATIC REPRESENTATION OF THE SERIAL MANIPULATOR

body-fixed coordinate from the fixed reference. The position vector, $\boldsymbol{R}_j$, can be found by summing the link lengths and joint offsets starting at the fixed base as shown in Figure A–1:

$$\boldsymbol{R}_j = S_{11}\boldsymbol{s}_1 + a_{12}\boldsymbol{a}_{12} + S_{22}\boldsymbol{s}_2 + \cdots + S_{jj}\boldsymbol{s}_j = S_{11}\boldsymbol{s}_1 + \sum_{l=2}^{j}(a_{(l-1)l}\boldsymbol{a}_{(l-1)l} + S_{ll}\boldsymbol{s}_l) \tag{A–1.3}$$

A–2 The first order influence coefficient

A–2.1 The rotational first-order influence coefficient

The angular velocity of link jk of a serial manipulator is given as the sum of the relative angular velocities between preceding links in the serial manipulator,

$$\boldsymbol{\omega}_{jk} = \boldsymbol{\omega}_{12}^{(01)} + \boldsymbol{\omega}_{23}^{(12)} + \cdots + \boldsymbol{\omega}_{jk}^{(ij)}, \tag{A–2.4}$$

or

$$\boldsymbol{\omega}_{jk} = \dot{\theta}_1\boldsymbol{s}_1 + \dot{\theta}_2\boldsymbol{s}_2 + \cdots + \dot{\theta}_j\boldsymbol{s}_j = \sum_{n=1}^{j}\dot{\theta}_n\boldsymbol{s}_j. \tag{A–2.5}$$

Then the above equation can be represented

$$\boldsymbol{\omega}_{jk} = [G^{jk}]\dot{\boldsymbol{\phi}} \tag{A–2.6}$$

where the rotational first-order influence coefficients for link jk are defined as

$$[G^{jk}] \equiv [\frac{\partial\boldsymbol{\omega}_{jk}}{\partial\dot{\phi}_1}, \frac{\partial\boldsymbol{\omega}_{jk}}{\partial\dot{\phi}_2}, \ldots, \frac{\partial\boldsymbol{\omega}_{jk}}{\partial\dot{\phi}_N}] \equiv [\boldsymbol{g}_1^{jk}, \boldsymbol{g}_2^{jk}, \ldots, \boldsymbol{g}_N^{jk}] \tag{A–2.7}$$

and $\dot{\phi}_n$, the nth component of the generalized velocity vector, is either $\dot{\theta}_n$ or $\dot{s}_n$ depending on whether joint n is a revolute or a prismatic joint. The above results can be summarized as follows;

$$[G_{\phi}^{jk}]_{;n} \equiv \boldsymbol{g}_n^{jk} = \begin{cases} \boldsymbol{s}_n, & n \le j,\ n - revolute \\ 0, & otherwise. \end{cases} \tag{A–2.8}$$

A–2.2 The translational first-order influence coefficient

Using the equations (A–1.2) and (A–1.3), the absolute position of the point can be written

$$\boldsymbol{P} = S_{11}\boldsymbol{s}_1 + \sum_{l=2}^{j}(a_{(l-1)l}\boldsymbol{a}_{(l-1)l} + S_{ll}\boldsymbol{s}_l) + [R_b^j]\boldsymbol{P}^{(j)}. \qquad \text{(A–2.9)}$$

By direct differention with respect to time, we get

$$\dot{\boldsymbol{P}} = \dot{S}_{11}\boldsymbol{s}_1 + \sum_{l=2}^{j}(a_{(l-1)l}\dot{\boldsymbol{a}}_{(l-1)l} + S_{ll}\dot{\boldsymbol{s}}_l + \dot{S}_l\boldsymbol{s}_l) + \frac{d}{dt}([R_b^j]\boldsymbol{P}^{(j)}). \qquad \text{(A–2.10)}$$

Now, since $\boldsymbol{a}_{(l-1)l}$ and $\boldsymbol{s}_l$ are unit vectors fixed in link $(l-1)l$ and $[R_b^j]\boldsymbol{P}^{(j)}$ is a vector fixed in link jk, the time rate of change of these vectors can be expressed in terms of the vector cross product as

$$\dot{\boldsymbol{a}}_{(l-1)l} = \boldsymbol{\omega}_{(l-1)l} \times \boldsymbol{a}_{(l-1)l} = (\sum_{n=1}^{l-1}\dot{\theta}_n\boldsymbol{s}_n) \times \boldsymbol{a}_{(l-1)l} \qquad \text{(A–2.11)}$$

$$\dot{\boldsymbol{s}}_l = \boldsymbol{\omega}_{(l-1)l} \times \boldsymbol{s}_l = (\sum_{n=1}^{l-1}\dot{\theta}_n\boldsymbol{s}_n) \times \boldsymbol{s}_l \qquad \text{(A–2.12)}$$

and

$$\frac{d}{dt}([R_b^j]\boldsymbol{P}^{(j)}) = \boldsymbol{\omega}_{jk} \times ([R_b^j]\boldsymbol{P}^{(j)}) = (\sum_{n=1}^{l-1}\dot{\theta}_n\boldsymbol{s}_n) \times ([R_b^j]\boldsymbol{P}^{(j)}). \qquad \text{(A–2.13)}$$

Substituting equations (A–2.11-A–2.13) into equation (A–2.10) and regrouping terms leads to

$$\begin{aligned}\dot{\boldsymbol{P}} &= \sum_{n=1}^{j}\{\dot{S}_n\boldsymbol{s}_n + \dot{\theta}_n\boldsymbol{s}_n \times [\sum_{l=n+1}^{j}(a_{(l-1)l}\dot{\boldsymbol{a}}_{(l-1)l} + S_{ll}\dot{\boldsymbol{s}}_l + \dot{S}_l\boldsymbol{s}_l) + [R_b^j]\boldsymbol{P}^{(j)}\} \\ &= \sum_{n=1}^{j}\{\dot{S}_n\boldsymbol{s}_n + \dot{\vartheta}_n\boldsymbol{s}_n \times (\boldsymbol{P} - \boldsymbol{R}_n)\} \qquad \text{(A–2.14)}\end{aligned}$$

where the term,

$$\sum_{l=n+1}^{j}(a_{(l-1)l}\dot{\boldsymbol{a}}_{(l-1)l} + S_{ll}\dot{\boldsymbol{s}}_l + \dot{S}_l\boldsymbol{s}_l) + [R_b^j]\boldsymbol{P}^{(j)} = \boldsymbol{P} - \boldsymbol{R}_n, \qquad \text{(A–2.15)}$$

represents a vector from the origin of the nth body-fixed coordinates to the point P. Finally, the velocity of point P can be expressed in the following form

$$\dot{\boldsymbol{P}} = [G_{\phi}^{p}]\dot{\boldsymbol{\phi}} = [\boldsymbol{g}_1^p,\ \boldsymbol{g}_2^p, \ldots, \boldsymbol{g}_N^p] \tag{A-2.16}$$

where

$$[G_{\phi}^{p}]_{;n} \equiv \boldsymbol{g}_n^p = \begin{cases} \boldsymbol{s}_n \times (\boldsymbol{P} - \boldsymbol{R}_n), & n \leq j;\ \phi_n = \theta_n(revolute) \\ \boldsymbol{s}_n, & n \leq j; \phi_n = S_n(prismatic) \\ 0, & n > j. \end{cases} \tag{A-2.17}$$

A–3 The second-order influence coefficient

A–3.1 The rotational second-order influence coefficient

The angular acceleration of link jk, $\boldsymbol{\alpha}_{jk}$, is obtained by differentiating equation (A–2.6)

$$\boldsymbol{\alpha}_{jk} = \frac{d}{dt}([G_{\phi}^{jk}])\dot{\boldsymbol{\phi}} + [G_{\phi}^{jk}]\ddot{\boldsymbol{\phi}}. \tag{A-3.18}$$

To find the first term, differentiate the expression for the nth component of $[G_{\phi}^{jk}]$ given in equation (A–2.7)

$$\frac{d}{dt}(\boldsymbol{g}_n^{jk}) = \begin{cases} \dot{\boldsymbol{s}}_n, & n \leq j; n - revolute \\ 0, & otherwise. \end{cases} \tag{A-3.19}$$

The controlling input dynamics can again be decoupled from the geometric parameters by defining the rotational second-order influence coefficients in the form

$$[H_{\phi\phi}^{jk}]_{m;n} = \frac{\partial}{\partial \dot{\phi}_m}\{\frac{d}{dt}(\boldsymbol{g}_n^{jk})\} \tag{A-3.20}$$

or

$$[H_{\phi\phi}^{jk}]_{m;n} = \frac{\partial}{\partial \phi_m}(\boldsymbol{g}_n^{jk}). \tag{A-3.21}$$

The $m;n$ subscript indicates the components of the mth row and nth column of the $[H^{jk}_{\phi\phi}]$ which are vectors. And the angular acceleration of link jk, can be expressed

$$\boldsymbol{\alpha}_{jk} = \dot{\boldsymbol{\phi}}^T [H^{jk}_{\phi\phi}]\dot{\boldsymbol{\phi}} + [G^{jk}_{\phi}]\ddot{\boldsymbol{\phi}}. \tag{A-3.22}$$

The rotational second-order influence coefficients can be obtained as

$$[H^{jk}_{\phi\phi}]_{m;n} \equiv \boldsymbol{h}^{jk}_{m;n} = \begin{cases} \boldsymbol{s}_m \times \boldsymbol{s}_n, & m < n \leq j; m, n - revolutes \\ 0, & otherwise. \end{cases} \tag{A-3.23}$$

A–3.2 The translational second-order influence coefficient

Analogously, by differentiating the equation (A–2.16) with respect to time, the translational acceleration, $\boldsymbol{a}_p$, of a point, P, are written in the following form to decouple the geometric parameters from the control inputs

$$\boldsymbol{a}_p = \dot{\boldsymbol{\phi}}^T [H^p_{\phi\phi}]\dot{\boldsymbol{\phi}} + [G^p_{\phi}]\ddot{\boldsymbol{\phi}} \tag{A-3.24}$$

where the translational second-order influence coefficients are defined as

$$[H^p_{\phi\phi}]_{m;n} = \frac{\partial}{\partial \dot{\phi}_m}\{\frac{d}{dt}(\boldsymbol{g}^p_n)\} \tag{A-3.25}$$

or

$$[H^p_{\phi\phi}]_{m;n} = \frac{\partial}{\partial \phi_m}(\boldsymbol{g}^p_n). \tag{A-3.26}$$

And these translational second-order influence coefficients can be obtained as follows

$$[H^p_{\phi\phi}]_{m;n} \equiv \boldsymbol{h}^p_{m;n} = \begin{cases} \boldsymbol{s}_m \times [\boldsymbol{s}_n \times (\boldsymbol{P} - \boldsymbol{R}_n)], & m \leq n \leq j; m, n - revolute \\ \boldsymbol{s}_n \times [\boldsymbol{s}_m \times (\boldsymbol{P} - \boldsymbol{R}_m)], & n < m \leq j; m, n - revolute \\ \boldsymbol{s}_n \times \boldsymbol{s}_m, \ n < m \leq j, & m - prismatic, n - revolute \\ \boldsymbol{s}_m \times \boldsymbol{s}_n, \ m < n \leq j, & m - revolute, n - prismatic \\ 0, & otherwise. \end{cases} \tag{A-3.27}$$

The obtained expressions for the kinematic influence coefficients of the serial manipulator are summarized in Table A–1.

Table A–1 KINEMATIC INFLUENCE COEFFICIENTS FOR SERIAL MANIPULATORS

Symbol	joint type:m	Joint type:n	Restrictions	Expressions
Rotational first-order influence coefficients				
$[G_{\phi}^{jk}]_{;n}$		R	$n \leq j$	$\boldsymbol{s}_n$
$[G_{\phi}^{jk}]_{;n}$		R	$n > j$	0
$[G_{\phi}^{jk}]_{;n}$		P	*all* n	0
Translational first-order influence coefficients				
$[G_{\phi}^{p}]_{;n}$		R	$n \leq j$	$\boldsymbol{s}_n \times (\boldsymbol{P} - \boldsymbol{R}_n)$
$[G_{\phi}^{p}]_{;n}$		P	$n \leq j$	$\boldsymbol{s}_n$
$[G_{\phi}^{p}]_{;n}$		R, P	$n > j$	0
Rotational second-order influence coefficients				
$[H_{\phi\phi}^{jk}]_{m;n}$	R	R	$m < n \leq j$	$\boldsymbol{s}_m \times \boldsymbol{s}_n$
$[H_{\phi\phi}^{jk}]_{m;n}$	R	R	$m \geq n$, *or* $n > j$	0
$[H_{\phi\phi}^{jk}]_{m;n}$	P	R	*all* m, n	0
$[H_{\phi\phi}^{jk}]_{m;n}$	P	P	*all* m, n	0
Translational second-order influence coefficients				
$[H_{\phi\phi}^{p}]_{m;n}$	R	R	$m < n \leq j$	$\boldsymbol{s}_m \times [\boldsymbol{s}_n \times (\boldsymbol{P} - \boldsymbol{R}_n)]$
$[H_{\phi\phi}^{p}]_{m;n}$	R	R	$n < m \leq j$	$\boldsymbol{s}_n \times [\boldsymbol{s}_m \times (\boldsymbol{P} - \boldsymbol{R}_m)]$
$[H_{\phi\phi}^{p}]_{m;n}$	P	R	$n < m \leq j$	$\boldsymbol{s}_n \times \boldsymbol{s}_m$
$[H_{\phi\phi}^{p}]_{m;n}$	R	P	$m < n \leq j$	$\boldsymbol{s}_m \times \boldsymbol{s}_n$
$[H_{\phi\phi}^{p}]_{m;n}$	P	R	$m < n \leq j$	0
$[H_{\phi\phi}^{p}]_{m;n}$	R	P	$n < m \leq j$	0
$[H_{\phi\phi}^{p}]_{m;n}$	R, P	R, P	*all* $m, n > j$	0
$[H_{\phi\phi}^{p}]_{m;n}$	P	P	*all* m, n	0

A–4 Modeling of dynamic equations of serial manipulators

The kinetic energy of a rigid link manipulator in motion can be expressed as the sum of the kinetic energies of the individual links in the following form

$$K.E. = \sum_{j=1}^{N} \frac{1}{2} \{ M_{jk} \boldsymbol{v}_{cj}^T \boldsymbol{v}_{cj} + \boldsymbol{\omega}_{jk}^T [\Pi_{jk}] \boldsymbol{\omega}_{jk} \} \tag{A–4.28}$$

where M_{jk} denotes the mass of link jk and the subscript cj denotes the mass centroid of the link. The $[\Pi_{jk}]$ denotes the inertia tensor about centroid for link jk in terms of the fixed reference coordinates. Let the inertia tensor about the centroid defined in terms of the body-fixed coordinate systems be denoted by $[\Pi_{jk}^{(j)}]$, which is a constant symmetric matrix for each link. Noting that the kinetic energy is independent of the coordinate systems, that is, using

$$\boldsymbol{\omega}_{jk}^T [\Pi_{jk}] \boldsymbol{\omega}_{jk} = \boldsymbol{\omega}_{jk}^{(j)^T} [\Pi_{jk}^{(j)}] \boldsymbol{\omega}_{jk}^{(j)} \tag{A–4.29}$$

and

$$\boldsymbol{\omega}_{jk} = [R_b^j] \boldsymbol{\omega}_{jk}^{(j)}, \tag{A–4.30}$$

the following relation can be obtained

$$[\Pi_{jk}] = [R_b^j] [\Pi_{jk}^{(j)}] [R_b^j]^T. \tag{A–4.31}$$

Equation (A–4.28) can be rewritten in terms of first-order kinematic influence coefficients and controlling input velocities as follows

$$K.E. = \frac{1}{2} \sum_{j=1}^{N} \{ M_{jk} \dot{\boldsymbol{\phi}}^T [G_\phi^{cj}]^T [G_\phi^{cj}] \dot{\boldsymbol{\phi}} + \dot{\boldsymbol{\phi}}^T [G_\phi^{jk}]^T [\Pi_{jk}] [G_\phi^{jk}] \dot{\boldsymbol{\phi}} \} = \frac{1}{2} \dot{\boldsymbol{\phi}}^T [I_{\phi\phi}^*] \dot{\boldsymbol{\phi}} \tag{A–4.32}$$

where each components of the effective inertia tensor, $[I_{\phi\phi}^*]$, can be obtained

$$[I_{\phi\phi}^*]_{m;n} = \sum_{j=1}^{N} \{ M_{jk} \boldsymbol{g}_m^{cj^T} \boldsymbol{g}_n^{cj} + \boldsymbol{g}_m^{jk^T} [\Pi_{jk}] \boldsymbol{g}_n^{jk} \}. \tag{A–4.33}$$

It can be noted that from this equation, the effective inertia matrix is a function of geometric parameters and is a real symmetric matrix(positive definite matrix).

Now using Lagrange's equations of motion, the generalized inertia torque at the nth input(joint) can be written

$$T_n^i = \frac{d}{dt}(\frac{\partial K.E.}{\partial \dot{\phi}_n}) - \frac{\partial K.E.}{\partial \phi_n} \tag{A-4.34}$$

or

$$T_n^i = \frac{d}{dt}(\dot{\phi}_n{}^T [I^*_{\phi\phi}]_{;n}) - \frac{1}{2}\dot{\phi}^T \frac{\partial}{\partial \phi_n}([I^*_{\phi\phi}])\dot{\phi} \tag{A-4.35}$$

where $[I^*_{\phi\phi}]_{;n}$ represents column n of the effective inertia matrix. Since

$$\frac{d}{dt}(\dot{\phi}^T [I^*_{\phi\phi}]_{;n}) = \ddot{\phi}^T [I^*_{\phi\phi}]_{;n} + \dot{\phi}^T \frac{d}{dt}([I^*_{\phi\phi}]_{;n}) \tag{A-4.36}$$

where

$$\frac{d}{dt}([I^*_{\phi\phi}]_{;n}) = \sum_{m=1}^{N} \frac{\partial}{\partial \phi_m}(\frac{d}{dt}([I^*_{\phi\phi}]_{;n})\dot{\phi}_m) = \frac{\partial}{\partial \phi}(\frac{d}{dt}([I^*_{\phi\phi}]_{;n})\dot{\phi}, \tag{A-4.37}$$

using equations (A-4.34-A-4.37) gives the generalized inertia torque at actuator n as

$$T_n^i = \ddot{\phi}^T [I^*_{\phi\phi}]_{;n} + \dot{\phi}^T \{\frac{\partial}{\partial \phi}([I^*_{\phi\phi}]_{;n}) - \frac{1}{2}\frac{\partial}{\partial \phi_n}([I^*_{\phi\phi}])\}\dot{\phi} = \ddot{\phi}^T [I^*_{\phi\phi}]_{;n} + \dot{\phi}^T [P_n]\dot{\phi} \tag{A-4.38}$$

where the components of the inertia power matrix, $[P_n]$, are defined by

$$[P_n]_{l;m} = \frac{\partial}{\partial \phi_m}([I^*_{\phi\phi}]_{l;n}) - \frac{1}{2}\frac{\partial}{\partial \phi_n}([I^*_{\phi\phi}]_{l;m}). \tag{A-4.39}$$

To reduce the computational burden, an alternative matrix $[P_n^*]$, which is a symmetric matrix, can be used in the final dynamic equation using

$$\dot{\phi}^T [P_n^*]\dot{\phi} = \dot{\phi}^T [P_n]\dot{\phi}. \tag{A-4.40}$$

Then

$$T_n^i = \ddot{\phi}^T [I_{\phi\phi}^*]_{;n} + \dot{\phi}^T [P_n^*]\dot{\phi} \qquad \text{(A–4.41)}$$

where the scalar component in row l and column m of the inertia power modeling matrix $[P_n^*]$ can be expressed in terms of the first and second-order influence coefficients as

$$[P_n^*]_{l;m} = \sum_{j=1}^{N} \{ M_{jk} [H_{\phi\phi}^{cj}]_{l;m}^T \boldsymbol{g}_n^{cj} + [H_{\phi\phi}^{jk}]_{l;m}^T [\Pi_{jk}] \boldsymbol{g}_n^{jk} + \boldsymbol{g}_l^{jk^T} [\Pi_{jk}] (\boldsymbol{g}_n^{jk} \times \boldsymbol{g}_m^{jk}) \}. \qquad \text{(A–4.42)}$$

Finally the controlling equations of serial manipulators can be expressed in following form

$$\boldsymbol{T}_a = [I_{\phi\phi}^*]\ddot{\phi} + \dot{\phi}^T [P_{\phi\phi\phi}^*]\dot{\phi} + \boldsymbol{T}_g + \boldsymbol{T}_L \qquad \text{(A–4.43)}$$

where $\boldsymbol{T}_a$ denotes the actuator input torque, $\boldsymbol{T}_g$ and $\boldsymbol{T}_L$ denotes the effective gravitational torque at joints and the effective external load at joints, respectively. However, in the above equation, the effects of the springs and viscous frictions are not included for convenience.

A–5 Operational space dynamic formulation via transfer of coordinates

In the previous section, the general dynamic equations in joint variables are derived. In this section, the dynamic equation in control point(such as end-effector or tool point) variables will be derived via transfer of coordinates technique. Detailed derivations can be found in [32].

Here, the universal generalized coordinates are denoted by

$$\boldsymbol{u} = (u_1,\ u_2, \ldots,\ u_M)^T \qquad \text{(A–5.44)}$$

and the joint variables by

$$\boldsymbol{\phi} = (\phi_1,\ \phi_2, \ldots,\ \phi_N)^T. \tag{A-5.45}$$

The first and second-order kinematic relations between them can be expressed as

$$\dot{\boldsymbol{u}} = [G^{\boldsymbol{u}}_{\boldsymbol{\phi}}]\dot{\boldsymbol{\phi}} \tag{A-5.46}$$

and

$$\ddot{\boldsymbol{u}} = [G^{\boldsymbol{u}}_{\boldsymbol{\phi}}]\ddot{\boldsymbol{\phi}} + \dot{\boldsymbol{\phi}}^T[H^{\boldsymbol{u}}_{\boldsymbol{\phi}\boldsymbol{\phi}}]\dot{\boldsymbol{\phi}}, \tag{A-5.47}$$

or

$$\dot{\boldsymbol{\phi}} = [G^{\boldsymbol{\phi}}_{\boldsymbol{u}}]\dot{\boldsymbol{u}} \tag{A-5.48}$$

and

$$\ddot{\boldsymbol{\phi}} = [G^{\boldsymbol{\phi}}_{\boldsymbol{u}}]\ddot{\boldsymbol{u}} + \dot{\boldsymbol{u}}^T[H^{\boldsymbol{\phi}}_{\boldsymbol{u}\boldsymbol{u}}]\dot{\boldsymbol{u}}. \tag{A-5.49}$$

From equations (A-5.46) and (A-5.48),

$$[G^{\boldsymbol{\phi}}_{\boldsymbol{u}}] = [G^{\boldsymbol{u}}_{\boldsymbol{\phi}}]^{-1}, \tag{A-5.50}$$

and using equations (A-5.46-A-5.49),

$$\ddot{\boldsymbol{\phi}} = [G^{\boldsymbol{\phi}}_{\boldsymbol{u}}]\ddot{\boldsymbol{u}} - \dot{\boldsymbol{u}}^T[G^{\boldsymbol{\phi}}_{\boldsymbol{u}}]^T([G^{\boldsymbol{\phi}}_{\boldsymbol{u}}] \bullet [H^{\boldsymbol{u}}_{\boldsymbol{\phi}\boldsymbol{\phi}}])[G^{\boldsymbol{\phi}}_{\boldsymbol{u}}]\dot{\boldsymbol{u}} = [G^{\boldsymbol{\phi}}_{\boldsymbol{u}}]\ddot{\boldsymbol{u}} + \dot{\boldsymbol{u}}^T[H^{\boldsymbol{\phi}}_{\boldsymbol{u}\boldsymbol{u}}]\dot{\boldsymbol{u}}. \tag{A-5.51}$$

That is,

$$[H^{\boldsymbol{\phi}}_{\boldsymbol{u}}\boldsymbol{u}] = -[G^{\boldsymbol{\phi}}_{\boldsymbol{u}}]^T([G^{\boldsymbol{\phi}}_{\boldsymbol{u}}] \bullet [H^{\boldsymbol{u}}_{\boldsymbol{\phi}\boldsymbol{\phi}}])[G^{\boldsymbol{\phi}}_{\boldsymbol{u}}]. \tag{A-5.52}$$

The operation $\bullet$ (called generalized dot product) is defined as followings when $[A] = P \times K$ and $[B] = K \times M \times N$;

$$([A] \bullet [B])_{p;m;n} \equiv \sum_{k=1}^{K}([A]_{p;k}[B]_{k;m;n}). \tag{A-5.53}$$

The dynamic equations in joint and in control point variables can be written, respectively,

$$\boldsymbol{T}^i_\phi = [I^*_{\phi\phi}]\ddot{\boldsymbol{\phi}} + \dot{\boldsymbol{\phi}}^T[P^*_{\phi\phi\phi}]\dot{\boldsymbol{\phi}} \tag{A-5.54}$$

and

$$\boldsymbol{T}^i_u = [I^*_{uu}]\ddot{\boldsymbol{u}} + \dot{\boldsymbol{u}}^T[P^*_{uuu}]\dot{\boldsymbol{u}}. \tag{A-5.55}$$

Since kinetic energy is independent of the coordinate systems,

$$K.E. = \frac{1}{2}\dot{\boldsymbol{\phi}}[I^*_{\phi\phi}]\dot{\boldsymbol{\phi}} = \frac{1}{2}\dot{\boldsymbol{u}}[I^*_{uu}]\dot{\boldsymbol{u}}, \tag{A-5.56}$$

using equation (A-5.46), the relation can be found

$$[I^*_{uu}] = [G^u_\phi]^{-T}[I^*_{\phi\phi}][G^u_\phi]^{-1}. \tag{A-5.57}$$

From the virtual work principle, we have

$$\boldsymbol{T}^i_\phi = [G^u_\phi]^T\boldsymbol{T}^i_u. \tag{A-5.58}$$

By inserting equations (A-5.54), (A-5.55), and (A-5.57) into the above equation, one can find

$$[P^*_{uuu}] = [G^u_\phi]^{-T}\{([G^u_\phi]^{-T} \bullet [P^*_{\phi\phi\phi}]) - ([I^*_{uu}] \bullet [H^u_{\phi\phi}])\}[G^u_\phi]^{-1}. \tag{A-5.59}$$

A–6 Kinematic/dynamic modeling of multi-loop parallel mechanisms

The dynamic formulation, which is presented in previous section, can be applied to the parallel mechanism in which the degrees of freedom of each subchain are the same as the degrees-of-freedom of the outputs of the system. The dynamic equation for a parallel system which has R serial subchains of

n dofs motion, can be obtained. First, from the each serial chain, the kinematic and dynamic parameters are developed, treating every joint variable as independent, that is

$$[{}^{r}G^{u}_{\phi}],\ [{}^{r}H^{u}_{\phi\phi}],\ [{}^{r}I^{*}_{\phi\phi}],\ [{}^{r}P^{*}_{\phi\phi\phi}],\ for\ r = 1, 2, \ldots, R. \tag{A–6.60}$$

To obtain the kinematic parameters for the desired generalized variables (i.e., actuated joints or ϕ_a) such as $[G^{u}_{\phi_a}]$ and $[H^{u}_{\phi_a\phi_a\phi_a}]$, the kinematic relations, which satisfy the geometric constraints imposed by the parallel system, can be used. For the first-order kinematic influence coefficients, noting

$$\dot{u} = [{}^{r}G^{u}_{\phi}]\dot{\phi}_r,\ for\ r = 1, 2, \ldots, R, \tag{A–6.61}$$

one can find

$$\dot{\phi}_r = [{}^{r}G^{u}_{\phi}]^{-1}\dot{u},\ for\ r = 1, 2, \ldots, R \tag{A–6.62}$$

where ϕ_r represent the joint variables of the rth serial subchain of the multi-loop parallel system. Then the kinematic equations for the desired variables can be obtained by selecting the corresponding equations from the above equations and writing in matrix form.

$$\dot{\phi}_a = [G^{u}_{\phi_a}]^{-1}\dot{u} \tag{A–6.63}$$

where $[G^{u}_{\phi_a}]$ is obtained by taking the inverse of $[G^{u}_{\phi_a}]^{-1}$.

For the second-order kinematic influence coefficients, each serial subchain yields the following equations:

$$\ddot{u} = [{}^{r}G^{u}_{\phi}]\ddot{\phi}_r + \dot{\phi}_r{}^{T}[{}^{r}H^{u}_{\phi\phi}]\dot{\phi}_r\ for\ r = 1, 2, \ldots, R. \tag{A–6.64}$$

Next, using equation (A–5.48) and (A–5.52), one can find

$$\ddot{\phi}_r = [{}^{r}G^{\phi}_{u}]\ddot{u} + \dot{u}^{T}[{}^{r}H^{\phi}_{uu}]\dot{u}\ for\ r = 1, 2, \ldots, R. \tag{A–6.65}$$

The second-order kinematic equations for the desired variables can be obtained by selecting the equations corresponding to the desired independent variables (input joints) from the above equations and writing in these matrix form.

$$\ddot{\boldsymbol{\phi}}_a = [G_u^{\phi_a}]\ddot{\boldsymbol{u}} + \dot{\boldsymbol{u}}^T[H_{uu}^{\phi_a}]\dot{\boldsymbol{u}}. \tag{A-6.66}$$

Note that the $[H^u_{\phi_a\phi_a}]$ array can be obtained using equation (A–5.52) with appropriate substitutions.

For the dynamic parameters in terms of the operational variables for the parallel system, by combining the effects of each subchain and including the centroidally referenced inertial effects of the platform if any ($[I_{uu}]$ and $[P_{uuu}]$), one can find obtain the following equivalent mass expressions

$$[I^*_{uu}] = [I_{uu}] + \sum_{r=1}^{R}[{}^r I^*_{uu}] \tag{A-6.67}$$

$$[P^*_{uuu}] = [P_{uuu}] + \sum_{r=1}^{R}[{}^r P^*_{uuu}]. \tag{A-6.68}$$

Finally, the mass coefficient description in terms of the driving input variables can be obtained as below, by inserting corresponding variables into (A–5.57) and (A–5.59);

$$[I^*_{\phi_a\phi_a}] = [G_u^{\phi_a}]^{-T}[I^*_{uu}][G_u^{\phi_a}]^{-1} \tag{A-6.69}$$

$$[P^*_{\phi_a\phi_a\phi_a}] = [G_u^{\phi_a}]^{-T}\{([G_u^{\phi_a}]^{-T} \bullet [P^*_{uuu}]) - ([I^*_{\phi_a\phi_a}] \bullet [H_{uu}^{\phi_a}])\}[G_u^{\phi_a}]^{-1}. \tag{A-6.70}$$

APPENDIX B

Kinematic Transformations of the Universal Teleoperator System

When the universal manual controller is applied in a teleoperation system, geometric differences between the manual controller and the remote manipulator need to be bridged by performing adequate transformations and scalings. In this section, various kinematic mappings between the manual controller and the remote manipulator are reviewed[64], and one method of the scaling of the rotation will be presented. Note that as opposed to translational scaling, rotational scaling has restrictions since finite rotational displacements do not have the properties of vectors.

The rotation of the body can be represented as a rotational matrix, in equivalent Euler angles, or in an equivalent single axis rotation. The direct application of the rotational gains to the Euler angles does not seem to be appropriate for the human operator, since for large angular displacements with scaling, the corresponding angular motions between the manual controller and the remote manipulator may be confusing. Also, recursive mapping in which the mapping is based on the current local or global reference frame, is not considered here due to its noncyclic property. In the scaling of the rotation of the body, *the rotational angle about the equivalent rotation axis* will be applied to the kinematic mapping for teleoperator systems. This method does provide cyclic

properties so that when the manual controller is at the initial orientation, the remote manipulator stays at its initial orientation.

B–1 Kinematic transformations of the universal teleoperator system

A rotation matrix $[R_A^B]$ represents the direction cosines of frame B with respect to frame A, in other words, an operator which transforms the orientation of frame A to the orientation of frame B. It is a linear transformation operator for which the transformed vectors preserve their lengths and angles. That is, $|[R_A^B]\boldsymbol{x}| = |\boldsymbol{x}|$ and $\cos([R_A^B]\boldsymbol{x}, [R_A^B]\boldsymbol{y})=\cos(\boldsymbol{x}, \boldsymbol{y})$ for any arbitrary vectors, $\boldsymbol{x}$ and $\boldsymbol{y}$. Let arbitrary vectors$(\boldsymbol{x}_B^{(B)})$ be in frame B and $(\boldsymbol{x}_A^{(A)})$ be in frame A. The linear transformation operator(or orthogonal tensor in this case) which transforms any arbitrary vector in frame A into the vector in frame B, can be obtained by imposing the following condition;

$$\boldsymbol{x}_B^{(B)} = \boldsymbol{x}_A^{(A)}. \tag{B–1.1}$$

That is, noting

$$\boldsymbol{x}_B^{(B)} = [R_B^A]\boldsymbol{x}_B^{(A)}, \tag{B–1.2}$$

$$\boldsymbol{x}_B^{(A)} = [R_A^B]\boldsymbol{x}_A^{(A)}, \tag{B–1.3}$$

$$\boldsymbol{x}_B^{(B)} = [R_B^O]\boldsymbol{x}_B, \tag{B–1.4}$$

and

$$\boldsymbol{x}_A^{(A)} = [R_A^O]\boldsymbol{x}_A, \tag{B–1.5}$$

one finds

$$\boldsymbol{x}_B = [R_O^B][R_A^O]\boldsymbol{x}_A. \tag{B–1.6}$$

As shown in equation (B–1.3) and (B–1.6), the operators, $[R_A^B]$ and $[R_O^B][R_A^O]$, denote the local mapping tensor and the global mapping tensor, respectively. In

the following, based on these two mapping tensors, four basic mappings will be presented for teleoperator system kinematics.

Let the current local reference frames of the manual controller and the remote manipulator be A and A', respectively, and O represents the global reference frame as shown in Figure B–1. Also A and A' represent the local reference frames which could be either in an initial position or in a redefined local position accomplished by re-referencing. These reference frames are redefined whenever the re-referencings in teleoperation are made. The direction cosine of those two local frames with respect to the global frame can be represented by $[R_O^A]$ and $[R_O^{A'}]$, respectively. Let the absolute position of the origin of the local frames of the manual controller and the remote manipulator be denoted by $\boldsymbol{r}_{OA}$ and $\boldsymbol{r}_{OA'}$, respectively. The local position vectors from A to B and from A' to B' in corresponding local reference frames will be denoted by $\boldsymbol{r}_{AB}^{(A)}$ and $\boldsymbol{r}_{A'B'}^{(A')}$, respectively, where B and B' represent the next local frames of the manual controller and the remote manipulator, respectively.

The four basic mappings between the manual controller and the remote manipulator are examined. These are the local-to-local, local-to-global, global-to-local, and global-to-global mappings. For each mapping, the required transform will be presented briefly.

B–1.1 Local-to-local mapping

In this mapping, the required conditions for the rotation matrix and position are

$$[R_A^B] = [R_{A'}^{B'}] \; for \; rotation \tag{B–1.7}$$

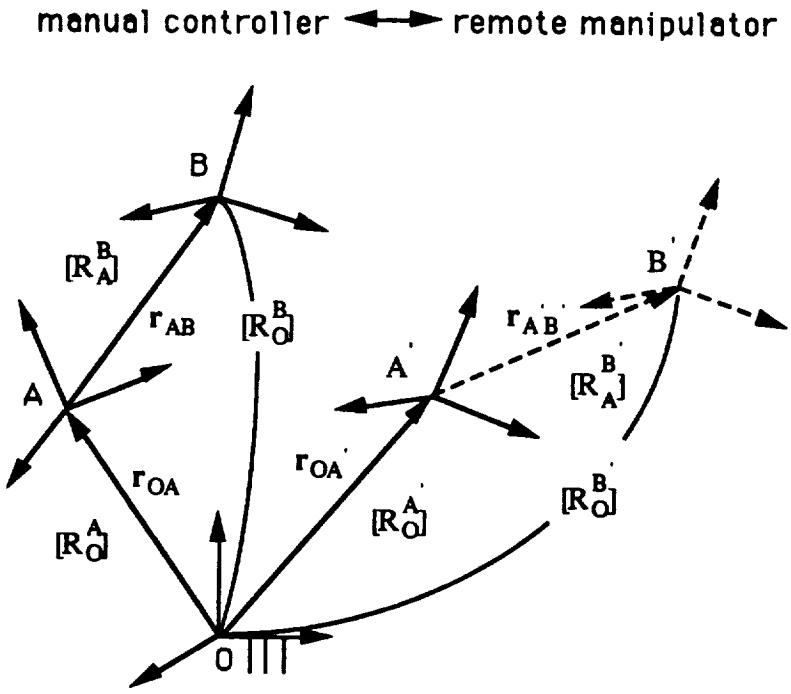

Figure B–1 KINEMATIC MAPPING OF A TELEOPERATOR SYSTEM

and

$$r_{AB}^{(A)} = r_{A'B'}^{(A')} \; for \; translation. \tag{B-1.8}$$

The remote manipulator's global rotation matrix at B, can be found using equation (B-1.7) as follows

$$[R_O^{B'}] = [R_O^{A'}][R_{B'}^{A'}] = [R_O^{A'}][R_A^B]. \tag{B-1.9}$$

The global position at B' of the remote manipulator can be obtained using equation (B-1.5) and (B-1.8). Noting

$$r_{OB} = r_{OA} + r_{AB}, \tag{B-1.10}$$

then,

$$r_{OB'} = r_{OA'} + r_{A'B'} = r_{OA'} + [R_O^{A'}]r_{A'B'}^{(A')} = r_{OA'} + [R_O^{A'}][R_A^O]r_{AB}. \tag{B-1.11}$$

B-1.2 Local-to-global mapping

In this mapping, the imposed mapping conditions can be written by

$$[R_A^B] = [R_O^{B'}][R_{A'}^O] \; for \; rotation \tag{B-1.12}$$

$$r_{AB}^{(A)} = r_{A'B'} \; for \; translation. \tag{B-1.13}$$

The remote manipulator's global rotation matrix at B can be found as follows using equation (B-1.12),

$$[R_O^{B'}] = [R_O^{B'}][R_{A'}^O][R_O^{A'}] = [R_A^B][R_O^{A'}]. \tag{B-1.14}$$

The global position at B' of the remote manipulator can be obtained using equation (B-1.13) and (B-1.5). Noting

$$r_{OB} = r_{OA} + r_{AB}, \tag{B-1.15}$$

then,

$$r_{OB'} = r_{OA'} + r_{A'B'} = r_{OA'} + r_{AB}^{(A)} = r_{OA'} + [R_A^O] r_{AB}. \qquad \text{(B–1.16)}$$

B–1.3 Global-to-local mapping

In this mapping, the mapping conditions can be written by

$$[R_O^B][R_A^O] = [R_{A'}^{B'}] \; for \; rotation \qquad \text{(B–1.17)}$$

$$r_{AB} = r_{A'B'}^{(A')} \; for \; translation. \qquad \text{(B–1.18)}$$

The remote manipulator's global rotation matrix at B, can be found using equation (B–1.17),

$$[R_O^{B'}] = [R_O^{A'}][R_{A'}^{B'}] = [R_{A'}^O][R_O^B][R_A^O]. \qquad \text{(B–1.19)}$$

The global position at B' can be obtained using equation (B–1.5) and (B–1.18)

$$r_{OB} = r_{OA} + r_{AB} \qquad \text{(B–1.20)}$$

$$r_{OB'} = r_{OA'} + r_{A'B'} = r_{OA'} + [R_O^{A'}] r_{A'B'}^{(A')} = r_{OA'} + [R_O^{A'}] r_{AB}. \qquad \text{(B–1.21)}$$

B–1.4 Global-to-global mapping

In this mapping, the mapping conditions are written by

$$[R_O^B][R_A^O] = [R_O^{B'}][R_{A'}^O] \; for \; rotation \qquad \text{(B–1.22)}$$

$$r_{AB} = r_{A'B'} \; for \; translation. \qquad \text{(B–1.23)}$$

The remote manipulator's global rotation matrix at B', can be found using equation (B–1.22),

$$[R_O^{B'}] = [R_O^{B'}][R_{A'}^O][R_O^{A'}] = [R_O^B][R_A^O][R_O^{A'}]. \qquad \text{(B–1.24)}$$

The global position at B' of the remote manipulator can be obtained using equation (B–1.23). Noting

$$\boldsymbol{r}_{OB} = \boldsymbol{r}_{OA} + \boldsymbol{r}_{AB}, \tag{B–1.25}$$

then

$$\boldsymbol{r}_{OB'} = \boldsymbol{r}_{OA'} + \boldsymbol{r}_{A'B'} = \boldsymbol{r}_{OA'} + \boldsymbol{r}_{AB}. \tag{B–1.26}$$

B–1.5 Kinematic scaling

For the translational motion, scaling can be made by post multiplying the constant gain matrix, $[g_p]$, in mapping conditions as shown in Table B–2. The scaling matrix can be defined by

$$[g_p] = \begin{bmatrix} a & 0 & 0 \\ 0 & b & 0 \\ 0 & 0 & c \end{bmatrix}. \tag{B–1.27}$$

However, the scalings for the rotational motion require more consideration. Among other cases, in this section, scaling of the rotational motion will be based on the equivalent rotational displacements about the equivalent axis, which can represent the general rotational motion of the body in space. Once equivalent axis ($\boldsymbol{k}$) and its angular displacement (ϕ_{AB}) are obtained, they can be applied to the scaling(g_r) for rotational motion in teleoperation. For example, the transform matrix, $[R_A^B]$, can be substituted by $[Rot(\boldsymbol{k},\ g_r\phi_{AB})]$.

In summary, implications for each mapping are given in Table B–1 and the results of the scaling on the rotational motion are shown in Table B–2. Note that as can be seen from the Table B–2, local and global mappings can

In Table, when $g_r \neq 1$, $[R_A^B]$ and $[R_O^B][R_A^O]$ are replaced by the cooresponding $[Rot(\boldsymbol{k},\ g_r\phi_{AB})]$.

be performed by post-multiplication and pre-multiplication of the corresponding transform tensors to the current orientation of the system. Note that the kinematic mapping from the remote manipulator to the manual controller can be made by exchanging the corresponding parameters; $A \leftrightarrow A'$, and $B \leftrightarrow B'$. In the next section, the procedure for finding the equivalent rotation axis and its equivalent rotation is provided briefly for reference.[75]

Table B–1 FOUR BASIC KINEMATIC MAPPING CONDITIONS

local-to-local mapping	$[R_A^B] = [R_{A'}^{B'}]$ for rotation $[g_p]\mathbf{r}_{AB}^{(A)} = \mathbf{r}_{A'B'}^{(A')}$ for translation
local-to-global mapping	$[R_A^B] = [R_O^{B'}][R_{A'}^O]$ for rotation $[g_p]\mathbf{r}_{AB}^{(A)} = \mathbf{r}_{A'B'}$ for translation
global-to-local mapping	$[R_O^B][R_A^O] = [R_{A'}^{B'}]$ for rotation $[g_p]\mathbf{r}_{AB} = \mathbf{r}_{A'B'}^{(A')}$ for translation
global-to-global mapping	$[R_O^B][R_A^O] = [R_O^{B'}][R_{A'}^O]$ for rotation $[g_p]\mathbf{r}_{AB} = \mathbf{r}_{A'B'}$ for translation

Table B–2 SUMMARY OF THE KINEMATIC MAPPING

mapping	rotational mapping	translational mapping
local-to-local	$[R_O^{B'}] = [R_O^{A'}][R_A^B]^*$	$\mathbf{r}_{OB'} = \mathbf{r}_{OA'} + [R_O^{A'}][R_A^O][g_p]\mathbf{r}_{AB}$
local-to-global	$[R_O^{B'}] = [R_A^B]^*[R_O^{A'}]$	$\mathbf{r}_{OB'} = \mathbf{r}_{OA'} + [R_A^O][g_p]\mathbf{r}_{AB}$
global-to-local	$[R_O^{B'}] = [R_O^{A'}]([R_O^B][R_A^O])^*$	$\mathbf{r}_{OB'} = \mathbf{r}_{OA'} + [R_O^{A'}][g_p]\mathbf{r}_{AB}$
local-to-local	$[R_O^{B'}] = ([R_O^B][R_A^O])^*[R_O^{A'}]$	$\mathbf{r}_{OB'} = \mathbf{r}_{OA'} + [g_p]\mathbf{r}_{AB}$

B–1.6 General rotation transformation of the body in space

Any combination of rotations of the body in space can be represented by a single rotation about some axis $\boldsymbol{k}$ by an angle ϕ. The followings describes a procedure of finding the equivalent rotation axis, $\boldsymbol{k}$, and the rotation angle, ϕ,

given a rotational transform matrix of the body, and its results (adapted from [75]).

The transformation matrix representing a rotation around an arbitrary vector $\boldsymbol{k}$ located at its origin can be represented by

$$[Rot(\boldsymbol{k},\phi)]=\begin{bmatrix} k_xk_x(1-c\phi)+c\phi & k_yk_x(1-c\phi)-k_zc\phi & k_zk_x(1-c\phi)-k_ys\phi \\ k_xk_y(1-c\phi)+k_zs\phi & k_yk_y(1-c\phi)+c\phi & k_zk_y(1-c\phi)-k_xs\phi \\ k_xk_z(1-c\phi)-k_ys\phi & k_yk_z(1-c\phi)+k_xs\phi & k_zk_z(1-c\phi)+c\phi \end{bmatrix} \tag{B-1.28}$$

where $\boldsymbol{k} = (k_x,\ k_y,\ k_z)^T$ is a global vector. Given a rotational transform matrix $[R_O^A]$

$$[R_O^A] = \begin{bmatrix} n_x & o_x & a_x \\ n_y & o_y & a_y \\ n_z & o_z & a_z \end{bmatrix}. \tag{B-1.29}$$

By equating the equation (B-1.28) and (B-1.29) with some manipulation, the following results can be obtained

$$\tan\phi = \frac{\sqrt{(o_x-a_y)^2+(a_x-n_z)^2+(n_y-o_x)^2}}{(n_x+o_y+a_z-1)} \tag{B-1.30}$$

and

$$k_x = \frac{o_x-a_y}{2\sin\phi} \tag{B-1.31}$$

$$k_y = \frac{a_x-n_z}{2\sin\phi} \tag{B-1.32}$$

$$k_z = \frac{n_y-o_x}{2\sin\phi}. \tag{B-1.33}$$

When the resulting rotation angle is small, the vector $\boldsymbol{k}$ should be normalized to ensure $|\boldsymbol{k}| = 1$. The resulting solution is effective when the rotation angle, ϕ, is within $0° < \phi < 150°$. But, when $\phi = 180°$, equations (B-1.31) to (B-1.33) becomes 0/0. Therefore if the rotation angle is greater than 90°, the following results and procedures are recommended;

- find the largest component of $\boldsymbol{k}$ in following expressions

$$k_x = sgn(o_z - a_y)\sqrt{\frac{n_x - \cos\phi}{1 - \cos\phi}} \tag{B-1.34}$$

$$k_y = sgn(a_x - n_z)\sqrt{\frac{a_y - \cos\phi}{1 - \cos\phi}} \tag{B-1.35}$$

$$k_z = sgn(n_y - o_x)\sqrt{\frac{a_z - \cos\phi}{1 - \cos\phi}} \tag{B-1.36}$$

  where $sgn(e) = 1$ if $e \geq 0$ and $sgn(e) = -1$ if $e \leq 0$.

- if k_x is the largest, then

$$k_y = \frac{n_y + o_x}{2k_x(1 - \cos\phi)} \tag{B-1.37}$$

$$k_z = \frac{a_x + n_z}{2k_x(1 - \cos\phi)}, \tag{B-1.38}$$

  if k_y is the largest, then

$$k_x = \frac{n_y + o_x}{2k_y(1 - \cos\phi)} \tag{B-1.39}$$

$$k_z = \frac{o_z + a_y}{2k_y(1 - \cos\phi)}, \tag{B-1.40}$$

  if k_z is the largest, then

$$k_x = \frac{a_x + n_z}{2k_z(1 - \cos\phi)} \tag{B-1.41}$$

$$k_y = \frac{o_z + a_y}{2k_z(1 - \cos\phi)}. \tag{B-1.42}$$

For more detailed discussion can be found in [37][75][100].

APPENDIX C

Hardware and Software for the Shoulder System

C–1 Listings of hardware/software for shoulder system

Table C–1 LISTINGS ON THE HARDWARE/SOFTWARE FOR SHOULDER SYSTEM

Contents	Model ID	Units	Company
Servo-disk Motor	S6M4H	3	PMI
Tachometer (analog)	S6T	3	PMI
Incremental Encoder	M23(1000-ABI-5-S-C)	3	PMI
Incremental Encoder	M23(2540-ABI-5-S-C)	1	PMI
Harmonic Drive	H6D-60	3	PMI
PWM Amplifier	VXA 48-8-16	3	PMI
Transformer	T-26-16	1	PMI
Parallel Interface Board	DRV11-J	2	DEC
Lord Force/Torque Sensor	FT 15/50	1	Lord
5 Volts Voltage Source		1	
A/D Board	ADV11-C	1	DEC
D/A Board	AAV11-C	3	DEC
Encoder's Counter IC	HCTL-2016	8	HP
Shoulder Construction		1	UT
Shoulder Supporting Frame		1	UT
Handgriper		1	UT
F/T sensor Mounting Device		1	UT
Encoder's Counter Circuit		4	UT
DRV11-J Driver	in Fortran		UT
Lord F/T Sensor Driver	in Fortran		UT
Control Software for Shoulder	in Fortran		UT

C–2 Actuator system components specifications

- Pulses of channel A and B has more than 90 degree phase difference, and pulses of Index channel, I, is generated for every revolution.

- Conversion factor of the encoders can be obtained as follows;

$$K_{enc} = \frac{2\pi}{4N_{cpr}N}(rad/count)$$

or

$$K_{enc} = \frac{360}{4N_{cpr}N}(deg/count).$$

Table C–2 ACTUATOR SYSTEM COMPONENTS SPECIFICATIONS I

S6M4H Servo-Disk Motor	
Peak Torque T_p	$186oz-in$
Continuous Stall Torque T_s	$16.6oz-in$
Peak Current I_p	$46amps$
Continuous Stall Current I_s	$4.2amps$
Rated Torque T_r	$18.9oz-in$
Rated Speed N_r	$3000rpm$
Torque Constant K_T	$4.06oz-in/amp$
Back EMF Constant K_b	$3.00volts/krpm$
Terminal Resistance R_T	$1.32ohm$
Armature Resistance R_a	$0.940ohm$
Friction Torque T_f	$0.90oz-in$
Viscous Damping Coefficient K_{vd}	$0.16oz-in/krpm$
Mass Moment of Inertia J_m	$8.510^{-4}oz-in-sec^2$
Armature Inductance L_a	less than 100 microHenry
Mechanical Time Constant T_m	$6.8msec$
Electrical Time Constant T_e	$0.11msec$
Operating current	$I=\frac{T_L+T_f+\frac{K_{vd}N}{1000}}{K_T}$
Operating voltate	$V=\frac{K_bN}{1000}+R_TI$
S6T Analog Tachometer	
Output Voltage K_{tach}	$0.75volts/krpm$
Mass Moment of Inertia J_{tach}	$0.00025oz-in-sec^2$
M23 Modular Incremental Encoder	
TTL Compatible	5 volts operation
Quadrature and Index Channels	A,B, and I
Frequency Response	$100KHz$
Mass Moment of Inertia J_{enc}	$0.00025oz-in-sec^2$
Encoder's Counter Resolution	16 bit

Table C–3 ACTUATOR SYSTEM COMPONENTS SPECIFICATIONS II

Encoder Conversion Factors	
Encoders on base actuated joints	
Number of cycles per revolution N_{cpr}	1000
Counts per cycle of HCTL-2016 IC	4
Conversion factor(rad/counts) K_{enc}	0.00002618
Conversion factor(deg/counts) K_{enc}	0.0015
Encoder on the top ternary joint	
Number of cycles per revolution N_{cpr}	2540
Counts per cycle of HCTL-2016 IC	4
Conversion factor(rad/counts) K_{enc}	0.0006184
Conversion factor(deg/counts) K_{enc}	0.03543
Harmonic Drive Reducer(HDC-3C)	
Gear Ratio N	60 to 1
Wave Generator Inertia I_wg	$0.00015lb - in - sec^2$
Friction input torque T_{cwg}	$2.5oz - in$
S6M4H/HD-60	
Mass Moment of Inertia J_{mh}	$0.7425lb - in - sec^2$
S6M4H/HD60/S6T/M23	
Mass Moment of Inertia J_{mwg}	$0.855lb - in - sec^2$
Friction Toruqe T_c	$12.75lb - in$
PWM Amplifier(VXA-48-8-16)	
Switching frequency	$> 20KHz$
Bandwidth	$500Hz$
Operational options	velocity mode and current mode
Maximum current output capacity	8 amps continuous
	16 amps peak current output
PWM Transformer(T-26-16)	
Transformer	continuous 26 volts and 16 amps.

C–3 Interfacing hardware specifications

Table C–4 INTERFACING HARDWARE SPECIFICATIONS

ADV11-C Analog Input Board	
Identification	A8000
Current configuration	16 single-ended channels
Input range	-10 to 10 volts;2's complement coding
Resolution	12-bit.
AAV11-C Analog Output Board	
Identification	A6006
Current configuration	Bipolar output, 4 channels
Output range	10 to 10 Volts
Resolution	12-bit.
DRV11-J Parallel Interface Board	
Identification	M8049
Device address	764160(encoder), 764140(F/T sensor)
Resolution	16-bit
Lord 15/50 F/T Sensor	
Maximum force/torque capacity	$15lb/50in-lb$
Force resolution	$Fx, Fy = 0.174oz; Fz = 0.576oz$
Torque resolution	$Tx, Ty, Tz = 0.391in-oz$
Communication	serial(ASCII or binary resolved data)
	parallel(strain gauge raw data)
Sampling time for F/T 15/50 sensor data	
Raw data via parallel port	$440Hz(2.27msec)$
Conv. into resol. data in μVAX II	$2.6msec$
Resol. data via. serial port	$100Hz(10.msec)$

C–4 A F/T sensor interface

The Lord F/T processor uses a Motorola MC-68B21 Peripherial Interface Adapter(PIA) for the parallel port. Through this port, strain gauge raw data are transmitted and transmission is record-oriented, where one record represents a complete set of eight strain gauge data. Interfacing MC-68B21 PIA in the F/T sensor to the DRV11-J parallel interface board in the microVAX II, is presented briefly. However, this outline provides the sufficient information for actual implementation.

First, transmission of each record is initiated by enabling DRV11-J RDY signal, which occurs when the DRV11-J is set as an input device. The DATA READY handshake line is enabled indicating to the DRV11-J that the next word is on 16-bit data bus. When the DRV11-J sees DATA READY signal high, it reads the word and replies by enabling the DRV11-J RPLY line. Note that since the DRV11-J is based on negative logic, the DATA READY and DRV11-J RPLY signals are inverted. After receiving a record, the DRV11-J is set as an output device. This causes the DRV11-J RDY signal to go high. This step is necessary for the next record since handshake lines are based on high-to-low transitions (edge triggered). For quick reference, the interface diagram and the relative signal timings of the two I/O devices are shown in Figure C–1 and Figure C–2. More details could be found in [22][53].

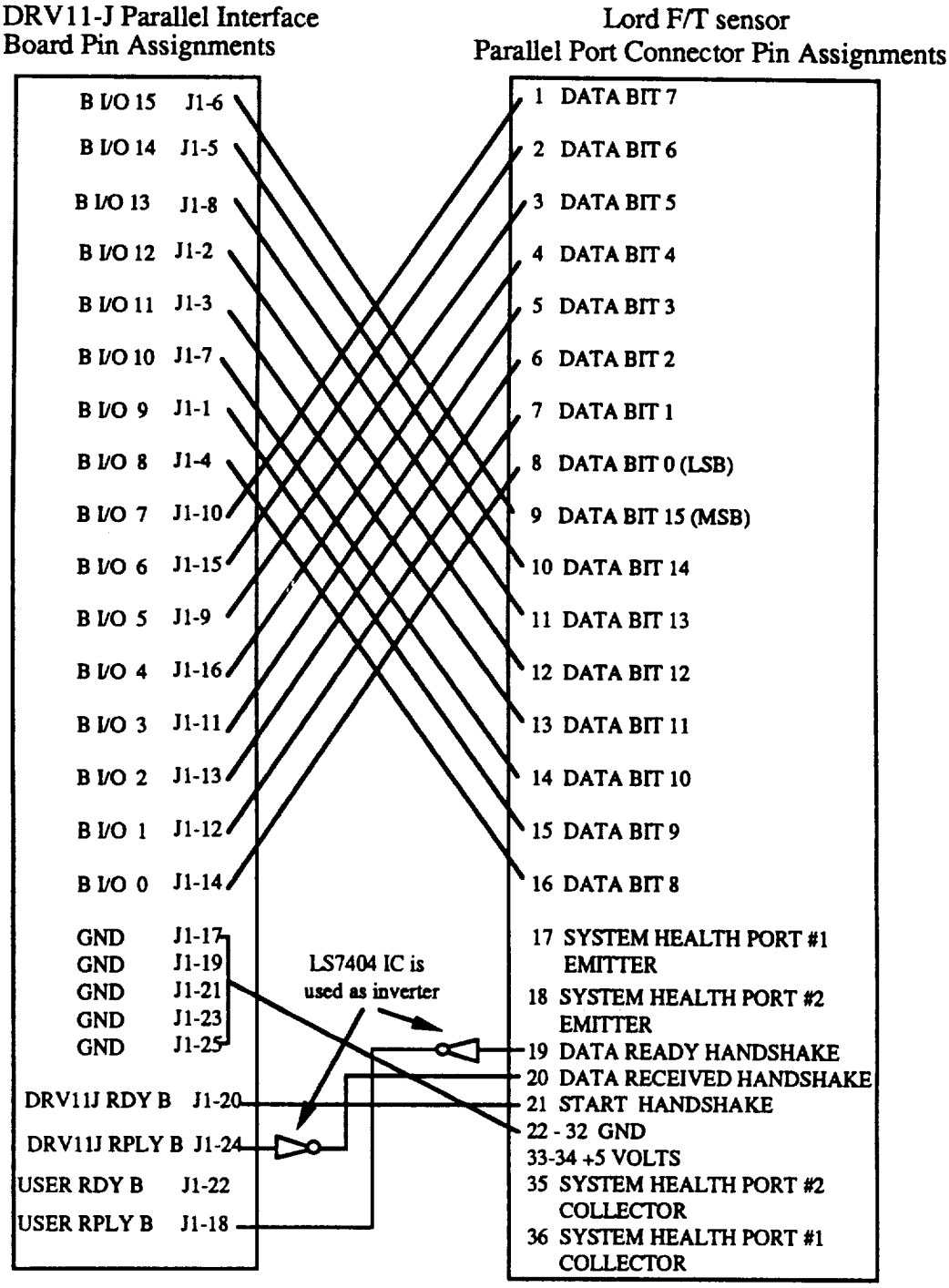

Figure C–1 PHYSICAL CONNECTIONS BETWEEN DRV11-J AND LORD F/T SENSOR

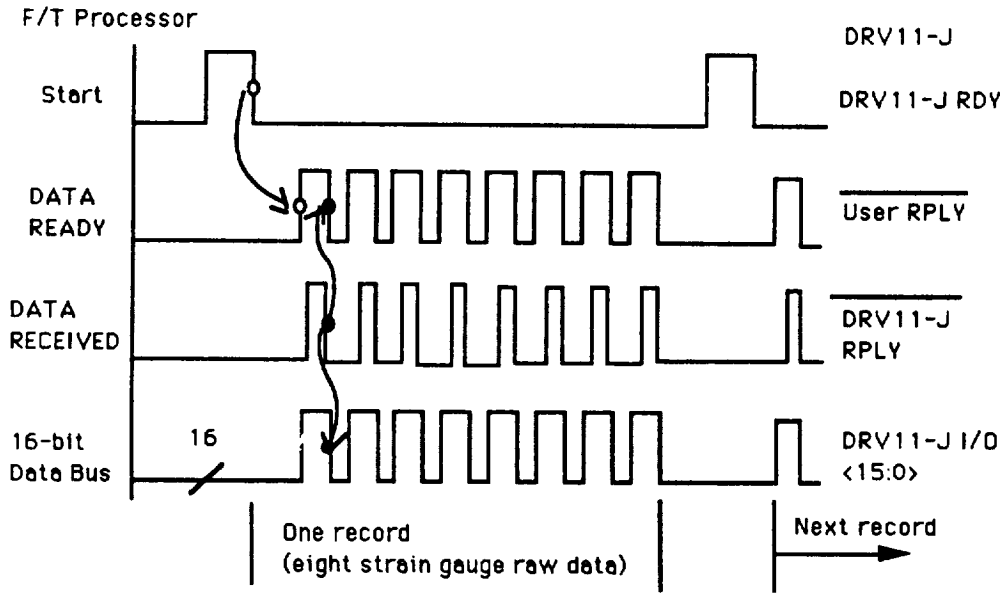

Figure C–2 SIGNAL TIMING BETWEEN THE DRV11-J AND THE F/T PROCESSOR

C–5 Hardware interfaces

C–5.1 Encoder interface diagram

C–5.2 Hardware connection diagram

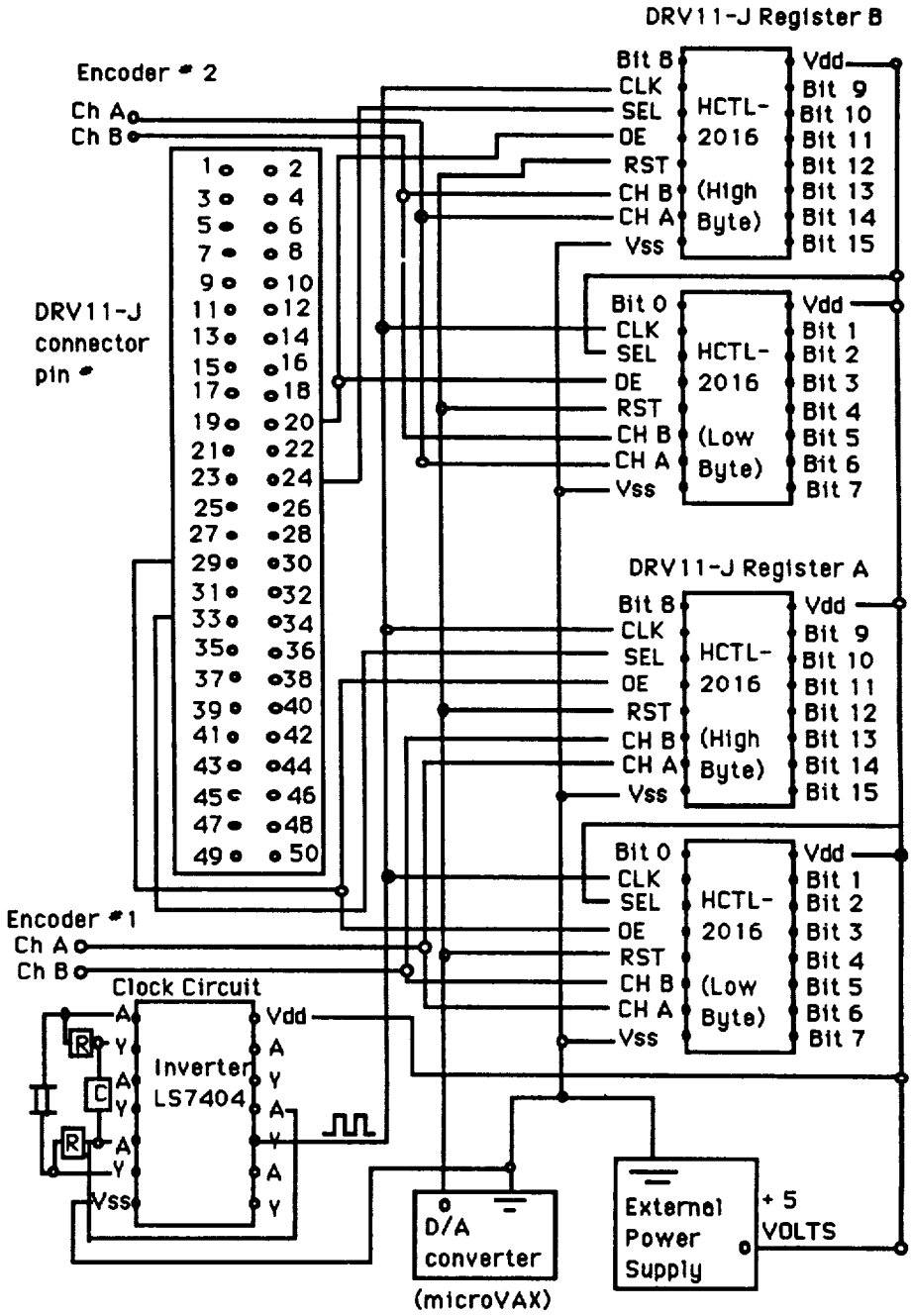

* For remaining 16-Bit data connections, refer to table C-5

* R = 330 ohms, C = 0.01 micro-farad, 5 MHz Crystal

* 5 Volts external power supply is required

Figure C-3 ENCODER'S COUNTER IC/DRV11-J INTERFACE DIAGRAM

Table C–5 PIN CONNECTIONS BETWEEN DRV11-J AND HCTL-2016 IC

DRV11-J A or D	HCTL-2016	DRV11-J B or C	HCTL-2016
37(bit 0)	D0(low byte)	14(bit 0)	D0(low byte)
39(bit 1)	D1	12(bit 1)	D1
38(bit 2)	D2	13(bit 2)	D2
40(bit 3)	D3	11(bit 3)	D3
35(bit 4)	D4	16(bit 4)	D4
42(bit 5)	D5	9(bit 5)	D5
36(bit 6)	D6	15(bit 6)	D6
41(bit 7)	D7	10(bit 7)	D7
47(bit 8)	D0(high byte)	4(bit 8)	D0(high byte)
50(bit 9)	D1	1(bit 9)	D1
44(bit 10)	D2	7(bit 10)	D2
48(bit 11)	D3	3(bit 11)	D3
49(bit 12)	D4	2(bit 12)	D4
43(bit 13)	D5	8(bit 13)	D5
46(bit 14)	D6	5(bit 14)	D6
45(bit 15)	D7	6(bit 15)	D7
29(DRV11J RDY)	OE	20(DRV11J RDY)	OE
33(DRV11J RPLY)	SEL(high byte)	24(DRV11J RPLY)	SEL(high byte)
26,28,30,32,34	Vss	17,19,21,23,25	Vss

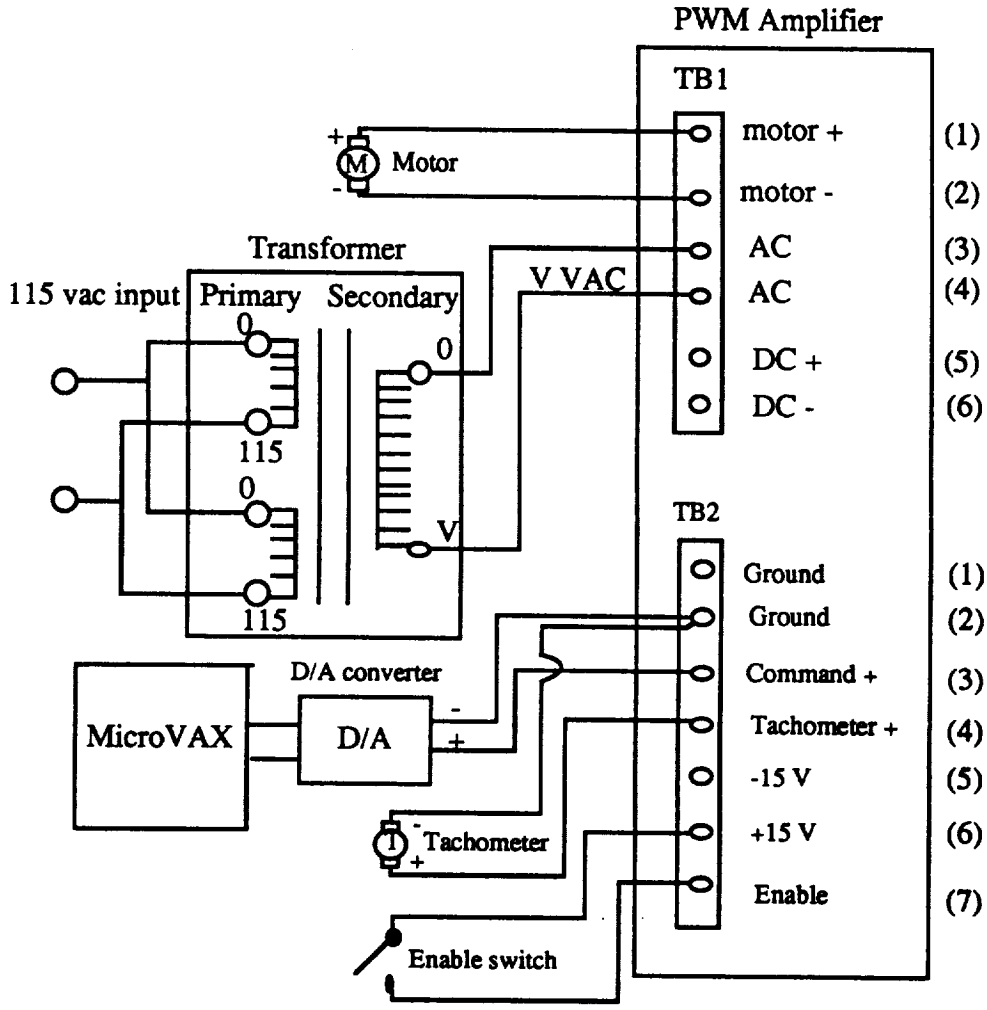

Figure C–4 ACTUATOR HARDWARE SYSTEM CONNECTION DIAGRAM

REFERENCES

[1] Abul-Haj, C., "The Design of an Elbow Prothesis Simulator for Testing Neurophysiologically Based Controller," *Proceedings of the 5th Annual Conference on Rehabilitation Engineering*, Houston, Tx, 1982.

[2] "Advancing Automation and Robotics Technology for the Space Station and for the U. S. Economy," NASA Technical Memorandum 100989, Progress Report 6, Mar., 1988.

[3] Agronin, M. and Tesar, D., "The Design and Software Formulation of a 9-string 6-Degree-of-Freedom Joystick for Telemanipulators," Master's Thesis, University of Texas at Austin, Aug., 1986.

[4] An, C.H. and Hollerback, J.M., "Kinematic Stability Issues in Force Control of Manipulators," *Proceedings of IEEE International Conference on Robotics and Automation*, Raleigh, North Carolina, Mar., 1987.

[5] An, C.H. and Hollerback, J.M., "Dynamic Stability Issues in Froce Control of Manipulators," *Proceedings of IEEE International Conference on Robotics and Automation*, Raleigh, North Carolina, Mar.,1987, pp. 890-896.

[6] Anderson, R.J. and Spong, M.W., "Bilateral Control of Teleoperators with Time Delay," *Proceedings of IEEE International Conference on Robotics and Automation*, 1988.

[7] Anderson, R.J. and Spong, M.W., "Hybrid Impedance Control of Robotic Manipulators," *IEEE Journal of Robotics and Automation*, Vol 4, No. 5, Oct., 1988.

[8] Anderson, R.J. and Spong, M.W., "Asymptotic Stability for Force Reflecting Teleoperators with Time Delay," *Proceedings of IEEE International Conference on Robotics and Automation*, Scottsdale, Arizona, May, 1989, pp. 1618-1625.

[9] Asada, H. and Granito, J.A.C., "Kinematic and Static Characterization of Wrist Joints and Their Optimal Design," *Proceedings of IEEE International Conference on Robotics and Automation*, St. Louis, Missouri, Mar., 1985, pp. 244-250.

[10] Bejczy, A.K. and Salisbury Jr., J.K., "Kinesthetic Coupling between operator and remote manipulator," *Int'l. Comp. Tech. Conf., ASME*, Aug., 1980.

[11] Brooks, T.L., "Supervisory Manipulation Based on the Concepts of Absolute vs. Relative and Fixed vs. Moving Tasks," *Proc. of ASME Int'l. Comp. Tech. Conf.*, San Francisco, Ca, Aug., 1980.

[12] Brooks, T. and Bejczy, A., "Hand Controllers for Teleoperation. A State-of-the-Art Technology Survey and Evaluation," Pasadena, CA; JPL publication 85-11.

[13] Brown, T., Matthew, G. and Tesar, D., "The Design and Fabrication of a Four Degree-of-Freedom Force Feedback Planar Manual Controller," Master's Thesis, at the University of Florida, 1983.

[14] Bryfogle, M., "The Design of a Universal Spatial Seven Degree of Freedom Manual controller for Teleoperator Systems," Master's Thesis, at the University of Florida, Aug., 1985.

[15] Caswell, D. and Gossain, D., "The Canadian Robotic Systems for the Space Station," *Second AIAA/USAF Symp. on Automation, Robotics and Advanced Computing for the National Space Program*, Arlington, VA, Mar., 1987.

[16] Chapel, J.D., "Performance Limitations of Bilateral Force Reflection Imposed by Operator Dynamic Characterisitcs," *NASA Conference on Space Telerobotics*, Pasadena, California, Jan. 31 - Feb. 2, 1989.

[17] Chiu, S.L., "Kinematic Characterization of Manipulators:An Approach to Defining Optimality," *Proceedings of IEEE International Conference on Robotics and Automation*, 1988, pp. 828-833.

[18] Cox, D.J. and Tesar, D., "The Dynamic Model of a Three Degree of Freedom Parallel Robotic Shoulder Module," *Proceedings of the 4th Int'l Conference on Advanced Robotics*, Columbus, Ohio, June, 1989.

[19] Cox, D.J. and Tesar, D., "The Dynamic Modeling and Command Signal Formulation for Parallel Multi-Parameter Robotic Devices," Master's Thesis, at the University of Florida, Sep., 1981.

[20] Craver, W.M. and Tesar, D., "Structural Analysis and Design of a Three Degree-of-Freedom Robotic Shoulder Module," Master Thesis, at the University of Texas at Austin, May, 1989.

[21] *Designer's Handbook*, Harmonic Drive 1986.

[22] *DRV11-J parallel line interface user's guide* EK-DRV1J-UG-002, digital equipment corporation, 1980.

[23] Duffy, J., *Analysis of Mechanisms and Robot Manipulators*, John Wiley and Sons, New York, NY, 1980.

[24] Eppinger, S.D. and Seering, W.P., "On Dynamic Models of Robot Force Control," *Proceedings of IEEE Conference on Robotics and Automation*, San Francisco, California, Apr., 1986, pp. 29-34.

[25] Eppinger, S.D. and Seering, W.P., "Understanding Bandwidth Limitation in Robot Force Control," *Proceedings of IEEE Conference on Robotics and Automation*, Raleigh, North Carolina, Mar., 1987, pp.904-909.

[26] Eppinger, S.D. and Seering, W.P., "Three Dynamic Problems in Robot Force Control," *Proceedings of IEEE Conference on Robotics and Automation*, Scottsdale, Arizona, May, 1989, pp. 392-397.

[27] Ferrell, W.R., "Remote Manipulation with Transmission Delay," *IEEE Transactions on Human Factors in Electronics*, Sep., 1965, pp. 24-32.

[28] Fitts, P.M., "The Information Capacity of Human Motor System in Controlling the Amplitude Movement," *Journal of Experimental Psychology*, Vol. 47, June, 1954, pp. 381-391.

[29] Flatau, C.R., "SM-229-A New Compact Servo Master-Slave Manipulator," *Proc. of the ANS 25th Conf. on Remote Systems Technology*, 1977.

[30] Fong, C.P., Dotson, R.S. and Bejczy, A.K., "Distributed Microcomputer Control System for Advanced Teleoperation," *Proceedings of IEEE International Conference on Robotics and Automation*, San Francisco, California, April, 1986.

[31] Freeman, R.A. and Tesar, D., "The Generalized Coordinate Selection for the Dynamics of Complex Planar Mechanical Systems," *Trans. of ASME, Journal of Mechanical Design*, Vol. 104, Jan., 1982.

[32] Freeman, R.A. and Tesar, D., "Dynamic Modeling of Serial and Parallel Mechanisms/Robotic Systems, Part I-Methodology, Part II-Applications," *Proceedings of 20th ASME Mechanisms Conference*, Orlando, FL, 1988.

[33] Freeman, R.A., "Feedforward Stiffness Control of Overconstrained Mechanisms/Robotic Linkage Systems," *ASME Winter Annual Meeting*, Chicago, 1988, pp. 251-269.

[34] Furuta, K., Kosuge, K., Shiote, Y. and Hatano, H., "Master-Slave Manipulator Based on Virtual Internal Model Following Control Concept," *Proc. of 1987 IEEE International Conference on Robotics and Automation*, Raleigh, Norh Carolina, March, 1987.

[35] Gelb, A. and Vander Velde, W.E., *Multiple-Input Describing Functions and Nonlinear System Design*, McGraw-Hill Book Company, New York, 1968.

[36] Goertz, R.C., "Manipulators Used for Handling Radioactive Materials," *Human Factors In Technology*, Chapter 27, edited by E.M. Bennett, McGraw-Hill, 1963.

[37] Hamilton, W.R., *Elements of Quaternions*, Chelsea Publishing Co, New York, 1969.

[38] Handlykken, M. and Turner, T., "Control System Analysis and Synthesis for a Six Degree-of-Freedom Universal Force-Reflecting Hand Controller," *Proceedings of the 19th IEEE International Conference on Decision and Control*, Dec., 1980, Albuquerque, New Mexico.

[39] Hannaford, B. and Anderson, R., "Experimental and Simulation Studies of Hard Contace in Force Reflecting Teleoperation," *Proceedings of IEEE International Conference on Robotics and Automation*, 1988.

[40] Hannaford. B., "A Design Framework for Teleoperators with Kinesthetic Feedback," *Journal of IEEE Transactions on Robotics and Automation*, Vol. 5, No. 4, Aug., 1989, pp. 426-434.

[41] Herdon, J. N., et al., "The State-of-the-Art Model M-2 Maintenance System," *Proc. of the ANS National Topical Meeting on Robotics and Remote Handling in Hostile Environments*, April 1984.

[42] Hewlett Packard Technical Data Manual on Quadrature Decoder/Counter Interface IC, Nov., 1988.

[43] Hill, J.W. and Salisbury, J.K., "Study to Design and Develop Remote Manipulator Systems," Annual report 2, SRI, 1977.

[44] Hirzinger, G., "Direct Digital Robot Control Using A Force-Torque Sensor," *IFAC Real Time Digital Control Applications*, Guadalajara, Mexico, 1983.

[45] Hogan, N., "Impedance Control: An Approach to Manipulation: Part I - Theory," *ASME Journal of Dynamic Systems, Measurements and Control*, Vol. 107, March, 1985.

[46] Hogan, N., "Impedance Control: An Approach to Manipulation: Part II - Implementation," *ASME Journal of Dynamic Systems, Measurements and Control*, Vol. 107, March, 1985.

[47] Hogan, N., "Impedance Control: An Approach to Manipulation: Part III - Applications," *ASME Journal of Dynamic Systems, Measurements and Control*, Vol. 107, March, 1985.

[48] Hogan, N., "Controlling Impedance at the Man/Mahcine Interface," *Proceedings of IEEE International Conference on Robotics and Automation*, Vol. 3, Scottsdale, Arizona, 1989, pp. 1626-1631.

[49] Hudgens, J.C., and Tesar, D., "A Fully-Parallel Six Degree-of-Freedom Micromanipulator:Kinematic Analysis and Dynamic Model", *Trends and Developments in Mechanisms, Machines, and Robotics*, ASME 20th Biennial Mechanisms Conference, Kissimmee, FL, Sep., 1988, pp29-37.

[50] Hunt, K.H., "Kinematic Geometry of Mechanisms," Clarendon Press, Oxford, 1978.

[51] Hunt, K.H., "Structural Kinematics of In-Parallel-Actuated Robot-Arms," *Trans. of ASME, Journal of Mechanisms, Transmissions, and Automation in Design*, Vol. 105, Dec., 1983.

[52] Inoue, H., et al., "Parallel Manipulator," *Proceedings of IEEE International Conference on Robotics and Automation*, 1987.

[53] *Installation and Operations Manual: F/T Series Force/Torque Sensing Systems*, Lord Industrial Automation, Industrial Automation Division, Cary, NC., Sep., 1985.

[54] Kazerooni, H., et al., "Robust Compliant Motion for Manipulators, Part I:The Fundamental concepts of Compliant Motion," *IEEE Journal of Robotics and Automation*, Vol. RA-2, No. 2, June, 1986, pp. 83-92.

[55] Kazerooni, H., et al., "Robust Compliant Motion for Manipulators, Part I:Design Method," *IEEE Journal of Robotics and Automation*, Vol. RA-2, No. 2, June, 1986, pp. 93-105.

[56] Kim, W.S., et al., "A Comparison of Position and Rate Control for Telemanipulations with Consideration of Manipulator System Dynamics," *IEEE Journal of Robotics and Automation*, vol. RA-3, no. 5, Oct., 1987.

[57] Kleinman, D.L., Baron, S. and Levison, W.H., "An Optimal Control Model of Human Response Part I: Theory and Validation," *Automatica*, Vol. 6, 1970, pp. 357-369.

[58] Klema, V.C. and Laub, A.J., "The Singular Value Decomposition:Its Computation and Some Applications," IEEE Trans. Auto. Cont., Vol. AC-25, No. 2, April, 1980.

[59] Kuban, D.P. and Martin, H.L., "An Advanced Remotely Maintenable Force-Reflecting Servomanipulator Concept," *Proc. of 1984 National Topical Meeting on Robotics and Remote Handling in Hostile Environments*, April, 1984.

[60] Landsberger, S.E. and Sheridan, T.B., "A New Design for Parallel Link Manipulators," *Proc. of 1985 IEEE International Conference on Robotics and Automation*, 1985.

[61] Lee, K., and Shah, K., "Kinematic Analysis of a Three Degrees of Freedom In-Parallel Actuated Manipulator," *Preceedings of IEEE International Conference on Robotics and Automation*, 1987, pp. 345-350.

[62] Li, S. and Matthew, G.K., "Closed Form Kinematic Analysis of Planar Assur II Groups," source (***).

[63] Lindemann, R., Tesar, D. and Tosunoglu, S., "Construction and Demonstration of a 9-String 6-DOF Force Reflecting Joystick for Telemanipulation," Master's Thesis, at the University of Texas at Austin, Dec., 1987.

[64] Lipkin, H., Duffy, J. and Tesar, D., "Kinematic Control of a Robotic Manipulator with a Universal Manual Controller," Master's Thesis, at the University of Florida, May, 1983.

[65] Lipkin, H. and Duffy, J., " Elliptic polarity of Screws," *Trans. of ASME, Journal of Mechanisms, Transmissions, and Automation in Design*, 107, 1985, pp377-387.

[66] Lipkin, H. and Duffy, J., "Hybrid Twist and Wrench Control for a Robotic Manipulator," *Journal of Mechanisms, Transmissions, and Automation in Design*, 1988, pp. 1-7.

[67] MaGovern, D.E., "Comparison of Two Manipulators Using a Standard Task of Varying Difficulty," ASME Paper 74-WA/Bio-4, 1974.

[68] Marco, D. and Tesar, D., "Computer Simulation and Design of a Three Degree-of-Freedom Shoulder Module," Master's Thesis, at the University of Texas at Austin, Aug., 1987.

[69] Martin, H. L. and Kuban, D.P., "Teleoperated Robotics in Hostile Environments", published by *Robotics International of SME*, 1985.

[70] Mcruer, D., "Human Dynamics in Man-Machine Systems," *Automatica*, Vol. 16, 1980, pp. 237-253.

[71] Miyazaki, F., et al., "A New Control Methodology Toward Advanced Teleoperation of Master-Slave Robot Systems," *Proc. of 1986 IEEE International Conference on Robotics and Automation*, San Francisco, California, April, 1986.

[72] Mosher, R.S. and Wendel, B., "Force-Reflecting Electrohydraulic Servomanipulator," *Electro-Technology*, Dec., 1960.

[73] *Operating Instructions: PMI VXA Series, PWM Servo Amplifier with Power Supply, Model VXA-48-8-16*, PMI Motion Technologies, Jan., 1988.

[74] Parsons, H.M., "Human Factors Engineering Issues in Army Field Robotics Applications," Preprard for the U.S. Army Human Engineering Laboratory, Aberdeen Proving Ground, MD. Huntsville, AL. Essex Corp., 1985.

[75] Paul, R., *Robot Manipulators*, The MIT Press, Cambridge, MA, 1981.

[76] Raibert, M.H. and Craig, J.J., "Hybrid Position/Force Control of Manipulators," *Transactions of the ASME*, Vol. 102, June, 1981.

[77] Raju, G.J., et al., "Design Issues in 2-Port Network Models of Bilateral Remote Manipulation," *Proceedings of IEEE International Conference on Robotics and Automation*, Scottsdale, Arizona, May, 1989, pp. 1316-1321.

[78] Ravindran, R., Assaf, S.A. and Nguyen, P.K., "Shuttle Remote Manipulator Control System and In-Flight Verification," *Int'l. symp. on Design and Synthesis*, Tokyo, July, 1984.

[79] Roberts, R.K., et al., "The Effect of Wrist Force Sensor Stiffness on the Control of Robot Manipulators", *Proceedings of IEEE International Conference on Robotics and Automation*, 1985.

[80] Salisbury, J.K., "Active Stiffness Control of a Manipulator in Cartesian Coordinates," *Proceedings of IEEE International Conference on Decision and Control*, Albuquerque, New Mexico, Nov., 1980.

[81] Sheridan, T.B. and Ferrel, W.R., "Remote Manipulative Control with Transmission Delay," IEEE Transactions on Human Factors in Electronics, Sep., 1963, pp. 25-29.

[82] Sheridan, T.B. and Verplank, W.L., "Human and Computer control of Underseas Teleoperators," Man-Machine System Laboratory Report, MIT, 1978.

[83] Sklar, M. and Tesar. D., "The Analysis of Hybrid Parallel/Serial Robotic Manipulators," Master's Thesis, at the University of Florida, Gainesville, FL, April, 1984.

[84] Sklar, M. and Tesar, D. "Dynamic Analysis of Hybrid Serial Manipulator Systems Containing Parallel Modules," *Trans. of ASME, Journal of Mechanisms, Transmissions, and Automation in Design*, Vol. 110, June, 1988.

[85] Stewart, D., "A Platform with Six Degrees of Freedom," *Proc. Inst. Mech. Engr.*, Vol 180, pt. 1, 1965-6, pp. 371-386.

[86] Strang, G., *Linear Algebra and Its Applications*, Academic Press, New York, 1980.

[87] Tesar, D., et al., "Controller Development for CESARm and Hermies III," DOE/NE Robotics Program DEME'89 User's Guide, Oct., 1989.

[88] Tesar, D. and Lipkin, H., "Assessment for the Man-Machine Interface Between the Human Operator and the Robotic Manipulator," CIMAR Report to the DOE and NSF, at the University of Florida, Oct., 1979.

[89] Tesar, D. and Kim, W., "Universal Man-Machine Interface Architecture for Teleoperator Control of Space Systems," Preliminary Internal Report, July, 1988.

[90] Tesar, D., Kim, W., Butler, M.S., and Joe, Fenwick, "Priliminary Road Map for Teleoperator Control Systems," Internal report, at TIMAR, Nov., 1988.

[91] Thomas, G.B., "Technology for Mobile Robotics in Nonmanufacturing Applications," *RI/SME West Conference*, Nov., 1984.

[92] Thomas, M and Tesar, D., "Dynamic Modeling of Serial Manipulator Arms," *Trans. of ASME, Journal of Dynamic Systems, Measurement, and Control*, Vol. 104, Sep., 1982.

[93] Townsend, W.T. and Salisbury Jr, J.K., "The Effect of Coulomb Friction and Stiction on Force Control," *Proceedings of IEEE International Conference on Robotics and Automation*, Raleigh, North Carolina, Mar., 1987.

[94] Vertut, J., et al., "Short Transmission Delay on a Froce Reflective Bilateral Manipulator," *Proceedings of 4th Rom-An-Sy, Warsaw*, 1981, pp.269.

[95] Walker, C., et al., "The Control and Implementation of a Four Degree of Freedom Force-Feedback Planar Manual Controller," at the University of Florida, 1981.

[96] Wayne, J.B., "Teleoperator Arm Design," chap 9, *Handbook of Industrial Robotics*, John Wiley & Sons, 1985.

[97] Wedel, D.L. and Saridis, G.N., "An Experiment in Hybrid Position/Froce control of a Six DOF Revolute Manipulator," *Proceedings of IEEE International Conference on Robotics and Automation*, Philadelphia, 1988, pp. 1638-1642.

[98] Whitney, D.E., "Resolved Motion Rate Control of Resolved Manipulators and Human Prostheses," *5th Annual NASA-University Conf. on Manual Control*, MIT, Cambridge, MA, Mar., 1969.

[99] Whitney, D.E., "Force Feedback Control of Manipulator Fine Motions," *Journal of Dyanmic Systems, Measurement and Control, ASME Transactions*, Dec., 1972.

[100] Whitney, D.E., "The Mathematics of Coordinated Control of Prosthetic Arms and Manipulators," *Trans. of ASME, Journal of Dynamics Systems, Measurement, and Control*, Dec., 1972, pp. 303-309.

[101] Whitney, D.E., "Historical Perspective and State of the Art in Robot Force Control," *International Journal of Robotics Research*, Vol. 6, No. 1, Spring, 1987.

[102] Whitney, D.E. and Nevins, T.L., "What is Remote Center Compliance and What Can It Do ?" *Proceedings of 9th Int'l. Symposium on Industrial Robots*, Washington, D.C., March 14, 1979, pp. 275-282.

[103] Wlassich, J.J., "Nonlinear Force Feedback Impedance Control," Master's Thesis, MIT, Feb., 1986.

[104] Yang, D.C.H. and Lee, T.W., "Feasibility Study of a Platform Type of Robotic Manipulators from a Kinematic Viewpoint," *Journal of Mechanisms, Transmissions, and Automation in Design*, Vol. 106, June, 1984.

[105] Yoshikawa, T., "Analysis and Control of Robot Manipulators with Redundancy," *Robotics Research:The First Int'l Symposium*, edited by M. Brady and R. Paul, MIT Press, 1984, pp. 735-747.

[106] Young, L.R., "On Adaptive Manual Control," *IEEE Transactions on Man-Machine Systems*, Dec. 1969, pp. 292-331.